

The Pennsylvania State University
The Graduate School
Eberly College of Science

**ATOMISTIC ELECTRODYNAMICS-QUANTUM MECHANICAL METHODS
TO MODEL SURFACE-ENHANCED NONLINEAR OPTICAL
SPECTROSCOPIES**

A Dissertation in
Chemistry
by
Zhongwei Hu

© 2017 Zhongwei Hu

Submitted in Partial Fulfillment
of the Requirements
for the Degree of

Doctor of Philosophy

December 2017

The dissertation of Zhongwei Hu was reviewed and approved* by the following:

Lasse Jensen
Associate Professor of Chemistry
Dissertation Advisor, Chair of Committee

Paul S. Cremer
J. Lloyd Huck Chair in Natural Sciences
Professor of Chemistry, Biochemistry and Molecular Biology

William G. Noid
Associate Professor of Chemistry

Zhiwen Liu
Professor of Electrical Engineering

Thomas E. Mallouk
Evan Pugh University Professor of Chemistry, Biochemistry and Molecular Biology,
Physics, and Engineering Science and Mechanics
Head of the Department of Chemistry

*Signatures are on file in the Graduate School.

Abstract

Spectroscopy, the study of interactions between radiation and matter, often becomes more complicated for intense radiation due to the cause of nonlinearity. At the molecular level, the nonlinear optical (NLO) properties can be described using higher-order polarizability tensors, such as the first and second hyperpolarizabilities. Providing an insight into these properties is essential for designing NLO devices, and thus theoretical tools that can accurately and efficiently model them are greatly needed. The sum-over-states model within a time-dependent density functional theory (TDDFT) framework is probably the most commonly used tool, and has shown success in calculating resonant NLO properties. However, this approach often assumes that a few states dominate the response, and consequently becomes less reliable when far from resonances or for systems that are characterized by a high density of states, such as metal clusters. To overcome this limitation, we have adopted response theory that takes all states into account by construction. With a phenomenological damping factor embedded into it, termed damped response theory, a balanced description of all off-, near-, and on-resonance optical properties can be enabled for both molecules and metal clusters. With the damped nonlinear response theory, we have performed simulations for the resonance hyper-Rayleigh scattering (HRayS) of both molecules and small Ag clusters, the frequency-scanned hyper-Raman scattering (HRS) of the octupolar molecule crystal violet (CV), and the two-photon absorption (TPA) of the thiolate-protected Au₂₅ cluster. These achievements allow for evaluating two-photon resonance enhanced HRayS of Ag clusters, indicate the HRS of CV is dominated by the Franck-Condon effects at the lowest two excitation energies, and reveal the one- and two-photon double resonance effect is not the main cause of the huge TPA cross sections of Au₂₅(SH)₁₈⁻ found experimentally. However, widespread of the NLO techniques is still impeded by their inherent low cross sections. One routine solution is to intensify the spectroscopic signals via chemical mechanism (CM), e.g., the molecular resonance effects; alternatively, electromagnetic mechanism (EMM) that arises from surface localized plasmons can also significantly enhance the signal intensities. For surface-enhanced Raman scattering (SERS), it has been found that the EMM plays a more important role in the signal enhancement as compared to the CM. To this end, we focus on the EMM and have developed two atomistic electrodynamic-quantum mechanical models to include the surface effects on HRS, termed surface-enhanced HRS (SEHRS). The first is the discrete interaction model/quantum mechanical model, which combines an atomistic electrodynamic model of the nanoparticle with a TDDFT description of the molecule. The second is a dressed-tensors method that accounts for the interactions between the molecule and the inhomogeneous local fields. With these methods, we have shown that the field gradient effects mainly determine the surface selection rules and the enhancements for SEHRS, and are more important than their counterparts in SERS. Combining the dressed-tensors approach with a wavepacket dynamics model, we have qualitatively predicted the orientation of Rhodamine 6G adsorbed onto silver nanoparticles.

Table of Contents

List of Figures	viii
List of Tables	x
List of Symbols	xi
Acknowledgments	xii
I Introductory Material	1
Chapter 1	
Introduction	2
Overview of Dissertation	4
II Describing Nonlinear Optical Properties with Damped Response Theory	7
Chapter 2	
Simulation of Resonance Hyper-Rayleigh Scattering of Molecules and Metal Clusters Using a Time-Dependent Density Functional Theory Approach	8
2.1 Introduction	9
2.2 Theory	10
2.3 Computational Details	13
2.4 Results and Discussion	13
2.4.1 HRayS of A Dipolar Chromophore: Para-nitroaniline	15
2.4.2 HRayS of A Octupolar Chromophore: Crystal Violet	16
2.4.3 HRayS of A Silver Cluster	20
2.5 Conclusion	22
Chapter 3	
Probing Two-Photon Molecular Properties with Surface-Enhanced Hyper-Raman Scattering: A Combined Experimental and Theoretical Study of Crystal Violet	23
3.1 Introduction	24
3.2 Experimental Methods	26

3.3	Theoretical Methods	26
3.4	Results and Discussion	27
3.4.1	Theory/Experiment Comparison	27
3.4.2	Theory/Experiment Discrepancies	29
3.4.3	SEHRS Peak-Area Ratios	30
3.5	Conclusion	32
Chapter 4		
	Simulating Third-order Nonlinear Optical Properties Using Damped Cubic Response Theory within Time-Dependent Density Functional Theory	33
4.1	Introduction	34
4.2	Theory	35
4.2.1	Damped Response Theory	35
4.2.1.1	Linear Response	36
4.2.1.2	Quadratic Response	37
4.2.1.3	Cubic Response	39
4.2.2	The SOS Approach	40
4.2.3	Two-Photon Absorption Cross Section	41
4.3	Computational Details	42
4.4	Results and Discussion	43
4.4.1	Comparing Response Theory and the SOS Approach for LiH	43
4.4.2	TPA and THG of DANS	47
4.5	Conclusion	49
Chapter 5		
	Importance of Double-Resonance Effects in Two-Photon Absorption Properties of $\text{Au}_{25}(\text{SR})_{18}^-$	51
5.1	Introduction	52
5.2	Theory	53
5.3	Computational Details	54
5.4	Results and Discussion	55
5.5	Conclusion	61
III Simulating Metal Surface Effects on Nonlinear Optical Properties		62
Chapter 6		
	Theory of Linear and Nonlinear Surface-enhanced Vibrational Spectroscopy	63
6.1	Introduction	64
6.2	Surface-Enhanced Raman Scattering	65
6.2.1	Electromagnetic Mechanism	66
6.2.1.1	Silberstein's Equations	66
6.2.1.2	Gersten-Nitzan Model	67
6.2.1.3	Image Field Effect	68
6.2.1.4	Dressed-Tensor Formalism	69
6.2.1.5	Local Field Gradients	70

6.2.1.6	Point-dipole / Point-quadrupole Molecule	71
6.2.2	Chemical Mechanism	73
6.2.2.1	Resonance Raman Mechanism	74
6.2.2.2	Charge-transfer Mechanism	74
6.2.2.3	Off-resonance Mechanism	75
6.3	Surface-Enhanced Raman Optical Activity	75
6.3.1	Electromagnetic Mechanism	76
6.3.2	Chemical Mechanism	78
6.4	Surface-Enhanced Hyper-Raman Scattering	78
6.4.1	Electromagnetic Mechanism	78
6.4.2	Chemical Mechanism	79
6.5	Surface-Enhanced Sum-Frequency Generation	80
6.6	Surface-Enhanced Coherent Anti-Stokes Raman Scattering	81
Chapter 7		
Simulating Surface-Enhanced Hyper-Raman Scattering Using Atomistic Electrostatics-Quantum Mechanical Models		83
7.1	Introduction	84
7.2	Theory	85
7.2.1	The DIM/QM Method	85
7.2.2	The Dressed-Tensors Formalism	87
7.3	Computational Details	88
7.4	Results and Discussion	89
7.4.1	SEHRS of Benzene	89
7.4.2	Importance of Molecular Resonance, Image and Local Fields Effects	92
7.4.3	The Field-Gradient Effects	94
7.4.4	SEHRS of Pyridine	96
7.4.5	Enhancement Factors in SEHRS	99
7.5	Conclusion	100
Chapter 8		
Surface-Enhanced Resonance Hyper-Raman Scattering Elucidates the Molecular Orientation of Rhodamine 6G on Silver Colloids		102
8.1	Introduction	103
8.2	Results and Discussion	104
8.3	Conclusion	107
IV Recent Research Progress		109
Chapter 9		
Application of Current Simulation Tools and Development of New Theoretical Methods		110
9.1	Application of Current Simulation Tools	111
9.1.1	Surface-Enhanced Hyper-Raman Scattering of Deuterated Rhodamine 6G	111
9.1.2	Tip-Enhanced Hyper-Raman Images at the Single-Molecule Level	113
9.1.3	Third-Harmonic Generation of a Na ₂₀ Dimer	114
9.2	Development of New Theoretical Methods	117

9.2.1	Surface-Enhanced Third-Order Nonlinear Optical Properties	117
V	Summary and Outlook	121
Chapter 10		
	Summary and Outlook	122
10.1	Dissertation Summary	122
10.2	Future Directions for the Damped Nonlinear Response Theory	123
10.3	Future Directions for the Nonlinear DIM/QM Method	124
	Appendices	126
Appendix A		
	Supporting Information for: Simulating Third-order Nonlinear Optical Properties Using Damped Cubic Response Theory within Time-Dependent Density Functional Theory	127
A.1	Derivation of the Relationship Between $\epsilon^{\alpha\beta\dagger}$ and $\epsilon^{\alpha\beta}$	127
A.2	Derivation of the Reduced IDRI Second Hyperpolarizability	130
A.3	Comparison of SZ and STO-3G Basis Sets	131
A.4	Comparison of Response Theory and SOS Approach at the FCI Level of Theory	132
A.5	Comparison of Response Theory and SOS Approach at the TDDFT Level of Theory	133
A.6	Derivation of the spectral representation for the first hyperpolarizability	138
Appendix B		
	Supporting Information for: Importance of Double-Resonance Effects in Two-Photon Absorption Properties of $\text{Au}_{25}(\text{SR})_{18}^-$	142
B.1	TPA Cross Sections per Gold Atom	142
Appendix C		
	Supporting Information for: Surface-Enhanced Resonance Hyper-Raman Scattering Elucidates the Molecular Orientation of Rhodamine 6G on Silver Colloids	143
C.1	Experimental Methods	143
C.2	Theoretical Methods	143
C.2.1	Transition Response Properties for Molecules	144
C.2.2	Surface Effects on Transition Response Properties	145
C.2.3	Differential Cross Section Calculations	146
C.3	A- and B-Terms in RRS and RHRS of R6G at S_1	146
C.4	Spectral Matching of the Experimental SEHRS of R6G	148
C.5	Simulated SEHRS Spectra at Optimal Geometry and Boundary Regions	149
C.6	Orientation Dependence of the β_{zzz} Values	154
	Bibliography	155

List of Figures

2.1	Simulated HRayS and depolarization ratio of <i>p</i> -NA	16
2.2	Comparison of simulated and experimental absorption of CV	17
2.3	Comparison of simulated and experimental HRayS of CV	18
2.4	Simulated depolarization ratio of CV	19
2.5	Simulated absorption and HRayS of Ag ₈	20
2.6	Simulated absorption and HRayS of Ag ₂₀	21
3.1	Experimental OPA, TPA, and SEHRS of CV	25
3.2	Comparison of simulated RS/HRS and experimental SERS/ SEHRS of CV	28
3.3	Comparison of experimental SEHRS, HRS, and SE2HRS of CV	29
3.4	Experimental SEHRS peak-area ratios of CV	31
4.1	Simulated TPA of LiH using γ_{IDRI}	44
4.2	Simulated TPA of LiH using γ_{TPA}	45
4.3	Simulated OKE of LiH	45
4.4	Simulated SHG of LiH	47
4.5	Comparison of simulated and experimental absorption of DANS	47
4.6	Comparison of simulated and experimental TPA of DANS	48
4.7	Comparison of simulated and experimental THG of DANS	49
5.1	Comparison of simulated and experimental absorption of Au ₂₅ (SR) ₁₈ ⁻	55
5.2	Simulated TPA of Au ₂₅ (SH) ₁₈ ⁻	56
5.3	Energy level diagram of Au ₂₅ (SR) ₁₈ ⁻	57
5.4	Simulated TPA of Au ₂₅ (SH) ₁₆ (SPh) ₂ ⁻	59
5.5	Comparison of calculated $\text{Re}\{\gamma^{\text{IDRI}}\}$, $\text{Im}\{\gamma^{\text{TPA}}\}$, and $\text{Im}\{\gamma^{\text{IDRI}}\}$ of Au ₂₅ (SH) ₁₈ ⁻	60
6.1	Illustration of the mechanisms of SERS	65
6.2	SERS surface selection rules from benzene	72
6.3	Normal Raman and SERS of pyridine on Ag ₂₀	76
6.4	Comparison of simulated HRS and experimental SEHRS of R6G	80
7.1	The benzene-Ag ₂₀₅₇ model system	90
7.2	Simulated NHRS and SEHRS of benzene	91
7.3	Specific normal modes of benzene.	92
7.4	Simulated RHRS and SEHRS of benzene	93
7.5	FG contributions to SEHRS of benzene	95
7.6	Simulated SEHRS of benzene titled at 10° with respect to the surface	96
7.7	The pyridine-Ag ₁₀₁₇₉ model system	97

7.8	Comparison of simulated and experimental SEHRS of pyridine	98
7.9	Enhancement factors for SEHRS and SERS of pyridine	101
8.1	Effect of adsorbate geometry for SERS and SEHRS of R6G	105
8.2	β unit sphere representations of R6G's modes at 1535.24 and 1657.91 cm^{-1}	105
8.3	Initial geometry and orientation scheme for R6G	106
8.4	Comparison of experimental and simulated SEHRS ($\theta = 79^\circ$, $\psi = 79^\circ$) of R6G, S_1	107
8.5	Heat map of the agreement between simulated and experimental SEHRS of R6G	108
9.1	Simulated TPA and experimental SEHRS of R6G-d0 and R6G-d4	112
9.2	Experimental SEHRS and simulated HRS of R6G-d0 and R6G-d4 in the lower frequency range.	112
9.3	Vibrational motions for three modes of benzene.	113
9.4	Simulated TER and TEHR images for three modes of benzene	114
9.5	Simulated spectral evolution of the absorption cross-sections of a Na_{20} dimer	115
9.6	Simulated spectral evolution of the THG intensities of a Na_{20} Dimer	116
A.1	Simulated EOPE of LiH	133
A.2	Simulated OR of LiH	134
A.3	Simulated EFIOR of LiH	135
A.4	Simulated EFISHG of LiH	136
A.5	Simulated THG of LiH	137
A.6	Simulated SHG of LiH with and without g_{xc}	141
B.1	Simulated TPA cross section on a per atom basis for three different gold species	142
C.1	α unit sphere representations of R6G's modes at 1535.24 and 1657.91 cm^{-1}	147
C.2	Comparison of experimental and simulated SEHRS ($\theta = 79^\circ$, $\psi = 79^\circ$) of R6G, S_2	149
C.3	Comparison of experimental and simulated SEHRS ($\theta = 50^\circ$, $\psi = 75^\circ$) of R6G	150
C.4	Comparison of experimental and simulated SEHRS ($\theta = 60^\circ$, $\psi = 90^\circ$) of R6G	151
C.5	Comparison of experimental and simulated SEHRS ($\theta = 90^\circ$, $\psi = 85^\circ$) of R6G	152
C.6	Comparison of experimental and simulated SEHRS ($\theta = 90^\circ$, $\psi = 100^\circ$) of R6G	153
C.7	β_{zzz} values of R6G's modes at 1535.24 and 1657.91 cm^{-1}	154

List of Tables

6.1	Contributions of the EMM enhancement factor to the intensity of SERS	73
9.1	Simulated Plasmon-Assisted EFISHG for LiH	120
A.1	Simulated static α , β and γ for LiH at the TDDFT level	131
A.2	Simulated static α , β and γ for LiH at the FCI level	132
A.3	Simulated resonant α and β for LiH at the FCI level	132
C.1	Modes Chosen for Comparison	148

List of Symbols

Below are a list of the most common sub- and super-scripts:

- i, j Occupied orbitals
- a, b Virtual or unoccupied orbitals
- $\alpha, \beta, \gamma, \delta$ Cartesian coordinates

Symbols will be defined as they are introduced, but the most common symbols are:

- ρ Electron Density
- ϕ Kohn-Sham Orbital
- χ Atomic Orbital
- ν_{xc} Exchange-Correlation (XC) Potential
- f_{xc} First-Order XC Kernel
- g_{xc} Second-order XC Kernel
- h_{xc} Third-order XC Kernel
- ω Incident Frequency
- E_α Electric Field
- $\alpha_{\alpha\beta}$ Polarizability
- $\beta_{\alpha\beta\gamma}$ First Hyperpolarizability
- $\gamma_{\alpha\beta\gamma\delta}$ Second Hyperpolarizability
- Γ Damping Factor
- $\delta_{\alpha\beta}$ Kronecker Delta
- $F_\beta^{\text{loc},\alpha}$ Local Field
- $F_\beta^{\text{loc},\alpha,\beta}$ Local Field Gradient

Acknowledgments

I am grateful to many people during my graduate study. Among them, I would like to first thank my advisor, Prof. Lasse Jensen, for his help, patience, and guidance throughout my entire Ph.D. research. I also sincerely appreciate Lasse's kindness during my difficult times at Penn State. Lasse's dedication to research is always respectful, and his attitude towards research, "only do useful things to move the field forward", is consistently encouraging me to think deeply. With that, I luckily become the only graduate student who unsurprisingly witnessed Lasse's promotion from Assistant Professor to Associate Professor in 2013, and to Full Professor in 2017. It is honestly difficult to express my appreciation to Lasse using words. I guess all I can say is, I feel extremely lucky to have Lasse as my advisor and it is undoubtedly a rewarding and enjoyable experience to be part of the Jensen group.

I would also like to thank the members of the Jensen research group for establishing a very comfortable atmosphere to work within. Dr. Daniel Silverstein is always a role model for me and I want to thank him for his help and guidance in my earlier years. Dr. Justin Moore is the computer expert in the Jensen group and I want to thank him for his help with many technical issues. I also owe thanks to Phil Weiss, and later Jeff Becca, Pengchong Liu, Mark Bronson, and Alicia Tripp for many challenge questions and interesting discussions about research. Finally, from the Jensen group I would like to thank Dr. Xing Chen and Dr. Dhabih Chulhai for being the "active" role models for four years. Their knowledge and passion about research always keep me working hard, and I also want to thank them for their careful reading of this dissertation.

Part of my thesis could never have been done without collaborations with Prof. Jon Camden's group. I want to thank Jon for many collaborative opportunities that help me gain extensive experience working with experimental chemists. From Jon's group, I thank Dr. Hubert Turkey for many useful discussions about how to make appropriate connections between experiment and theory, and how to present the results in a way such that they are attracting from both experimental and theoretical points of view. All the projects presented in my dissertation would not have been possible without support from Research Computing and Cyberinfrastructure at the High Performance Computing Center (now Institute for CyberScience Advanced CyberInfrastructure) at Penn State. I thank Penn State for providing this wonderful service.

I could never have a successful graduate career without the help from professors at both Penn State and my undergraduate institute Juniata College. I want to first thank Prof. Paul Cremer, Prof. Will Noid, and Prof. Zhiwen Liu, for serving on my committee during the past four years. A special thanks to Will for providing me a lab rotation opportunity when I first came to Penn State. Will also happened to attend my senior concert at Juniata College, and I appreciate that he still remembers I said "I will do science" after five years. I want to thank my undergraduate chemistry advisor, Prof. Paul Schettler, for introducing computational chemistry to me. I always appreciate the research opportunity with Schetts and what I have learnt from him. This year marks his amazing 50th year of service at Juniata College, and I wish to use this thesis to thank his lifetime

dedication to teaching chemistry. I also want to thank my undergraduate math instructor, Prof. Benjamin Sunderland, for making me well prepared for computational chemistry by teaching me many math skills. Ben served at Juniata College for more than 30 years and recently retired. I always appreciate the communications with him and the encouragement from him, and I wish to use this thesis to thank his lifetime dedication to teaching math.

Finally, I would like to thank my family. I thank my parents, Hua Zhong and Ruisheng Hu, for all of their love and support throughout my education. I thank my wife, Lili Gai, for coming to my world in the right place at the right time and consistently encouraging me during the difficult times. Last but not least, I thank my 7-month baby girl, Shihan Lisa Hu, for bringing so much joy to our family and making my graduate life more “productive”.

Dedication

To my family

Part I

Introductory Material

Chapter 1

Introduction

The interaction of intense light with a molecule often leads to complex spectroscopic features due to the nonlinear scaling of the optical response with respect to the electric field. Such nonlinear optical (NLO) processes are inherently weak as compared to their linear counterparts. However, under certain conditions, their signals can be significantly intensified. In regard to the molecule itself, this happens for the energy of the incident radiation matches that of the molecular absorption, attributed to the *molecular resonance effects*. When the molecule is placed near a metal nanoparticle, this could also happen if the incident radiation excites the surface plasmons, attributed to the *plasmonic resonance effects*. These resonance enhancements make the NLO processes easier to be detected, which consequently allows for a detailed understanding of the structure-property relationship for NLO materials, and further contributes to the design of NLO devices.

At the molecular level, the second- and third-order NLO responses are described by the first and second hyperpolarizabilities (β and γ), respectively. Understanding the origin of these microscopic properties is essential for developing macroscopic NLO materials, however, this is generally difficult to realize by using experimental approaches alone. Theoretical modeling can often complement experiment by providing insights into the microscopic properties. For NLO properties, the sum-over-states (SOS) model¹ is the traditional approach and has shown success in simulating the resonant ones. This is benefiting from the fact that, under resonance conditions, most of the response features are governed by only a few states. However, many more states ought to be included for systems that are characterized by a high density of states, such as metal clusters, which is beyond the practical use of the SOS model. The metal clusters were recently found to exhibit extraordinarily large nonlinear responses,² and thus suitable simulation tools are urgently needed.

Response theory takes all the states into account by construction, hence fulfills the role to describe the optical properties of metal clusters. However, traditional response theory remains problematic in describing resonant properties due to the unphysical behaviors of response functions in the resonance region.³ To correctly account for the *molecular resonance effects*, response theory with a phenomenological damping factor, termed damped response theory, is needed.⁴ This modification extends the response functions to the complex plane to avoid unphysical divergence, and has shown great promise for describing all off-, near-, and on-resonance response properties.^{5,6} At the nonlinear level, it allows for reasonable evaluations of the complex β and γ tensors. As a

consequence, it can serve a robust tool to simulate nonlinear spectra that are related to the real and imaginary parts of β or γ , such as resonance hyper-Rayleigh scattering (HRayS), frequency-scanned hyper-Raman scattering (HRS), two-photon absorption (TPA), and third-harmonic generation (THG).

HRayS is an elastic process in which two photons with the same energy are simultaneously absorbed and one photon with twice the energy is scattered. It can be related to the microscopic second harmonic generation (SHG) hyperpolarizability, i.e., $\beta(-2\omega; \omega, \omega)$, and has been widely used to measure β^{SHG} of molecules in solution.⁷⁻⁹ TPA and THG involve simultaneous absorption of two and three photons, respectively, and have seen applications in many areas such as optical limiting, optical storage, all-optical switching, and biological imaging.¹⁰⁻¹³ In comparison to HRayS, the descriptions of TPA and THG require higher-order NLO properties, where the intensity dependent refractive index (IRDI) second hyperpolarizability, i.e., $\gamma(-\omega; \omega, \omega, -\omega)$, is needed for the former, while the THG second hyperpolarizability, i.e., $\beta(-3\omega; \omega, \omega, \omega)$ is needed for the latter. Consider the outstanding performance of metal clusters in regard to the nonlinear responses, it is of great interest to explore their HRayS, TPA, and THG, especially under resonance conditions.

Hyper-Raman scattering (HRS) is an inelastic process that gives rise to scattering at $2\omega_L \pm \omega_{\text{vib}}$, where ω_L is the incident frequency and ω_{vib} is the vibrational frequency of the molecule.¹⁴ It can be treated as the inelastic version of HRayS, and thus is also related to β^{SHG} . Alternatively, HRS can be considered as the two-photon analogue of Raman scattering (RS), ascribed to the fact that only one photon is absorbed in RS to cause scattering at $\omega'_L \pm \omega_{\text{vib}}$. When ω'_L or $2\omega_L$ matches the excitation energy, the *molecular resonance effects* will play an important role in RS or HRS. This has led to the fields termed resonance RS (RRS) and resonance HRS (RHRS), respectively.^{14,15} To probe the same excited state using RRS and RHRS, ω'_L will be equal to $2\omega_L$ but the vibrational information provided by them will differ. The non-linearity of RHRS makes it useful for studying the normal modes that are IR- and Raman-inactive and the electronic excited states that are one-photon forbidden but two-photon accessible.¹⁶⁻¹⁸ However, the widespread use of RHRS is still impeded due to two main reasons, the relatively low signal intensity despite the contributions from *molecular resonance effects* and the long acquisition time in experiment.^{19,20}

It was discovered 40 years ago that the Raman intensity of a molecule can be enhanced by orders of magnitude in the vicinity of a metal nanoparticle.²¹⁻²³ This finding has motivated the development of surface-enhanced spectroscopies,²⁴ of which surface-enhanced Raman scattering (SERS) is very popular and has drawn significantly growing attention during the past three decades.²⁵ The enhancement mechanism for SERS is often divided into two categories, the chemical mechanism (CM) and the electromagnetic mechanism (EMM). The CM arises from the chemical interactions between the molecule and the nanoparticle while the EMM can be understood as the *plasmonic resonance effects* that are caused by the excitations of surface plasmons.²⁶ When placed near a nanoparticle, the molecule's HRS can benefit from both CM and EMM on an equal footing to the RS, termed surface-enhanced hyper-Raman scattering (SEHRS).²⁷⁻³⁰ However, SEHRS is far less frequently used as compared to SERS, mainly due to the lacking of well-developed theoretical methods. Since EMM is the determinant factor for the large enhancement in SERS,^{31,32} it is of great need to appropriately incorporate the *plasmonic*

resonance effects into HRS to simulate SEHRS.

In this dissertation, damped quadratic and cubic response theory within a time-dependent density functional theory (TDDFT) framework are developed for simulating resonance HRayS of molecules and small Ag clusters, frequency-scanned HRS of the octupolar molecule crystal violet (CV), and TPA of the thiolate-protected Au₂₅ cluster. These efforts allow us to evaluate the two-photon enhanced HRayS of Ag clusters, to demonstrate the RHRS of CV is dominated by the Franck-Condon effects at the lowest two excitation energies, and to reveal the one- and two-photon double resonance effect is not the main cause of the huge TPA cross sections of Au₂₅(SH)₁₈⁻ found experimentally. With a focus on the EMM, two atomistic electrodynamic-quantum mechanical models are developed to simulate SEHRS. The first is the discrete interaction model/quantum mechanical model, which combines an atomistic electrodynamic model of the nanoparticle with a TDDFT description of the molecule. The second is a dressed-tensors method that describes the molecule as a point-dipole and point-quadrupole object interacting with the enhanced local field and field-gradients (FG) from the nanoparticle. With those methods, we are able to show the FG effects are important in SEHRS than in SERS, which also mainly determine the surface selection rules and the enhancements for SEHRS. Combining the dressed-tensors approach with a wavepacket dynamics model, for the first time we are able to show that SEHRS can serve as a spectroscopic tool to predict the molecular adsorbate geometry on silver colloids.

Overview of Dissertation

In the following, a brief outline of each chapter will be presented. Chapters 2 through 8 are all adapted from published work.

Chapter 2: Simulation of Resonance Hyper-Rayleigh Scattering of Molecules and Metal Clusters Using a Time-Dependent Density Functional Theory Approach

The implementation of damped quadratic response theory is presented within a time-dependent density functional theory framework for simulating hyper-Rayleigh scattering. It is found that, on a per atom basis, the small silver clusters possess two-photon enhanced hyper-Rayleigh intensity comparable to that of larger nanoparticles.

Chapter 3: Probing Two-Photon Molecular Properties with Surface-Enhanced Hyper-Raman Scattering: A Combined Experimental and Theoretical Study of Crystal Violet

A combined experimental and theoretical study on the surface-enhanced hyper-Raman scattering is presented for crystal violet. The results show that the hyper-Raman spectral features of crystal violet are dominated by strong A-term scattering across the range of its lowest two excitation energies.

Chapter 4: Simulating Third-order Nonlinear Optical Properties Using Damped Cubic Response Theory within Time-Dependent Density Functional Theory

The implementation of damped cubic response theory is presented within a time-dependent density functional theory framework for simulating two-photon absorption and third-harmonic generation. It is found that care must be taken when calculating higher-order response functions in the vicinity of one-photon poles due to the approximate kernels typically used in the simulations.

Chapter 5: Importance of Double-Resonance Effects in Two-Photon Absorption Properties of $\text{Au}_{25}(\text{SR})_{18}^-$

A theoretical investigation on the two-photon absorption properties is presented for the thiolate-protected gold cluster $\text{Au}_{25}(\text{SR})_{18}^-$. The results show that the one- and two-photon double resonance effect does not lead to significantly enhanced two-photon absorption cross sections, which suggests that an alternative focus is needed to understand the huge two-photon absorption intensities found experimentally.

Chapter 6: Theory of Linear and Nonlinear Surface-enhanced Vibrational Spectroscopy

A review of theoretical approaches is presented for various linear and nonlinear surface-enhanced vibrational spectroscopies, including surface-enhanced Raman scattering, surface-enhanced Raman optical activity, surface-enhanced hyper-Raman scattering, surface-enhanced sum-frequency generation, and surface-enhanced coherent anti-Stokes Raman scattering.

Chapter 7: Simulating Surface-Enhanced Hyper-Raman Scattering Using Atomistic Electrostatics-Quantum Mechanical Models

The implementations of two atomistic electrostatics-quantum mechanical models are presented for simulating surface-enhanced hyper-Raman scattering. It is found that the field-gradients effects play an important role in determining both the surface selection rules and the enhancements of surface-enhanced hyper-Raman spectroscopy.

Chapter 8: Surface-Enhanced Resonance Hyper-Raman Scattering Elucidates the Molecular Orientation of Rhodamine 6G on Silver Colloids

A combined experimental and theoretical approach is presented to probe the adsorbate geometry of rhodamine 6G on silver colloids using surface-enhanced hyper-Raman scattering. The results show that rhodamine 6G adsorbs mostly perpendicular to the nanoparticle surface along the ethylamine groups with the xanthen ring oriented edgewise.

Chapter 9: Application of Current Simulation Tools and Development of New Theoretical Methods

A brief overview of recent research progress is provided. This contains application of current simulation tools and development of new theoretical methods.

Chapter 10: Summary and Outlook

The findings of this dissertation are summarized, and several potential future projects

using the methods described within are proposed.

In addition to these chapters, there are three appendices.

Appendix A: Supporting Information for: Simulating Third-order Nonlinear Optical Properties Using Damped Cubic Response Theory within Time-Dependent Density Functional Theory

Supporting information for Chapter 4 is given.

Appendix B: Supporting Information for: Importance of Double-Resonance Effects in Two-Photon Absorption Properties of $\text{Au}_{25}(\text{SR})_{18}^-$

Supporting information for Chapter 5 is given.

Appendix C: Supporting Information for: Surface-Enhanced Resonance Hyper-Raman Scattering Elucidates the Molecular Orientation of Rhodamine 6G on Silver Colloids

Supporting information for Chapter 8 is given.

Part II

Describing Nonlinear Optical Properties with Damped Response Theory

Chapter 2 | Simulation of Resonance Hyper-Rayleigh Scattering of Molecules and Metal Clusters Using a Time- Dependent Density Functional Theory Approach

Hu, Z.; Autschbach, J.; Jensen, L. “*Simulation of Resonance Hyper-Rayleigh Scattering of Molecules and Metal Clusters Using a Time-Dependent Density Functional Theory Approach*” *J. Chem. Phys.* **2014**, *141*, 124350.

Abstract

Resonance hyper-Rayleigh scattering (HRS) of molecules and metal clusters have been simulated based on a time-dependent density functional theory (TD-DFT) approach. The resonance first-order hyperpolarizability (β) is obtained by implementing damped quadratic response theory using the $(2n + 1)$ rule. To test this implementation, the prototypical dipolar molecule para-nitroaniline (*p*-NA) and the octupolar molecule crystal violet (CV) are used as benchmark systems. Moreover, small silver clusters Ag_8 and Ag_{20} are tested with a focus on determining the two-photon resonant enhancement arising from the strong metal transition. Our results show that, on a per atom basis, the small silver clusters possess two-photon enhanced HRS comparable to that of larger nanoparticles. This finding indicates the potential interest of using small metal clusters for designing new nonlinear optical (NLO) materials..

2.1 Introduction

The nonlinear optical (NLO) properties of materials are of great importance in many applications such as optical data processing,^{1,11} biological imaging,^{33,34} and two-photon phototherapy.³⁵⁻³⁷ At the molecular level, the second order response is characterized by the first-order hyperpolarizabilities (β).¹ Experimentally, the first-order hyperpolarizability of molecules in solution can be measured using hyper-Rayleigh scattering (HRS), where two photons with the same energy are simultaneously absorbed and one photon with twice the energy is scattered.^{7-9,38-44} Thus, there has been a significant effort in establishing structure-property relationships for optimizing the first-order hyperpolarizabilities of molecules.¹ Despite these efforts, it has been found that currently the magnitude of the first-order hyperpolarizabilities falls short of the maximum quantum limit predicted by theory.⁴⁵⁻⁴⁷

Recently, HRS has been used to study the NLO properties of metal nanoparticles, where it was found that silver and gold nanoparticles exhibited significantly larger response than typical molecular chromophores.^{48,49} The large HRS signal was interpreted as arising from a two-photon resonance enhancement due to the plasmon excitation. This is consistent with the observation that Pt nanoparticles did not show any HRS signal as they do not have any plasmon resonance in the visible range. For small nanoparticles, it has been shown that the HRS response is dipolar and most likely due to a lack of centrosymmetry in the particles, whereas for large nanoparticles quadrupolar response has been demonstrated due to field retardation effects.^{50,51} While the HRS properties of large nanoparticles have been studied extensively very little is known about the HRS properties of small metal nanoparticles with dimension comparable to the more traditional molecular chromophores. A recent study found that small gold clusters (< 2nm) showed increased two-photon absorption cross sections on a per atom basis than larger gold clusters.² Therefore, it is of interest to understand if such small clusters also show large two-photon enhanced HRS.

First-principles simulations can be used to understand the NLO properties of such small metal clusters. However, in contrast to the large literature focusing on linear optical properties of small noble metal clusters, much less work is on exploring their NLO properties. The calculations of NLO properties of molecules from first-principles pose a significant challenge due to the requirements of accurate treatment of electron correlation, large basis sets and the inclusion of solvent effects. High level *ab initio* wave functions methods can reliably predict accurate first-order hyperpolarizabilities, however, such methods are limited to rather small systems due to their high computational burden. Alternatively, time-dependent density functional theory (TD-DFT)⁵²⁻⁵⁶ can be used which is much less computationally demanding and thus applicable to large systems while providing sufficient accuracy.

Resonant HRS is typically modeled using a sum-over-states (SOS) model which assumes that a few essential states (often one or two excited states) dominate the response.¹ These models are very successful close to resonance but become inaccurate far from resonance or if many states are involved. Since the metal clusters of interest here are characterized by a high density of states, it becomes important to go beyond such few state models. Quadratic response theory can be used

to solve for the first-order hyperpolarizability far from resonance and by construction includes implicitly a sum over all electronic states. Norman *et al.*^{4,6} have recently extended the normal linear and quadratic response formalism to also describe the resonance case by including a finite lifetime of the electronic states. This approach has been used to study a wide range of linear and nonlinear optical properties.^{4-6,57-62}

In this work we will present our implementation of finite lifetimes into TD-DFT for the calculation of quadratic response properties using the Amsterdam Density Functional (ADF) program package.⁶³⁻⁶⁵ This is an extension of the damped linear response implementation already in ADF.⁵ We will use an efficient implementation of damped quadratic response theory based on the $2n + 1$ rule. As a test of the implementation, we will study the HRayS of the prototypical dipolar molecule para-nitroaniline (*p*-NA) and the octupolar molecule crystal violet (CV). The HRayS properties of these molecules have been studied extensively from both theoretical⁶⁶⁻⁷⁰ and experimental perspectives^{7,8,38,39,41,42,71-75} and thus serve as good benchmark systems for the current implementation. Following these studies, we will study the HRayS of small silver cluster Ag₈ and Ag₂₀ focusing on determining the two-photon resonant enhancement arising from the strong metal transition. These two clusters were chosen because their absorption spectra are dominated by a strong plasmon-like transition and thus often used as microscopic model systems.⁷⁶

2.2 Theory

In damped response theory, one solves the time-dependent Kohn-Sham (TDKS) equations where the following transformation of the orbital energy has been made $\varepsilon_i \rightarrow \varepsilon_i - i\Gamma$. Here Γ corresponds to an energy broadening term that can be related to the finite lifetime of the excited state.⁷⁷ Since the lifetime of each excited state is different, Γ should be distinct for each state. However, for practical reasons we will assume a common phenomenological energy broadening parameter. A more rigorous derivation has been presented by Norman *et al.*⁶ based on a quantum Liouville approach, however, the final equations become identical once a common damping parameter is adopted. The inclusion of this damping parameter ensures that the response equations are convergent at all frequencies. We will follow the general derivations of the response equations without damping presented by Karna and Dupuis⁷⁸ for Hartree-Fock theory and later adapted by Van Gisbergen within a TD-DFT formalism.⁷⁹ In this way, the TDKS equation^{78,79} is given by

$$FC - iS \frac{\partial C}{\partial t} = SC(\varepsilon - i\Gamma), \quad (2.1)$$

subject to the orthonormality constraint

$$\frac{\partial}{\partial t} C^\dagger SC = 0, \quad (2.2)$$

where C is the coefficient matrix of the spatial orbitals ($\phi = \chi C$), S is the time-independent overlap matrix defined over the atomic orbitals (AOs) ($S_{\mu\nu} = \int d\mathbf{r} \chi_\mu(\mathbf{r})^* \chi_\nu(\mathbf{r})$), ε is the Lagrangian

multiplier matrix, and Γ is the phenomenological damping factor. Further, F is the KS matrix expressed in the AO form as^{78,79}

$$F = h + D \times (2J) + \nu_{xc}, \quad (2.3)$$

where h is the one-electron integral matrix, J is the Coulomb matrix, D is the density matrix, and ν_{xc} is the exchange correlation (xc) potential. We note in passing that when the basis set is dependent on the time-dependent external field, the left hand side of Eq. (2.1) has an additional term⁸⁰ involving $\int d\mathbf{r} \chi_\mu(\mathbf{r}, t)^* \frac{\partial}{\partial t} \chi_\nu(\mathbf{r}, t)$. However, for the present work this term can be ignored.

Here we consider a closed shell molecule interacting with an external electric field E that consists of a monochromatic oscillating part and a static part^{78,79}

$$H^1 = E(e^{+i\omega t} + e^{-i\omega t} + 1) = E(e^{\pm i\omega t} + 1). \quad (2.4)$$

The density matrix D can then be expanded in terms of the perturbation as

$$D = D^0 + [e^{\pm i\omega t} D^a(\pm\omega) + D^a(0)] E^a + \frac{1}{2!} \{e^{\pm 2i\omega t} D^{ab}(\pm\omega, \pm\omega) + e^{\pm i\omega t} [D^{ab}(0, \pm\omega) + D^{ab}(\pm\omega, 0)] + D^{ab}(\pm\omega, \mp\omega) + D^{ab}(0, 0)\} E^a E^b + \dots, \quad (2.5)$$

where the superscript indicates the *direction* (x, y, z) of the perturbation and the number of superscripts indicates the *order* of the perturbation.^{78,79} From the perturbed density matrix, we can obtain the molecular response properties as⁷⁸

$$\alpha_{ab}(\mp\omega; \pm\omega) = -\text{Tr}[H^a D^b(\pm\omega)], \quad (2.6)$$

$$\beta_{abc}(\mp(\omega_1 + \omega_2); \pm\omega_1, \pm\omega_2) = -\text{Tr}[H^a D^{bc}(\pm\omega_1, \pm\omega_2)], \quad (2.7)$$

where α_{ab} is the component of the polarizability tensor, β_{abc} is the component of the hyperpolarizability tensors, ‘‘Tr’’ stands for trace of a matrix and H^a is the dipole moment matrix.

The first-order density matrix can then be found by solving the damped first-order coupled-perturbed KS (CPKS) equations as

$$G^a(\pm\omega) + (\varepsilon^0 U^a(\pm\omega) - U^a(\pm\omega) \varepsilon^0) \pm (\omega + i\Gamma) U^a(\pm\omega) = \varepsilon^a(\pm\omega), \quad (2.8)$$

where $G^a(\pm\omega)$ is the first-order KS matrix in the MO basis and the $U^a(\pm\omega)$ is the first-order transformation matrix that relates the perturbed MO coefficients to the unperturbed MO coefficients as $C^a(\pm\omega) = C^0 U^a(\pm\omega)$. Only the occupied-virtual block of the transformation matrix is needed which is given by

$$U_{ia}^a(\pm\omega) = \frac{G_{ia}^a(\pm\omega)}{\varepsilon_a^0 - \varepsilon_i^0 \mp \omega \mp i\Gamma}, \quad (2.9)$$

where $\varepsilon_a^0, \varepsilon_i^0$ are the KS one-electron energies of the virtual and occupied orbitals, respectively. The first-order transformation matrix is then solved for iteratively as the first-order KS matrix

reads^{78,79}

$$G_{ia}^a(\pm\omega) = H_{ia}^a + \sum_{j,b} K_{ia,jb}^{HXC} U_{jb}^a(\pm\omega) + K_{ia,bj}^{HXC} U_{bj}^{a*}(\mp\omega), \quad (2.10)$$

where K^{HXC} is the coupling matrix given by

$$K_{ia,jb}^{HXC} = \int d\mathbf{r}_1 \int d\mathbf{r}_2 \phi_i^*(\mathbf{r}_1) \phi_a(\mathbf{r}_1) \left[\frac{1}{r_{12}} + f_{xc}^{\text{ALDA}}(\mathbf{r}_1, \mathbf{r}_2, \pm\omega) \right] \phi_j(\mathbf{r}_2) \phi_b^*(\mathbf{r}_2), \quad (2.11)$$

in which $f_{xc}^{\text{ALDA}}(\mathbf{r}_1, \mathbf{r}_2, \pm\omega)$ is the adiabatic local density approximation (ALDA)⁸¹ of the xc kernel.^{78,79} The coupling matrix is never constructed explicitly as only $K \cdot U^a$ is needed which can be calculated efficiently as described previously.⁷⁹ Once a self-consistent solution for the transformation matrix is obtained, the perturbed density matrix can be calculated as

$$D^a(\pm\omega) = C^a(\pm\omega) n C^{0\dagger} + C^0 n C^{a\dagger}(\mp\omega), \quad (2.12)$$

from which the polarizability can be calculated as described above. The damped linear response equations have previously been implemented within the ADF program package.^{5,58}

To obtain the damped first-order hyperpolarizability β , we could directly solve for the second-order density matrix by solving a set of damped second-order CPKS equations. This approach has the advantage that the obtained response properties can be partitioned easily into contributions from localized orbitals.⁸² However, this requires the solution of several quadratic response equations. Therefore, it becomes computational advantageous to use the $2n+1$ rule⁸³ to rewrite the quadratic response in terms of quantities that can be obtained by only solving linear response equations.^{78,79,84-86} Here, we adapt the latter approach for calculating the damped β . Using the $2n+1$ rule, the final expression for the damped β can be written as

$$\begin{aligned} \beta_{abc}(\mp(\omega_1 + \omega_2); \pm\omega_1, \pm\omega_2) = & \\ & \text{Tr}[n\{U^a(\mp(\omega_1 + \omega_2))G^b(\pm\omega_1)U^c(\pm\omega_2) + U^c(\pm\omega_2)G^b(\pm\omega_1)U^a(\mp(\omega_1 + \omega_2)) \\ & + U^b(\pm\omega_1)G^c(\pm\omega_2)U^a(\mp(\omega_1 + \omega_2)) + U^a(\mp(\omega_1 + \omega_2))G^c(\pm\omega_2)U^b(\pm\omega_1) \\ & + U^c(\pm\omega_2)G^a(\mp(\omega_1 + \omega_2))U^b(\pm\omega_1) + U^b(\pm\omega_1)G^a(\mp(\omega_1 + \omega_2))U^c(\pm\omega_2)\}] - \\ & \text{Tr}[n\{U^a(\mp(\omega_1 + \omega_2))U^c(\pm\omega_2)\varepsilon^b(\pm\omega_1) + U^c(\pm\omega_2)U^a(\mp(\omega_1 + \omega_2))\varepsilon^b(\pm\omega_1) \\ & + U^b(\pm\omega_1)U^a(\mp(\omega_1 + \omega_2))\varepsilon^c(\pm\omega_2) + U^a(\mp(\omega_1 + \omega_2))U^b(\pm\omega_1)\varepsilon^c(\pm\omega_2) \\ & + U^c(\pm\omega_2)U^b(\pm\omega_1)\varepsilon^a(\mp(\omega_1 + \omega_2)) + U^b(\pm\omega_1)U^c(\pm\omega_2)\varepsilon^a(\mp(\omega_1 + \omega_2))\}] + \\ & \text{Tr}[g_{xc}(\mathbf{r}, \mathbf{r}', \mathbf{r}'', \pm\omega_1, \pm\omega_2)D^a(\mp(\omega_1 + \omega_2))D^b(\pm\omega_1)D^c(\pm\omega_2)], \end{aligned} \quad (2.13)$$

where ε^a , U^a , and G^a can be obtained by solving the linear response equations as described above. The only additional term not available from solving the linear equations is the second-order xc kernel, $g_{xc}(\mathbf{r}, \mathbf{r}', \mathbf{r}'', \pm\omega_1, \pm\omega_2)$, which can be calculated as^{79,82}

$$\begin{aligned} \text{Tr}[g_{xc}(\mathbf{r}, \mathbf{r}', \mathbf{r}'', \pm\omega_1, \pm\omega_2)D^a(\mp(\omega_1 + \omega_2))D^b(\pm\omega_1)D^c(\pm\omega_2)] = & \\ \int d^3\mathbf{r} g_{xc}^{\text{ALDA}}(\mathbf{r}, 0, 0)\rho^a(\mathbf{r}, \mp(\omega_1 + \omega_2))\rho^b(\mathbf{r}, \pm\omega_1)\rho^c(\mathbf{r}, \pm\omega_2), & \end{aligned} \quad (2.14)$$

where ρ^a, ρ^b, ρ^c are the perturbed densities from the damped linear response theory.⁷⁹

2.3 Computational Details

We have implemented the damped quadratic response theory based on the $(2n + 1)$ rule into a locally modified version of the ADF program package.^{63–65} Geometry optimization was performed using the Becke-Perdew (BP86)^{87,88} XC potential with a triple- ζ polarized Slater type (TZP) basis set from the ADF library. All response properties were calculated using the statistical average of orbital model exchange-correlation potentials (SAOP)⁸⁹ and a triple- ζ polarized Slater type (TZP) basis set. The SAOP functional was chosen since it has previously been shown to provide reasonable accurate hyperpolarizabilities for small molecules, see e.g. Refs. 89, 90. Larger basis sets with many diffuse functions are needed for accurate calculation of the first-order hyperpolarizability of small molecules with low-energy diffuse excitations. For larger π -conjugated organic chromophores, the basis set requirements are less demanding since the nonlinear optical response is dominated by low-energy valence excitations.⁹¹ Here we choose to focus on results obtained using the smaller TZP basis set to limit the computational requirements. Solvent effects are not included in the simulations although they are important for quantitative comparison with experimental results.⁶⁹ The finite lifetime of the electronic excited states is included phenomenologically using a damping parameter of 0.0034 a.u. ($\sim 800 \text{ cm}^{-1}$), which was previously found to be acceptable.⁵ Additionally, the keyword “*FitAODeriv*” was invoked to provide a correction term to the response equations due to the incomplete fit basis sets.⁸⁰ This correction is typically minor, but it is needed here to obtain a β tensor that obeys the expected permutation symmetry. The excitation energies were obtained from the band maxima of the imaginary part of the polarizability as calculated using damped linear response theory with the “*FitAODeriv*” keyword. This was done to ensure consistency with the damped hyperpolarizability calculations. For all silver cluster calculations, scalar relativistic effects have been accounted for by means of the zeroth-order regular approximation (ZORA).^{92,93} In this work, we will use cgs units and the **T** convention to describe the first-order hyperpolarizability.⁹⁴ The conversion factor to cgs units for β ⁹⁵: 1 a.u. = 8.6392×10^{-33} esu.

2.4 Results and Discussion

The damped β value corresponding to the hyper-Rayleigh scattering technique (β^{HRayS}) is calculated as

$$\beta^{HRayS} = \sqrt{\langle \beta_{ZZZ}^2 \rangle + \langle \beta_{XZZ}^2 \rangle}, \quad (2.15)$$

where capital indices represent Cartesian components and $\langle \beta_{ABC}^2 \rangle$ represents the orientational average of the square of the β tensor component,⁷⁵ which can be expressed as a combination of

the damped $\beta_{abc}(-2\omega; +\omega, +\omega)$ tensor elements as,^{96,97}

$$\begin{aligned} \langle \beta_{ZZZZ}^2 \rangle &= \frac{1}{7} \sum_a \beta_{aaa} \beta_{aaa}^* + \frac{4}{35} \sum_{a \neq b} \beta_{aab} \beta_{aab}^* + \frac{2}{35} \sum_{a \neq b} \beta_{aaa} \beta_{abb}^* + \frac{4}{35} \sum_{a \neq b} \beta_{baa} \beta_{aab}^* \\ &+ \frac{4}{35} \sum_{a \neq b} \beta_{aaa} \beta_{bba}^* + \frac{1}{35} \sum_{a \neq b} \beta_{baa} \beta_{baa}^* + \frac{4}{105} \sum_{a \neq b \neq c} \beta_{aab} \beta_{bcc}^* + \frac{1}{105} \sum_{a \neq b \neq c} \beta_{baa} \beta_{bcc}^* \\ &+ \frac{4}{105} \sum_{a \neq b \neq c} \beta_{aab} \beta_{ccb}^* + \frac{2}{105} \sum_{a \neq b \neq c} \beta_{abc} \beta_{abc}^* + \frac{4}{105} \sum_{a \neq b \neq c} \beta_{abc} \beta_{bac}^*, \end{aligned} \quad (2.16)$$

$$\begin{aligned} \langle \beta_{XZZZ}^2 \rangle &= \frac{1}{35} \sum_a \beta_{aaa} \beta_{aaa}^* + \frac{4}{105} \sum_{a \neq b} \beta_{aaa} \beta_{abb}^* - \frac{4}{70} \sum_{a \neq b} \beta_{aaa} \beta_{bba}^* + \frac{8}{105} \sum_{a \neq b} \beta_{aab} \beta_{aab}^* \\ &+ \frac{3}{35} \sum_{a \neq b} \beta_{abb} \beta_{abb}^* - \frac{4}{70} \sum_{a \neq b} \beta_{aab} \beta_{baa}^* + \frac{1}{35} \sum_{a \neq b \neq c} \beta_{abb} \beta_{acc}^* - \frac{4}{210} \sum_{a \neq b \neq c} \beta_{aac} \beta_{bbc}^* \\ &- \frac{4}{210} \sum_{a \neq b \neq c} \beta_{aab} \beta_{bcc}^* + \frac{2}{35} \sum_{a \neq b \neq c} \beta_{abc} \beta_{abc}^* - \frac{4}{210} \sum_{a \neq b \neq c} \beta_{abc} \beta_{bac}^*, \end{aligned} \quad (2.17)$$

where “*” indicates complex conjugation.

Before discussing the results, it is instructive to consider the resonant behavior of HRayS if only one electronic excited state contributes. The general form for the SOS expression of $\beta_{abc}(-2\omega; +\omega, +\omega)$ can be written as⁹⁸

$$\beta_{abc}(-2\omega; +\omega, +\omega) = \sum_{k,l} \sum_P \frac{\langle 0 | \mu_a | k \rangle \langle k | \mu_b | l \rangle \langle l | \mu_c | 0 \rangle}{(E_k - E_0 - 2\omega - i\Gamma)(E_l - E_0 - \omega - i\Gamma)}, \quad (2.18)$$

where $|0\rangle$, $|k\rangle$ and $|l\rangle$ are the electronic states, E_0 , E_k and E_l are their corresponding eigen-energies, μ_a is the dipole moment operator, ω is the energy of the incident radiation, and \sum_P represents the summation over all terms obtained by permutations of $(-2\omega, a)$, $(-\omega, b)$, and $(-\omega, c)$. If we consider the situation where the incident light is close to a two-photon resonance with the first excited state ($E_{k=1} - E_0 \sim 2\omega$), then the dominant term becomes

$$\beta_{abc}(-2\omega; +\omega, +\omega) = \sum_P \frac{\langle 0 | \mu_a | 1 \rangle}{E_1 - E_0 - 2\omega - i\Gamma} \sum_l \frac{\langle 1 | \mu_b | l \rangle \langle l | \mu_c | 0 \rangle}{E_l - E_0 - \omega - i\Gamma}, \quad (2.19)$$

which can be used to describe two-photon resonance enhanced HRayS if no other electronic states are close to being either one- or two-photon resonant with the incident light. However, as discussed by Kristensen *et al.*⁹⁹, two-photon absorption cross sections cannot in general be obtained from products of the two-photon resonant first-order hyperpolarizability.

It is also possible that the incident light is close to being one-photon resonant with the first excited state ($E_{l=1} - E_0 \sim \omega$) and two-photon resonant with a higher electronic state ($E_{k=2} - E_0 \sim 2\omega$). Under these conditions, the dominant contribution to the HRayS is

$$\beta_{abc}(-2\omega; +\omega, +\omega) = \sum_P \frac{\langle 0 | \mu_a | 2 \rangle \langle 2 | \mu_b | 1 \rangle \langle 1 | \mu_c | 0 \rangle}{(E_2 - E_0 - 2\omega - i\Gamma)(E_1 - E_0 - \omega - i\Gamma)}, \quad (2.20)$$

which corresponds to doubly resonant enhanced HRayS. This doubly resonant effect is expected to lead to very large HRayS.

2.4.1 HRayS of A Dipolar Chromophore: Para-nitroaniline

Molecules that consist of a donor group and an acceptor group connected through a molecular bridge are of interest for NLO applications due to their large first-order hyperpolarizability.^{1,100} This class of NLO chromophores is typically referred to as dipolar due to its 1D conjugation network with the prototypical example being *p*-NA. *p*-NA is among the simplest dipolar chromophores and thus there exists in the literature many theoretical and experimental studies of its first-order hyperpolarizability. The first-order hyperpolarizability has been measured to be $\beta^{\parallel} = 12.90 \times 10^{-30}$ esu (where $\beta^{\parallel} = \frac{1}{5} \sum_{\alpha} \beta_{z\alpha\alpha} + \beta_{\alpha z\alpha} + \beta_{\alpha\alpha z}$ for the dipole moment oriented along the z-axis) in 1,4-dioxane solution at 1064 nm⁴¹, and in the gas phase at the same wavelength to be $\beta^{\parallel} = 9.26 \times 10^{-30}$ esu⁴² showing a modest solvation effect of around 30%. Theoretical studies have shown that the solvation effect on β^{\parallel} is on the order of 30-50% in good agreement with the experimental results.⁶⁶⁻⁶⁹

Using the TZP basis set, we calculated a static first-order hyperpolarizability of $\beta_0^{\parallel} = 14.87 \times 10^{-30}$ esu for *p*-NA in the gas phase. Using a larger basis set with many diffuse functions (ET-QZ3P-hypol), we find a value of $\beta_0^{\parallel} = 7.77 \times 10^{-30}$ esu. The result obtained with the large basis set is in good agreement with results obtained from high-level *ab initio* simulations where $\beta_0^{\parallel} = 8.22 \times 10^{-30}$ esu was obtained using CCSD/aug-pVTZ.⁷⁰ At 1064 nm we find a value of $\beta^{\parallel} = 30.80 \times 10^{-30}$ esu, which is significantly higher than the experimental results. This has been noted before⁶ and is likely due to an overestimation of the dispersion in the first-order hyperpolarizability using DFT.¹⁰¹ As the first excited state of *p*-NA is a charge-transfer state, the root cause of this overestimation can likely be traced back to an underestimation of the first excitation energy using DFT. In support of this, we find an excitation energy of 3.4 eV whereas CCSD finds an excitation energy of 4.6 eV.¹⁰² It is noted that a ‘tuned’ functional with range-separated exchange gives a significantly improved charge-transfer excitation energy and a more accurate hyperpolarizability.^{91,103} The development of corresponding functionality in the response modules of the ADF code is presently under way.

Simulated HRayS for *p*-NA is shown in Figure 2.1(a). We see that the HRayS spectrum is characterized by a two-photon resonance with the first excited state at 735 nm. Experimentally, it is known that *p*-NA has significant two-photon absorption at 720 nm in dimethyl sulfoxide (DMSO).¹⁰⁴ This is consistent with the two-photon resonance found in the simulated HRayS, however, the good agreement between theory and experiments is fortuitous. The peak value on resonance is found to be around $\beta^{HRayS} = 224 \times 10^{-30}$ esu compared to $\beta_0^{HRayS} = 10 \times 10^{-30}$ esu in the static limit. Thus, a significant two-photon resonance enhancement of about a factor of 20 of the HRayS is observed for *p*-NA. In Figure 2.1(a), also shown is the deconvolution of the HRayS spectrum into contributions arising from the real and imaginary part of the first-order hyperpolarizability tensor, respectively. We see that the spectrum is dominated by the imaginary part in the resonance region, whereas the real part dominates when detuned from resonance by around 50 nm. Furthermore, we plot in Figure 2.1(a) the HRayS spectrum calculated using

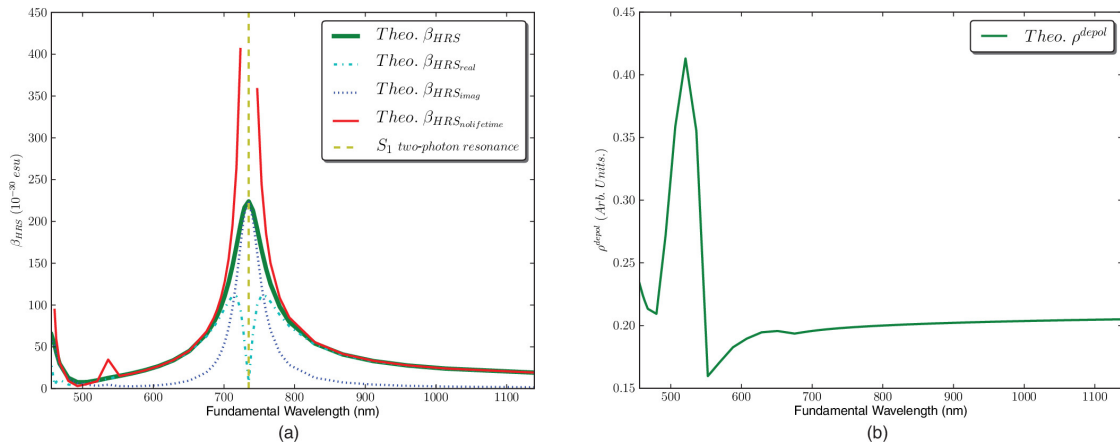


Figure 2.1. (a) Simulated HRayS for p -NA in the gas phase. Also, plotted is the contributions from the real and imaginary first-order hyperpolarizability as well as the HRayS calculated without including the finite lifetime. The yellow vertical line indicates the resonance due to the first excited state. (b) Simulated depolarization ratio for p -NA in the gas phase.

standard response theory that does not account for the finite lifetime. As expected, this leads to a significant overestimation of the HRayS values close to the resonance and a singularity at resonance.

We also calculated the depolarization ratio defined as $\rho^{depol} = \frac{\langle \beta_{xzz}^2 \rangle}{\langle \beta_{zzz}^2 \rangle}$ which reflects the symmetry of the molecule far from resonance.^{41,105} The depolarization ratio as a function of the wavelength of the incident lights is depicted in Figure 2.1(b). On resonance the depolarization ratio provides information about the contributions from multiple transitions to the scattering.¹⁰⁵ As expected for a molecule with C_{2v} symmetry, we find the depolarization ratio to be $\frac{1}{3}$ both in the off-resonance region and close to the two-photon resonance with the first excited state. The dominant contribution to the HRayS scattering of p -NA is the β_{zzz} component (when the dipole moment is aligned with the z -axis) in both regions. However, significant derivations from the expected value of $\frac{1}{3}$ is observed below 600 nm due to resonance contributions from other electronic states with comparatively weaker oscillator strengths. Thus, the depolarization ratio is a sensitive reporter on the contributions from multiple transitions that are not easily detectable in the HRayS spectrum.

2.4.2 HRayS of A Octupolar Chromophore: Crystal Violet

In contrast to dipolar molecules like p -NA, which can be considered one-dimensional NLO chromophores, octupolar molecules can be classified according to their two-dimensional NLO properties. Probably the best known example of an octupolar chromophore is CV, and a large number of studies have measured its NLO properties.^{41,75} A recent experimental study by Campo *et al.*⁷⁵ provided a detailed characterization of the resonance HRayS of CV in solutions for the few lowest excited states and thus constitutes an excellent benchmark system for which to compare our implementation.

CV formally has D_3 symmetry with a propeller-like structure with three blades consisting

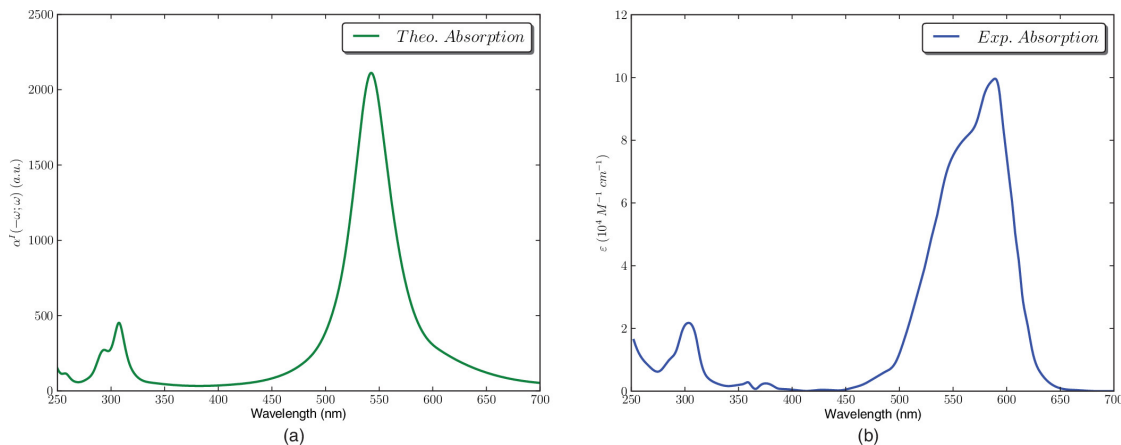


Figure 2.2. The simulated (a) and experimental (b) absorption spectrum of CV. The experimental absorption spectrum is measured in methanol and taken from Ref. 75.

of p-(dimethylamino)phenyl groups. The photodissociation spectra of CV measured in the gas phase show a single absorption band around 550 nm consistent with the D_3 symmetry.¹⁰⁶ In solution the absorption spectrum of CV is characterized by a main band at 587 nm and a weaker band at 539 nm,¹⁰⁶ which indicates a slight lowering of the D_3 symmetry due to the interactions with the solvent. Two very weak overlapping absorption bands are found at 374 nm and 354 nm in addition to a slightly stronger absorption band at 304 nm.⁷⁵ The simulated absorption spectrum of CV is shown in Figure 2.2(a). In the gas phase, we find the lowest strong excitation ($f = 0.5640$ a.u., f : oscillator strength) to be at 542 nm in good agreement with the gas phase experiments (550 nm¹⁰⁶). The splitting of the first excited state is obviously not accounted for as we use a gas phase structure with D_3 symmetry. A second excitation with significant oscillator strength is found at 307 nm ($f = 0.1825$ a.u.). Several weaker transitions are found in between. In Figure 2.2(b) we show the experimental absorption spectrum of CV in methanol from Ref. 75. For simplicity, we will in the following refer to the two bands at 587/539 nm as S_1 , the band at 374/354 nm as S_2 , and the band at 304 nm as S_3 .

For CV, a static HRayS first-order hyperpolarizability has been estimated by Shelton and co-workers^{41,42} to be $\beta_0^{HRayS} = 25.6 \times 10^{-30}$ esu, which was extrapolated using a three-state model and CCl_4 as a reference. For comparison, the same study reported the static HRayS first-order hyperpolarizability of *p*-NA to be $\beta_0^{HRayS} = 4.4 \times 10^{-30}$ esu. In the work by Campo *et al.*⁷⁵ a value of $\beta_0^{HRayS} = 54 \times 10^{-30}$ esu was reported. The difference in the experimentally reported values is likely due to the use of different references and conventions for reporting the first-order hyperpolarizability. This is a well known problem that complicates a quantitative comparison between theory and experiments, especially when data from several groups are compared.¹⁰⁷ However, previous work reported by Shelton and co-workers has shown good agreement between theory and the experimental values once large basis sets with many diffuse functions are used.⁶⁹

We find a value of $\beta_0^{HRayS} = 55 \times 10^{-30}$ esu in agreement with the experimental value reported by Campo *et al.*⁷⁵ and around a factor of two larger than the values from Shelton and co-workers.^{41,42} However, the good agreement with the results of Campo *et al.*⁷⁵ is likely accidental

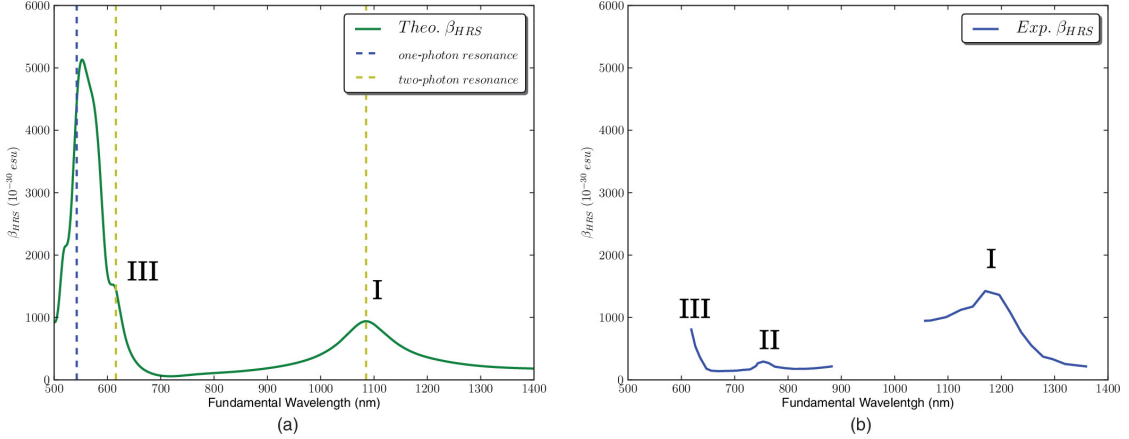


Figure 2.3. (a) Simulated hyper-Rayleigh spectrum for CV in the gas phase. (b) Experimental hyper-Rayleigh spectrum for CV in methanol taken from Ref.⁷⁵ The yellow vertical line corresponds to the two-photon resonances whereas the blue vertical line corresponds to the one-photon resonance. I, II, III indicate three regions as referred to in the text.

as we are using a small basis set which likely overestimates the first-order hyperpolarizability as shown above for *p*-NA. We find that HRayS of CV is about a factor of 5 greater than *p*-NA, which is in good agreement with the factor of about 6 reported by Shelton and co-workers. The work by Campo *et al.* also used a different convention for reporting the HRayS than the one employed in this work and thus cannot be compared directly. However, we can estimate the difference arising from the conventions by comparing the β standard used in the two experiments. Campo *et al.* used chloroform as reference with a $\beta^{HRayS} \sim 0.20 \times 10^{-30}$ esu (here reported as $\beta^{HRayS} \sim \sqrt{\frac{6}{35}}|\beta_{zzz}|$).^{41,42} Shelton and co-workers reported a measured value for chloroform of $\beta^{HRayS} \sim 0.15 \times 10^{-30}$ esu (here reported as $\beta^{HRayS} \sim \sqrt{\frac{6}{5}}\beta_L$, where β_L is the HRayS measured using VV polarization).^{41,42} Thus, accounting for the differences in internal standards would bring the experimental results in better agreement with each other, although the results by Campo *et al.* for CV are still larger than the values reported by Shelton and co-workers. Despite these differences, we will continue to compare our results with that of Campo *et al.* as we are mainly interested in understanding the resonance-enhancement.

In Figure 2.3(a) we plot the simulated HRayS spectrum of CV and compare with the experimental spectrum in Figure 2.3(b) obtained by Campo *et al.* in methanol.⁷⁵ Experimentally, three distinct regions of the HRayS spectrum of CV are observed. A two-photon resonance with S_1 is observed in region I with an enhancement of around 25. The largest enhancement is found around 1180 nm with a clear shoulder around 1080 nm. A weaker HRayS band is found in region II around 780 nm and corresponds to a two-photon resonance with S_2 . As this state is one-photon forbidden, Campo *et al.* described the resonance to be enhanced in HRayS spectrum by a vibronic mechanism.⁷⁵ Finally, in region III around 600 nm, the onset of a double resonance effect is due to a combined two-photon resonance with S_3 and one-photon resonance with S_1 is observed.

The simulated spectrum is dominated by two bands in qualitative good agreement with the experimental spectrum. The first band is found at 1084 nm and corresponds to a two-photon

resonance with S_1 . The enhancement for the first two-photon resonance is about a factor of 20 in good agreement with the measured enhancement. The shoulder observed in the experimentally HRayS spectrum is not found in the simulations as a D_3 gas phase structure is used where the two excitations are degenerate. The second band in the simulated HRayS spectrum arises from a two-photon resonance with S_3 at 614 nm and a one-photon resonance with S_1 at 543 nm. The near overlap between the two resonances leads to a strongly enhanced HRayS in this region. Near the two-photon resonance with S_3 the enhancement is around a factor of 30, whereas closer to the one-photon resonance the enhancement is about two orders of magnitude larger. The fact that the enhancement near S_3 is larger than that near S_1 is most likely a result of the double resonant effect as S_3 is much weaker than S_1 in the linear absorption spectrum.

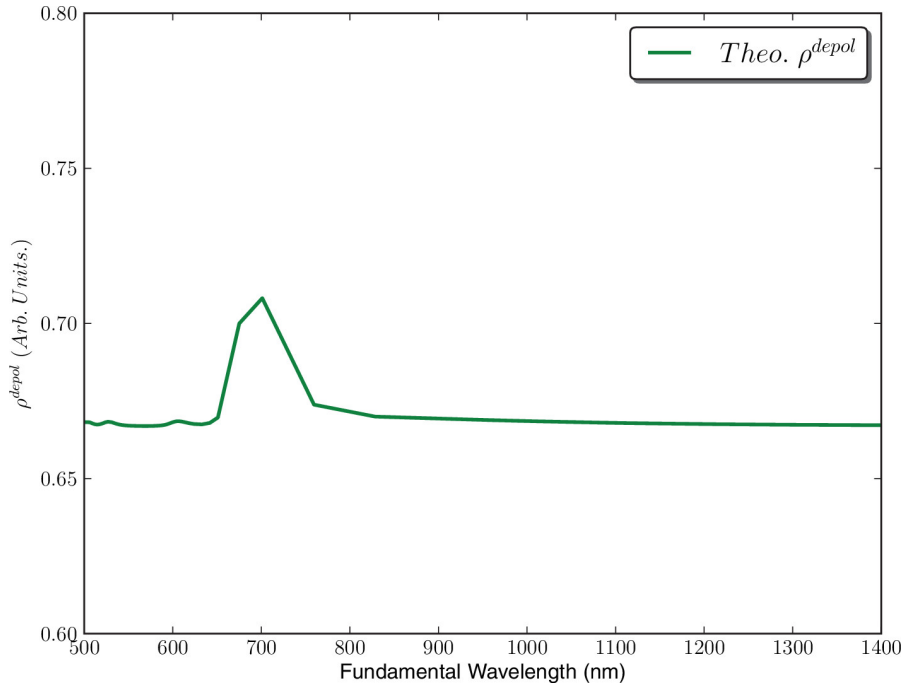


Figure 2.4. Simulated depolarization ratio for CV in the gas phase.

The most noticeable disagreement between theory and experiments is the lack of the HRayS band found experimentally around 780 nm. However, this is not that surprising as this band has been shown to derive its intensity from a vibronic mechanism which is not included in the current model. Intriguingly, even though we do not see evidence of this resonance in the HRayS spectrum as it is too weak, we do see a signature reflecting this resonance in the depolarization ratio. In Figure 2.4 we plot the simulated depolarization ratio as a function of the incident wavelength. We see that the ratio is around $\frac{2}{3}$ for most wavelength as expected for a molecule with D_3 symmetry. However, around 700 nm we see a slight increase in the ratio which indicates the contributions from S_2 as the ratio stays around $\frac{2}{3}$ for the S_1 and S_3 resonances.

2.4.3 HRayS of A Silver Cluster

As discussed in the introduction, HRayS measurements of gold and silver nanoparticles have found that they have significantly larger HRayS response than typical organic molecules.^{48–51} However, it is not straightforward to compare the NLO response of these large nanoparticles with that of small organic molecules due to the large differences in the number of atoms for these systems. Therefore, a figure of merit as $\beta' = \beta/\sqrt{N_{atom}}$ was introduced by Johnson *et al.*⁴⁸ to facilitate this comparison. Using this method, silver was reported to have a value of $\beta'_{Ag} \sim 5600 \times 10^{-30}$ esu with slightly smaller values being found for gold ($\beta'_{Au} \sim 2800 \times 10^{-30}$ esu) and copper ($\beta'_{Cu} \sim 1600 \times 10^{-30}$ esu)⁴⁸ at 820 nm. Similarly sized Pt nanoparticles showed no detectable HRayS signal. For comparison, the prototypical dipolar molecule *p*-NA has a value of $\beta'_{p-NA} \sim 50 \times 10^{-30}$ esu and the octupolar molecule CV has a value of $\beta'_{CV} \sim 184 \times 10^{-30}$ esu under similar conditions.⁷⁵ This large enhancement was attributed to a two-photon resonance with the strong plasmon excitation in the metal nanoparticles. Small metal clusters are often used as model systems for understanding the microscopic origin of the plasmon excitation.⁷⁶ Here, we will study the resonance HRayS scattering of Ag_8 and Ag_{20} clusters.

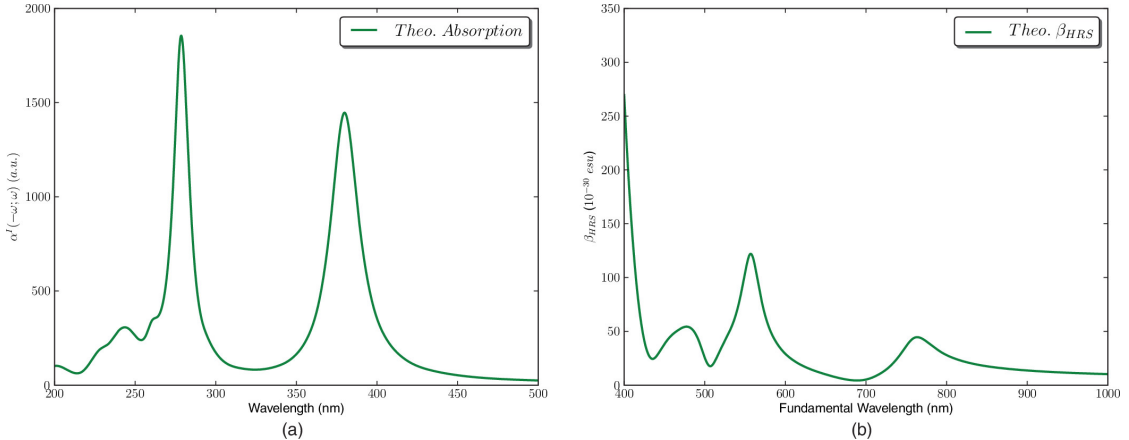


Figure 2.5. (a) Simulated absorption spectrum, and (b) simulated HRayS spectrum for a Ag_8 cluster.

In Figure 2.5(a) we plot the absorption spectrum of a Ag_8 cluster with T_d symmetry. Experimentally, two main absorption bands at 318 nm and 392 nm are found for the cluster embedded in an Ar matrix which causes a slight red shift.^{108,109} We see that the simulated absorption spectrum is characterized by three bands at 244 nm, 278 nm and 380 nm in reasonable agreement with the experiments. The corresponding HRayS spectrum for Ag_8 cluster is shown in Figure 2.5(b) where we see the two-photon resonance due to the three main absorption features. We also see a very steep rise in the HRayS near 400 nm resulting from the one-photon resonance enhancement from the lowest absorption band. For Ag_8 cluster, we find a static HRayS first-order hyperpolarizability of $\beta_0^{HRayS} = 4.9 \times 10^{-30}$ esu, which is comparable to that of *p*-NA. The strongest two-photon enhancement of around a factor of 25 is found for the second absorption band, whereas smaller enhancements of around a factor of 10 are found for the two other absorption bands. The fact that the two-photon enhancement of the first and third band is comparable

is likely a result of an additional enhancement of the third band originating from the strong one-photon resonance near 400 nm.

The experimental absorption spectrum for the Ag_{20} cluster embedded in an Ar matrix is dominated by a single strong absorption band at 335 nm.^{108,109} This is in good agreement with the plasmon resonance for small silver nanoparticles which is found at 354 nm using Mie theory.⁷⁶ The simulated absorption spectrum of Ag_{20} cluster is shown in Figure 2.6(a), where we find a strong band at 325 nm in good agreement with the experiments. In Figure 2.6(b) we plot the HRayS spectrum of the Ag_{20} cluster which is dominated by a large two-photon resonance enhancement due to the strong absorption band at 325 nm. The static HRayS first-order hyperpolarizability of Ag_{20} cluster is found to be $\beta_0^{\text{HRayS}} = 198 \times 10^{-30}$ esu which is significantly larger than that of CV. The resonance enhancement due to the two-photon absorption is about a factor of 10. On resonance, the two-photon enhanced HRayS of Ag_{20} cluster is comparable to the resonance value for CV.

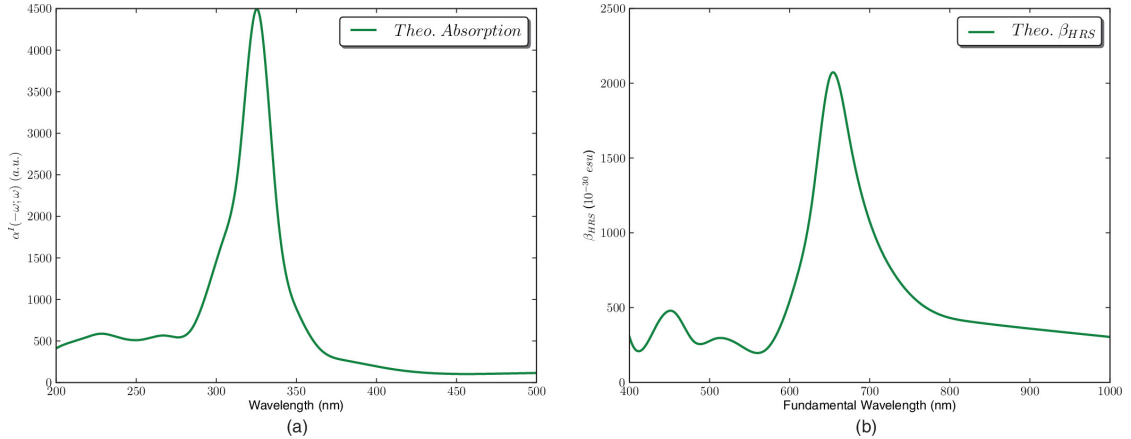


Figure 2.6. (a) Simulated absorption spectrum, and (b) simulated HRayS spectrum for a Ag_{20} cluster.

To compare our HRayS results with data obtained for large nanoparticles we can calculate the HRayS figure of merit for the silver clusters. For the Ag_8 cluster we find $\beta' \sim 1.7 \times 10^{-30}$ esu and for Ag_{20} cluster we find $\beta' \sim 447 \times 10^{-30}$ esu. Thus, we find a significant increased β' for the Ag_{20} cluster likely due to the more plasmonic nature of the absorption for this cluster. However, the values still fall short of the $\beta' \sim 5600 \times 10^{-30}$ esu found for large nanoparticles by about an order of magnitude. The experimental value was determined using water as an internal standard with $\beta^{\text{HRayS}} \sim 0.56 \times 10^{-30}$ esu. Shelton and co-workers reported a value for water of $\beta^{\text{HRayS}} \sim 0.07 \times 10^{-30}$ esu (here reported as $\beta^{\text{HRayS}} \sim \sqrt{\frac{6}{5}}\beta_L$, where β_L is the HRayS measured using VV polarization).^{41,42} This value is in reasonable agreement with $\beta_0^{\text{HRayS}} \sim 0.1 \times 10^{-30}$ esu calculated for water using the TZP basis set. Again, our calculated value is slightly larger than the value reported by Shelton and co-workers most likely due to the small basis set used. However, the value reported by Shelton and co-workers is about a factor of 8 lower than the value used by Johnson *et al.* Accounting for the difference in the β^{HRayS} of water would bring the agreement between theory and experiments to within a factor of two. Although we cannot rule out other

reasons for the discrepancy between the theory and the experiments, the reasonable agreement found for *p*-NA and CV is certainly suggestive that a large portion of this discrepancy is due to the different internal standards used. This points towards that small silver clusters possess comparable two-photon enhanced HRayS to that of larger nanoparticles on a per atom basis. Thus, these small metal clusters are potentially interesting for designing new NLO materials as their optical properties can be tuned by changing their size as well as incorporating electronic donating and accepting ligands.

2.5 Conclusion

In this work, we reported the simulated HRayS of *p*-NA, CV and silver clusters in the gas phase based on a TD-DFT approach. To better demonstrate the non-linear response of metal clusters that are characterized by a high density of states, we calculated the damped first-order hyperpolarizability (β) by using damped quadratic response theory with the $(2n + 1)$ rule. Our simulated results are in reasonable agreement with previous work from both experimental and theoretical perspectives, and we believe the discrepancy between theory and experiments for silver clusters is mainly caused by using different internal standards. Our results show the basis set effect on the first-order hyperpolarizability calculations, as well as the usage of the depolarization ratio as a sensitive reporter on the contributions from multiple transitions. Intriguingly, we find that the small silver clusters possess comparable two-photon enhanced HRayS to that of larger nanoparticles on a per atom basis, which indicates the potential interest of using small metal cluster for designing new NLO materials.

Chapter 3 |

Probing Two-Photon Molecular Properties with Surface-Enhanced Hyper-Raman Scattering: A Combined Experimental and Theoretical Study of Crystal Violet

Hubert, T. K.; Hu, Z.; Silverstein, D. W.; Cooper, D. A.; Jensen, L.; Camden, J. P. “*Probing Two-Photon Molecular Properties with Surface-Enhanced Hyper-Raman Scattering: A Combined Experimental and Theoretical Study of Crystal Violet*” *J. Phys. Chem. C* **2016**, *120*, 20936.

Abstract

The surface-enhanced hyper-Raman scattering spectra of crystal violet are experimentally measured and theoretically calculated for excitation energies spanning the two lowest-lying electronic states (12,700–27,400 cm^{-1}). The theory and experiment are in qualitative agreement over the measured energy range, indicating that first-principles calculations capture many of the complex resonance contributions in this prototypical octupolar system. The discrepancies between theory and experiment are investigated by comparing spectra obtained in different local environments as well as from higher-order surface-enhanced spectroscopies. A comparison between relative surface-enhanced hyper-Raman scattering band ratios plotted as a function of excitation wavelength and crystal violet’s absorption spectra elucidates correlations between groups of vibrations and the excited-electronic states. Our results suggest that the spectral features across the range of resonance excitation energies ($\sim 15,500$ – $27,400 \text{ cm}^{-1}$) are dominated by strong A-term scattering.

3.1 Introduction

Motivated by the rapid expansion of nonlinear optical (NLO) technologies, many studies target low cost organic materials with strong two-photon properties¹¹⁰ for applications such as multiphoton imaging¹¹¹ and all-optical switching.¹¹² From the perspective of the electric-field-induced molecular dipole moment (μ), the relative strength of a molecule’s two-photon response is directly related to the first hyperpolarizability, β .^{113,114} As a class of nonlinear materials, highly conjugated molecules with octupolar symmetry are advantageous due to their inherently large¹¹⁵ β and ability to form noncentrosymmetric bulk materials.¹¹⁶ The common triphenylmethane dye¹¹⁷ crystal violet (tris[p-(dimethylamino)phenyl]methyl chloride or CV) serves as a prototypical octupolar system and has been the subject of numerous previous studies.^{73,75,105,115,117–136}

As understanding excited-state contributions to the molecule’s optical response benefits the design and optimization of future NLO materials, we briefly review the electronic structure of CV. The left panel of Figure 3.1 displays the absorption spectra of CV in the region containing the lowest lying electronic excited states. The one-photon absorption (OPA) spectrum of CV in water (blue trace) is dominated by a resonance near 17,000 cm^{-1} , which we label S_1 in the following discussion. The strong shoulder on the blue side of S_1 ($\sim 18,600 \text{ cm}^{-1}$) is attributed to the splitting of a group of states which are initially degenerate in D_3 symmetry but become non-degenerate through solvent induced symmetry breaking.^{75,133} The two-photon absorption (TPA) spectrum, adapted from Rao et al.,¹²⁸ displays a strong resonance near 26,700 cm^{-1} , which we label S_2 for our discussion and is symmetry forbidden in linear absorption methods; i.e., it does not appear in the OPA. Although the experimental TPA spectrum in Figure 3.1 does not extend to the energy range of S_1 , previously reported hyper-Rayleigh scattering measurements⁷⁵ from this region demonstrate that S_1 is strongly two-photon allowed as well.

A more complete picture of the excited-state contributions to CV’s NLO response can be formed by combining both one- and two-photon probes. In regard to two-photon probes, many previous studies probe CV’s β by utilizing elastic nonlinear light scattering and hyper-Rayleigh scattering.^{73,75,122,128} Although most of these studies are limited to a few excitation energies, Campo *et al.*⁷⁵ provide an in-depth analysis of the dispersion of CV’s β across a broad energy range that includes both S_1 and S_2 . Herein, we extend the analysis of CV’s NLO response over the lowest electronic states using inelastic nonlinear light scattering and hyper-Raman (HR) scattering.

In analogy to Raman scattering, vibrational HR scattering¹⁴ gives rise to inelastic scattering at $2\omega_L \pm \omega_{\text{vib}}$, where ω_L is the laser frequency and ω_{vib} is a vibrational frequency of the molecule. Compared to its linear counterpart, however, the HR effect is extremely weak and easily overwhelmed by competing effects such as two-photon fluorescence. Practical applications often rely on surface enhancement from plasmonic nanoparticles to amplify scattered signal and quench fluorescence. As CV demonstrates a large HR cross section and strong affinity for plasmonic substrates, a majority of studies that report the HR scattering of CV do so using surface-enhanced hyper-Raman scattering (SEHRS). While most HR studies^{120,123,125,126,129–133,135} involving CV utilize the molecule as a SEHRS chemical probe, others^{119,124,128} utilize comparisons between the

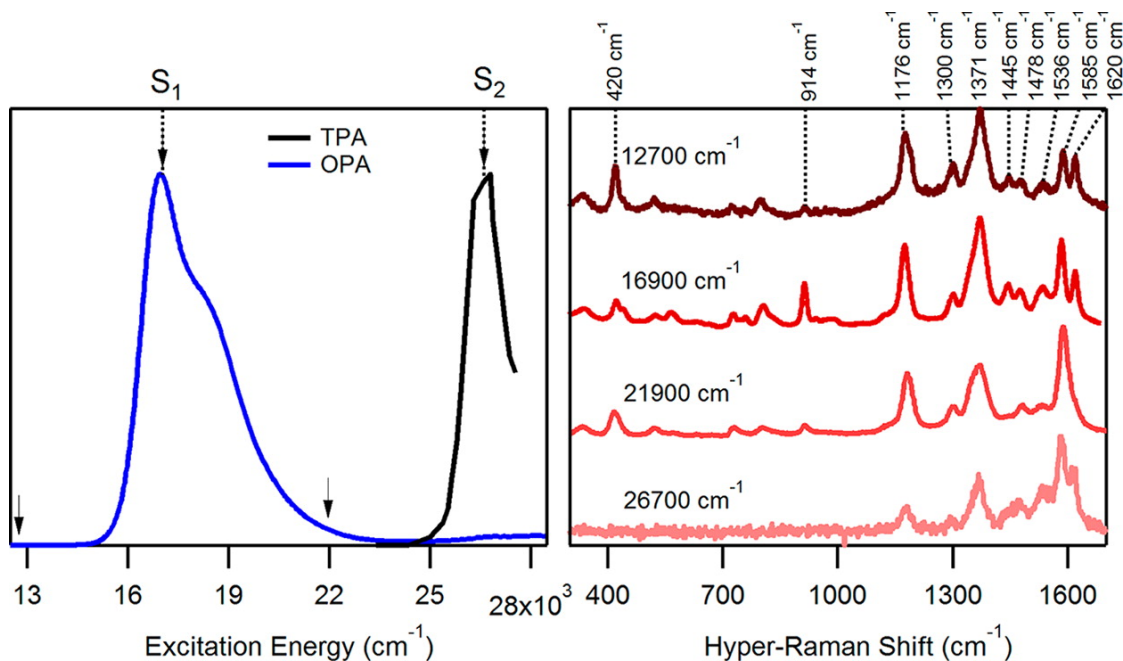


Figure 3.1. One-photon absorption (left panel, blue trace) and two-photon absorption¹²⁸ (left panel, black trace) of CV in water and methanol, respectively, spanning the energy range 12,500–28,500 cm^{-1} that includes the two lowest-lying electronic states, which are labeled S_1 and S_2 . The surface-enhanced hyper-Raman scattering spectra of CV (right panel, 10^{-7} M) with excitation energies at 12,700 cm^{-1} (1570 nm), 16,900 cm^{-1} (1180 nm), 21,900 cm^{-1} (915 nm), and 26,700 cm^{-1} (750 nm) demonstrate characteristic hyper-Raman scattering under different resonance scattering conditions. The arrows in the left panel reference the location of the surface-enhanced hyper-Raman scattering excitation energies.

HR signatures and complementary spectroscopies such as surface-enhanced Raman scattering (SERS), infrared, and hyper-Rayleigh scattering to discuss the assignment of CV’s vibrational modes and symmetry.

Under resonance conditions, the structural information encoded in the HR effect provides insights into the geometry of two-photon-accessible electronic states. In a series of HR studies of rhodamine 6G (R6G), for example, we recently demonstrated that a comparison of resonance-enhanced SEHRS data to first-principles resonance cross-section calculations provided unique access to vibronic-coupling terms in the one- and two-photon electronic transitions and further aided in interpretation of the two-photon absorption spectrum.^{18,137,138} The SEHRS spectra of CV in Figure 3.1 demonstrate several modes, e.g., 914 and 1620 cm^{-1} , change dramatically as a function of excitation energy; however, we find that the simple correlation between the absorption spectrum and the hyper-Raman spectra obtained for R6G is not preserved in CV.

In this manuscript, we present a wavelength-scanned approach to theoretical and experimental comparisons utilizing resonance SEHRS that overcomes the complex situation in CV. We extend the short-time approximation, previously used to describe resonance Raman scattering,⁵⁷ to our simulations of resonance HR scattering allowing us to account for the many overlapping electronic excited states in CV. While reasonable agreement between SERS and SEHRS measurements and theory simulations is obtained, significant discrepancies remain. We explore the nature of these

discrepancies through HR scattering measurements of CV in different solvents and higher-order light scattering. Lastly, we examine relative SEHRS band intensities as a function of excitation energy to illustrate correlations between excited states and groups of vibrations.

3.2 Experimental Methods

Silver colloids were prepared using a previously detailed method¹³⁹ that relies on citrate reduction in ultrapure water. Aliquots of the silver colloid solution were incubated with CV (Sigma) for 1 h and then aggregated with 1 M NaBr (Alfa Aesar). The same CV sample (10^{-7} M) was used for all surface-enhanced spectra. Solutions of CV (0.3 mM) in ultrapure water, benzonitrile (TCI), and chloroform (Alfa Aesar) were used for normal HR scattering measurements. UV/vis of CV in water (10^{-6} M) was taken with a scanning spectrophotometer (VWR, UV-3100PC).

All scattering spectra were collected in the backscattering geometry on an inverted Nikon microscope (Nikon, Ti-U) with a 20 \times objective (Nikon, NA = 0.5, air). The scattered signal was then analyzed by one of two methods. Scattered signal over the range 365–430 nm was coupled into a dispersive imaging spectrometer (PI Acton Research, $f = 0.3$ m) with a 1800 g/mm grating and detected by a liquid-nitrogen-cooled, backilluminated CCD (PIXIS, Spec-10, Princeton Instruments). Meanwhile, scattered signal over the ranges 410–775 and 775–900 nm was coupled into a second dispersive imaging spectrometer (PI Acton Research, $f = 0.3$ m) with a 1200 and 600 g/mm grating, respectively, and detected by a liquidnitrogen-cooled, back-illuminated, Deep Depletion eXcelon CCD (PIXIS, Spec-10, Princeton Instruments).

Two excitation sources were used to generate scattered spectra. A 532 nm pumped optical parametric oscillator (APE, PicoEmerald, ~ 6 ps, 80 MHz) provided fundamental wavelengths over the range 820–990, 1064, and 1155–1570 nm. A 532 nm pumped Ti:sapphire (Spectra-Physics, Tsunami, ~ 5 ps, 80 MHz) provided fundamental wavelengths over the range 730–790 and 1000–1030 nm. Fundamental wavelengths for SERS measurements over the range 410–633 nm were obtained using second-harmonic generation from a BBO crystal. Typical laser power/exposure times for the SERS, SEHRS, and SE2HRS measurements were 30 μ W/30 s, 2 mW/2 min, and 8 mW/5 min, respectively. Typical laser power/exposure times for HR scattering measurements in solution were 250 mW/20 min. The spectra were processed using a peak-fitting routine in Igor software (Wavemetrics) that assumed Lorentzian peak shape and a cubic baseline.

3.3 Theoretical Methods

The differential hyper-Raman scattering cross section is given by¹⁹

$$\frac{d\sigma^{\text{HRS}}}{d\Omega} = \frac{16\pi^2 h^3 \alpha_f^3 \nu_s^4 P_i}{Nc^2 e^6} \langle \beta'_{\alpha\beta\gamma} \rangle^2 \quad (3.1)$$

where α is the fine structure constant, ν_s is the frequency of the scattered radiation, P_i is the population of the initial vibrational state, N is the number of scatters per unit volume, h is Planck's constant, and c is the speed of light. The bracket indicates that the hyperpolarizability

tensors are obtained assuming averaging over all orientations of the molecule with respect to the incident light. $\beta'_{\alpha\beta\gamma}$ is referred to as the transition hyperpolarizability and is given by the partial derivative of the hyperpolarizability with respect to the normal mode Q_a as

$$\beta'_{\alpha\beta\gamma} = \sqrt{\frac{\hbar}{8\pi^2 c \nu_a}} \frac{\partial \beta_{\alpha\beta\gamma}(-2\omega, \omega, \omega)^{\text{el}}}{\partial Q_a} \quad (3.2)$$

where ν_a is the vibrational frequency of the a th normal mode.⁹⁶ The hyperpolarizability derivatives are calculated using a three-point finite-differentiation of the hyperpolarizability obtained using a recently implemented damped quadratic response formalism.¹⁴⁰ This is an extension of previous work for describing resonance Raman scattering based on damped linear response theory, and allows us to treat both resonance and nonresonance hyper-Raman scattering on an equal footing based on a short-time approximation to resonance (hyper-)Raman scattering.⁵⁷ Previous work⁹⁷ for describing the resonance hyper-Raman scattering was based on the time-dependent theory of Raman scattering, which allowed for the inclusion of vibronic effects but required separate treatment of the Franck–Condon (A) and Herzberg–Teller (B) scattering terms and only accounted for a few of the lowest excited electronic states. In contrast to this, the approach adapted in this work includes both the A and B terms as well as contributions from all excited electronic states, but other vibronic effects are not included in the simulations.

All calculations in this work were performed using a locally modified version of the Amsterdam Density Functional (ADF) program package.^{63,64,141} The optimized geometry and normal modes for CV were determined using the Becke-Perdew (BP86)^{87,88} XC potential with a triple- ζ polarized Slater type (TZP) basis set from the ADF library. In the simulations, we assumed a single, isolated chromophore with a geometry near D_3 symmetry, but the symmetry was not enforced for the calculations of the response properties. The statistical average of orbital model exchange-correlation potentials (SAOP)^{89,90} and the TZP basis set were used for calculating both linear and nonlinear response properties of CV, in which the incomplete fit basis sets in ADF were accounted for by invoking the key word “FitAOrderiv”, and the electronic broadening parameter was included phenomenologically as 0.0034 a.u. ($\sim 800 \text{ cm}^{-1}$).

3.4 Results and Discussion

3.4.1 Theory/Experiment Comparison

To address the mechanism underpinning excited-state contributions to CV’s two-photon response, we compare Raman and HR spectra with first-principles simulations for conditions on resonance with S_1 , on resonance with S_2 , and off-resonance (Figure 3.2). The theoretical spectra are calculated neglecting solvent interactions and adsorption to the silver particle, where CV adopts a near D_3 symmetry. For consistency, the excitation energies utilized for the nonresonant, S_1 , and S_2 spectra are obtained from the simulated OPA and TPA spectra. The experimental data displayed in Figure 3.2 are obtained using surface enhancement, as the unenhanced spectra of CV in water are too weak to be measured from off-resonance conditions and are overwhelmed by

fluorescence at many of the wavelengths in this study. Where possible, we have experimentally verified that the surface-enhanced and the normal HR agree (Figure 3.3); therefore, we believe the surface-enhanced spectra are representative of the CV spectra.

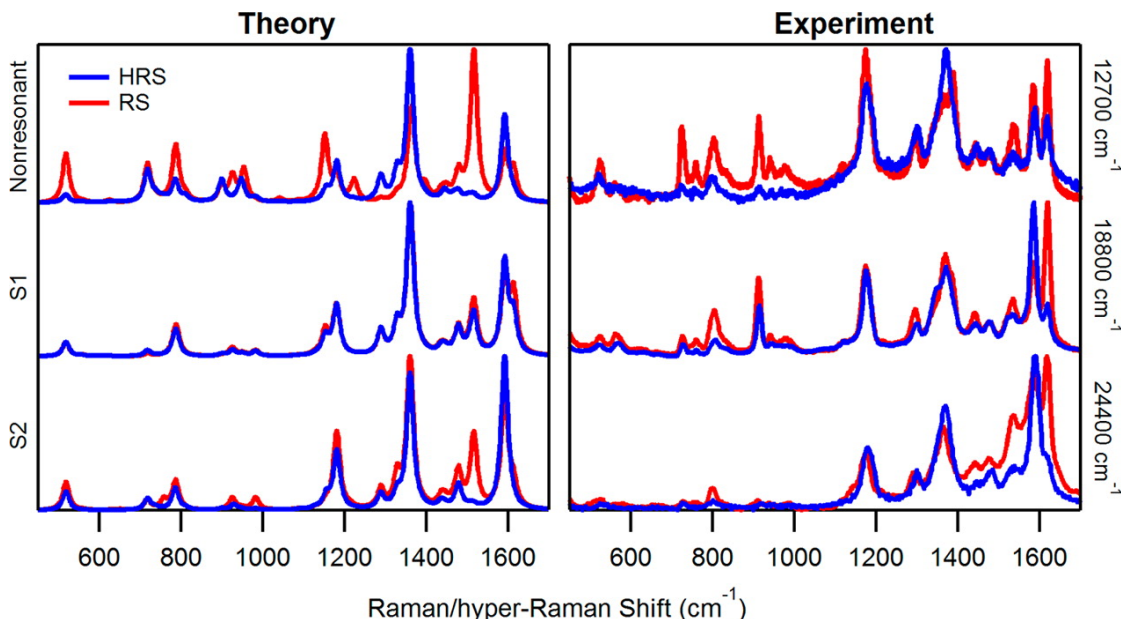


Figure 3.2. Comparison of theoretically calculated (left panel) hyper-Raman (blue) and Raman (red) scattering with experimentally measured surface-enhanced spectra (right panel). The top set of traces display spectra far from electronic resonance, while the middle and bottom traces display spectra on resonance with the two lowest electronic transitions, S_1 and S_2 , respectively. The corresponding excitation energies are noted to the right of the experimental panel.

Consistent with previous reports,^{119,124,128} both the theory and experiment demonstrate that the Raman and hyper-Raman scattering contain the same vibrational modes across all three excitation energies probed in Figure 3.2. The fact that new bands are not observed as the excitation energy changes stands in contrast to the parallel experiment using R6G¹³⁸ and indicates that CV's symmetry does not result in selection rules that are mutually exclusive between Raman and HR. Additionally, the comparison at $12,700\text{ cm}^{-1}$ ($785\text{ nm}/1570\text{ nm}$) is the first report of CV's HR scattering from nonresonant conditions. Comparing the nonresonant SERS and SEHRS spectra (top traces, Figure 3.2), there are clear differences in the relative peak intensities in both theory and experiment; however, these differences become smaller as one approaches resonance with S_1 .

SERS and SEHRS are compared at an excitation energy of $18,800\text{ cm}^{-1}$ ($532\text{ nm}/1064\text{ nm}$) to illustrate resonance scattering on S_1 and to be consistent with theoretical¹³⁴ and experimental¹³⁶ evidence that adsorption to the silver colloids modifies the location of the dominant peak in CV's OPA. According to the vibronic theory¹⁴² of resonance HR scattering, A-term scattering dominates the resonance contributions when the excited state is both one- and two-photon allowed. In the simulations, S_1 corresponds to a set of degenerate states, and thus, the HR scattering simulation is nearly identical to the Raman scattering simulation. The fact that the relative

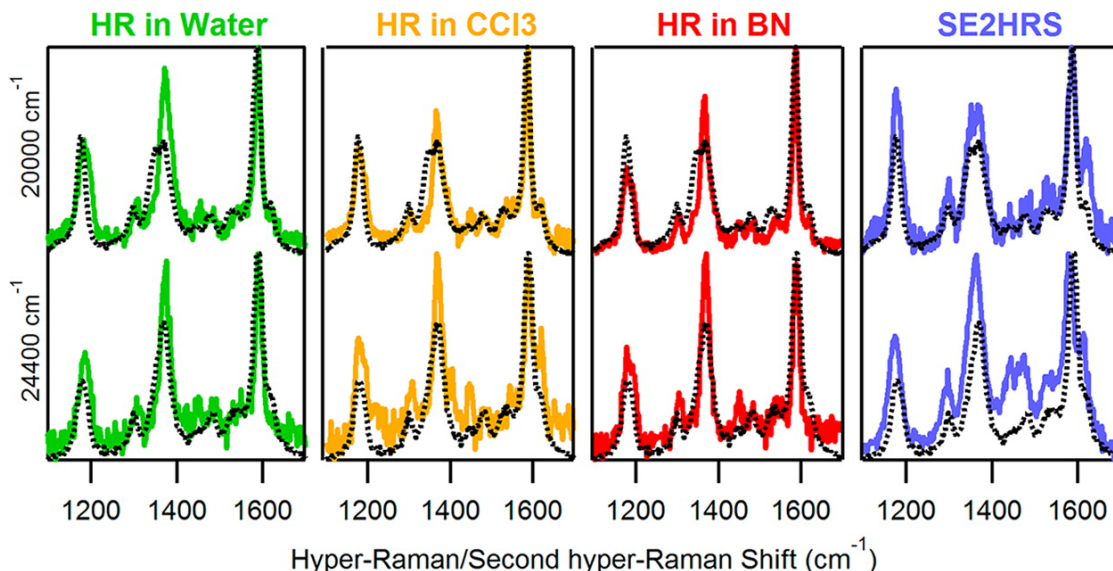


Figure 3.3. Comparison of SEHRS (dotted, black) with the HR scattering of CV in water (solid, green), chloroform (CCl₃, solid, orange), and benzonitrile (BN, solid, red) as well as its SE2HRS (solid, blue). The top row displays spectra from an excitation energy near S₁ at 20,000 cm⁻¹ (1500 nm for SE2HRS and 1000 nm for SEHRS/HR scattering), and the bottom row displays spectra from an excitation energy near S₂ at 24,400 cm⁻¹ (1230 nm for SE2HRS and 820 nm for SEHRS/HR scattering).

vibrational band intensities in the experimental SERS and SEHRS spectra become more similar as the excitation energy is moved from 12,700 to 18,800 cm⁻¹ indicates that the scattering in the region of S₁ is indeed dominated by A-term scattering from a single state or a set of nearly degenerate states.

In contrast to S₁, S₂ is one-photon forbidden but two-photon accessible; therefore, the scattering mechanisms on resonance with S₂ are more complex. The theory predicts the relative band intensities in the HR spectrum to be similar to those in the Raman spectrum except for a few cases; e.g., the band at 1516 cm⁻¹ appears more strongly in Raman than HR. While the experimental setup restricts the SERS and SEHRS spectra on resonance with S₂ to an excitation energy of 24,400 cm⁻¹ (410 nm/820 nm), we expect these conditions to be close to resonant and, therefore, a reasonable comparison with theory. The SERS/SEHRS comparison at 24,400 cm⁻¹ shows generally good agreement with the exception of the 1536 cm⁻¹ band. Overall, the general features of both the SERS and SEHRS spectra are reproduced by the theory, which indicates that first-principles calculations can capture the complex interplay of overlapping excited states in this region.

3.4.2 Theory/Experiment Discrepancies

The largest discrepancies between theory and experiment typically involve the 1536, 1585, and 1620 cm⁻¹ modes, corresponding to a combination of C–C stretching and C–H bending in the aromatic rings. Since these discrepancies occur in both on- and off-resonance conditions, they likely arise from symmetry-lowering effects not captured by the theory. Previous studies^{75,105} report

that interactions with the environment or possibly the existence of multiple species with different symmetry influence the observed optical properties. In particular, Kelley *et al.*¹⁰⁵ reported a HR depolarization ratio of 0.5 and 0.6 on resonance with S_2 in acetone and methanol, respectively. The theoretical studies in this work predict a depolarization ratio of 2/3, which arises from the gas-phase, D_3 symmetry of CV in the calculations. The experimental depolarization ratios near S_2 , therefore, remain consistent with either a symmetry lowering of CV or contributions from another species with reduced symmetry. Interestingly, even when D_3 symmetry of CV is preserved, our theory predicts that the depolarization ratio drops to 0.55 near S_1 and further reduces to 0.14 off resonance due to the increased importance of a single diagonal hyperpolarizability component. This suggests that future studies of the HR depolarization would contribute to an understanding of CV’s solution-phase structure.

To investigate the interactions with the environment, we compare the SEHRS with HR scattering from CV in water, chloroform, and benzonitrile at two excitation energies in the first three columns of Figure 3.3. While there are subtle differences between the SEHRS and solution-based spectra, each spectrum displays the same general features indicating that surface effects are minor. Furthermore, the small differences in the relative band intensities likely arise from perturbations to CV’s electronic structure due to the local environment. Next, we explore the origin of the discrepancies between theoretical and experimental spectra through the higher-order scattering mechanism, surface-enhanced second hyper-Raman scattering¹⁴³ (SE2HRS). The second hyper-Raman (2HR) effect is a weak nonlinear process in which three photons at ω_L inelastically scatter one photon at $3\omega_L \pm \omega_{\text{vib}}$ and provides complementary information to HR scattering. In contrast to a previous experiment with R6G,¹⁴³ no new bands appear between the SE2HRS and SEHRS from the same sample and excitation energies (last column, Figure 3.3). The similarities between all of the spectroscopies in Figure 3.3 clearly suggest that A-term scattering dominates.

3.4.3 SEHRS Peak-Area Ratios

In a parallel study¹⁸ using R6G, we interpreted the correlations between vibrational modes and electronic-excited states by comparing the integrated-band intensities to a reference mode over a broad range of excitation energies. This simple approach yielded surprising insights into the nuclear motions responsible for the vibronic coupling mechanism that underpins R6G’s two-photon absorption spectrum.^{137,138} Adapting a similar approach, we integrated the area under prominent vibrational bands between 1100 and 1700 cm^{-1} in CV’s SEHRS spectra and examined how the peak-area ratios change as a function of excitation energy from 12,700 to 27,400 cm^{-1} (730–1570 nm). The ratios (Figure 3.4) indicate the interplay of electronic transitions and vibrational modes is more complex in CV than R6G, which is consistent with the larger number of nearly degenerate electronic states present in CV as compared to R6G. Three major trends, however, emerge upon comparison with CV’s absorption spectra. The correlation between the group of ratios in Figure 3.4a, which displays a peak at an excitation energy of 27,000 cm^{-1} (740 nm), and the TPA spectrum indicates the 1620 and 1536 cm^{-1} modes are preferentially enhanced on resonance with S_2 . The correlation between the group of ratios in Figure 3.4b, which displays two peaks at 18,800

cm^{-1} (1064 nm) and $27,000 \text{ cm}^{-1}$ (740 nm), and S_1 and S_2 indicate the 1585 , 1371 , and 1176 cm^{-1} modes are preferentially enhanced by multiple electronic states. Furthermore, the fact that the features captured by the groups of ratios in Figure 3.4a and b are blue-shifted in comparison to the maxima in the absorption spectra is in good accord with previous work on CV's shifted absorbance on silver colloids.^{134,136}

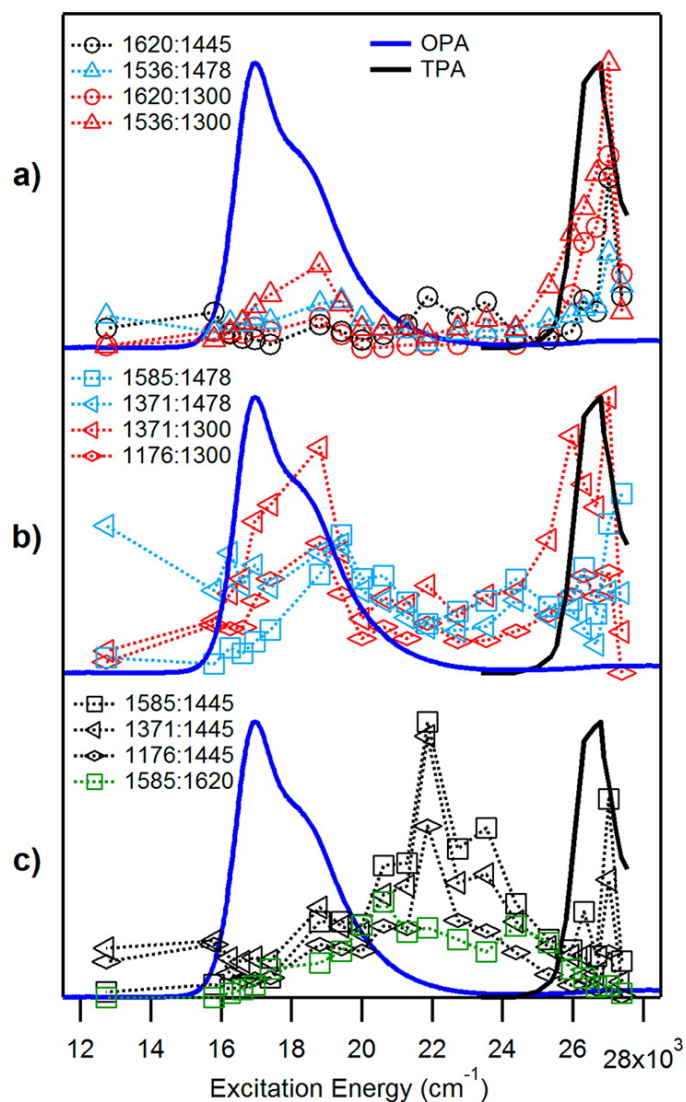


Figure 3.4. In each panel, a group of ratios (dotted lines with markers) from CV's SEHRS bands between 1100 and 1700 cm^{-1} are plotted as a function of excitation energy over the range from $12,700 \text{ cm}^{-1}$ to $27,400 \text{ cm}^{-1}$ (730 – 1570 nm) and compared to the OPA (solid blue) spectrum in water and TPA¹²⁸ (solid black) spectrum in methanol. Each group of ratios and the absorption spectra are normalized to facilitate comparisons.

In contrast to the previous comparisons, the group of ratios in Figure 3.4c displays a broad peak at $21,900 \text{ cm}^{-1}$ (915 nm) that does not correlate with any known electronic state of CV. It is possible these ratios compare modes from CV and another species with similar optical properties

such as the protonated form of CV, which is reported¹¹⁸ to have an electronic transition near $22,200\text{ cm}^{-1}$ (900 nm). Since interference from nearby electronic states could also affect these ratios, a conclusive identification of this broad peak requires further investigation.

3.5 Conclusion

In summary, we have presented a detailed comparison of experimentally measured and theoretically calculated nonlinear scattering spectra of a prototypical octupolar molecule, CV, for excitation energies spanning its two lowest-lying electronic states. While reasonable agreement between first-principles calculations and surface-enhanced spectra is obtained, a quantitative comparison is not yet possible. Comparing the SEHRS with HR in multiple solvents and SE2HRS indicates varying the local environments or utilizing higher-order scattering mechanisms cannot directly probe the discrepancies between theory and experiment. Further, examining the ratio of prominent SEHRS bands as a function of excitation energy reveals correlations between certain groups of vibrations and excited states. This work extends the current understanding of CV's NLO properties and expands our understanding of SEHRS-based methods for obtaining chemical information that is complementary to hyper-Rayleigh scattering.

Chapter 4 | Simulating Third-order Nonlinear Optical Properties Using Damped Cubic Response Theory within Time-Dependent Density Functional Theory

Hu, Z.; Autschbach, J.; Jensen, L. “*Simulating Third-order Nonlinear Optical Properties Using Damped Cubic Response Theory within Time-Dependent Density Functional Theory*” *J. Chem. Theory Comput.* **2016**, *12*, 1294.

Abstract

A general implementation for damped cubic response properties is presented using time-dependent Density functional theory (TDFFT) and Slater-type orbital (STO) basis sets. To directly calculate two-photon absorption (TPA) cross sections, we also present an implementation of a reduced damped cubic response approach. Validation of the implementations includes a detailed comparison between response theory and the sum-over-states (SOS) approach for calculating the nonlinear optical (NLO) properties of LiH, as well as a comparison between the simulated and experimental TPA and third-harmonic generation (THG) spectra for the dimethyl-amino-nitrostilbene (DANS) molecule. The study of LiH demonstrates the incorrect pole structure obtained in response theory due to the adiabatic approximation typically employed for the exchange-correlation (XC) kernel. For DANS, we find reasonable agreement between simulated and experimental TPA and THG spectra. Overall, this work shows that care must be taken when calculating higher-order response functions in the vicinity of one-photon poles due to the approximate kernels typically used in the simulations.

4.1 Introduction

Nonlinear optical (NLO) processes involving interactions with multiple photons have seen applications in optical power-limiting^{10,144–147} optical data storage,^{11,148–151} and optical image processing.^{13,130,152–155} There is significant interest in developing new materials for all-optical switching devices by exploiting the intensity-dependence of the refractive index (IDRI), which at the microscopic level is described by the second hyperpolarizability $\gamma(-\omega; \omega, \omega, -\omega)$.¹ The requirement for all-optical switching applications is NLO materials characterized by a large $\text{Re}(\gamma)$ and a small $\text{Im}(\gamma)$, meaning low losses caused by weak two-photon absorption (TPA) processes.^{12,156} Thus, to understand the molecular response relevant for all-optical switching, it is important to describe both the real and imaginary contributions to the third-order nonlinear response.

The characterization of the third-order response is typically done using a simplified sum-over-states (SOS) approach. This approach assumes that a few states dominate the response, which provides a good description near resonances but not far from resonances.¹ While this deficiency can be remedied by including all states, it is not suitable for practical use. However, the SOS expressions can be recast in a computational efficient form that includes all electronic states, which was recently used to describe TPA at the equation-of-motion coupled-cluster level of theory.¹⁵⁷ Alternatively, response theory provides a general framework for deriving response functions using both approximate and exact methods without the need to explicitly consider the sum over all electronic states.^{98,158} For the exact wavefunction, these different formalisms give identical results but differ when approximate methods are used.¹⁵⁸

Standard response theory fails to predict the correct behaviors for molecular properties in the resonance region due to the divergence of response functions when optical frequencies, or the sum of them, equal an excitation energy. Although this divergence can be exploited using residual analysis to identify transition matrix elements for multi-photon transitions,^{98,158} damped response theory that takes the broadening of electronic states into account can avoid the unphysical behaviors for molecular properties on resonance. Norman *et al.*^{4,6} pioneered the extension of standard linear and quadratic response formalisms to also describe the resonance case, where an empirical damping factor was included into the standard Ehrenfest equation. The introduction of the damping factor leads to naturally broadened absorption spectra, but vibronic effects are neglected, which can be important for describing linear and NLO properties.^{97,159–161} Recently, Kristensen *et al.*³ reported a quasi-energy formulation of damped response theory by using complex excitation energies. This approach is intrinsically equivalent to the one reported by Norman and co-workers,⁶ and has been used to describe TPA spectra based on modified damped cubic response functions.⁹⁹

In this work, we present a general implementation of damped cubic response properties using time-dependent density functional theory (TDDFT) and Slater-type orbital (STO) basis sets in the Amsterdam Density Functional (ADF) program package.^{63–65} This is an extension of the damped linear⁵ and quadratic¹⁴⁰ response theory implementations in ADF. We have implemented damped cubic response theory based on the $2n + 1$ rule that leads to an efficient algorithm, as well

as a direct solver for the third-order density matrix by solving a set of damped third-order response equations. The latter approach facilitates the direct partitioning of the response into contributions from localized orbitals.⁸² For calculating the TPA cross sections, we also implemented a reduced damped cubic response approach similar to that presented by Kristensen *et al.*³ In this work, we consider only the pure electronic response even though the vibrational response can be significant, especially when considering IDRI.^{162–164} As a test of our implementation, we present a detailed comparison between response theory and the SOS approach for calculating the NLO properties of LiH. In addition to this, we also study TPA and third-harmonic generation (THG) of dimethyl-amino-nitrostilbene (DANS). The NLO properties of DANS have been extensively studied from both experimental and theoretical perspectives;^{165–169} thus, it serves a good benchmark system for the current implementation.

4.2 Theory

4.2.1 Damped Response Theory

In damped response theory, a complex orbital energy ($\varepsilon_i - i\Gamma$) is involved in the time-dependent Kohn-Sham (TDKS) equation, where Γ corresponds to an energy broadening term that can be related to the finite lifetime of the excited state.⁷⁷ In our previous work, we have shown that the damped response properties can be derived from the Γ -dependent TDKS equation in the presence of an external perturbation.¹⁴⁰ This follows the general derivations of the response equations without damping presented by Karna and Dupuis⁷⁸ for Hartree-Fock theory and later adapted by Van Gisbergen within a TDDFT formalism.⁷⁹ Here we will present the main results for the damped linear, quadratic and cubic response formalisms. Assuming the perturbation independence of the basis set,¹⁷⁰ the damped TDKS equation is given by^{78,79}

$$FC - iS \frac{\partial C}{\partial t} = SC(\varepsilon - i\Gamma), \quad (4.1)$$

subject to the orthonormality constraint

$$\frac{\partial}{\partial t} C^\dagger SC = 0, \quad (4.2)$$

where C is the coefficient matrix of the spatial orbitals ($\phi = \chi C$), S is the time-independent overlap matrix of the atomic orbitals (AOs), ε is the Lagrangian multiplier matrix, and Γ is the phenomenological damping factor. Further, F is the KS matrix expressed in the AO form as^{78,79}

$$F = h + D \times (2J) + \nu_{xc}, \quad (4.3)$$

where h is the one-electron integral matrix, J is the Coulomb matrix, D is the density matrix, and ν_{xc} is the exchange correlation (XC) potential. If we consider a closed shell molecule interacting with an external electric field E that consists of a monochromatic oscillating part and a static

part^{78,79}, we can expand the density matrix D in terms of the perturbation as

$$D = D^0 + \left[e^{\pm i\omega t} D^\alpha(\pm\omega) + D^\alpha(0) \right] E^\alpha + \frac{1}{2!} \left\{ e^{\pm 2i\omega t} D^{\alpha\beta}(\pm\omega, \pm\omega) + e^{\pm i\omega t} \right. \\ \left. \times \left[D^{\alpha\beta}(0, \pm\omega) + D^{\alpha\beta}(\pm\omega, 0) \right] + D^{\alpha\beta}(\pm\omega, \mp\omega) + D^{\alpha\beta}(0, 0) \right\} E^\alpha E^\beta + \dots, \quad (4.4)$$

where the superscript indicates the *direction* (x, y, z) of the perturbation and the number of superscripts indicates the *order* of the perturbation.^{78,79} From the perturbed density matrix, we can obtain the molecular response properties as described below.⁷⁸

4.2.1.1 Linear Response

The molecular polarizability is given as⁷⁸

$$\alpha_{\alpha\beta}(\mp\omega; \pm\omega) = -\text{Tr}[H^\alpha D^\beta(\pm\omega)], \quad (4.5)$$

where ω denotes the incident frequency and “Tr” stands for the trace. Here H^α is the dipole moment matrix with elements given by

$$H_{st}^\alpha = \langle \chi_s | \hat{\mu}_\alpha | \chi_t \rangle, \quad (4.6)$$

and D^β is the first-order perturbed density matrix given by

$$D^\beta(\pm\omega) = C^\beta(\pm\omega) n C^{0\dagger} + C^0 n C^{\beta\dagger}(\mp\omega), \quad (4.7)$$

where n is the occupation number matrix and $C^\beta(\pm\omega)$ represents the first-order perturbed MO coefficients. The first-order perturbed MO coefficients are related to the unperturbed MO coefficients as $C^\beta(\pm\omega) = C^0 U^\beta(\pm\omega)$, where $U^\beta(\pm\omega)$ is the first-order transformation matrix. Only the occupied-virtual block of the first-order transformation matrix is needed, for which the elements are given by

$$U_{ia}^\beta(\pm\omega) = \frac{G_{ia}^\beta(\pm\omega)}{\varepsilon_a^0 - \varepsilon_i^0 \mp (\omega + i\Gamma)}, \quad (4.8)$$

where $\varepsilon_a^0, \varepsilon_i^0$ are the KS one-electron energies of the virtual and occupied orbitals, respectively. Here $G^\beta(\pm\omega) = C^{0\dagger} F^\beta(\pm\omega) C^0$ is the first-order KS matrix in the MO basis.⁷⁸ The first-order Lagrangian multiplier matrix needed for the higher-order response can be calculated from $G^\beta(\pm\omega)$ and $U^\beta(\pm\omega)$ as

$$\varepsilon^\beta(\pm\omega) = G^\beta(\pm\omega) + (\varepsilon^0 U^\beta(\pm\omega) - U^\beta(\pm\omega) \varepsilon^0) \pm (\omega + i\Gamma) U^\beta(\pm\omega). \quad (4.9)$$

The first-order KS matrix in the AO basis is given as⁷⁹

$$F^\beta(\pm\omega) = h^\beta + D^\beta(\pm\omega) \times (2J) + \nu_{xc}^\beta(\pm\omega), \quad (4.10)$$

where the elements of the first-order XC potential $\nu_{xc}^\beta(\pm\omega)$ are⁷⁹

$$[\nu_{xc}^\beta(\pm\omega)]_{\kappa\lambda} = \sum_{\mu\nu} [f_{xc}(\pm\omega)]_{\kappa\lambda\mu\nu} [D^\beta(\pm\omega)]_{\mu\nu}, \quad (4.11)$$

for which the adiabatic local density approximation (ALDA)⁸¹ is used for the XC kernel

$$[f_{xc}(\pm\omega)]_{\kappa\lambda\mu\nu} \approx \int d\mathbf{r} \int d\mathbf{r}' \chi_\kappa(\mathbf{r}) \chi_\lambda(\mathbf{r}) \left[f_{xc}^{\text{ALDA}}(\mathbf{r}, \mathbf{r}', 0) \right] \chi_\mu(\mathbf{r}') \chi_\nu(\mathbf{r}'). \quad (4.12)$$

However, as discussed previously,⁷⁹ these matrix elements are never actually constructed during the simulations since only the potentials are needed. Once a self-consistent solution of U^β is obtained, the molecular polarizability can be calculated as described above.

4.2.1.2 Quadratic Response

The molecular first hyperpolarizability is given as⁷⁸

$$\beta_{\alpha\beta\gamma}(\mp\omega_\sigma; \pm\omega_1, \pm\omega_2) = -\text{Tr}[H^\alpha D^{\beta\gamma}(\pm\omega_1, \pm\omega_2)], \quad (4.13)$$

where ω_σ represents the sum of the two incident frequencies as $\omega_\sigma = \omega_1 + \omega_2$, and $D^{\beta\gamma}$ is the second-order perturbed density matrix given by

$$\begin{aligned} D^{\beta\gamma}(\pm\omega_1, \pm\omega_2) &= C^{\beta\gamma}(\pm\omega_1, \pm\omega_2) n C^{0\dagger} + C^0 n C^{\beta\gamma\dagger}(\mp\omega_1, \mp\omega_2) \\ &\quad + C^\beta(\pm\omega_1) n C^{\gamma\dagger}(\mp\omega_2) + C^\gamma(\pm\omega_2) n C^{\beta\dagger}(\mp\omega_1), \end{aligned} \quad (4.14)$$

where $C^{\beta\gamma}(\pm\omega_1, \pm\omega_2)$ represents the second-order perturbed MO coefficients. In our previous study, we have shown that damped β can be calculated efficiently using only linear response terms by exploiting the $2n + 1$ rule.¹⁴⁰ However, in order to calculate an even higher order response property, i.e., second hyperpolarizability γ , the quadratic response terms are also needed. This requires the calculation for the second-order transformation matrix $U^{\beta\gamma}(\pm\omega_1, \pm\omega_2)$ that connects the second-order perturbed MO coefficients with the unperturbed MO coefficients as $C^{\beta\gamma}(\pm\omega_1, \pm\omega_2) = C^0 U^{\beta\gamma}(\pm\omega_1, \pm\omega_2)$. Unlike the linear case which only requires the occupied-virtual block of U^β , both the diagonal and off-diagonal blocks of $U^{\beta\gamma}$ are necessary and can be further divided into two parts. The *constant* part only contains the terms obtained from solving the linear response equations and is given by

$$U_{ij, \text{const}}^{\beta\gamma}(\pm\omega_1, \pm\omega_2) = \begin{cases} \frac{1}{2} \left\{ U_{ij}^\beta(\pm\omega_1) U_{ij}^\gamma(\pm\omega_2) + U_{ij}^\gamma(\pm\omega_2) U_{ij}^\beta(\pm\omega_1) \right\} & \text{diagonal} \\ \frac{T_{ij}^{\beta\gamma}(\pm\omega_1, \pm\omega_2)}{\varepsilon_j^0 - \varepsilon_i^0 \mp (\omega_1 + \omega_2 + i\Gamma)} & \text{off-diagonal} \end{cases} \quad (4.15)$$

where

$$T_{ij}^{\beta\gamma}(\pm\omega_1, \pm\omega_2) = \sum_k^{all} \left[G_{ik}^\beta(\pm\omega_1)U_{kj}^\gamma(\pm\omega_2) + G_{ik}^\gamma(\pm\omega_2)U_{kj}^\beta(\pm\omega_1) \right. \\ \left. - U_{ik}^\beta(\pm\omega_1)\varepsilon_{kj}^\gamma(\pm\omega_2) - U_{ik}^\gamma(\pm\omega_2)\varepsilon_{kj}^\beta(\pm\omega_1) \right]. \quad (4.16)$$

The *non-constant* part reads

$$U_{ij,non-const}^{\beta\gamma}(\pm\omega_1, \pm\omega_2) = \begin{cases} 0 & \text{diagonal} \\ \frac{G_{ij}^{\beta\gamma}(\pm\omega_1, \pm\omega_2)}{\varepsilon_j^0 - \varepsilon_i^0 \mp (\omega_1 + \omega_2 + i\Gamma)} & \text{off-diagonal} \end{cases} \quad (4.17)$$

where $G^{\beta\gamma} = C^{0\dagger}F^{\beta\gamma}(\pm\omega_1, \pm\omega_2)C^0$ is the second-order KS matrix in the MO basis⁷⁸. The second-order Lagrangian multiplier matrix needed for the cubic response equations is given by

$$\varepsilon^{\beta\gamma}(\pm\omega_1, \pm\omega_2) = G^{\beta\gamma}(\pm\omega_1, \pm\omega_2) \\ + G^\beta(\pm\omega_1)U^\gamma(\pm\omega_2) + G^\gamma(\pm\omega_2)U^\beta(\pm\omega_1) \\ - U^\beta(\pm\omega_1)\varepsilon^\gamma(\pm\omega_2) - U^\gamma(\pm\omega_2)\varepsilon^\beta(\pm\omega_1) \\ + \varepsilon^0 U^{\beta\gamma}(\pm\omega_1, \pm\omega_2) - U^{\beta\gamma}(\pm\omega_1, \pm\omega_2)\varepsilon^0 \\ \pm (\omega_1 + \omega_2 + i\Gamma)U^{\beta\gamma}(\pm\omega_1, \pm\omega_2). \quad (4.18)$$

The second-order KS matrix in the AO basis can be written as⁷⁹

$$F^{\beta\gamma}(\pm\omega_1, \pm\omega_2) = D^{\beta\gamma}(\pm\omega_1, \pm\omega_2) \times (2J) + \nu_{xc}^{\beta\gamma}(\pm\omega_1, \pm\omega_2), \quad (4.19)$$

where the elements of the second-order XC potential are⁷⁹

$$[\nu_{xc}^{\beta\gamma}(\pm\omega_1, \pm\omega_2)]_{\kappa\lambda} = \sum_{\mu\nu} [f_{xc}(\pm\omega_\sigma)]_{\kappa\lambda\mu\nu} [D^{\beta\gamma}(\pm\omega_1, \pm\omega_2)]_{\mu\nu} \\ + \sum_{\mu\nu} \sum_{\sigma\tau} [g_{xc}(\pm\omega_1, \pm\omega_2)]_{\kappa\lambda\mu\nu\sigma\tau} \times [D^\beta(\pm\omega_1)]_{\mu\nu} [D^\gamma(\pm\omega_2)]_{\sigma\tau}, \quad (4.20)$$

for which both the first- and second-order ALDA kernels are employed and the latter one reads

$$[g_{xc}(\pm\omega_1, \pm\omega_2)]_{\kappa\lambda\mu\nu\sigma\tau} \approx \int d\mathbf{r} \int d\mathbf{r}' \int d\mathbf{r}'' \chi_\kappa(\mathbf{r})\chi_\lambda(\mathbf{r}) \\ \times [g_{xc}^{\text{ALDA}}(\mathbf{r}, \mathbf{r}', \mathbf{r}'', 0, 0)] \chi_\mu(\mathbf{r}')\chi_\nu(\mathbf{r}')\chi_\sigma(\mathbf{r}'')\chi_\tau(\mathbf{r}''). \quad (4.21)$$

Once a self-consistent solution for the *non-constant* part of $U^{\beta\gamma}$ is obtained, the first hyperpolarizability can be calculated as described above by summing up both the *constant* and *non-constant* parts.

4.2.1.3 Cubic Response

The molecular second hyperpolarizability is given as⁷⁸

$$\gamma_{\alpha\beta\gamma\delta}(\mp\omega_\sigma; \pm\omega_1, \pm\omega_2, \pm\omega_3) = -\text{Tr}[H^\alpha D^{\beta\gamma\delta}(\pm\omega_1, \pm\omega_2, \pm\omega_3)], \quad (4.22)$$

where ω_σ represents the sum of the three incident frequencies as $\omega_\sigma = \omega_1 + \omega_2 + \omega_3$, and $D^{\beta\gamma\delta}$ is the third-order perturbed density matrix. To obtain the damped second-order hyperpolarizability γ , we could directly solve for the third-order density matrix by solving a set of damped third-order CPKS equations. However, this requires the solution of several cubic response equations. Therefore, it becomes computational advantageous to use the $2n + 1$ rule⁸³ to rewrite the cubic response in terms of quantities that can be obtained by only solving linear and quadratic response equations.^{78,171} Here, we adopt the latter approach for calculating the damped γ but we note that the direct solution of the third-order density matrix have also been implemented. Using the $2n + 1$ rule, the final expression for the damped γ can be written as

$$\begin{aligned} & \gamma_{\alpha\beta\gamma\delta}(\mp\omega_\sigma; \pm\omega_1, \pm\omega_2, \pm\omega_3) = \\ & \text{Tr} \left[n \sum_P \left\{ U^\alpha(\mp\omega_\sigma) G^\beta(\pm\omega_1) U^{\gamma\delta}(\pm\omega_2, \pm\omega_3) + U^\beta(\pm\omega_1) G^\alpha(\mp\omega_\sigma) U^{\gamma\delta}(\pm\omega_2, \pm\omega_3) \right. \right. \\ & \quad - U^\alpha(\mp\omega_\sigma) U^\beta(\pm\omega_1) \varepsilon^{\gamma\delta}(\pm\omega_2, \pm\omega_3) - U^\beta(\pm\omega_1) U^\alpha(\mp\omega_\sigma) \varepsilon^{\gamma\delta\dagger}(\mp\omega_2, \mp\omega_3) \\ & \quad + U^\alpha(\mp\omega_\sigma) G^{\gamma\delta}(\pm\omega_2, \pm\omega_3) U^\beta(\pm\omega_1) + U^\beta(\pm\omega_1) G^{\gamma\delta}(\pm\omega_2, \pm\omega_3) U^\alpha(\mp\omega_\sigma) \\ & \quad - U^\alpha(\mp\omega_\sigma) U^{\gamma\delta}(\pm\omega_2, \pm\omega_3) \varepsilon^\beta(\pm\omega_1) - U^\beta(\pm\omega_1) U^{\gamma\delta}(\pm\omega_2, \pm\omega_3) \varepsilon^\alpha(\mp\omega_\sigma) \\ & \quad + U^{\gamma\delta\dagger}(\mp\omega_2, \mp\omega_3) U^\alpha(\mp\omega_\sigma) \varepsilon^\beta(\pm\omega_1) + U^{\gamma\delta\dagger}(\mp\omega_2, \mp\omega_3) U^\beta(\pm\omega_1) \varepsilon^\alpha(\mp\omega_\sigma) \\ & \quad \left. - U^{\gamma\delta\dagger}(\mp\omega_2, \mp\omega_3) G^\alpha(\mp\omega_\sigma) U^\beta(\pm\omega_1) - U^{\gamma\delta\dagger}(\mp\omega_2, \mp\omega_3) G^\beta(\pm\omega_1) U^\alpha(\mp\omega_\sigma) \right\} \Big] \\ & + \text{Tr} \left[h_{xc}(\mathbf{r}, \mathbf{r}', \mathbf{r}'', \mathbf{r}''', \pm\omega_1, \pm\omega_2, \pm\omega_3) D^\alpha(\mp\omega_\sigma) D^\beta(+\omega_1) D^\gamma(\pm\omega_2) D^\delta(\pm\omega_3) \right. \\ & \quad \left. + \sum_P \left\{ g_{xc}(\mathbf{r}, \mathbf{r}', \mathbf{r}'', \pm\omega_2, \pm\omega_3) D^\alpha(\mp\omega_\sigma) D^\beta(\pm\omega_1) D^{\gamma\delta}(\pm\omega_2, \pm\omega_3) \right\} \right], \end{aligned} \quad (4.23)$$

where \sum_P represents a summation over corresponding terms obtained by permuting $(\pm\omega_1, \beta)$ and $(\pm\omega_2, \pm\omega_3, \gamma\delta)$. For example, $\sum_P \{U^\alpha(\mp\omega_\sigma) G^\beta(\pm\omega_1) U^{\gamma\delta}(\pm\omega_2, \pm\omega_3)\}$ is equivalent to $U^\alpha(\mp\omega_\sigma) \left[G^\beta(\pm\omega_1) U^{\gamma\delta}(\pm\omega_2, \pm\omega_3) + G^\gamma(\pm\omega_2) U^{\beta\delta}(\pm\omega_1, \pm\omega_3) + G^\delta(\pm\omega_3) U^{\beta\gamma}(\pm\omega_1, \pm\omega_2) \right]$, where $(\mp\omega_\sigma, \alpha)$ is not involved. It is important to note that the relationship $\varepsilon^{\alpha\beta}(+\omega_1, +\omega_2) = \varepsilon^{\alpha\beta\dagger}(-\omega_1, -\omega_2)$ given in Ref. 78 does not hold when the damping factor is included. Instead, the following is true $\varepsilon^{\alpha\beta\dagger}(-\omega_1, -\omega_2) = \varepsilon^{\alpha\beta}(+\omega_1, +\omega_2) + i\Gamma W^{\alpha\beta}(+\omega_1, +\omega_2)$, where $W^{\alpha\beta}(+\omega_1, +\omega_2) = U^\alpha(+\omega_1) U^\beta(+\omega_2) + U^\beta(+\omega_2) U^\alpha(+\omega_1)$. See the Supporting Information for the derivation. For Equation (9.5) above, most terms can be obtained directly by solving either the linear or quadratic response functions. The only one that requires additional calculation is the third-order XC kernel, $h_{xc}(\mathbf{r}, \mathbf{r}', \mathbf{r}'', \mathbf{r}''', \pm\omega_1, \pm\omega_2, \pm\omega_3)$, which can be acquired using ALDA as

$$\begin{aligned} & \text{Tr} \left[h_{xc}(\mathbf{r}, \mathbf{r}', \mathbf{r}'', \mathbf{r}''', \pm\omega_1, \pm\omega_2, \pm\omega_3) D^\alpha(\mp\omega_\sigma) D^\beta(\pm\omega_1) D^\gamma(\pm\omega_2) D^\delta(\pm\omega_3) \right] = \\ & \int d^3\mathbf{r} h_{xc}^{\text{ALDA}}(\mathbf{r}) \rho^\alpha(\mathbf{r}, \mp\omega_\sigma) \rho^\beta(\mathbf{r}, \pm\omega_1) \rho^\gamma(\mathbf{r}, \pm\omega_2) \rho^\delta(\mathbf{r}, \pm\omega_3), \end{aligned} \quad (4.24)$$

where ρ^α , ρ^β , ρ^γ and ρ^δ are the first-order perturbed densities from the damped linear response theory.⁷⁹

4.2.2 The SOS Approach

In the SOS approach, the finite lifetime of excited states is introduced in terms of the complex excitation energy. Adopting the phenomenological damping factor, the complex excitation energy can be obtained as $E_i \rightarrow E_i - i\Gamma$. We note that this Γ used here is equivalent to that adopted for the response formalism as all single-particle states are assumed to have a common energy broadening parameter in damped response theory.^{5,140} Consequently, the damped first-, second- and third-order response properties can be calculated as^{94,98,158,166,172-174}

$$\alpha_{\alpha\beta}(-\omega; \omega) = \frac{1}{\hbar} \sum_{m \neq 0} \left\{ \frac{\langle 0 | \mu^\alpha | m \rangle \langle m | \mu^\beta | 0 \rangle}{(\omega_{m0} - \omega - i\Gamma)} + \frac{\langle 0 | \mu^\beta | m \rangle \langle m | \mu^\alpha | 0 \rangle}{(\omega_{m0} - \omega + i\Gamma)} \right\}, \quad (4.25)$$

$$\begin{aligned} \beta_{\alpha\beta\gamma}(-\omega_\sigma; +\omega_1, +\omega_2) &= \frac{1}{\hbar^2} P(\beta, \gamma; +\omega_1, +\omega_2) \\ &\times \sum_{m \neq 0} \sum_{n \neq 0} \left\{ \frac{\langle 0 | \mu^\alpha | m \rangle \langle m | \bar{\mu}^\gamma | n \rangle \langle n | \mu^\beta | 0 \rangle}{(\omega_{m0} - \omega_\sigma - i\Gamma)(\omega_{n0} - \omega_1 - i\Gamma)} + \frac{\langle 0 | \mu^\gamma | m \rangle \langle m | \bar{\mu}^\beta | n \rangle \langle n | \mu^\alpha | 0 \rangle}{(\omega_{m0} + \omega_2 + i\Gamma)(\omega_{n0} + \omega_\sigma + i\Gamma)} \right. \\ &\left. + \frac{\langle 0 | \mu^\gamma | m \rangle \langle m | \bar{\mu}^\alpha | n \rangle \langle n | \mu^\beta | 0 \rangle}{(\omega_{m0} + \omega_2 + i\Gamma)(\omega_{n0} - \omega_1 - i\Gamma)} \right\}, \end{aligned} \quad (4.26)$$

and

$$\begin{aligned} \gamma_{\alpha\beta\gamma\delta}(-\omega_\sigma; +\omega_1, +\omega_2, +\omega_3) &= \frac{1}{\hbar^3} P(\beta, \gamma, \delta; +\omega_1, +\omega_2, +\omega_3) \\ &\times \left\{ \sum_{m \neq 0} \sum_{n \neq 0} \sum_{p \neq 0} \left[\frac{\langle 0 | \mu^\alpha | m \rangle \langle m | \bar{\mu}^\delta | n \rangle \langle n | \bar{\mu}^\gamma | p \rangle \langle p | \mu^\beta | 0 \rangle}{(\omega_{m0} - \omega_\sigma - i\Gamma)(\omega_{n0} - \omega_1 - \omega_2 - i\Gamma)(\omega_{p0} - \omega_1 - i\Gamma)} \right. \right. \\ &\quad + \frac{\langle 0 | \mu^\delta | m \rangle \langle m | \bar{\mu}^\alpha | n \rangle \langle n | \bar{\mu}^\gamma | p \rangle \langle p | \mu^\beta | 0 \rangle}{(\omega_{m0} + \omega_3 + i\Gamma)(\omega_{n0} - \omega_1 - \omega_2 - i\Gamma)(\omega_{p0} - \omega_1 - i\Gamma)} \\ &\quad + \frac{\langle 0 | \mu^\beta | m \rangle \langle m | \bar{\mu}^\gamma | n \rangle \langle n | \bar{\mu}^\alpha | p \rangle \langle p | \mu^\delta | 0 \rangle}{(\omega_{m0} + \omega_1 + i\Gamma)(\omega_{n0} + \omega_1 + \omega_2 + i\Gamma)(\omega_{p0} - \omega_3 - i\Gamma)} \\ &\quad \left. + \frac{\langle 0 | \mu^\beta | m \rangle \langle m | \bar{\mu}^\gamma | n \rangle \langle n | \bar{\mu}^\delta | p \rangle \langle p | \mu^\alpha | 0 \rangle}{(\omega_{m0} + \omega_1 + i\Gamma)(\omega_{n0} + \omega_1 + \omega_2 + i\Gamma)(\omega_{p0} + \omega_\sigma + i\Gamma)} \right] \\ &\quad - \sum_{m \neq 0} \sum_{n \neq 0} \left[\frac{\langle 0 | \mu^\alpha | m \rangle \langle m | \mu^\delta | 0 \rangle \langle 0 | \mu^\gamma | n \rangle \langle n | \mu^\beta | 0 \rangle}{(\omega_{m0} - \omega_\sigma - i\Gamma)(\omega_{m0} - \omega_3 - i\Gamma)(\omega_{n0} - \omega_1 - i\Gamma)} \right. \\ &\quad + \frac{\langle 0 | \mu^\alpha | m \rangle \langle m | \mu^\delta | 0 \rangle \langle 0 | \mu^\gamma | n \rangle \langle n | \mu^\beta | 0 \rangle}{(\omega_{m0} - \omega_3 - i\Gamma)(\omega_{n0} + \omega_2 + i\Gamma)(\omega_{n0} - \omega_1 - i\Gamma)} \\ &\quad + \frac{\langle 0 | \mu^\delta | m \rangle \langle m | \mu^\alpha | 0 \rangle \langle 0 | \mu^\beta | n \rangle \langle n | \mu^\gamma | 0 \rangle}{(\omega_{m0} + \omega_\sigma + i\Gamma)(\omega_{m0} + \omega_3 + i\Gamma)(\omega_{n0} + \omega_1 + i\Gamma)} \\ &\quad \left. + \frac{\langle 0 | \mu^\delta | m \rangle \langle m | \mu^\alpha | 0 \rangle \langle 0 | \mu^\beta | n \rangle \langle n | \mu^\gamma | 0 \rangle}{(\omega_{m0} + \omega_3 + i\Gamma)(\omega_{n0} - \omega_2 - i\Gamma)(\omega_{n0} + \omega_1 + i\Gamma)} \right] \left. \right\}, \end{aligned} \quad (4.27)$$

respectively. Here, $P(\beta, \gamma, \delta; +\omega_1, +\omega_2, +\omega_3)$ is a permutation operator that takes all the possible combinations among $(\beta, +\omega_1)$, $(\gamma, +\omega_2)$ and $(\delta, +\omega_3)$ into account, $\langle 0 | \mu | m \rangle$ is the transition dipole moment between the ground state and the m th excited state, $\langle m | \bar{\mu} | n \rangle = \langle m | \mu | n \rangle - \langle 0 | \mu | 0 \rangle$ is the fluctuation of the dipole moment between m th and n th excited states from its ground state value, and ω_{m0} is the transition frequency that relates to the excitation energy between the ground and m th excited states as $\hbar\omega_{m0} = E_{m0} = E_m - E_0$.

4.2.3 Two-Photon Absorption Cross Section

Assuming two degenerate photons that are linearly polarized,¹⁷⁵ the TPA cross section (σ_{TPA}) can be calculated using the imaginary part of the third-order response property as^{97,176}

$$\begin{aligned} \sigma_{\text{TPA}}(\omega) = \frac{N\pi^3\alpha_f^2\omega^2\hbar^3}{15e^4} \sum_{\alpha\beta} \text{Im} \left[\gamma_{\alpha\alpha\beta\beta}(-\omega; \omega, \omega, -\omega) \right. \\ \left. + \gamma_{\alpha\beta\beta\alpha}(-\omega; \omega, \omega, -\omega) + \gamma_{\alpha\beta\alpha\beta}(-\omega; \omega, \omega, -\omega) \right], \end{aligned} \quad (4.28)$$

where α_f is the fine structure constant, and the σ_{TPA} unit is given as Göppert-Mayer (1 GM = 10^{-50} cm⁴ s photon⁻¹).¹⁷⁷ The integer value N is related to the experimental setup and in this work $N = 4$ is used for all simulated TPA spectra.¹⁷⁶ The specific second hyperpolarizability used in Eq. (4.28) governs both TPA and IDRI processes, and in the vicinity of one-photon poles the third-order response becomes negative due to saturated absorption.^{173,174} In the SOS approach, the expression for IDRI second hyperpolarizability can be simplified if ω is far from any one-photon resonances as

$$\gamma_{\alpha\beta\gamma\delta}^{\text{TPA}}(-\omega; \omega, \omega, -\omega) = \frac{1}{\hbar^3} \sum_n \left\{ \frac{S_{0n}^{\alpha\delta}(\omega - i\Gamma, \omega - i\Gamma) S_{0n}^{\beta\gamma}(\omega + i\Gamma, \omega + i\Gamma)}{\omega_{n0} - 2\omega - i\Gamma} \right\}, \quad (4.29)$$

where we have introduced the TPA transition moments

$$S_{0n}^{\alpha\delta}(\omega \pm i\Gamma, \omega \pm i\Gamma) = \sum_m \left\{ \frac{\langle 0 | \mu^\alpha | m \rangle \langle m | \bar{\mu}^\delta | n \rangle}{\omega_{m0} - (\omega \pm i\Gamma)} + \frac{\langle 0 | \mu^\delta | m \rangle \langle m | \bar{\mu}^\alpha | n \rangle}{\omega_{m0} - (\omega \pm i\Gamma)} \right\}. \quad (4.30)$$

The full derivation is presented in the Supporting Information, but it is important to note that this simplification requires the elimination of many terms from Eq. (4.27) that become important in the vicinity of one-photon poles. Far from any one-photon resonances, the damping terms in Eq. (4.30) can be neglected and the TPA transition moments can be calculated using standard response theory.^{98,158} However, standard response functions are divergent in the case of a double resonance where there is a one-photon resonance at half the energy of the TPA transition. The damped response formalism presented by Kristensen *et al.*³ allows for the calculation of TPA intensities also in the case of double resonance effect by using a modified damped cubic response formalism. Using the same strategy, the reduced IDRI second hyperpolarizability can be obtained

using the damped response theory framework presented in this work as

$$\begin{aligned}
& \gamma_{\alpha\beta\gamma\delta}^{\text{TPA}}(-\omega; \omega, \omega, -\omega) = \\
& \text{Tr} \left[n \left\{ U^\alpha(-\omega) G^\delta(-\omega) U^{\beta\gamma}(\omega, \omega) + U^\delta(-\omega) G^\alpha(-\omega) U^{\beta\gamma}(\omega, \omega) \right. \right. \\
& \quad - U^\alpha(-\omega) U^\delta(-\omega) \varepsilon^{\beta\gamma}(\omega, \omega) - U^\delta(-\omega) U^\alpha(-\omega) \varepsilon^{\beta\gamma\dagger}(-\omega, -\omega) \\
& \quad + U^\alpha(-\omega) G^{\beta\gamma}(\omega, \omega) U^\delta(-\omega) + U^\delta(-\omega) G^{\beta\gamma}(\omega, \omega) U^\alpha(-\omega) \\
& \quad - U^\alpha(-\omega) U^{\beta\gamma}(\omega, \omega) \varepsilon^\delta(-\omega) - U^\delta(-\omega) U^{\beta\gamma}(\omega, \omega) \varepsilon^\alpha(-\omega) \\
& \quad + U^{\beta\gamma\dagger}(-\omega, -\omega) U^\alpha(-\omega) \varepsilon^\delta(-\omega) + U^{\beta\gamma\dagger}(-\omega, -\omega) U^\delta(-\omega) \varepsilon^\alpha(-\omega) \\
& \quad \left. \left. - U^{\beta\gamma\dagger}(-\omega, -\omega) G^\alpha(-\omega) U^\delta(-\omega) - U^{\beta\gamma\dagger}(-\omega, -\omega) G^\delta(-\omega) U^\alpha(-\omega) \right\} \right] \\
& + \text{Tr} \left[g_{xc}(\mathbf{r}, \mathbf{r}', \mathbf{r}'', \omega, \omega) D^\alpha(-\omega) D^\delta(-\omega) D^{\beta\gamma}(\omega, \omega) \right], \tag{4.31}
\end{aligned}$$

where only the two-photon terms are included. This reduced form is consistent with the SOS expression given in Eq. (4.29), and will be used for all simulated TPA spectra in this work unless specified.

4.3 Computational Details

We have implemented the damped cubic response theory into a locally modified version of the **ADF** program package.^{63–65} Geometry optimization was performed using the Becke-Perdew (BP86)^{87,88} XC functional with a triple- ζ polarized Slater type (TZP) basis set from the **ADF** library. Response properties of LiH were calculated using the local density approximation (LDA) through **ADF** with a single- ζ (SZ) Slater type basis set, and Dalton¹⁷⁸ with a STO-3G basis set. For LiH, we also performed full configuration interaction (FCI) calculations using Dalton with the STO-3G basis set. Response properties of DANS were calculated using **ADF** with the statistical average of orbital model exchange-correlation potentials (SAOP)^{89,90} and a triple- ζ polarized Slater type (TZP) basis set. To account for the incomplete fit basis sets in **ADF**, the keyword “*FitAODeriv*” was invoked for all response calculations. Unless specified, the finite lifetime of the electronic excited states is included phenomenologically using a damping parameter of 0.0034 a.u. ($\sim 800 \text{ cm}^{-1}$), which was previously found to be acceptable.^{5,140}

The isotropic average of the response properties was calculated for the polarizability as

$$\bar{\alpha}(-\omega; \omega) = \frac{1}{3} \left(\alpha_{xx}(-\omega; \omega) + \alpha_{yy}(-\omega; \omega) + \alpha_{zz}(-\omega; \omega) \right), \tag{4.32}$$

for the first hyperpolarizability as^{69,179}

$$\begin{aligned}
\bar{\beta}(-\omega_\sigma; +\omega_1, +\omega_2) &= \frac{1}{5} \sum_{\alpha} \left(\beta_{z\alpha\alpha}(-\omega_\sigma; +\omega_1, +\omega_2) \right. \\
& \quad \left. + \beta_{\alpha z\alpha}(-\omega_\sigma; +\omega_1, +\omega_2) + \beta_{\alpha\alpha z}(-\omega_\sigma; +\omega_1, +\omega_2) \right), \tag{4.33}
\end{aligned}$$

and for the second hyperpolarizability as^{179–181}

$$\begin{aligned} \bar{\gamma}(-\omega_\sigma; +\omega_1, +\omega_2, +\omega_3) = \frac{1}{15} \sum_{\alpha\beta} & \left(\gamma_{\alpha\alpha\beta\beta}(-\omega_\sigma; +\omega_1, +\omega_2, +\omega_3) \right. \\ & \left. + \gamma_{\alpha\beta\beta\alpha}(-\omega_\sigma; +\omega_1, +\omega_2, +\omega_3) + \gamma_{\alpha\beta\alpha\beta}(-\omega_\sigma; +\omega_1, +\omega_2, +\omega_3) \right). \end{aligned} \quad (4.34)$$

Unless otherwise stated, in the following all SOS and response calculations have been done using Dalton and ADF, respectively.

4.4 Results and Discussion

4.4.1 Comparing Response Theory and the SOS Approach for LiH

As an initial test of our implementation, we will present a detailed comparison between response theory and the SOS approach for calculating the NLO properties of LiH. The excitation energies, transition dipole moments, and dipole fluctuations operators needed in the SOS calculations were obtained using a STO-3G basis set and the LDA XC-functional. While this minimum basis set will not provide accurate results for the NLO properties, it allows for a straightforward inclusion of all excited states in the SOS approach. In the Supporting Information, we show that the α , β , and γ obtained using response theory with the SZ basis set are in good agreement with those obtained from the SOS approach using the STO-3G basis set. It is important to note that the agreement between response theory and the SOS approach for NLO properties is not exact at the level of TDDFT since the manifold of excited states is not explicitly resolved. Therefore, we also include SOS results obtained at the FCI level using the STO-3G basis set. For the FCI results, it is shown in the Supporting Information that there is near exact agreement between response theory and the SOS approach as expected for an exact theory.

In Figure 4.1 we compare the σ_{TPA} calculated using response theory at the TDDFT level, the SOS approach at the TDDFT level, and the SOS approach at the FCI level. The calculation of σ_{TPA} has been done using the full expression of γ^{IDRI} and thus also contains the one-photon processes. The σ_{TPA} for excitation energies up to 4.5 eV are shown, which covers the two lowest two-photon transitions and the lowest one-photon transition. This shows that good agreement is found for all three approaches in the two-photon region below 3.0 eV. However, in the vicinity of the one-photon resonance, we find that the result obtained using response theory differs significantly from the SOS results. The magnitude calculated using response theory is two orders of magnitude larger than the SOS results and the band shape is also very different. Consider the good agreement between the two SOS spectra with respect to both the magnitude and the band shape, this finding indicates a potential issue in TDDFT response theory that will be addressed below.

As the full expression of γ^{IDRI} includes one-photon processes that are large and negative near one-photon resonances, it is interesting to perform a similar comparison using the reduced response functions γ^{TPA} that only contains the TPA process. The comparison among the TPA

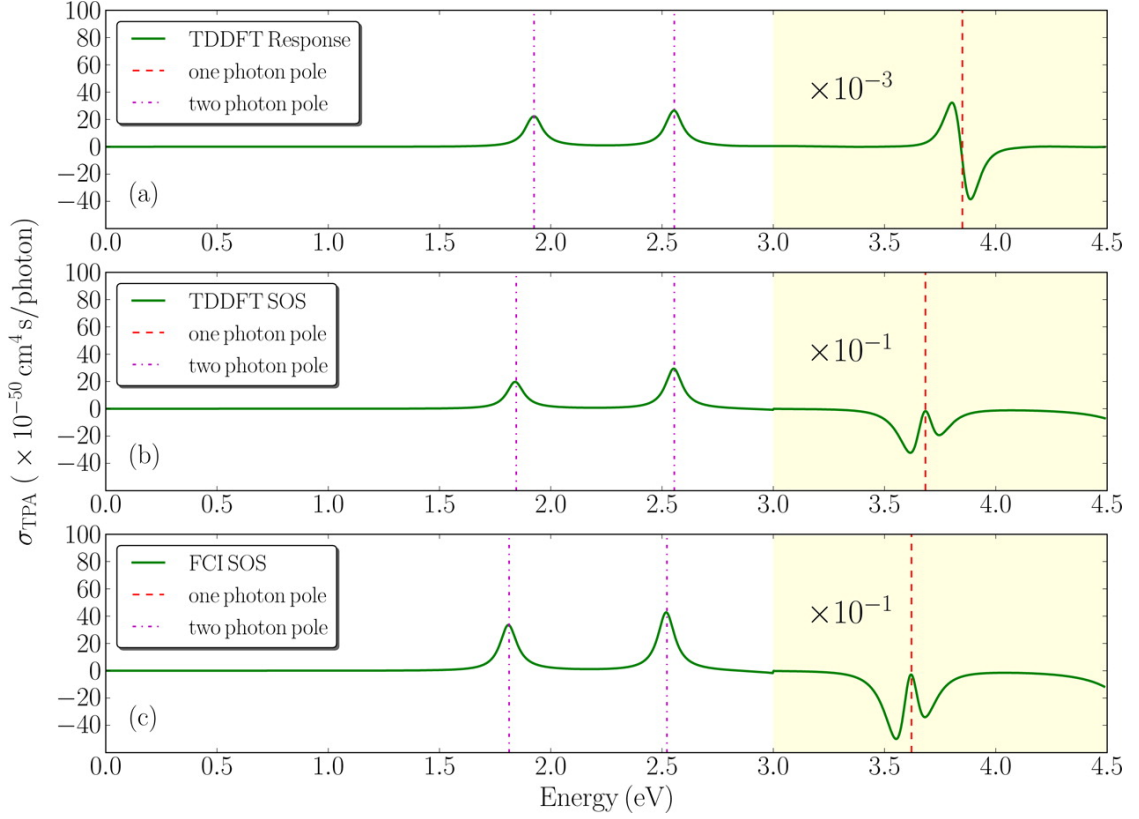


Figure 4.1. Simulated TPA spectra for LiH using the full expression of γ_{IDR1} through (a) TDDFT response theory, (b) TDDFT SOS approach, and (c) FCI SOS approach. The vertical “-” and “-.” lines indicate the one- and two-photon resonances due to the excited states, respectively. Values in the shaded region are scaled by the labeled factor.

dominant terms calculated using response theory and the SOS approach at the TDDFT level and the SOS approach at the FCI level is shown in Figure 4.2. As expected, the two-photon regions are nearly identical to those obtained using the full expression and show good agreement between response theory and the SOS approach. The one-photon region above 3.0 eV is now all positive as per construction of the reduced response function, however, the σ_{TPA} obtained using response theory is still about an order of magnitude larger than that obtained using the SOS approach.

We found similar trends when comparing response theory with the SOS approach for other NLO processes involving multiple photons, such as second harmonic generation (SHG), electric field induced SHG (EFISHG), and THG. In all cases, good agreement is found except in the vicinity of one-photon poles. In opposition to this, NLO processes involving only one photon, such as electrooptic Pockels effect (EOPE), optical rectification (OR), optical Kerr effect (OKE), and electric field induced OR (EFIOR), all show good agreement between response theory and the SOS approach at all wavelengths. Part of this is illustrated in Figure 4.3, where we compare averaged $\gamma_{\text{OKE}}(-\omega; \omega, 0, 0)$ spectra obtained by response theory and the SOS approach at the TDDFT level of theory. The comparison between response theory and the SOS approach for the other NLO processes can be found in the Supporting Information.

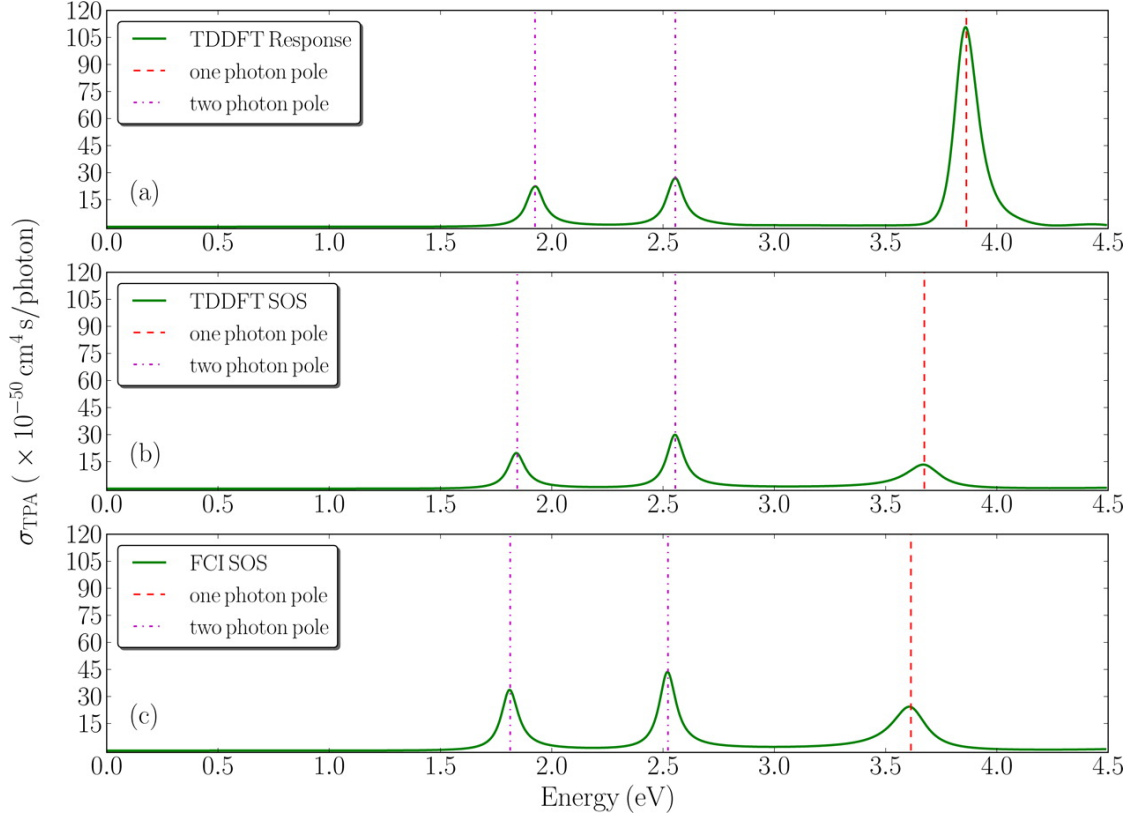


Figure 4.2. Simulated TPA spectra for LiH using the reduced expression of $\gamma_{\text{IDRI}} (\gamma^{\text{TPA}})$ through (a) TDDFT response theory, (b) TDDFT SOS approach, and (c) FCI SOS approach. The vertical “- -” and “- .” lines indicate the one- and two-photon resonances due to the excited states, respectively.

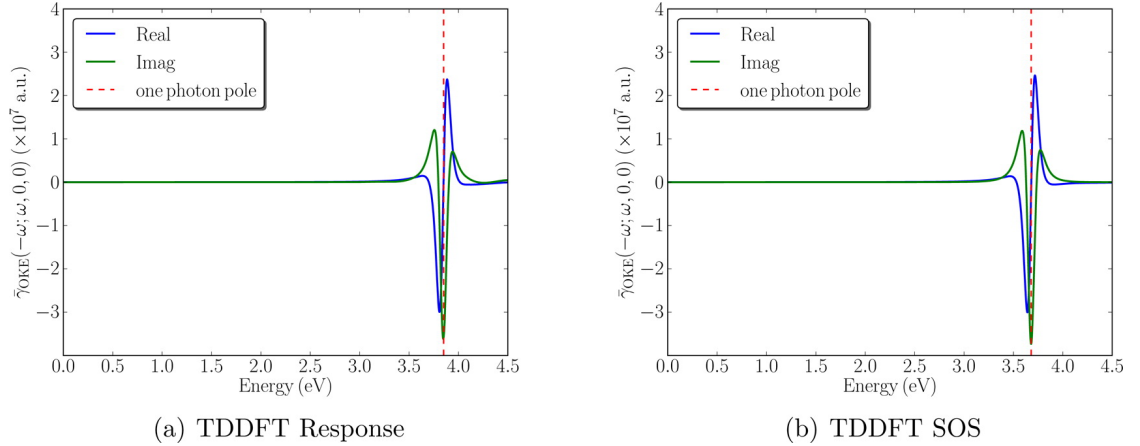


Figure 4.3. Simulated OKE spectra for LiH using (a) response theory and (b) the SOS approach at the TDDFT level of theory. The vertical “- -” line indicates the one photon resonance due to the excited state.

To further understand in detail the origin of the differences in the NLO properties obtained using response theory and the SOS approach near one-photon resonances, we will for simplicity

consider the SHG process. Near a one-photon resonance, the SHG response is dominated by the following terms in the SOS approach

$$\beta_{\text{SHG}}^{\text{SOS}} \approx \sum_{m \neq 0} \sum_{n \neq 0} \left[\frac{\langle 0 | \mu^\alpha | m \rangle \langle m | \overline{\mu^\beta} | n \rangle \langle n | \mu^\gamma | 0 \rangle}{(\omega_{m0} - 2\omega - i\Gamma)(\omega_{n0} - \omega - i\Gamma)} + \frac{\langle 0 | \mu^\alpha | m \rangle \langle m | \overline{\mu^\gamma} | n \rangle \langle n | \mu^\beta | 0 \rangle}{(\omega_{m0} - 2\omega - i\Gamma)(\omega_{n0} - \omega - i\Gamma)} \right. \\ \left. + \frac{\langle 0 | \mu^\beta | m \rangle \langle m | \overline{\mu^\alpha} | n \rangle \langle n | \mu^\gamma | 0 \rangle}{(\omega_{m0} + \omega + i\Gamma)(\omega_{n0} - \omega - i\Gamma)} + \frac{\langle 0 | \mu^\gamma | m \rangle \langle m | \overline{\mu^\alpha} | n \rangle \langle n | \mu^\beta | 0 \rangle}{(\omega_{m0} + \omega + i\Gamma)(\omega_{n0} - \omega - i\Gamma)} \right]. \quad (4.35)$$

If there is no double resonance effect (i.e., $2\omega \rightarrow \omega_{m0}$ and $\omega \rightarrow \omega_{n0}$), as is the case for LiH, then we would expect the SHG to be dominated by a single resonance term determined by $(\omega_{n0} - \omega - i\Gamma)^{-1}$ when $\omega \rightarrow \omega_{n0}$. For comparison, we also derived the spectral representation of the SHG response function as obtained from damped response theory. The full details are given in the Supporting Information. The one-photon dominant term is found to be

$$\beta_{\text{SHG}}^{\text{Response}} \approx n \sum_p \sum_{ij}^{\text{occ}} \sum_b^{\text{virt}} \sum_{kl}^{\text{all}} \sum_{mnp \neq 0}^{\text{exc. no.}} \left[\frac{Y_{m,ik}^* \mu_{0m,ik}^\alpha \cdot K_{kl,jb}^{\text{HXC}} \cdot X_{n,jb} \mu_{n0,jb}^\beta \cdot X_{p,li} \mu_{p0,li}^\gamma}{(\omega_m - 2\omega - i\Gamma)(\omega_n - \omega - i\Gamma)(\omega_p - \omega - i\Gamma)} \right. \\ - \frac{Y_{m,ik}^* \mu_{0m,ik}^\alpha \cdot X_{p,kl} \mu_{p0,kl}^\gamma \cdot K_{li,jb}^{\text{HXC}} \cdot X_{n,jb} \mu_{n0,jb}^\beta}{(\omega_m - 2\omega - i\Gamma)(\omega_p - \omega - i\Gamma)(\omega_n - \omega - i\Gamma)} \\ + \frac{Y_{m,ik}^* \mu_{0m,ik}^\alpha \cdot K_{kl,bj}^{\text{HXC}} \cdot Y_{n,jb} \mu_{n0,jb}^\beta \cdot X_{p,li} \mu_{p0,li}^\gamma}{(\omega_m - 2\omega - i\Gamma)(\omega_n - \omega - i\Gamma)(\omega_p - \omega - i\Gamma)} \\ \left. - \frac{Y_{m,ik}^* \mu_{0m,ik}^\alpha \cdot X_{p,kl} \mu_{p0,kl}^\gamma \cdot K_{li,bj}^{\text{HXC}} \cdot Y_{n,jb} \mu_{n0,jb}^\beta}{(\omega_m - 2\omega - i\Gamma)(\omega_p - \omega - i\Gamma)(\omega_n - \omega - i\Gamma)} \right], \quad (4.36)$$

where X_n and Y_n are the spectral representation of the response vectors obtained from the linear response equations. It is important to note that the coupling matrix K^{HXC} , as introduced in section 4.2.1.1, includes the adiabatic XC kernel and thus is frequency independent. The spectral representation reveals that response theory shows a different pole structure than that found in the SOS approach, where the one-photon dominant term contains only one pole for the latter one. This is further illustrated in Figure 4.4, where we compare the SHG response obtained using damped response theory and the SOS approach. Similar to the cubic response properties discussed above, we find good agreement between the two approaches in the two-photon region below 3.0 eV.

In the one-photon region, we find that the band structure differs significantly between the two approaches. For the SOS approach, the band shape is Lorentzian as expected based on the one-photon pole structure given in Eq. (4.35). The band structure obtained using damped response theory is more complicated due to the additional pole found in the spectral presentation of the response function. Thus, the differences between damped response theory and the SOS approach can be traced back to the different pole structures of the response functions. This incorrect pole structure obtained in response theory has previously been recognized by Dalgaard¹⁸² in the context of time-dependent Hartree Fock (TDHF) response theory. Within TDDFT, the spurious pole arises from the adiabatic approximation that renders the K^{HXC} frequency independent. Such deficiencies of the TDDFT response function have also recently been pointed out when

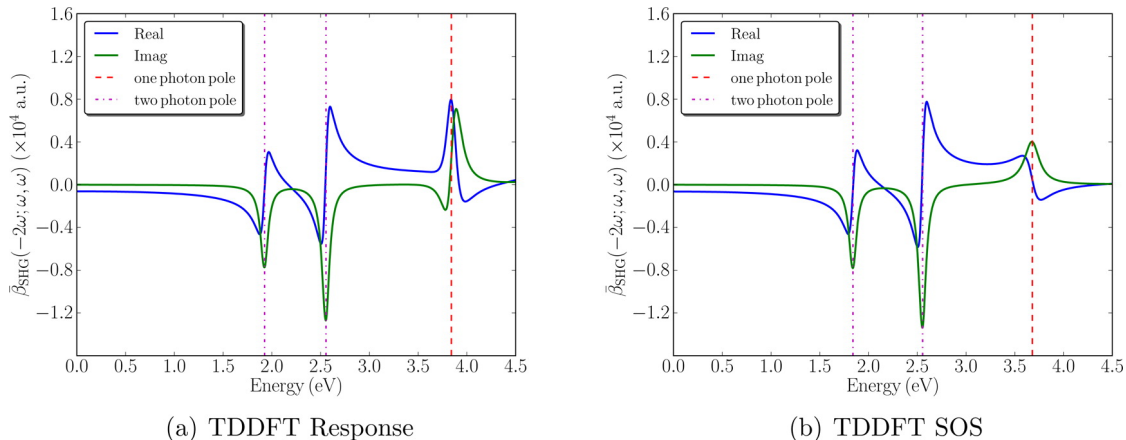


Figure 4.4. Simulated SHG spectra for LiH using (a) response theory and (b) the SOS approach at the TDDFT level of theory. The vertical “- -” and “- .” lines indicate the one- and two-photon resonances due to the excited states, respectively.

calculating the derivative couplings between excited states.^{183–185}

4.4.2 TPA and THG of DANS

To further test our implementation of damped cubic response theory, we consider TPA and THG of DANS. The TPA of DANS has been measured experimentally using the femtosecond Z-scan technique,¹⁶⁷ and THG has been determined experimentally for the DANS chromophore embedded in a polymer matrix¹⁶⁶. Therefore, DANS serves as a good benchmark system here. To better approximate the observed band width found in the experimental spectra,¹⁶⁷ we used a larger damping factor of $\Gamma = 0.0068$ a.u. for the simulations.

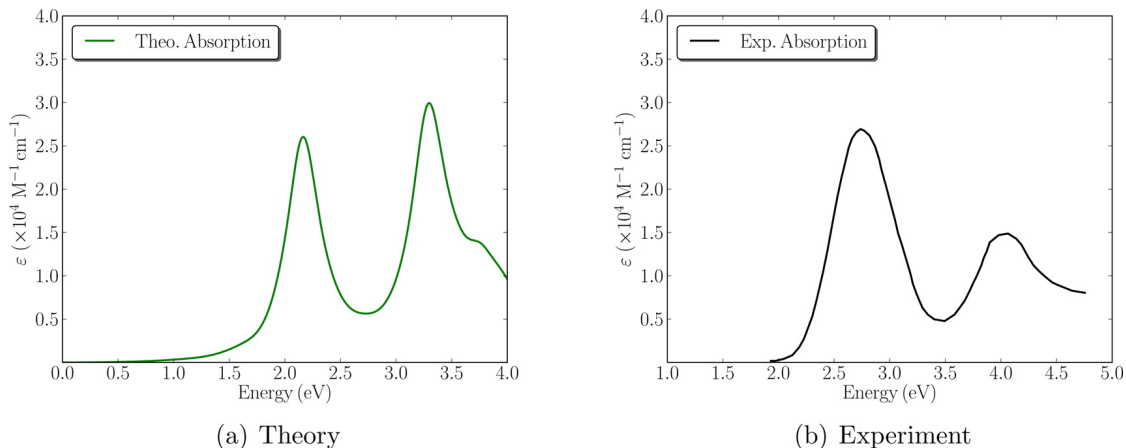


Figure 4.5. (a) Simulated absorption spectrum for DANS in the gas phase. (b) Experimental absorption spectrum for DANS in DMSO taken from Ref. 167.

In Figure 4.5 we compare the simulated and experimental absorption spectra for DANS. The simulated spectrum is characterized by two main bands, which are found at 2.15 eV and 3.29

eV with the lowest band being relatively weaker. In contrast to this, the experimental spectrum shows opposite relative intensities for the two bands located at 2.75 eV and 4.10 eV, respectively. Such a discrepancy is likely caused by the SAOP XC potential used in the simulation. In addition to this, a weak shoulder found around 3.70 eV in the simulated spectrum is also not seen in the experimental spectrum. The underestimation of the excitation energies in the simulation is expected as the lowest excitation of DANS was found to be of charge-transfer character.¹⁶⁷ Even though the solvent effects that would likely have caused a red shift¹⁸⁶ were not included in the simulation, the lowest band is still found red shifted by about 0.6 eV related to the lowest band in the experimental spectrum.

In Figure 4.6(a) we plot the simulated TPA spectrum of DANS in the gas phase and compare with the experimental spectrum in Figure 4.6(b) obtained by Antonov *et al.*¹⁶⁷ in DMSO.

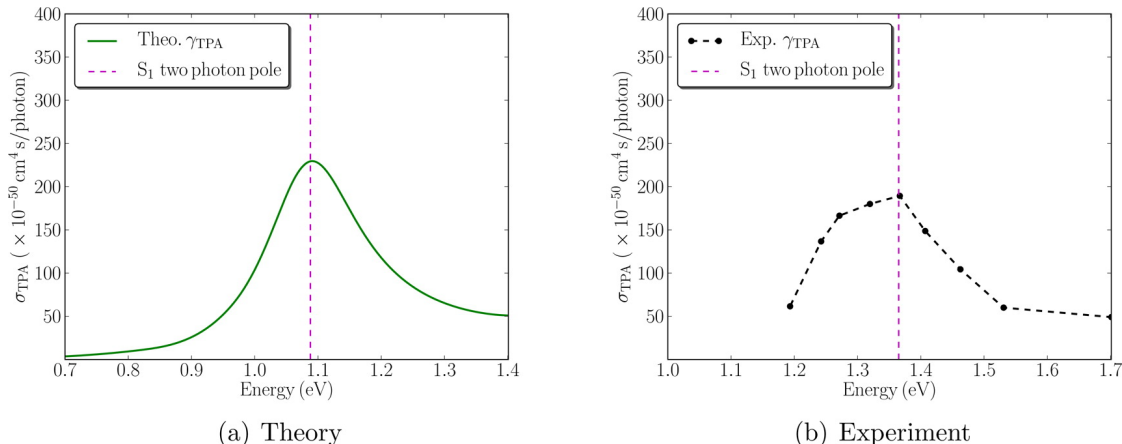


Figure 4.6. (a) Simulated TPA spectrum for DANS in the gas phase. (b) Experimental TPA spectrum for DANS in DMSO taken from Ref. 167. The vertical “- -” line in (a) and (b) indicates the two-photon resonance due to the calculated and measured S_1 , respectively.

The simulated spectrum shows a dominant TPA band at 1.09 eV compared to the experimental TPA band at 1.37 eV. The maximum cross section of the simulated band is found around 229 GM, which is in good agreement with its experimental counterpart measured as 190 ± 10 GM.¹⁶⁷ However, this is potentially fortuitous due to the XC potential used in the simulation as well as the neglect of solvent effects. Furthermore, it is important to note that the intensities depend strongly on the damping parameter used in the simulations; thus, it is important to choose appropriate values. Here we choose to fix the Γ value based on the experimental absorption spectrum.

The THG measurement of DANS (as a side-chain polymer containing the chromophore) was carried out in a vacuum cell by means of the Maker fringes technique, and the reported THG spectrum was normalized with respect to the maximum $\gamma(3\omega)$ tensor.¹⁶⁶ Thus for consistency, in Figure 4.7(a) we normalize the simulated THG spectrum of gas-phase DANS and compare with the experimental spectrum obtained by Beljonne *et al.*¹⁶⁶ as shown in Figure 4.7(b).

Both simulated and experimental spectra are dominated by two main bands, locating at 0.72 eV and 1.10 eV for the former one while 0.94 eV and 1.29 eV for the latter one. The differences in band position are again attributed to the XC potential in conjunction with the

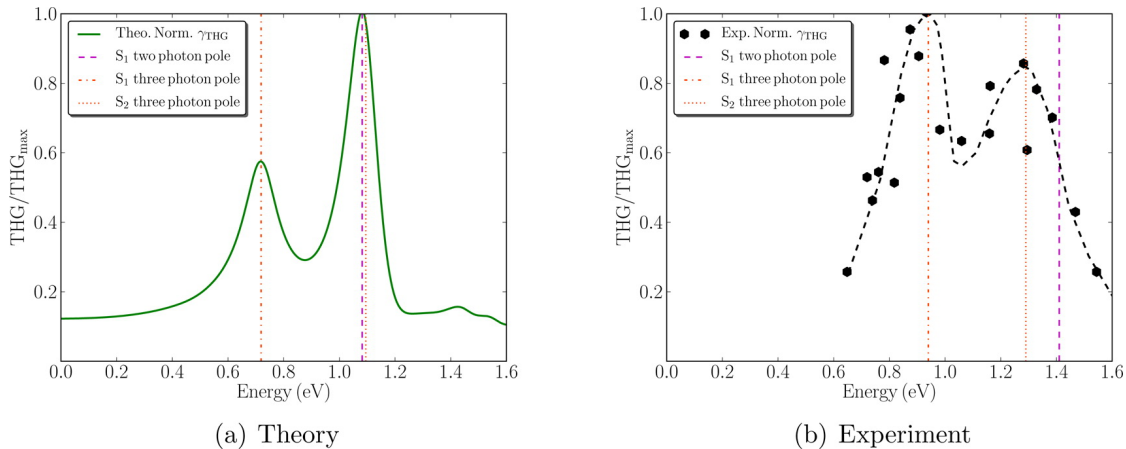


Figure 4.7. (a) Simulated THG spectrum for DANS in the gas phase. (b) Experimental THG spectrum for DANS taken from Ref. 167. The vertical “- -”, “- .”, and “. .” lines in (a)/(b) indicate the two-photon resonance due to the calculated/measured S_1 , three-photon resonance due to the calculated/measured S_1 , and three-photon resonance due to the calculated/measured S_2 , respectively. The dashed curve in (b) is manually fitted for experimental data and shown for eye guide. Note that the experimental two- and three-photon resonance energies are all obtained according to Ref. 165.

missing environmental effects in the simulation. In the simulated spectrum, the second band is found to be the most intense whereas in the experimental spectrum the lowest band is found to be the strongest. Part of this difference can be attributed to the stronger oscillator strength found in the simulation for the second absorption band. However, we find it is more interesting that there is a potential stronger double resonance effect in the simulated spectrum as indicated in Figure 4.7(a). This double resonance effect is caused by a three-photon resonance with S_2 and a two-photon resonance with S_1 . In the experimental spectrum, the overlap between these two resonances is weak due to the energy separation between the two lowest excited states and thus will cause a less pronounced double resonance effect. Therefore, for accurately describing these higher-order response properties, it becomes important to not only capture the absolute band positions but also their relative positions.

4.5 Conclusion

In this work, we have presented a general implementation of the damped cubic response properties within a TDDFT framework. To calculate the TPA cross sections, we also have presented a reduced damped cubic response approach. By providing a detailed comparison between response theory and SOS approach for calculating the NLO properties of LiH, we illustrate the inconsistent behaviors for multi-photon NLO processes near one-photon resonances and demonstrate the incorrect pole structure obtained in response theory. The root cause of this is the adiabatic approximation that renders the XC kernel frequency independent. The TPA and THG spectra of DANS were simulated and compared with experimental spectra, where reasonable agreement was found in general. More importantly, this work shows that care must be taken when calculating higher-order

response functions in the vicinity of one-photon poles when the adiabatic approximation is used.

Chapter 5 | Importance of Double-Resonance Effects in Two-Photon Absorption Properties of $\text{Au}_{25}(\text{SR})_{18}^-$

Hu, Z.; Jensen, L. “Importance of Double-Resonance Effects in Two-Photon Absorption Properties of $\text{Au}_{25}(\text{SR})_{18}^-$ ” *Chem. Sci.* **2017**, *8*, 4595.

Abstract

The two-photon absorption (TPA) cross sections of small thiolate-protected gold clusters have been shown to be much larger than typical small organic molecules. In comparison with larger nanoparticles, their TPA cross sections per gold atom are also found to be larger. Theoretical simulations have suggested that the large enhancement of these TPA cross sections comes from a one-photon double resonance mechanism. However, it remains difficult to simulate TPA cross sections of thiolate-protected gold clusters due to their large system size and a high density of states. In this work, we report a time-dependent density functional theory (TDDFT) study of the TPA spectra of $\text{Au}_{25}(\text{SR})_{18}^-$ cluster based on a damped response theory formalism. Damped response theory enables a consistent treatment of on- and off-resonance molecular properties even for molecules with a high density of states, and thus is well-suited for studying TPA properties for gold clusters. Our results indicate that the one- and two-photon double resonance effect is much smaller than previously found, and thus unlikely the main cause of the large TPA cross sections found experimentally. The effect of symmetry-breaking of the $\text{Au}_{25}(\text{SR})_{18}^-$ cluster due to the ligands on the TPA cross sections has been studied and found to only slightly increase the cross section. Furthermore, by comparing with larger nanoparticles we find that the TPA cross section per gold atom scales linearly with the diameter of the particles, and that the Kerr nonlinear response of the $\text{Au}_{25}(\text{SR})_{18}^-$ cluster is on the same order as that of bulk gold films.

5.1 Introduction

Thiolate-protected gold nanoparticles have attracted a significant interest in recent years due to their exceptional stability and applications in biomedicine, catalysis, electronics, photonics and sensing.^{187–192} While larger gold nanoparticles (> 5 nm) are characterized by the localized surface plasmon resonance, small gold clusters (< 3 nm) exhibit molecular-like properties due to the quantum confinement effects.¹⁸⁹ Although the exact boundary between molecular and plasmonic response has not been established, experiments have shown that a small nanoparticle containing only ~ 330 gold atoms exhibits a plasmonic response.¹⁹³ Simulations using time-dependent density functional theory (TDDFT) indicate that the boundary between molecular and plasmonic behaviors occurs for the $\text{Au}_{144}(\text{SR})_{60}$ monolayer-protected cluster with a 1.5 nm core.¹⁹⁴

Numerous gold clusters ($\text{Au}_n(\text{SR})_m$) have been explored both experimentally and theoretically since the total structural determination of the nanoclusters $\text{Au}_{102}(\text{SR})_{44}$ and $\text{Au}_{25}(\text{SR})_{18}^-$ using X-ray crystallography.^{195–198} $\text{Au}_{25}(\text{SR})_{18}^-$ is probably the most extensively studied cluster due to its extraordinary atomic packing structure and the well established structure-property relationship.^{196–198} The stability of the $\text{Au}_{25}(\text{SR})_{18}^-$ cluster can be understood by considering it to consist of a Au_{13}^{5+} core surrounded by 6 anionic $\text{RS}-(\text{Au}-\text{SR})_2^-$ units. According to the “super-atom” model,¹⁹⁹ which is commonly used to understand the stability of gold clusters, this leads to a shell-closing of 8 electrons in the core that strengthens its stability. The existence of a crystal structure of the $\text{Au}_{25}(\text{SR})_{18}^-$ cluster has enabled a detailed correlation between its structure and optical properties through TDDFT simulations.^{198,200,201}

There is a large literature on the linear optical properties of small gold clusters. This is mainly because such properties are sensitive to the specific atomic arrangement, and thus can aid in the structural determination. Furthermore, understanding the linear properties of these small clusters provides insights into the emergence of the plasmonic response found in larger nanoparticles. The nonlinear optical (NLO) properties of small gold clusters have also attracted attention due to their potential use in multiphoton imaging and optical limiting applications. Although much less work has been devoted for the NLO properties of thiolate-protected gold clusters in contrast to their linear counterparts, experimental two-photon absorption (TPA), nonlinear transmission, hyper-Rayleigh scattering, and second- and third-harmonic generation measurements have been performed for the prototypical thiolate-protected Au_{25} cluster.^{2,202–206} However, few theoretical studies of the NLO properties of these small ligand-protected gold clusters are available in the literature due to a high computational burden.^{207–209}

The most intriguing NLO property of the $\text{Au}_{25}(\text{SR})_{18}^-$ cluster is probably its large TPA cross section in the communication wavelength region, which has been reported by Ramakrishna *et al.*² as 2700 GM for excitation at 1290 nm. This value is much larger than that of many organic chromophores, and promotes the $\text{Au}_{25}(\text{SR})_{18}^-$ cluster as a potentially well-qualified candidate for various NLO applications including biological imaging, nanolithography, and optical limiting.²⁰² More interestingly, a very large TPA cross section of 427000 GM was also found for this cluster for excitation at 800 nm.² Furthermore, the TPA cross sections per gold atom for it and a few

other small gold clusters were shown to exhibit a different size-scaling as compared to larger nanoparticles.² To understand this unusual behavior, Day *et al.*²⁰⁹ used TDDFT simulations based on the single residue of quadratic response functions to obtain the TPA cross section of the $\text{Au}_{25}(\text{SR})_{18}^-$ cluster. These calculations suggested that a one-photon double resonance effect could lead to the large TPA cross sections observed experimentally. Recent work has also found that the optical Kerr response in 3 nm gold films is many orders of magnitude larger than that of the bulk metal.²¹⁰ These results suggest that quantum size effects could lead to significant third-order nonlinear response for small gold clusters. However, simulations of resonance nonlinear properties of metal clusters pose a significant challenge due to the high number of states contributing to the spectra, which raises the possibility of resonance effects that need to be dealt with carefully to avoid unphysically large response properties. This is particularly a problem when using standard response theory to calculate the molecular properties since the response functions diverge when optical frequencies, or the sum of them, equal an excitation energy.

In this work, we report simulated TPA spectra for the $\text{Au}_{25}(\text{SR})_{18}^-$ cluster using TDDFT. To avoid unphysical resonance effects, we will use a recently implemented damped cubic response formalism²¹¹ to calculate the TPA cross sections. Damped response theory^{4-6,140,211} takes the broadening of electronic states into account and thus avoids the unphysical behaviors for molecular properties on resonance. In addition to TPA cross sections, we will also characterize the resonance optical Kerr effect for the $\text{Au}_{25}(\text{SR})_{18}^-$ cluster. Both of these optical processes can be described by a third-order nonlinear response tensor obtained using damped response theory. Our results show that the one-photon double resonance effect is smaller than previously found. We also find that the quantum size effects for the $\text{Au}_{25}(\text{SR})_{18}^-$ cluster do not lead to significantly enhanced third-order nonlinear response.

5.2 Theory

Considering the simultaneous absorbance process for two linearly polarized photons with identical energies,¹⁷⁵ one can utilize the imaginary part of orientationally averaged third-order response properties to express the TPA cross section (σ^{TPA}) as⁹⁷

$$\begin{aligned} \sigma^{\text{TPA}}(\omega) = \frac{N\pi^3\alpha_f^2\omega^2\hbar^3}{15e^4} \sum_{\alpha\beta} \text{Im} \left[\gamma_{\alpha\alpha\beta\beta}(-\omega; \omega, \omega, -\omega) \right. \\ \left. + \gamma_{\alpha\beta\beta\alpha}(-\omega; \omega, \omega, -\omega) + \gamma_{\alpha\beta\alpha\beta}(-\omega; \omega, \omega, -\omega) \right], \end{aligned} \quad (5.1)$$

where α_f is the fine structure constant, ω is the incident frequency, and N is an integer value related to the experimental setup.¹⁷⁶ In this work, $N = 4$ is used for all simulated TPA spectra and the unit of σ^{TPA} is given as Göppert-Mayer ($1 \text{ GM} = 10^{-50} \text{ cm}^4 \text{ s photon}^{-1}$).¹⁷⁷ The term $\gamma(-\omega; \omega, \omega, -\omega)$ is denoted as γ^{IDRI} in this work as its real part corresponds to the intensity dependent refractive index (IDRI). The imaginary part of γ^{IDRI} includes both saturated linear absorption and two-photon absorption, and in the traditional sum-over-states (SOS) approach the two processes can be related to the negative and two-photon terms (“N-terms” and “T-terms”),

respectively.²¹² The “N-terms” provides large negative contributions to γ tensors^{173,174} and corresponds to purely one-photon processes, hence should not be considered when describing TPA. By eliminating the “N-terms”, one can obtain a reduced form for IDRI, of which the imaginary part corresponds to the pure TPA process. This reduced IDRI, termed γ^{TPA} in this work, can be given using the SOS expression as

$$\gamma_{\alpha\beta\gamma\delta}^{\text{TPA}}(-\omega; \omega, \omega, -\omega) = \frac{1}{\hbar^3} \sum_n \left\{ \frac{S_{0n}^{\alpha\delta}(\omega - i\Gamma, \omega - i\Gamma) S_{0n}^{\beta\gamma}(\omega + i\Gamma, \omega + i\Gamma)}{\omega_{n0} - 2\omega - i\Gamma} \right\}, \quad (5.2)$$

where ω_{n0} is the excitation energy of state n , Γ is the energy broadening parameter, and $S^{\alpha\beta}$ is the TPA transition moment that involves the transition dipole moments between ground and excited states ($\langle 0 | \mu^\alpha | m \rangle$) as well as two excited states ($\langle m | \bar{\mu}^\delta | n \rangle$), i.e.,

$$S_{0n}^{\alpha\delta}(\omega \pm i\Gamma, \omega \pm i\Gamma) = \sum_m \left\{ \frac{\langle 0 | \mu^\alpha | m \rangle \langle m | \bar{\mu}^\delta | n \rangle}{\omega_{m0} - (\omega \pm i\Gamma)} + \frac{\langle 0 | \mu^\delta | m \rangle \langle m | \bar{\mu}^\alpha | n \rangle}{\omega_{m0} - (\omega \pm i\Gamma)} \right\}. \quad (5.3)$$

The corresponding expression for γ^{TPA} in a damped response formalism has been previously reported by Kristensen *et al.*⁹⁹ and Hu *et al.*²¹¹ The use of γ^{TPA} avoids any negative TPA intensities caused by the pure one-photon processes and allows for appropriate σ^{TPA} calculations in the presence of one- and two-photon double resonance effects. Therefore, we adopt it for all TPA simulations in this work.

5.3 Computational Details

All calculations in this work were carried out through a locally modified version of the Amsterdam Density Functional (ADF) 2014 program package.^{63,64,141} The starting geometry for the $\text{Au}_{25}(\text{SH})_{18}^-$ cluster is based on the crystal structure,^{196,198} and the initial atomic coordinates for the $\text{Au}_{25}(\text{SH})_{16}(\text{SPh})_2^-$ cluster were obtained from Ref. 207. Geometry optimization was performed using the Becke-Perdew (BP86)^{87,88} XC functional with a small frozen-core triple- ζ polarized Slater type (TZP) basis set from the ADF library. The BP86 XC functional with a large frozen-core TZP basis set was adopted to calculate the first- and third-order response properties. Scalar relativistic effects have been accounted for by means of the zeroth-order regular approximation (ZORA).^{92,93} Solvent effects are not included in the simulations, but good agreement between theory and experiment has been previously¹⁹⁸ demonstrated for the absorption spectrum of the $\text{Au}_{25}(\text{SH})_{18}^-$ cluster. The finite lifetime of the electronic excited states is included phenomenologically using a damping parameter of 0.0034 a.u. (~ 0.1 eV), which was previously found acceptable^{5,140} and also roughly the same as the Lorentzian fitting width used in Ref. 198. The conversion factor to SI and cgs units for γ^{TPA} : 1 a.u. = 7.0423×10^{-54} m⁵ V⁻² = 5.0367×10^{-40} esu.

5.4 Results and Discussion

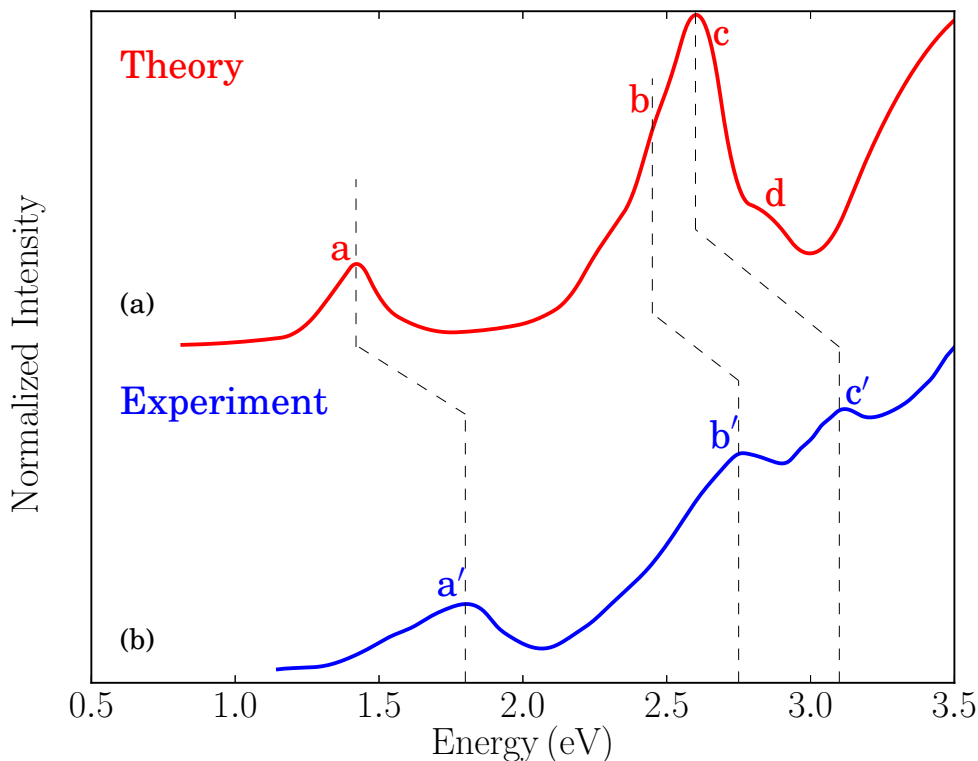


Figure 5.1. (a) Simulated absorption spectrum for the $\text{Au}_{25}(\text{SR})_{18}^-$ ($\text{R} = \text{H}$) cluster in the gas phase. (b) Experimental absorption spectrum for the $\text{Au}_{25}(\text{SR})_{18}^-$ ($\text{R} = \text{CH}_2\text{CH}_2\text{Ph}$) cluster in toluene taken from Ref. 198.

The one-photon absorption spectrum of the $\text{Au}_{25}(\text{SR})_{18}^-$ cluster is characterized by three main bands found at 1.8, 2.8, and 3.1 eV, respectively.¹⁹⁸ The lowest band is a HOMO to LUMO transition which can be characterized as an intraband transition ($\text{sp} \leftarrow \text{sp}$), the second band arises from a mixed intraband ($\text{sp} \leftarrow \text{sp}$) and interband ($\text{sp} \leftarrow \text{d}$) transitions, while the third band arises predominantly from interband transitions ($\text{sp} \leftarrow \text{d}$).^{198,200,201,213} While initially the lowest transition at 1.8 eV was described in terms of the electronic and geometric structure of the Au_{13} core, recent work has shown that the optical absorption spectra are not separable into core and ligand contributions.²⁰⁰ A comparison between the simulated and experimental absorption spectra for the $\text{Au}_{25}(\text{SR})_{18}^-$ cluster is shown in Figure 5.1. The simulated spectrum is obtained in the gas phase by using $-\text{SH}$ group as the ligand while the experimental one is measured in toluene for the gold cluster passivated by the $\text{SCH}_2\text{CH}_2\text{Ph}$ ligands.¹⁹⁸

The theoretical spectrum consists of a major band at 1.43 eV and a broader band ranging from $2.2 \rightarrow 3.1$ eV. The former one (labeled as “a”) corresponds to the lowest band in the experimental spectrum at 1.8 eV (labeled as “a’”) and is primarily characterized by a HOMO to LUMO

transition. The latter one has contributions from three groups of transitions at 2.4, 2.6, and 2.8 eV, labeled as “b”, “c” and “d”, respectively. The “b” band corresponds to the mixed intraband and interband experimental transitions at 2.8 eV (labeled as “b’”), and the “c” band corresponds to the experimental transitions at 3.1 eV (labeled as “c’”). Although the “d” band is not resolved in the experimental spectrum due to thermal broadening and its weak oscillator strength, low temperature measurements of the absorption spectrum have shown several additional bands above 3 eV.²¹⁴ The red-shift of the simulated spectrum is likely a result of the neglect of solvent effects, the choice of xc functionals, and the simplified ligand used in the simulations.²¹⁵ The band assignment presented here follows that of Ref. 198, where a larger splitting of the “b” and “c” bands was obtained by using the SAOP XC potential. We refer to Ref. 201 for a comprehensive discussion of the optical absorption of the thiolate-protected Au₂₅ cluster.

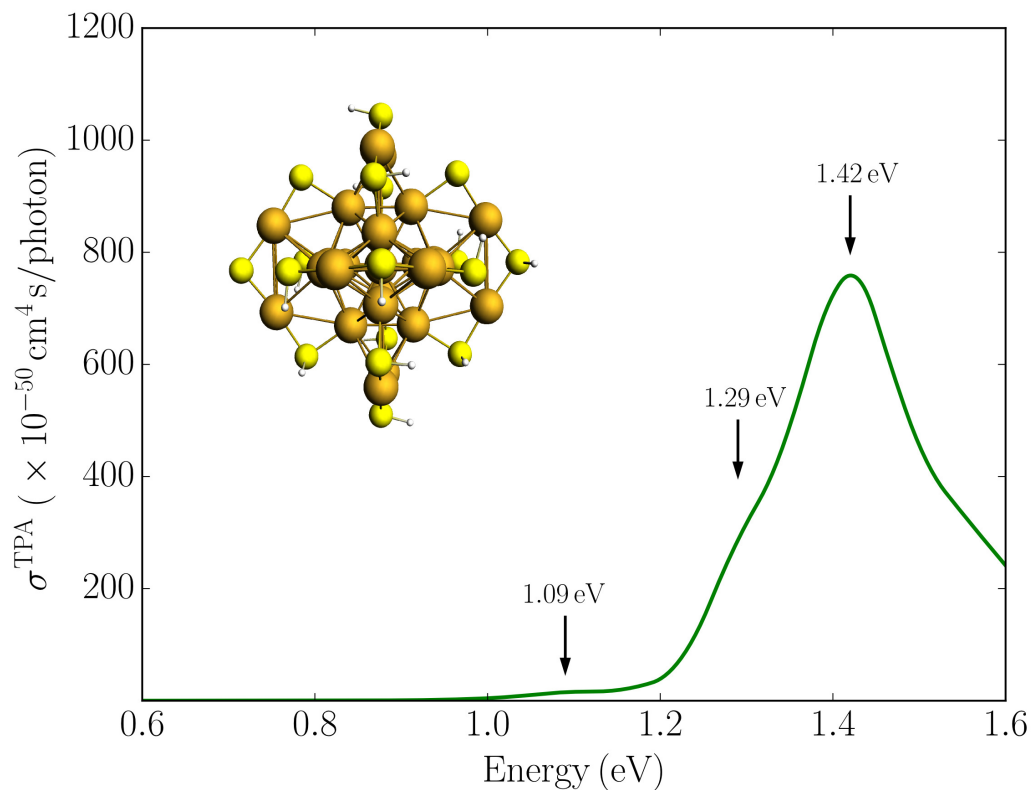


Figure 5.2. Simulated TPA spectrum for the Au₂₅(SH)₁₈⁻ clusters in the gas phase.

In Figure 5.2 we plot the simulated TPA spectrum for the Au₂₅(SH)₁₈⁻ cluster as a function of the one-photon energy. The spectrum is dominated by a broad band at 1.4 eV with a shoulder at 1.3 eV and a weaker band at 1.1 eV. The weak low-energy band corresponds to two-photon excitations into a set of weaker states found as a shoulder to the “b” band in the one-photon absorption spectrum. The stronger shoulder at 1.3 eV in the two-photon spectrum corresponds to excitation into the strong “c” band in the one-photon absorption spectrum. Finally, the largest

two-photon absorption cross section is found around 753 GM for excitation into the “d” band at 1.4 eV. This σ^{TPA} value is comparable to that of large organic TPA chromophores,²¹⁶ mainly due to a double-resonance effect where the two-photon transition into the “d” band is enhanced by a one-photon resonance with the “a” band. We demonstrate this double-resonance effect by plotting a schematic energy diagram with the most important transitions in Figure 5.3. From Eq. 5.3, we see that the two-photon transition moments S_{0n} become large for photon energies near the one-photon transitions.

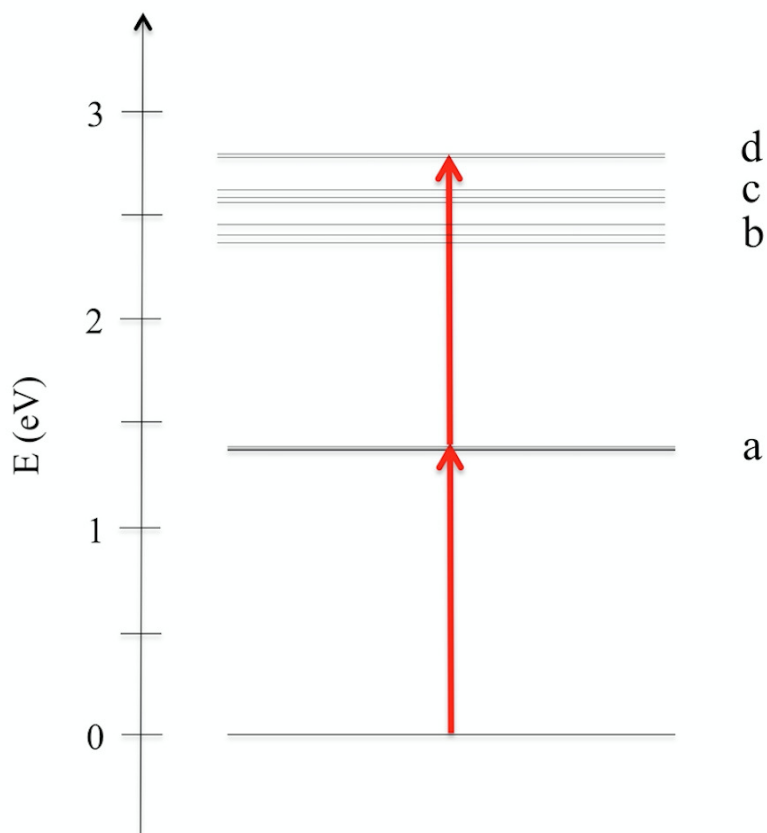


Figure 5.3. Schematic energy diagram showing the most important transitions for the $\text{Au}_{25}(\text{SH})_{18}^-$ cluster in the gas phase.

Experimentally, a huge TPA cross section of 427000 GM was found for a photon energy of 1.55 eV.² Since this corresponds to excitation into the “a”-band in the one-photon absorption spectrum, the huge TPA cross section is likely resulting from enhancement by one-photon processes, either a double-resonance effect or other effects such as excited state absorption. Previous simulations have found very large TPA cross sections for small monolayer protected gold and silver clusters due to double-resonance effects.^{209,217,218} A TPA cross section of 620000 GM at a photon energy

of 1.58 eV was reported for the $\text{Au}_{25}(\text{SH})_{18}^-$ cluster using B3LYP and a SDD-DZ basis set, with similar values found for other functionals tested.²⁰⁹ The large TPA cross section is in good agreement with the experimental observation and was attributed to resonance enhancement from the lowest excited state. However, in contrast to these huge TPA cross sections found in the previous simulations, our results are several orders of magnitude smaller with the largest value found around 753 GM. Previous simulations used traditional quadratic response theory within a TDDFT formalism to simulate the TPA cross section, which can produce unphysically large TPA cross sections due to double-resonance effects.^{99,211,219} A major advantage of using damped response theory is that the two-photon transition moments remain finite even if in the vicinity of one-photon resonances, and thus can correctly describe this double-resonance effect.²⁰⁹

Experimentally, it was also found that the TPA cross sections per gold atom for the small gold clusters were significantly larger than those for larger nanoparticles, following a different size dependence.² This was attributed to quantum size effects and indicated a transition from small clusters characterized in terms of discrete transitions to larger nanoparticles characterized in terms of plasmon resonances. For the $\text{Au}_{25}(\text{SH})_{18}^-$ cluster, a TPA cross section per gold atom of 17080 GM was reported² while we find a much smaller value of 30 GM per gold atom. However, our results compare well with the expected value based on the size-scaling observed for the TPA cross sections of the larger nanoparticles. This is illustrated in the Supporting information, where we plot the experimental $\sigma^{\text{TPA}}/\text{gold}$ as a function of the size for the Au_{976} (3.0 nm) and the Au_{2406} (4.0 nm) nanoparticles² compared with the simulated results for the $\text{Au}_{25}(\text{SH})_{18}^-$ cluster.

The experiments also reported a large TPA cross section of 2700 GM for a photon energy of 0.96 eV, corresponding to a two-photon excitation into the “a’” band.² As this is the lowest one-photon band, the possible double-resonance effects can be ruled out. Considering the fact that the orientation of the ligands with respect to the $\text{Au}_{25}\text{S}_{18}$ core makes the entire cluster roughly centrosymmetric,^{196–198} one should expect the lowest excited state to be one-photon allowed but two-photon forbidden. This is consistent with our simulations, where no significant TPA cross section is found for excitation into the “a” band. This is also in agreement with the results reported by Day and co-workers.²⁰⁹ The large TPA cross section at 0.96 eV was speculated by Day et al.²⁰⁹ as the result of the tail of the very large TPA cross section for excitation into the “d” band at 1.4 eV. However, that is not seen in our simulations.

Alternatively, symmetry breaking of the ligand shell could lead to an increased TPA cross section. Previous work has demonstrated that such symmetry breaking leads to the observation of hyper-Rayleigh scattering of the $\text{Au}_{25}(\text{SR})_{18}^-$ cluster which otherwise would be symmetry forbidden due the centrosymmetry.^{204,207} To investigate the symmetry breaking effects on the TPA cross section, we also considered the $\text{Au}_{25}(\text{SH})_{16}(\text{SPh})_2^-$ cluster where two phenyl groups have been substituted. This structure is taken from previous work investigating the symmetry breaking effects on the first hyperpolarizabilities.²⁰⁷ The TPA spectrum for the $\text{Au}_{25}(\text{SH})_{16}(\text{SPh})_2^-$ cluster is shown in Figure 5.2. In comparison to the $\text{Au}_{25}(\text{SH})_{18}^-$ cluster, the addition of the two phenyl groups leads to slightly larger TPA cross sections with a maximum of 905 GM. However, no significant TPA cross section is found for excitation into the “a” band, and thus symmetry breaking is unlikely the reason for the strong TPA cross section observed experimentally.

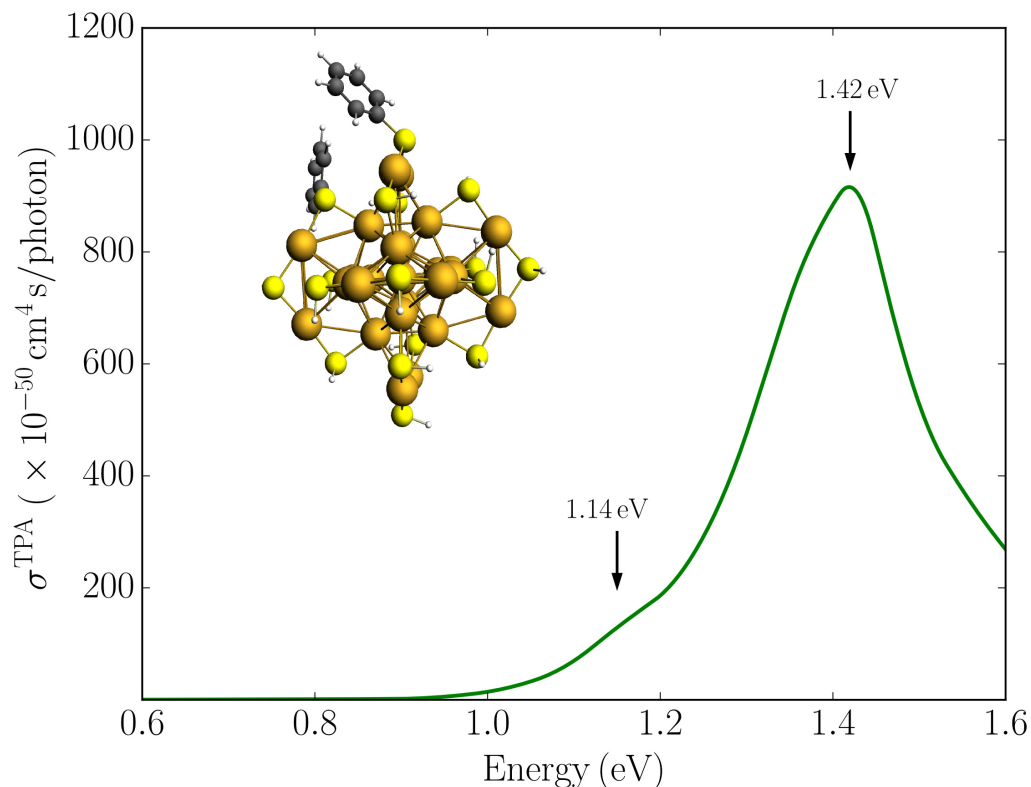


Figure 5.4. Simulated TPA spectrum for the $\text{Au}_{25}(\text{SH})_{16}(\text{SPh})_2^-$ cluster in the gas phase.

To investigate the importance of other one-photon resonance enhancements in the third-order nonlinearity of $\text{Au}_{25}(\text{SH})_{18}^-$, we simulated the optical Kerr response corresponding to the $\gamma(-\omega; \omega, \omega, -\omega)$ tensor with all one-photon terms included. The real part of the optical Kerr response is related to IDRI and its imaginary part corresponds to two-photon and saturated one-photon absorption processes. In Figure 5.5 we plot both $\text{Re}[\gamma^{\text{IDRI}}]$ and $\text{Im}[\gamma^{\text{IDRI}}]$ for the $\text{Au}_{25}(\text{SH})_{18}^-$ cluster as a function of the one-photon energy, together with the contribution arising only from two-photon absorption, i.e., $\text{Im}[\gamma^{\text{TPA}}]$. The $\text{Re}[\gamma^{\text{IDRI}}]$ curve is characterized by a large positive band at 1.43 eV and a small negative band at 1.31 eV. In contrast, a large negative band at 1.37 eV with a small positive band at 1.46 eV mainly constitutes the $\text{Im}[\gamma^{\text{IDRI}}]$ curve. The $\text{Im}[\gamma^{\text{TPA}}]$ is much larger than $\text{Im}[\gamma^{\text{IDRI}}]$ demonstrating a strong destructive interference between the one- and two-photon processes. This seems to indicate that the one-photon processes are more dominant compared to the two-photon processes, and could be the reason that only relatively modest TPA cross sections are found for the $\text{Au}_{25}(\text{SH})_{18}^-$ cluster. The magnitude of the optical Kerr response determined here is comparable to that of the pure electronic response in organic molecules.²²⁰ Although there are no direct measurements of the optical Kerr response of small gold clusters, Qian *et al.*²¹⁰ reported the optical Kerr response of 3 nm gold films. They found large Kerr susceptibility of $2.06 \times 10^{-15} \text{ m}^2 \text{ V}^{-2}$, which is about four orders of magnitude larger

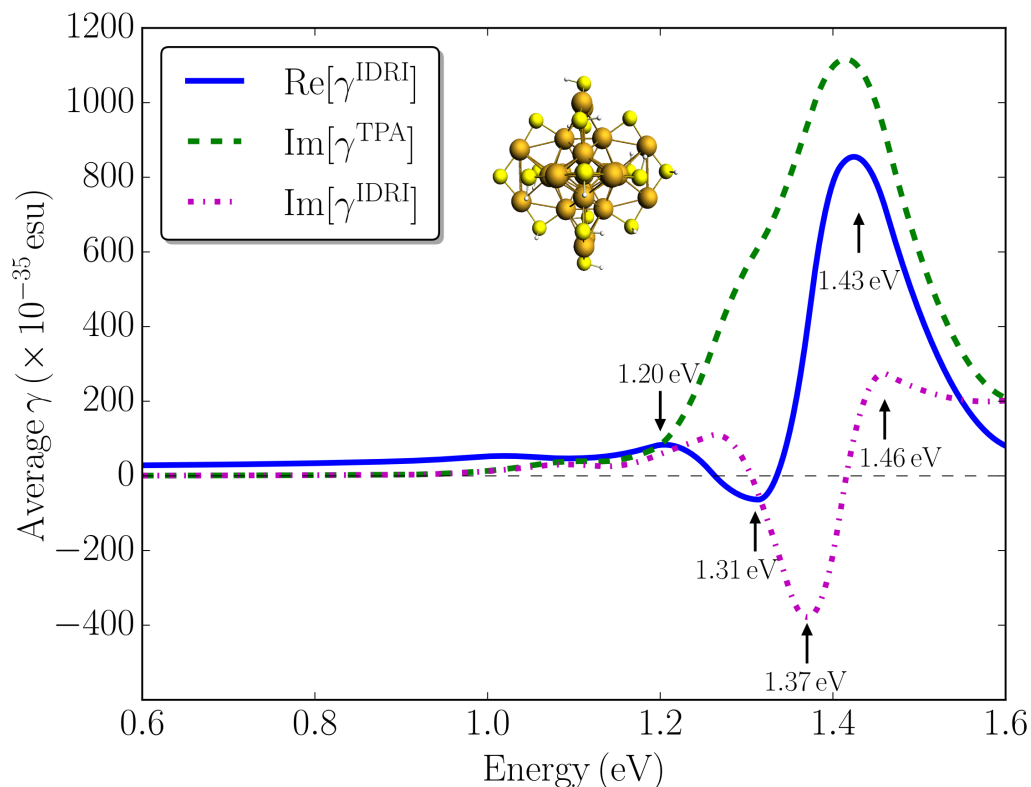


Figure 5.5. Calculated $\text{Re}[\gamma^{\text{IDRI}}]$ (blue solid line), $\text{Im}[\gamma^{\text{TPA}}]$ (green dashed line), and $\text{Im}[\gamma^{\text{IDRI}}]$ (magenta dash-dotted line) for the $\text{Au}_{25}(\text{SH})_{18}^-$ cluster in the gas phase. The black dashed line shows a value of 0 esu.

than that determined for bulk gold films. The large nonlinear response observed was attributed to quantum size effects in the thin gold film. Here we calculated the $|\chi^3|$ to be $3.26 \times 10^{-19} \text{ m}^2 \text{ V}^{-2}$ for the $\text{Au}_{25}(\text{SH})_{18}^-$ cluster by assuming a diameter of $\sim 1.1 \text{ nm}$. Our calculated value is comparable to the bulk value of $9.11 \times 10^{-19} \text{ m}^2 \text{ V}^{-2}$ for a 15 nm thick gold film reported in the same work, but much smaller than the thin film result.²¹⁰ Thus, in general we do not find that quantum size effects lead to significantly enhanced nonlinear response in the small monolayer protected clusters.

Although our simulations show that the TPA cross sections for the $\text{Au}_{25}(\text{SH})_{18}^-$ cluster are enhanced by a double-resonance effect, they are much smaller than what indicated by previous simulations or found experimentally. In general, our results seem to suggest that quantum size effects in these small $\text{Au}_{25}(\text{SR})_{18}^-$ clusters do not lead to extremely large TPA cross sections. However, it is important to note that the results presented here are sensitive to the exact value used for the energy broadening parameter (Γ). In this work, Γ was chosen to match the experimental absorption spectrum. Using a smaller Γ value would lead to larger TPA cross sections, but one would need unphysically small values to match the experimental TPA cross sections. Finally, the TDDFT simulations presented here all employ an adiabatic approximation for the exchange-

correlation kernels. Previously, it was shown that the such an typical approximation could cause spurious pole effects near one-photon resonances.²¹¹ For small molecules, these spurious poles lead to significantly larger TPA cross sections, yet the behavior is still unknown for systems like the $\text{Au}_{25}(\text{SR})_{18}^-$ clusters that have a high density of states.

5.5 Conclusion

In summary, we have reported first-principles simulations of TPA spectra for two thiolate-protected Au_{25} clusters based on a damped cubic response formalism within TDDFT. We find the calculated TPA cross sections are much smaller than their experimental counterparts, which indicates the previously suggested one- and two-photon double resonance effect is unlikely the only cause for the large TPA intensities reported experimentally. The calculation of TPA cross sections on a per gold atom basis, as well as the Kerr nonlinear responses, is in-line with those expected from larger nanoparticles. Symmetry breaking was shown to only lead to small enhancements of the TPA cross sections. Overall, this work represents the first cubic response theory approach to TPA simulations of the $\text{Au}_{25}(\text{SR})_{18}^-$ clusters, and shows that quantum size effects do not lead to significantly enhanced third-order nonlinear response. This is in agreement with the molecular origin of the electronic transitions in the small gold clusters.

Part III

Simulating Metal Surface Effects on Nonlinear Optical Properties

Chapter 6 | Theory of Linear and Nonlinear Surface-enhanced Vibrational Spectroscopy

Chulhai, D. V.; Hu, Z.; Moore, J. E.; Chen, X.; Jensen, L. “*Theory of Linear and Nonlinear Surface-Enhanced Vibrational Spectroscopy*” *Annu. Rev. Phys. Chem.* **2016**, *67*, 541–564.

Abstract

Vibrational spectroscopy of molecules adsorbed on metal nanoparticles can be enhanced by many orders of magnitude such that the detection and identification of single molecules are possible. Enhancement of most linear and nonlinear vibrational spectroscopies has been demonstrated. In this review we will discuss theoretical approaches to understand linear and nonlinear surface-enhanced vibrational spectroscopies. A unified description of enhancement mechanisms classified as either electromagnetic or chemical in nature will be presented. Emphasis will be on understanding the spectral changes necessary for interpretation of linear and nonlinear surface-enhanced vibrational spectroscopies.

6.1 Introduction

The ability of plasmonic metal nanostructures to localize light well below the diffraction limit offers unique opportunities for enhancing the spectroscopy of molecules situated at the surface of these metallic nanostructures²²¹. By taking advantage of carefully designed nanostructures, it becomes possible to enhance and localize the near-field with resolutions that are starting to reach the length-scale of molecules²²². The enhancement of a large variety of linear spectroscopies, such as surface-enhanced infra-red absorption (SEIRA), surface-enhanced Raman scattering (SERS), tip-enhanced-Raman scattering (TERS), and surface-enhanced Raman optical activity (SEROA), as well as nonlinear spectroscopies, such as surface-enhanced hyper-Raman scattering (SEHRS), surface-enhanced coherent anti-Stokes Raman spectroscopy (SECARS), surface-enhanced femto-second stimulated Raman scattering (SE-FRSR), and surface-enhanced sum-frequency generation (SESFG), have been demonstrated^{14,221,223,224}. In particular, the strong near-field provided by these nano-antennas supplies sufficient enhancement that vibrational spectroscopy at the single-molecule level is possible. Using the bi-analyte method^{225,226}, where two molecules or isotopologues with distinct vibrational signatures are used, single-molecule sensitivity has been demonstrated for SERS^{225,226}, TERS²²⁷, SEHRS¹³⁵, and SECARS²²⁸.

There are two main mechanisms that contribute to enhancing the vibrational signal of molecules on metal surfaces^{26,76}. The first is the electromagnetic mechanism (EMM) caused by the enhanced near-field generated by exciting the plasmon. The second mechanism is loosely called the chemical mechanism (CM) and lumps together all other changes to the molecule’s geometric and electronic structure that arises from binding to the metal surface. Although there has been a great deal of controversy over their relative importance, it is by now well established that the EMM is responsible for the bulk of the enhancement, while the CM only contributes a little to the total enhancements. As our understanding of the enhancement mechanisms are being refined, it remains a significant challenge to explain in detail the specific spectral changes that occur in surface-enhanced spectroscopies^{26,76,229}. The reason for this is that although the EMM dominates the enhancement, the CM often dominates the spectral changes. A prime example of this is the SERS of p-aminothiophenol (ATP) adsorbed on silver, where certain strong bands not present in the normal Raman spectrum of the molecule are observed²³⁰. This was initially ascribed to a resonance Raman mechanism involving a metal-molecule charge-transfer (CT) state²³⁰, however, it was later proposed using theoretical simulations²³¹ and demonstrated experimentally²³² that the band arose from a new chemical species formed during the SERS experiments. It therefore remains a significant theoretical challenge to correctly describe the spectral changes that occur in surface-enhanced vibrational spectroscopies through these mechanisms.

In this review we will provide a unified description of the EMM and the CM for surface-enhanced linear and non-linear vibrational spectroscopies. Although the EMM has been presented numerous times before, we will here provide a simple general framework based on a dressed-tensor formalism that naturally allows for the incorporating of field gradient effects. The discussion will begin by considering these effects in SERS, since most theories have been developed for this phenomenon, before doing so for other surface-enhanced spectroscopies. Emphasis of this review

will be on describing general approaches for understanding the spectral changes necessary for the interpretation of linear and nonlinear surface-enhanced vibrational spectroscopies.

6.2 Surface-Enhanced Raman Scattering

Raman scattering is the inelastic scattering of light, where the Raman intensity for normal mode k may be written as¹⁵

$$I_k^{\text{Raman}} \propto \left| \frac{\partial \alpha}{\partial Q_k} \cdot \mathbf{E}^0 \right|^2, \quad (6.1)$$

where α is the molecule's electric dipole-dipole polarizability, Q_k is the normal mode coordinates for the k th vibration, and \mathbf{E}^0 is the perturbing incident electric field. We will not discuss how one may obtain α in this review, except to say that considerations must be made for excitations off-, near- and on-resonance with a molecular electronic (or vibronic) transition. In SERS, where the molecule is adsorbed on to a plasmonic nanoparticle (NP), this polarizability α is simply the polarizability of the total molecule-NP system (hereinafter represented as α^{tot}).

In order to understand the mechanisms of SERS, we often like to separate the contributions to $\frac{\partial \alpha^{\text{tot}}}{\partial Q_k}$, which has led to confusion and disagreement, into what is commonly referred to as the EMM and the CM. This separation is often made because surface plasmons, the driving force behind the SERS EMM, are accurately described using classical electrodynamics (ED)—though ideally one would treat the entire molecule-NP system using first principles^{233,234}. In reality, the clear separation of this total polarizability into these two distinct contributions is not always possible.

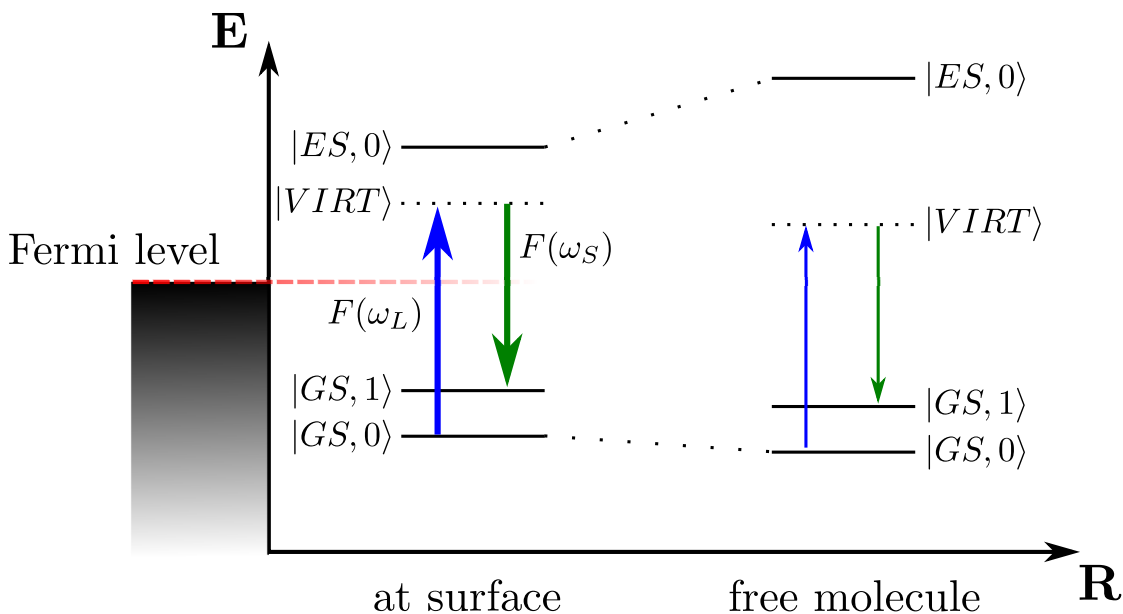


Figure 6.1. Illustration of the mechanisms of surface-enhanced Raman scattering. Abbreviations: ES, excited state; GS, ground state; VIRT, virtual state.

We will proceed to discuss the EMM and CM by re-writing the SERS intensity as

$$I_k^{\text{SERS}} \propto \left| \frac{\partial \alpha^{\text{M}}}{\partial Q_k} \cdot \mathbf{F}(\omega_S) \mathbf{F}(\omega_0) \cdot \mathbf{E}^0 \right|^2, \quad (6.2)$$

where $\mathbf{F}(\omega_0)$ and $\mathbf{F}(\omega_S)$ are the enhancement of the incident and scattered fields, respectively, and constitute the EMM. The α^{M} term describes the contribution to the total molecule-NP polarizability not accounted for by the EMM. All effects that contribute to the changing of the free-molecule polarizability (α^{M}) to $\alpha^{\text{M}'}$, such as changes to the electronic and geometric structure of the molecule, constitute the CM. A schematic of this is illustrated in Figure 6.1. In the remainder of this section, we will review a selection of the theoretical models of these two types of enhancement mechanisms in SERS.

6.2.1 Electromagnetic Mechanism

The EMM (sometimes referred to as the plasmonic theory) of SERS dates back to the late 1970s through the 1980s^{235–241}. It originates from the classical interaction between the molecule and NP, solved using ED. As such, this mechanism can be derived without knowledge of the electronic structure of the molecule or the NP. The EMM has been reviewed a number of times (see for example Refs. 24,242–244). Here we will review the EMM theory by discussing three equivalent models (Silberstein’s equations, the Gersten-Nitzan model, and the dressed-tensor formalism), each with increasing complexity in the description of the molecule and NP. These discussions are made independent of surface plasmons, though one should recognize that the large NP polarizabilities and large local electric field enhancements result from surface plasmons.

6.2.1.1 Silberstein’s Equations

The simplest derivation of the EMM can be made using Silberstein’s equations^{245,246}, which is the solution of the addition of two isotropic polarizabilities. In these equations, we assume that the molecule and the NP are two point polarizable objects, with isotropic polarizability α^{M} and α^{NP} , respectively, separated by some distance R . According to Silberstein’s equations, the total system polarizability is given by

$$\alpha_{\parallel}^{\text{tot}} = \frac{\alpha^{\text{M}} + \alpha^{\text{NP}} + 4\alpha^{\text{M}}\alpha^{\text{NP}}/R^3}{1 - 4\alpha^{\text{M}}\alpha^{\text{NP}}/R^6} \quad \text{and} \quad \alpha_{\perp}^{\text{tot}} = \frac{\alpha^{\text{M}} + \alpha^{\text{NP}} - 2\alpha^{\text{M}}\alpha^{\text{NP}}/R^3}{1 - \alpha^{\text{M}}\alpha^{\text{NP}}/R^6}, \quad (6.3)$$

where $\alpha_{\parallel}^{\text{tot}}$ and $\alpha_{\perp}^{\text{tot}}$ are the components of the total polarizability parallel and perpendicular to the separation axis, respectively. We now take the derivative with respect to normal mode coordinate Q_k , assuming that the polarizability of the NP is not affected by the normal modes of the molecule ($\frac{\partial \alpha^{\text{NP}}}{\partial Q_k} = 0$), which leaves the Raman polarizabilities as²⁶

$$\frac{\partial \alpha_{\parallel}^{\text{tot}}}{\partial Q_k} = \frac{\partial \alpha^{\text{M}}}{\partial Q_k} \frac{(1 + 2\alpha^{\text{NP}}/R^3)^2}{(1 - 4\alpha^{\text{NP}}\alpha^{\text{M}}/R^6)^2} \quad \text{and} \quad \frac{\partial \alpha_{\perp}^{\text{tot}}}{\partial Q_k} = \frac{\partial \alpha^{\text{M}}}{\partial Q_k} \frac{(1 - \alpha^{\text{NP}}/R^3)^2}{(1 - \alpha^{\text{NP}}\alpha^{\text{M}}/R^6)^2}. \quad (6.4)$$

Ignoring the terms in the denominator of Equation 6.4, which are contributions to the image field effect and will be discussed later, we are left with the parallel and perpendicular components of the local electric field enhancement (E_{\parallel} and E_{\perp}), respectively. These lead to the following expressions for the SERS intensity:

$$I_{\parallel}^{\text{SERS}} \propto \left| \frac{\partial \alpha^{\text{M}}}{\partial Q_k} \right|^2 |E_{\parallel}|^4 \quad \text{and} \quad I_{\perp}^{\text{SERS}} \propto \left| \frac{\partial \alpha^{\text{M}}}{\partial Q_k} \right|^2 |E_{\perp}|^4, \quad (6.5)$$

which gives the familiar $|\mathbf{E}|^4$ EMM enhancement factor.

Using Silberstein's equations to simulate the SERS spectrum is equivalent to scaling the Raman spectrum by the $|\mathbf{E}|^4$ factor, with the largest enhancement for polarization along the NP-molecular axis. However, this scaling ignores the rich information that may be available in the observed SERS spectrum. Therefore, this method is only appropriate for molecules approximately described by isotropic polarizabilities, such as in Albrecht A-term scatterers, for example, where the polarizability is diagonal dominated and the relative mode intensities are not due to the tensorial nature of the polarizability-field interactions²⁴⁷. In all other cases, one would need a more rigorous method to account for the tensorial nature of the molecular polarizability and the local electric field in order to simulate the SERS mode selectivity.

6.2.1.2 Gersten-Nitzan Model

Gersten & Nitzan²⁴¹ first outlined the electromagnetic theory of SERS, which takes into consideration the tensorial nature of the interactions. In this derivation, we start by writing the induced dipoles for both the molecule and NP as

$$\mu^{\text{M}} = \alpha^{\text{M}} \cdot (\mathbf{E}^0 + \mathbf{T}^{(2)} \cdot \mu^{\text{NP}}) \quad \text{and} \quad \mu^{\text{NP}} = \alpha^{\text{NP}} \cdot (\mathbf{E}^0 + \mathbf{T}^{(2)} \cdot \mu^{\text{M}}), \quad (6.6)$$

where \mathbf{R} is the vector between the systems, and $\mathbf{T}^{(x)}$ are the interaction tensors^{134,248}, generally defined as

$$\mathbf{T}^{(x)}(\mathbf{R}) = \nabla^x \frac{1}{|\mathbf{R}|}. \quad (6.7)$$

Solving Equation 6.6 leads to the effective polarizabilities of the molecule and NP, and finally to the following expression for the total Raman polarizability:

$$\begin{aligned} \frac{\partial \alpha^{\text{tot}}}{\partial Q_k} &= \left(\mathbf{I} - \alpha^{\text{M}} \cdot \mathbf{T}^{(2)} \cdot \alpha^{\text{NP}} \cdot \mathbf{T}^{(2)} \right)^{-1} \cdot \frac{\partial \alpha^{\text{M}}}{\partial Q_k} \cdot \left[\mathbf{I} + \mathbf{T}^{(2)} \cdot \alpha^{\text{NP}} \cdot \mathbf{T}^{(2)} \right. \\ &\quad \left. \cdot \left(\mathbf{I} - \alpha^{\text{M}} \cdot \mathbf{T}^{(2)} \cdot \alpha^{\text{NP}} \cdot \mathbf{T}^{(2)} \right)^{-1} \cdot \alpha^{\text{M}} \right] \cdot \left(\mathbf{I} + \mathbf{T}^{(2)} \cdot \alpha^{\text{NP}} \right) \\ &\quad + \left(\mathbf{I} - \alpha^{\text{NP}} \cdot \mathbf{T}^{(2)} \cdot \alpha^{\text{M}} \cdot \mathbf{T}^{(2)} \right)^{-1} \cdot \alpha^{\text{NP}} \cdot \mathbf{T}^{(2)} \cdot \frac{\partial \alpha^{\text{M}}}{\partial Q_k} \\ &\quad \cdot \left[\mathbf{I} + \mathbf{T}^{(2)} \cdot \left(\mathbf{I} - \alpha^{\text{NP}} \cdot \mathbf{T}^{(2)} \cdot \alpha^{\text{M}} \cdot \mathbf{T}^{(2)} \right)^{-1} \cdot \alpha^{\text{NP}} \cdot \left(\mathbf{I} + \mathbf{T}^{(2)} \cdot \alpha^{\text{M}} \right) \right], \end{aligned} \quad (6.8)$$

where \mathbf{I} is the identity matrix.

We may ignore terms of the form $\alpha \cdot \mathbf{T}^{(2)} \cdot \alpha \cdot \mathbf{T}^{(2)}$, which have been argued to be negligible in Ref. 26 since they are approximately R^{-3} (in Ref. 241, they are referred to as the image field effect, which we will discuss later). This leads to

$$\frac{\partial \alpha^{\text{tot}}}{\partial Q_k} \approx \left(\mathbf{I} + \alpha^{\text{NP}} \cdot \mathbf{T}^{(2)} \right) \cdot \frac{\partial \alpha^{\text{M}}}{\partial Q_k} \cdot \left(\mathbf{I} + \mathbf{T}^{(2)} \cdot \alpha^{\text{NP}} \right). \quad (6.9)$$

This equation is different from Equation 1.10 in Ref. 241, and contains the additional term $\alpha^{\text{NP}} \cdot \mathbf{T}^{(2)} \cdot \frac{\partial \alpha^{\text{M}}}{\partial Q_k} \cdot \mathbf{T}^{(2)} \cdot \alpha^{\text{NP}}$, which is the major SERS term and is responsible for the $|\mathbf{E}|^4$ enhancement. One can easily see that Equation 6.9 is similar to Equation 6.4, with the tensoral nature of α^{M} , $\mathbf{T}^{(2)}$, and α^{NP} taken into account. This equation has been the most relevant when describing the EMM in SERS and leads directly into the dressed-tensor formalism.

6.2.1.3 Image Field Effect

The image field is an EMM effect resulting from the $(\mathbf{I} - \alpha \cdot \mathbf{T}^{(2)} \cdot \alpha \cdot \mathbf{T}^{(2)})^{-1}$ terms in the Gersten-Nitzan equation (or the denominator in Silberstein’s equations), and was considered by some early theories to be the major contributing factor in SERS^{235,249–251}. This effect is the result of the fields reflected back and forth between the NP and the molecule, ad infinitum.

The Gersten-Nitzan model could be Taylor expanded to include the image field effect as follows

$$\begin{aligned} \frac{\partial \alpha^{\text{tot}}}{\partial Q_k} = & \sum_{i,j=0}^{\infty} \left(\mathbf{I} + \alpha^{\text{NP}} \cdot \mathbf{T}^{(2)} \right) \cdot \left(\alpha^{\text{M}} \cdot \mathbf{T}^{(2)} \cdot \alpha^{\text{NP}} \cdot \mathbf{T}^{(2)} \right)^i \cdot \frac{\partial \alpha^{\text{M}}}{\partial Q_k} \\ & \cdot \left(\mathbf{T}^{(2)} \cdot \alpha^{\text{NP}} \cdot \mathbf{T}^{(2)} \cdot \alpha^{\text{M}} \right)^j \cdot \left(\mathbf{I} + \mathbf{T}^{(2)} \cdot \alpha^{\text{NP}} \right). \end{aligned} \quad (6.10)$$

The case where $i = j = 0$ gives the Gersten-Nitzan formula without image effects, all other terms describe some order of the reflected field in the image field effect. Since the terms that depend on i (or j) scale as $(R^{-3})^i$, one can see that the image field depends strongly on distance between the molecule and the NP, and quickly becomes insignificant for $i, j > 1$.

This Taylor expansion form of the image field effect breaks down in the case where $\alpha^{\text{M}} \mathbf{T}^{(2)} \alpha^{\text{NP}} \mathbf{T}^{(2)} \approx 1$, and a more explicit incorporation of the image field is required. In the work of Masiello and coworkers^{252,253}, the term “plasmon-dressed” is used to refer to the image field modified polarizability—and is not the same as the dressed-tensor formalism described later in this article. Their model describes the image field coupling between the molecule (from first principles) and NP (from classical ED) using Green’s function theory. Many other hybrid quantum mechanical (QM) / classical ED methods incorporate the image field effect^{254–264}, often using a continuum model of the NP system. However, methods that include the image field effect (along with the EMM field enhancement) using an atomistic description of the NP system(s) have been presented^{134,265–268}.

6.2.1.4 Dressed-Tensor Formalism

The dressed-tensor formalism^{269,270} is similar to the Gersten-Nitzan result (without image field effects), except the interactions $\alpha^{\text{NP}} \cdot \mathbf{T}^{(2)}$ and $\mathbf{T}^{(2)} \cdot \alpha^{\text{NP}}$ have been replaced by the field enhancement matrix \mathbf{F} ,

$$\frac{\alpha_{\alpha\beta}^{\text{tot}}}{\partial Q_k} = [\delta_{\alpha\gamma} + F_\gamma^\alpha(\omega_S)] \frac{\partial \alpha_{\gamma\delta}^{\text{M}}}{\partial Q_k} [\delta_{\delta\beta} + F_\delta^\beta(\omega_L)]. \quad (6.11)$$

The Einstein summation convention is assumed for repeated indices, where Greek indices represent Cartesian directions. F_β^α is the unitless local electric field matrix describing the fields induced in the β Cartesian direction due to a unit incident perturbation in the α Cartesian direction, calculated at the incident laser (ω_L) and Raman shifted (ω_S) frequencies.

This equation removes the point-dipole approximation of the NP in Equation 6.9, and one can simulate the field enhancements from complex NP geometries using any classical ED method. It also makes it easier to increase the level of interaction between the molecule and NP. While this change may appear trivial, the dressed-tensor formalism implicitly includes other advantages, including: (a) a higher order multipole description of the NP, (b) multiple polarizable sources (such as the description from a discrete dipole approximation calculation or multiple point-polarizable NPs), and (c) inclusion of retardation effects. We will show how the field enhancement matrix accounts for each of these effects in turn.

To show that the field enhancement implicitly includes contributions from a NP with higher order multipoles, we shall consider a NP described by α^{NP} , dipole-quadrupole (A^{NP}), quadrupole-dipole (\mathcal{A}^{NP}), and quadrupole-quadrupole (C^{NP}) polarizabilities. The QM definition of these tensors and how they relate to the induced multipoles are defined in Ref. 271, except that the C -tensor is not defined with the $1/3$ factor to maintain consistency with the definition of the other polarizability tensors. All these response tensors will be frequency-dependent and complex, which we will ignore for simplicity.

The induced multipoles in the NP due to an external field are $\mu_\alpha^{\text{NP}} = \alpha_{\alpha\beta}^{\text{NP}} E_\beta^0$ and $\theta_{\alpha\beta}^{\text{NP}} = \mathcal{A}_{\alpha\beta,\gamma}^{\text{NP}} E_\gamma^0$. The A^{NP} and C^{NP} do not contribute to the induced multipoles in the quasistatic limit since the field gradient of the incident field is effectively zero. The local field ‘‘felt’’ by the molecule due to these multipoles is

$$E_\alpha^{\text{loc}} = T_{\alpha\beta}^{(2)} \mu_\beta^{\text{NP}} - \frac{1}{3} T_{\alpha\beta\gamma}^{(3)} \theta_{\beta\gamma}^{\text{NP}} = \left(T_{\alpha\gamma}^{(2)} \alpha_{\gamma\beta}^{\text{NP}} - \frac{1}{3} T_{\alpha\gamma\delta}^{(3)} \mathcal{A}_{\gamma\delta,\beta}^{\text{NP}} \right) E_\beta^0 = F_\alpha^\beta E_\beta^0. \quad (6.12)$$

And similarly, the dipole induced in the NP at the Raman shifted frequency due to the induced molecular dipole is

$$\mu_\alpha^{\text{NP,scat}} = \left(\alpha_{\alpha\gamma}^{\text{NP}} T_{\gamma\beta}^{(2)} + \frac{1}{3} A_{\alpha,\gamma\delta}^{\text{NP}} T_{\gamma\delta\beta}^{(3)}(-\mathbf{R}) \right) \mu_\beta^{\text{M}} = F_\beta^\alpha \mu_\beta^{\text{M}}. \quad (6.13)$$

The relationship above has been achieved using $-T^{(3)}(\mathbf{R}) = T^{(3)}(-\mathbf{R})$, $\mathcal{A}_{\alpha\beta,\gamma}^{\text{NP}} = A_{\gamma,\alpha\beta}^{\text{NP}}$, and the fact that the far-field radiation of the quadrupole induced in the NP does not contribute

significantly to the scattering. Thus showing that the field enhancement matrix \mathbf{F} implicitly accounts for higher order multipole descriptions of the NP.

We will show that the field enhancement matrix also accounts for a multiple-dipole approximation of the NP. In such cases, we assume that the NP consists of a series of N point-polarizable objects with polarizability $\alpha^{\text{NP},i}$ at position \mathbf{r}^i ($i \in N$). The induced dipoles in such a system may be solved as $\mu_\alpha^{\text{NP},i} = \sum_j^N (\mathbf{A}^{-1})_{ij,\alpha\beta} \cdot E_\beta^{0,j}$, where \mathbf{A} is the $3N \times 3N$ interaction matrix defined elsewhere^{272,273}. The local field is then written as

$$E_\alpha^{\text{loc}}(\mathbf{r}^{\text{M}}) = \left[\sum_{i,j}^N T_{i,\alpha\beta}^{(2)}(\mathbf{r}^{\text{M}} - \mathbf{r}^i) (\mathbf{A}^{-1})_{ij,\beta\gamma} \right] E_\gamma^0 = F_\alpha^\beta E_\beta^0, \quad (6.14)$$

where \mathbf{r}^{M} is the position of the molecular point-dipole, thereby defining the field enhancement matrix at this point.

For the total dipole induced in the NP at the scattered field due to the induced molecular dipole, one obtains

$$\mu_\alpha^{\text{NP,scat}} = \left[\sum_{i,j}^N (\mathbf{A}^{-1})_{ij,\alpha\beta} T_{j,\beta\gamma}^{(2)}(\mathbf{r}^j - \mathbf{r}^{\text{M}}) \right] \mu_\gamma^{\text{M}} = F_\beta^\alpha \mu_\beta^{\text{M}}, \quad (6.15)$$

thereby showing that the field enhancement matrix in the dressed-tensor formalism may also describe multiple point-dipole NP systems.

Finally, to include retardation effects in the dressed-tensor formalism the $\mathbf{T}^{(2)}$ interaction matrix becomes the dipole relay tensor with retardation effects^{15,244}, which still retains the necessary symmetry ($T_{\alpha\beta}^{(2)} = T_{\beta\alpha}^{(2)}$ and $T^{(2)}(\mathbf{R}) = T^{(2)}(-\mathbf{R})$) to justify the above made claims for the dressed-tensor formalism.

6.2.1.5 Local Field Gradients

More recent changes to the EMM have come through exploration of the local field gradients^{269,270,274-278}. In most cases, the local field varies greatly over the dimensions of the molecule^{268,279}. This can often lead to the observation of Raman-inactive modes, as was observed and briefly discussed in the early 1980s²⁸⁰⁻²⁸³.

The near-field gradients (in the quasi-static limit) are described by the $\mathbf{T}^{(3)}$ interaction tensor^{134,248}, which leads one to write the induced dipole in the molecule (using the Gersten-Nitzan model) as

$$\mu^{\text{M}} = \left[\alpha^{\text{M}} \cdot \left(\mathbf{I} + \mathbf{T}^{(2)} \cdot \alpha^{\text{NP}} \right) + \frac{1}{3} A^{\text{M}} \cdot \mathbf{T}^{(3)} \cdot \alpha^{\text{NP}} \right] \cdot \mathbf{E}^0, \quad (6.16)$$

where A^{M} is the molecule's electric dipole-quadrupole polarizability tensor.

One consideration of the effects of the local field gradients was proposed by Jahncke and

coworkers^{274,275}, who suggested that the induced molecular dipole may be expanded as

$$\frac{\partial \mu^{\text{M}}}{\partial Q_k} = \left[\frac{\partial \alpha^{\text{M}}}{\partial Q_k} \cdot (\mathbf{I} + \mathbf{T}^{(2)} \cdot \alpha^{\text{NP}}) + \alpha^{\text{M}} \cdot \frac{\partial (\mathbf{T}^{(2)} \cdot \alpha^{\text{NP}})}{\partial Q_k} + \frac{1}{3} \frac{\partial A}{\partial Q_k} \cdot \mathbf{T}^{(3)} \cdot \alpha^{\text{NP}} \right] \cdot \mathbf{E}^0. \quad (6.17)$$

This is a modified form of Equation 3 from Ref. 274, rewritten in the style of the Gersten-Nitzan model and assuming a point-dipole NP. The first term is effectively the SERS term (without field gradients), the second term has been labeled as the “gradient-field Raman” term, while the third is the traditional field gradient SERS term. It is in fact this third term that results, as originally proposed^{280–283}, from the local electric field gradient.

We can easily account for this term in the dressed-tensor formalism, assuming that the molecule is described as a point-dipole with α^{NP} and A^{NP} tensors. This leads to the dressed-tensor expression for the Raman polarizability as^{24,270,281}

$$\frac{\partial \alpha_{\alpha\beta}^{\text{tot}}}{\partial Q_k} = [\delta_{\alpha\gamma} + F_{\gamma}^{\alpha}(\omega_S)] \left\{ \frac{\partial \alpha_{\gamma\delta}^{\text{M}}}{\partial Q_k} [\delta_{\beta\delta} + F_{\delta}^{\beta}(\omega_L)] + \frac{1}{3} \frac{\partial A_{\gamma,\delta\epsilon}^{\text{M}}}{\partial Q_k} F_{\delta\epsilon}^{\beta}(\omega_L) \right\}, \quad (6.18)$$

where we have introduced the field enhancement matrix $F_{\beta\gamma}^{\alpha}$ (in units of inverse length), describing the field gradient in the $\beta\gamma$ Cartesian direction due to an incident unit field in the α direction.

6.2.1.6 Point-dipole / Point-quadrupole Molecule

With large field gradients, one may argue that a point-dipole description is often insufficient at describing the molecule. We will therefore describe the molecule as a point-dipole (described by α^{M} and A^{M}) and a point-quadrupole (described by the quadrupole-dipole (\mathcal{A}^{M}) and the quadrupole-quadrupole (C^{M}) polarizabilities). One may write the induced quadrupole in the molecule as

$$\theta^{\text{M}} = \mathcal{A}^{\text{M}} \cdot (\mathbf{E}^0 + \mathbf{T}^{(2)} \cdot \mu^{\text{NP}}) + \frac{1}{3} C^{\text{M}} \cdot \mathbf{T}^{(3)} \cdot \mu^{\text{NP}}, \quad (6.19)$$

and the induced dipole of the NP as

$$\mu^{\text{NP}} = \alpha^{\text{NP}} \cdot \left(\mathbf{E}^0 + \mathbf{T}^{(2)}(-\mathbf{R}) \cdot \mu^{\text{M}} - \frac{1}{3} \mathbf{T}^{(3)}(-\mathbf{R}) \cdot \theta^{\text{M}} \right). \quad (6.20)$$

Solving these equations as in Ref. 241, ignoring the image field effects, substituting $\mathbf{T}^{(2)}(\mathbf{R}) = \mathbf{T}^{(2)}(-\mathbf{R})$ and $\mathbf{T}^{(3)}(\mathbf{R}) = -\mathbf{T}^{(3)}(-\mathbf{R})$, and replacing $\mathbf{T}^{(2)} \cdot \alpha^{\text{NP}}$ and $\mathbf{T}^{(3)} \cdot \alpha^{\text{NP}}$ with the appropriate local field or gradient enhancement matrix \mathbf{F} , we end up with the dressed-tensor

formalism²⁷⁰

$$\begin{aligned}
\frac{\partial \alpha_{\alpha\beta}^{\text{tot}}}{\partial Q_k} &= [\delta_{\alpha\gamma} + F_\gamma^\alpha(\omega_S)] \frac{\partial \alpha_{\gamma\delta}^M}{\partial Q_k} [\delta_{\beta\delta} + F_\delta^\beta(\omega_L)] \\
&+ \frac{1}{3} [\delta_{\alpha\gamma} + F_\gamma^\alpha(\omega_S)] \frac{\partial A_{\gamma,\delta\epsilon}^M}{\partial Q_k} F_{\delta\epsilon}^\beta(\omega_L) \\
&+ \frac{1}{3} F_{\gamma\delta}^\alpha(\omega_S) \frac{\partial \mathcal{A}_{\gamma\delta,\epsilon}^M}{\partial Q_k} [\delta_{\beta\epsilon} + F_\epsilon^\beta(\omega_L)] \\
&+ \frac{1}{9} F_{\gamma\delta}^\alpha(\omega_S) \frac{\partial C_{\gamma\delta,\epsilon\zeta}^M}{\partial Q_k} F_{\epsilon\zeta}^\beta(\omega_L).
\end{aligned} \tag{6.21}$$

In Ref. 270, it was noted that the induced point-quadrupole interaction with the NP's polarizability occurs through $\mathbf{T}^{(3)}$, which is the same level of interaction as the field gradients with a point-dipole molecule, and therefore should be considered simultaneously. The dressed-tensor, therefore allows one to easily account for higher order multipole description of the molecule as well as higher order gradients of the local electric field. We note that these four terms are effectively the same as those identified in the quadrupolar SERS theory of Polubotko²⁸⁴.

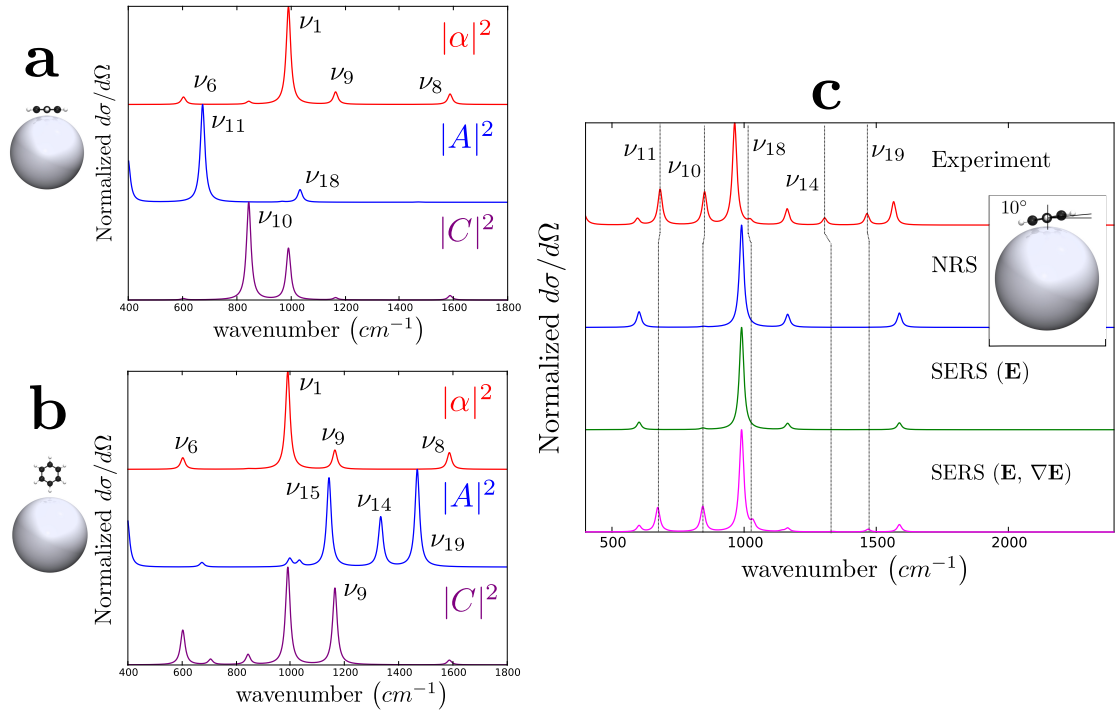


Figure 6.2. (a,b) SERS surface selection rules from the α , A , and C tensors for benzene (a) flat and (b) vertical orientations. (c) Higher-order tensors may assist in assigning binding orientations. Abbreviations: NRS, normal Raman scattering; SERS, surface-enhanced Raman scattering. Figure adapted from Ref. 270 with permission.

This field gradient theory of SERS is not separate from the main $|\mathbf{E}|^4$ EMM of SERS but rather a supplement to it. Importantly, the main SERS contribution is from the local fields and the dipole-dipole polarizability. The 1/3 prefactor for the dipole-quadrupole terms and the 1/9 prefactor for the quadrupole-quadrupole term indicate that they will be minor modifications

Table 6.1. Contributions of the electromagnetic mechanism enhancement factor to the intensity of surface-enhanced Raman scattering

Terms	Prefactor	Enhancement
$ \alpha ^2$	1	$ \mathbf{E} ^4$
$\mathbf{Re}(\alpha A^\dagger), \mathbf{Re}(\alpha \mathcal{A}^\dagger)$	$\frac{1}{3}$	$\mathbf{E}^3 \cdot \nabla \mathbf{E}$
$ A ^2, \mathcal{A} ^2, \mathbf{Re}(A \mathcal{A}^\dagger), \mathbf{Re}(\alpha C^\dagger)$	$\frac{1}{9}$	$\mathbf{E}^2 \cdot (\nabla \mathbf{E})^2$
$\mathbf{Re}(AC^\dagger), \mathbf{Re}(\mathcal{A}C^\dagger)$	$\frac{1}{27}$	$\mathbf{E} \cdot (\nabla \mathbf{E})^3$
$ C ^2$	$\frac{1}{81}$	$ \nabla \mathbf{E} ^4$

to the SERS spectrum, and only significant for very large field gradient to field ratios or large quadrupolar polarizabilities. It allows for the observation of Raman inactive modes in molecules through an EMM, rather than through symmetry lowering from adsorption to the surface—though both effects may be relevant. This is illustrated in Figure 6.2, where the A and C surface selection rules are shown. The contributions to the EMM enhancement (up to the $\mathbf{T}^{(3)}$ interaction level) is given in Table 6.1, with their relevant prefactors. Each of the terms in Table 6.1 may select for specific modes within a molecule. The $|\alpha|^2$ term select for the the Raman-active modes in the gas-phase molecules, and is the major contributing SERS term. The selection rules for the $|A|^2$ and $|\mathcal{A}|^2$ terms were also previously considered^{280,281}, and these terms select for modes that belong to representations that include cubic transformations.

6.2.2 Chemical Mechanism

The interactions between a metal surface and a molecule lead to changes in its electronic structure and geometry, which are reflected in the CM^{285–288}. It is important to account for these changes as it is this perturbed molecule that is being probed in SERS. These changes are local in nature and depend strongly on the specific molecule as it results from the overlap between the wavefunctions of the molecule and the metal NP. Accounting for these often subtle changes are notoriously difficult, and our lack of understanding of the CM has plagued the field of SERS from its beginning. As the CM is highly molecule specific, it is best understood on a case-by-case basis using modern electronic structure methods^{76,285,286,289}. However, here we will present simplified arguments which highlight certain aspects of the CM.

Instead of considering the full electronic structure of the molecule, we will adapt a two-states model with the transition dipole moment oriented normal to the metal surface. The Raman polarizability of the molecule can then be expressed as

$$\frac{\partial \alpha_{zz}}{\partial Q_k} \approx \frac{\partial}{\partial Q_k} \left(\frac{\mu_z^{01} \mu_z^{10}}{\omega_e - \omega - i\Gamma} \right) \approx -\frac{\mu_z^{01} \mu_z^{10}}{(\omega_e - \omega - i\Gamma)^2} \frac{\partial \omega_e}{\partial Q_k} + \left(\frac{2 \frac{\partial \mu_z^{01}}{\partial Q_k} \mu_z^{10}}{\omega_e - \omega - i\Gamma} \right), \quad (6.22)$$

where μ_z^{01} is the transition dipole moment, ω_e the excitation energy, and Γ the the excited state

damping parameter related to the excited state lifetime. For simplicity, we have neglected vibronic coupling effects in this expression. These two terms are the so-called A-term (or Franck-Condon scattering) and B-term (or Hertzberg-Teller scattering) well known from the theory of resonance Raman scattering²⁹⁰. While this expression often is too simplified for practical simulations, it offers a convenient framework for discussing several different types of contributions to the CM which will be presented below.

6.2.2.1 Resonance Raman Mechanism

On resonance with a strong transition, the A-term dominates and the SERS intensity within the two-states model can be written as

$$I^{\text{SERS,RRM}} \approx \left(\frac{\mu_z^{01}}{\Gamma} \right)^4 \left(\frac{\partial \omega_e}{\partial Q_k} \right)^2 |E_{\parallel}|^4, \quad (6.23)$$

which we will label as the resonance Raman mechanism (RRM) and is responsible for surface-enhanced resonance-Raman scattering (SERRS). From this expression, we see that the intensity is largely determined by the transition dipole moment and the electric field, and depends strongly on the damping parameter. We include this as a CM since the interactions with the metal surface lead to changes in the molecule that will affect the RRM. For example, the damping factor is often larger on the surface due to additional non-radiative decay channels, which then will lead to a reduction in the SERS intensity⁷⁶. The selection rules are determined by the excited state gradient, for which it becomes convenient to introduce the dimensionless displacements given by $\Delta_k \propto \frac{\partial \omega_e}{\partial Q_k}$. The Δ_k can be thought of as the difference between the ground and excited state structure along the k 'th normal mode. Thus, for molecules that are only weakly coupled to the surface we expect that the spectral selection rules are determined by the resonance effect on the molecule and that the spectral features only depend weakly on the orientation of the surface-bound molecule. This was recently used to show that the intensity fluctuations in single-molecule tip-enhanced-resonance Raman scattering of rhodamine 6G could arise from small changes in the excited state properties²⁹¹.

6.2.2.2 Charge-transfer Mechanism

The interactions between the molecule and the metal NP can lead to the formation of low-lying CT states that could potentially be excited by the incident light. Due to the often weak interactions between the molecule and metal, these transitions are weak in nature and thus dominated by B-term scattering as²⁹²

$$I^{\text{SERS,CTM}} \approx \left(\frac{\mu_z^{10}}{\Gamma} \right)^2 \left(\frac{\partial \mu_z^{01}}{\partial Q_k} \right)^2 |E_{\parallel}|^4, \quad (6.24)$$

and thus we refer to this as the charge-transfer mechanism (CTM). However, these CT transitions can gain intensity by coupling to other close-lying transitions, such as the plasmon excitation, through a Herzberg-Teller mechanism. More importantly, the spectral signatures are determined by $\frac{\partial \mu_z^{01}}{\partial Q_k}$, which leads to selection rules that differ from traditional Raman scattering and allows

for the detection of non-totally symmetric modes²⁹². The direct detection of the CT bands in the background of the plasmon excitation is not possible and thus indirect evidence for the CT states is used. For this reason, CTM is often invoked to explain observations of unusual bands in the SERS spectra. However, as the recent debate on the interpretation of the SERS spectrum of 4-aminobenzenethiol shows, this is not without problems^{230–232,293}.

6.2.2.3 Off-resonance Mechanism

The final mechanism that we are to consider can be classified as an off-resonance mechanism (ORM), where the incident light is far from resonance with any molecular transitions and any CT excitations in the system. For such a situation, the two-state model gives

$$I^{\text{SERS,ORM}} \approx \left(\frac{\mu_z^{01}}{\omega_e} \right)^4 \left(\frac{\partial \omega_e}{\partial Q_k} \right)^2 |E_{\parallel}|^4, \quad (6.25)$$

where ω_e now refers to the lowest excitation in the system, which is often a CT excitation between the metal and the molecule. Here, the selection rules are determined by the $\frac{\partial \omega_e}{\partial Q_k}$, which has metal-molecule mixed character and thus could be significantly different from that of the free molecule. We also see that the intensity scales with ω_e^{-4} , and thus a reduction in the CT excitation leads to an increased ORM enhancement. This two-states model was used to show that the ORM enhancement scales as $EF_{\text{model}}^{\text{SERS}} \propto \left(\frac{\omega_x}{\omega_e} \right)^4$, where ω_x is the HOMO–LUMO excitation energy of the free molecule and ω_e is lowest CT excitation energy of the metal–molecule complex²⁸⁶. This model explains why molecules that readily accept π -backbonding are found experimentally to exhibit larger enhancements. Such a scaling has recently been demonstrated experimentally by the van Duyne group²⁹⁴. This model has also been extended to describe the enhancement of individual normal modes by considering the deformation potential related to $\frac{\partial \omega_e}{\partial Q_k}$ ²⁹⁵. This is illustrated in Figure 6.3 for pyridine, where modes with a significant Δ are highlighted and correspond to modes with large enhancement, in agreement with simple ORM selection rules. Although the model provides a simple model for rationalizing the ORM enhancement in SERS, it is too simple to correctly predict the spectral signatures. Furthermore, it is well known that conventional functionals in time-dependent density functional theory (TDDFT) have certain failures, such as incorrectly describing CT excitations. It has been shown that traditional functionals overestimate the enhancement by orders of magnitude due to an underestimation of the CT excitation energy²⁸⁵.

6.3 Surface-Enhanced Raman Optical Activity

Raman optical activity (ROA) is the measure of the difference in the Raman intensities involving light of two different polarization states. In the semiclassical theory of ROA^{271,296}, this difference is primarily due to the far-field scattering of the induced electric quadrupoles and magnetic dipoles. As such, simulating the SEROA spectrum requires the relevant electric dipole-dipole (α^{tot}), electric dipole-quadrupole (A^{tot}), electric quadrupole-dipole (\mathcal{A}^{tot}), electric dipole-magnetic dipole (G^{tot}), and magnetic dipole-electric dipole (\mathcal{G}^{tot}) polarizabilities of the total molecule-NP system. Like

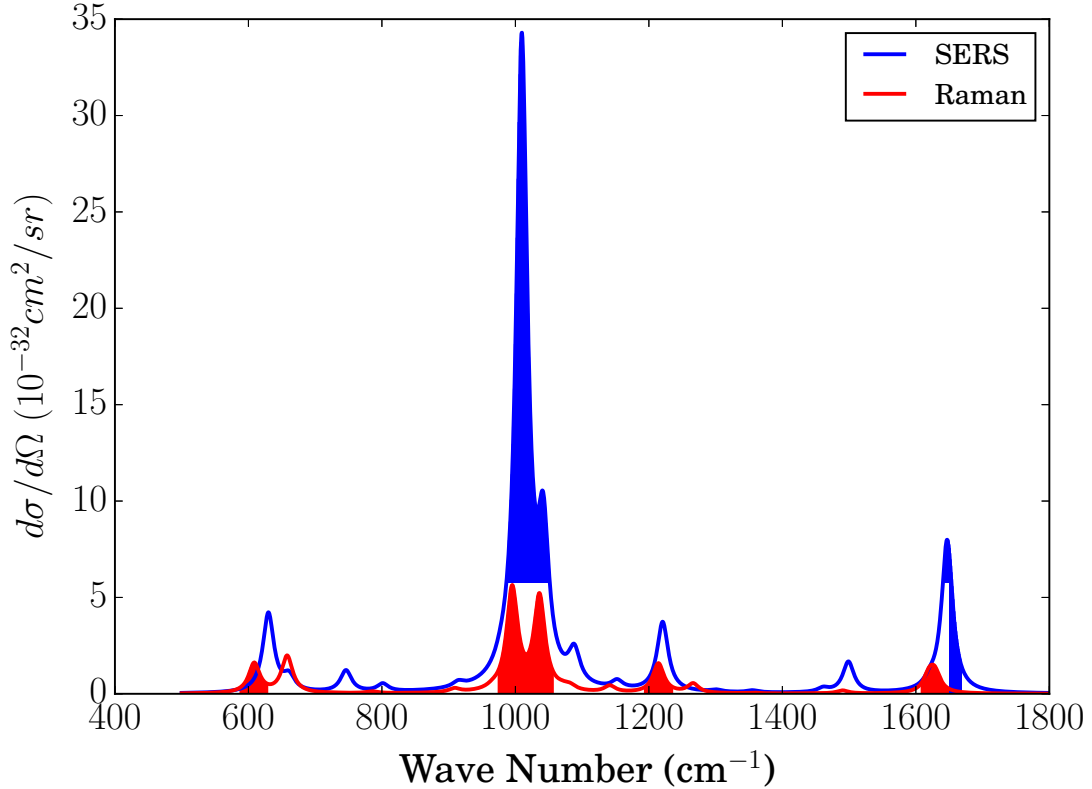


Figure 6.3. Normal Raman and surface-enhanced Raman scattering (SERS) spectra for pyridine on a Ag_{20} cluster. The shaded areas indicate modes from the two-state model that have a non-zero dimensionless displacement $\Delta \geq 0.02$.

SERS, the changes from the gas-phase or bulk-phase molecular polarizability tensors (α^{M} , A^{M} , \mathcal{A}^{M} , G^{M} , and \mathcal{G}^{M}) into the total system polarizability tensors (α^{tot} , A^{tot} , \mathcal{A}^{tot} , G^{tot} , and \mathcal{G}^{tot}) may be attributed to both an EMM and a CM. However, identifying and separating these mechanisms in SEROA may be more difficult than in SERS due to the number of polarizability tensors involved in the expression.

6.3.1 Electromagnetic Mechanism

There have only been a handful of theoretical treatments of the EMM of SEROA^{248,269,297-305}, and the earlier theories have been reviewed before (see, for example, Refs. 76,306). In this article, we will primarily focus on the dressed-tensor formalism by reviewing how it has been used to describe the EMM of SEROA, and then discuss how it relates to the other theories.

The dressed-tensor SEROA formalism was first considered by Janesko & Scuseria²⁶⁹, where the general theory was outlined, and later expanded by Chulhai & Jensen²⁴⁸ to include the $\mathbf{T}^{(3)}$ level of interaction. Combining these two sets of dressed-tensor formalism gives the following generalized expressions for the relevant tensor derivatives (the dressed dipole-dipole polarizability

remains the same as in SERS)

$$\frac{\partial A_{\alpha,\beta\gamma}^{\text{tot}}}{\partial Q_p} = 3F_\delta^\alpha \frac{\partial \alpha_{\delta\epsilon}^{\text{M}}}{\partial Q_p} (\nabla F)_\epsilon^{\beta\gamma} + F_\delta^\alpha \frac{\partial A_{\delta,\epsilon\zeta}^{\text{M}}}{\partial Q_p} (\nabla F)_{\epsilon\zeta}^{\beta\gamma} + F_{\delta\epsilon}^\alpha \frac{\partial \mathcal{A}_{\delta\epsilon,\zeta}^{\text{M}}}{\partial Q_p} (\nabla F)_\zeta^{\beta\gamma} + \frac{1}{3} F_{\delta\epsilon}^\alpha \frac{\partial C_{\delta\epsilon,\zeta\eta}^{\text{M}}}{\partial Q_p} (\nabla F)_{\zeta\eta}^{\beta\gamma}, \quad (6.26)$$

$$\frac{\partial \mathcal{A}_{\alpha\beta,\gamma}^{\text{tot}}}{\partial Q_p} = (\nabla F)_\delta^{\alpha\beta} \frac{\partial \alpha_{\delta\epsilon}^{\text{M}}}{\partial Q_p} F_\epsilon^\gamma + \frac{1}{3} (\nabla F)_\delta^{\alpha\beta} \frac{\partial A_{\delta,\epsilon\zeta}^{\text{M}}}{\partial Q_p} F_{\epsilon\zeta}^\gamma + (\nabla F)_{\delta\epsilon}^{\alpha\beta} \frac{\partial \mathcal{A}_{\delta\epsilon,\zeta}^{\text{M}}}{\partial Q_p} F_\zeta^\gamma + \frac{1}{3} (\nabla F)_{\delta\epsilon}^{\alpha\beta} \frac{\partial C_{\delta\epsilon,\zeta\eta}^{\text{M}}}{\partial Q_p} F_{\zeta\eta}^\gamma, \quad (6.27)$$

$$\frac{\partial G_{\alpha\beta}^{\text{tot}}}{\partial Q_p} = F_\gamma^\alpha \frac{\partial G_{\gamma\beta}^{\text{M}}}{\partial Q_p} + \frac{1}{3} F_{\gamma\delta}^\alpha \frac{\partial \mathcal{G}_{\gamma\delta,\beta}^{\text{M}}}{\partial Q_p}, \text{ and} \quad (6.28)$$

$$\frac{\partial \mathcal{G}_{\alpha\beta}^{\text{tot}}}{\partial Q_p} = \frac{\partial \mathcal{G}_{\alpha\gamma}^{\text{M}}}{\partial Q_p} F_\gamma^\beta + \frac{1}{3} \frac{\partial D_{\alpha,\gamma\delta}^{\text{M}}}{\partial Q_p} F_{\gamma\delta}^\beta. \quad (6.29)$$

We have introduced the gradient field enhancement matrix $\nabla \mathbf{F}$, where $(\nabla F)_\gamma^{\alpha\beta}$ describes the field in the γ direction due to an incident field gradient in the $\alpha\beta$ directions (in units of length), and $(\nabla F)_{\gamma\delta}^{\alpha\beta}$ is the unitless matrix describing the field gradient enhancement in the $\gamma\delta$ directions due to the incident field gradient in the $\alpha\beta$ directions.

The equations in Ref. 269 contain placeholders for additional magnetic enhancement terms, which we neglect here since they contribute negligibly to the local field and gradients for non-magnetic NPs. Additionally, the $\nabla \mathbf{F}$ terms are only important for quadrupolar NPs. The $(\nabla F)_\gamma^{\alpha\beta}$ and $(\nabla F)_{\gamma\delta}^{\alpha\beta}$ enhancement terms are the $\mathbf{T}^{(2)}$ and $\mathbf{T}^{(3)}$ interactions from the multipoles in the NP induced by an incident electric field gradient. For dipolar NPs, we obtain $(\nabla F)_\gamma^{\alpha\beta} = 0$ and $(\nabla F)_{\gamma\delta}^{\alpha\beta} = \delta_{\alpha\gamma} \delta_{\beta\delta}$, which results in the equations presented in Ref. 248. These equations are also a generalized form of the equations by Johnson and coworkers^{304,305}, where the $\mathbf{T}^{(3)}$ interactions were not included.

Of course, as with SERS, the dressed-tensor formalism completely ignores the image field effect. Chulhai & Jensen have shown that the image field can be important in describing the (electronic) optical activity of certain systems^{248,307}. Bouř and coworkers^{302,303} have reformulated this multipolar interaction into matrix form, the solution for which implicitly includes image field effects. This matrix form is analogous to the Gersten-Nitzan model for SERS, except that it includes the multipoles and orders of interaction necessary for SEROA, and is generalizable to more than two point-polarizable objects. However, in order to be consistent with the dressed-tensor formalism above, the polarization matrix \mathbf{P} in Refs. 302 and 303 needs to also include the relevant polarizabilities for the electric quadrupole and magnetic dipole (namely: C^{M} , \mathcal{D}^{M} , D^{M} , and χ^{M} , where χ^{M} is the magnetic dipole-magnetic dipole susceptibility tensor).

Efrima^{297,298}, who was the first to present a theory for SEROA, originally proposed that the conditions needed to observe large SEROA are (i) large field gradients, (ii) phase difference between the electric field and gradients, or (iii) a resonance mechanism. The dressed-tensor formalism does not give insight into changes that may occur due to phase differences between the field and gradient, but it does give insight into the effects of the field gradients. If we ignore the enhanced field gradients (and by this we mean the terms enhanced by $F_{\beta\gamma}^\alpha$ and $(\nabla F)_{\gamma\delta}^{\alpha\beta}$), then we observe that the SEROA signal is enhanced as \mathbf{E}^3 . The circular intensity differences (CIDs) are correspondingly enhanced as $\mathbf{E}^3/|\mathbf{E}|^4$ —a result of the SERS spectrum being enhanced more than

the SEROA spectrum. Enhanced CIDs from SEROA/SERS (as was predicted in Ref. 269) are therefore dependent on large field gradient to field ratios, which would lead to a more complicated expression of the enhancement factor(s). Additionally, orientational averaging may also result in a cancellation of the signed signals and lead to SEROA signals that are weaker than those of unenhanced ROA. These observations suggest that, unlike SERS, the field gradient in SEROA is much more important in the determining the resulting signal.

6.3.2 Chemical Mechanism

There has only been a few theoretical investigations into the CM of SEROA, and none with a simple mathematical expression. Jensen³⁰⁸, and Janesko & Scuseria³⁰¹ both used TDDFT to explore the SEROA of molecules attached to small metal clusters. Jensen found that optical activity was induced into an adenine-Ag₂₀ system, and the CM enhancement contribution to SEROA was larger than those observed in SERS. Janesko & Scuseria found that the induced SEROA signal depended strongly on the binding orientation of the attached molecule and may be cancelled in ensemble measurements, similar to what has been observed for the EMM²⁴⁸. Of course, these TDDFT studies do not entirely negate contributions from the EMM.

6.4 Surface-Enhanced Hyper-Raman Scattering

Hyper-Raman scattering (HRS) is the two-photon analogue of Raman scattering in which the scattered frequency is shifted relative to twice of the incident radiation ($\omega_S = 2\omega_L - \omega_k$, where ω_k is the vibrational frequency). The HRS intensity may be written as^{14,15,28}

$$I_k^{\text{HRS}} \propto \left| \frac{\partial \beta}{\partial Q_k} : \mathbf{E}^0 \mathbf{E}^0 \right|^2, \quad (6.30)$$

where β is the first hyperpolarizability, and we have ignored the specific orientational averaging. The enhancement of the HRS signal due to surface plasmons is termed SEHRS^{27,30,123,132,309}.

6.4.1 Electromagnetic Mechanism

We start our discussion on the EMM of SEHRS by presenting its dressed-tensor formalism

$$\frac{\partial \beta_{\alpha\beta\gamma}^{\text{tot}}}{\partial Q_k} = [\delta_{\alpha\delta} + F_\delta^\alpha(\omega_S)] \frac{\partial \beta_{\delta\epsilon\zeta}^{\text{M}}}{\partial Q_k} [\delta_{\beta\epsilon} + F_\epsilon^\beta(\omega_L)] [\delta_{\gamma\zeta} + F_\zeta^\gamma(\omega_L)], \quad (6.31)$$

where β^{M} and β^{tot} are the hyperpolarizability tensors of the bulk-phase molecule and the molecule-NP complex, respectively. This formalism provides us with an EMM enhancement factor of $|\mathbf{E}(\omega_S)|^2 |\mathbf{E}(\omega_L)|^4$, which is the generally accepted contribution to the EMM enhancement for SEHRS^{29,310,311}. However, unlike in SERS, ω_S and ω_L may be different enough to allow only one of these frequencies to be plasmon-enhanced³¹⁰. This equation allows one to easily account for the orientation and mode selectivity in the EMM of SEHRS.

This dressed-tensor formalism is a more simplistic account of the EMM enhancement captured in the combined QM and classical ED model of Mullin and coworkers³¹⁰. In that paper, they investigated both the EMM and CM enhancement factors for SEHRS, where the adsorbed molecule (with a small portion of the metal particle) was described within a TDDFT framework and the metal particle was treated using Mie theory. This hybrid approach resulted in the SEHRS enhancement factor on the order of 10^9 , with the EMM contribution estimated to be 10^6 – 10^7 . However, since it was noted that the large changes in the relative mode intensities observed in SEHRS were due to the CM, and not the EMM³¹⁰, we will dedicate the next subsection on reviewing the various theories that have accounted for this mechanism.

6.4.2 Chemical Mechanism

There have been a handful of papers on the CM of SEHRS—most of which are centered around understanding the magnitude of the enhancement factor possible from such a mechanism. Early work estimated that the CM enhancement was larger for SEHRS than for SERS²⁸. Yang & Schatz²⁹ suggested that the SEHRS CM enhancement may be as large as 10^5 . Recent work using TDDFT³¹² found CM enhancement of SEHRS to be on the order of 10^2 – 10^5 . The two state model used to describe the ORM²⁸⁶ was also extended to describe SEHRS³¹². This model leads to the following expression of ORM of SEHRS

$$I^{\text{SEHRS,ORM}} \approx \frac{(\mu_z^{01})^4 (\Delta\mu_z^{10})^2}{\omega_e^6} \left(\frac{\partial\omega_e}{\partial Q_k} \right)^2 |E_{\parallel}|^6, \quad (6.32)$$

where $\Delta\mu^{10}$ is the difference in dipole moment between ground and excited state³¹². This expression reveals that the intensity scales as ω_e^{-6} in contrast to the ω_e^{-4} found for SERS, explaining the large CM for SEHRS. The selection rules are similarly determined by this state through the $\partial\omega_e/\partial Q_k$ term. This study also revealed that the ORM enhancement factor may be determined by the change in the HOMO/LUMO energy, using $EF_{\text{model}}^{\text{SEHRS}} \propto \left(\frac{\omega_x}{\omega_e}\right)^6$ ³¹².

For SEHRS, owing to the larger contribution from the CM to the enhancement, one would expect that the spectral signatures (for resonantly excited molecules) to be mostly determined by the resonance hyper-Raman spectrum (RHRS). This is illustrated in Figure 6.4 for SEHRS of rhodamine 6G. As such, we may apply the same approximations to develop a simple model in order to understand how the CM may affect spectral signatures in SEHRS. Doing this, we end up with

$$\begin{aligned} I^{\text{SEHRS,RRM}} &\approx \frac{(\mu_z^{01})^4 (\Delta\mu_z^{10})^2}{\Gamma^4(\omega_e - \omega_L)^2} \left(\frac{\partial\omega_e}{\partial Q_k} \right)^2 |E_{\parallel}|^6 \\ &+ \frac{(\mu_z^{01})^4 (\Delta\mu_z^{10})^2}{\Gamma^2(\omega_e - \omega_L)^4} \left(\frac{\partial\omega_e}{\partial Q_k} \right)^2 |E_{\parallel}|^6 \\ &+ \frac{\left[\frac{\partial}{\partial Q_k} \left((\mu_z^{01})^2 \Delta\mu_z^{10} \right) \right]^2}{\Gamma^2(\omega_e - \omega_L)^2} |E_{\parallel}|^6 + \dots \end{aligned} \quad (6.33)$$

The first two terms are the contributions from the A-terms, and third term is the contribution from the B-terms^{14,142}; we have ignored the potential cross-terms for simplicity. The first term

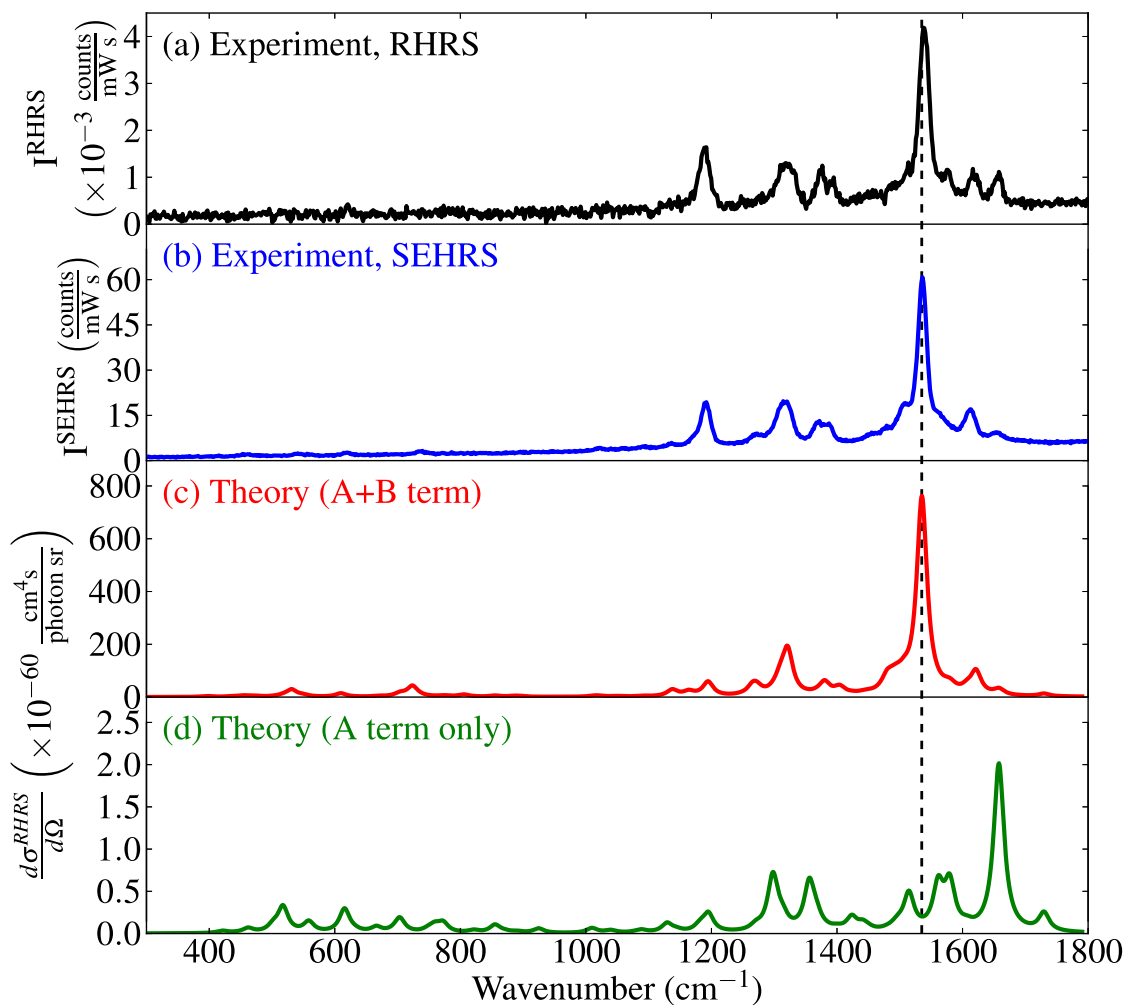


Figure 6.4. Comparison between simulated and experimental (SE)HRS spectra of rhodamine 6G. Abbreviations: RHRs, resonance hyper-Raman scattering; SEHRS, surface-enhanced hyper-Raman scattering. Figure adapted from Ref. 137 with permission.

depends on Γ^{-4} , and will be greatly weakened if the damping factor of the molecule is increased on adsorption on to a surface. Moving away from the two-states model, the many-states vibronic theory of RHRs^{14,142,161,313,314} has been used to analyze the results of SEHRS with much success^{18,97,132,137,315}.

6.5 Surface-Enhanced Sum-Frequency Generation

Sum-frequency generation (SFG) is a three-photon process used to probe the vibrational states of a molecule. Due to its outstanding surface selectivity, it has been adopted to examine surface adsorption and surface reactions involving catalysis, and used in material science, electrochemistry and biocompatibility^{316–322}. The SFG intensity is given as $I^{\text{SFG}} \propto |\langle \beta^{\text{SFG}} \cdot \mathbf{E}_{vis}^0 \cdot \mathbf{E}_{IR}^0 \rangle|^2$, where ω_{vis} is the incident visible laser frequency, and ω_{IR} is the incident IR laser frequency—the

resulting (sum) frequency is $\omega_{SFG} = \omega_{vis} + \omega_{IR}$ ^{323–326}. The resonant (and main) contribution to the second-order tensor has been given as³²⁶

$$\beta_{\alpha\beta\gamma}^{SFG} \approx - \sum_k \frac{1}{2\omega_k} \left[\frac{\partial\alpha_{\alpha\beta}}{\partial Q_k} \right] \left(\frac{\partial\mu_\gamma}{\partial Q_k} \right) \left(\frac{1}{\omega_{IR} - \omega_k + i\Gamma_k} \right), \quad (6.34)$$

where ω_k is the frequency of normal mode k , μ is the molecule’s dipole moment, and Γ_k is the inverse lifetime of vibrational mode k . SESFG refers to the enhanced SFG spectrum due to surface plasmons^{327,328}. Compared to SFG, the intensity of vibrational bands in SESFG may be enhanced between 10–10⁵ times^{327,329–334}, resulting in high signal-to-noise ratio and excellent spectral resolution. Because of this, there has been a growing number of research groups investigating SESFG and its applications^{327,329–334}.

While several experimental studies have been presented, there is a lack of theoretical treatments of SESFG. We can assume that $\beta^{SFG,tot}$ may have contributions, as in SERS, from both an EMM and CM. We start our discussion of the EMM of SESFG by presenting the dressed-tensor formalism, where the external field arising from the NP(s) is independently calculated and coupled into the molecular SFG tensor ($\beta^{SFG,M}$). This dressed-tensor formalism is given as

$$\beta_{\alpha\beta\gamma}^{SFG,tot} = [F_\delta^\alpha(\omega_{SFG}) + \delta_{\alpha\delta}] \beta_{\delta\epsilon\zeta}^{SFG,M} [F_\epsilon^\beta(\omega_{vis}) + \delta_{\beta\epsilon}] [F_\zeta^\gamma(\omega_{IR}) + \delta_{\gamma\zeta}], \quad (6.35)$$

where the field enhancement matrices \mathbf{F} have been previously described. A quick analysis of this formalism reveals the SESFG EMM enhancement factor as $|\mathbf{E}_{SFG}|^2 |\mathbf{E}_{vis}|^2 |\mathbf{E}_{IR}|^2$. This is effectively an $|\mathbf{E}|^6$ enhancement mechanism, though designing plasmonic systems with large EMM enhancements at each of these frequencies may be difficult, resulting in EMM enhancements similar to those observed in SERS ($\sim |\mathbf{E}|^4$) or SEIRA ($\sim |\mathbf{E}|^2$). This type of SERS-like enhancement of SESFG has also been recently suggested by Yeh and coworkers³³⁵.

Yeh and coworkers also proposed a second (resonance) mechanism, which may be considered to be a part of the CM of SESFG³³⁵. This proposed mechanism relies on a doubly resonant (both vibrational and electronic) condition through relaxation of the electronic states of the molecule when near a metal surface—which occurs through the dipole-dipole polarizability term in β^{SFG} . In general, one may assume that CM effects of SERS (as discussed earlier) will be relevant when discussing the CM of SESFG.

6.6 Surface-Enhanced Coherent Anti-Stokes Raman Scattering

Coherent anti-Stokes Raman scattering (CARS)^{336–338} is a four-wave mixing process. The resonant contribution to the CARS intensity may be written as³³⁸

$$\gamma_{\alpha\beta\gamma\delta}^{CARS} \approx \frac{2}{\hbar} \sum_k \left[\frac{\left(\frac{\partial\alpha_{\alpha\beta}}{\partial Q_k} \right) \left(\frac{\partial\alpha_{\gamma\delta}}{\partial Q_k} \right)}{\omega_k - (\omega_L - \omega_S) + 2i\epsilon} + \frac{\left(\frac{\partial\alpha_{\alpha\delta}}{\partial Q_k} \right) \left(\frac{\partial\alpha_{\gamma\beta}}{\partial Q_k} \right)}{\omega_k + (\omega_L - \omega_S) + 2i\epsilon} \right], \quad (6.36)$$

where ϵ is the inverse of the finite lifetime of the vibrationally excited states, and ω_k is the frequency of vibrational state k . The CARS intensity is then obtained from $I^{\text{CARS}} \propto |\gamma^{\text{CARS}}: \mathbf{E}_L^0 \mathbf{E}_S^0 \mathbf{E}_L^0|^2$. Its surface-enhanced analogue is SECARS, and because CARS is a non-linear optical process, the large enhancements afforded by surface plasmons could make SECARS a common spectroscopic tool.

There have been some amount of experimental studies on SECARS (see, for example, Refs. 228,339–344), but with very few theoretical exploration. The first work on the EMM of SECARS was by Chew and coworkers³⁴⁵, who predicted large enhancement factors (10^{12} – 10^{21}). This analysis is supported by Kneipp and coworkers³¹¹ who, through a brief analysis, showed an enhancement factor of $|\mathbf{E}_L|^4 |\mathbf{E}_S|^2 |\mathbf{E}_{AS}|^2$, where \mathbf{E}_L is the enhancement at the laser pump/probe frequency, \mathbf{E}_S is the enhancement at the Stokes frequency, and \mathbf{E}_{AS} is the enhancement at the anti-Stokes frequency. The same enhancement factor may be derived from the dressed-tensor formalism for SECARS:

$$\gamma_{\alpha\beta\gamma\delta}^{\text{CARS,tot}} = [F_\epsilon^\alpha(\omega_{AS}) + \delta_{\alpha\epsilon}] \gamma_{\epsilon\zeta\eta\iota}^{\text{CARS,M}} \left[F_\zeta^\beta(\omega_L) + \delta_{\beta\zeta} \right] [F_\eta^\gamma(\omega_S) + \delta_{\gamma\eta}] [F_\iota^\delta(\omega_L) + \delta_{\delta\iota}], \quad (6.37)$$

where $\gamma^{\text{CARS,M}}$ and $\gamma^{\text{CARS,tot}}$ are the CARS non-linear susceptibility tensors for the isolated molecule and total molecule-NP system, respectively. By modeling the NP's plasmon response as a Lorentzian, Hua and coworkers³⁴⁶ found that the local fields (due to phase differences) can interfere destructively, leading to EMM enhancement factors that are less than unity, although recent experimental work have demonstrated that single-molecule detection using SECARS is possible^{228,344}.

Even fewer studies are available on the CM of SECARS. Parkhill and coworkers³⁴⁷ simulated SECARS of pyridine using TDDFT, and found enhancement factors of 10^2 for the CM. They showed that by using the two-states model, the ORM contribution to SECARS may be approximated as $EF_{\text{model}}^{\text{SECARS}} \propto \left(\frac{\omega_x}{\omega_e}\right)^8$ ³⁴⁷, showing that the CM of SECARS might be greater than that of SERS.

Chapter 7 | Simulating Surface-Enhanced Hyper-Raman Scattering Using Atomistic Electrodynamics-Quantum Mechanical Models

Hu, Z.; Chulhai, D. V.; Jensen, L. “*Simulating Surface-Enhanced Hyper-Raman Scattering Using Atomistic Electrodynamics-Quantum Mechanical Models*” *J. Chem. Theory Comput.* **2016**, *12*, 5968.

Abstract

Surface-enhanced hyper-Raman scattering (SEHRS) is the two-photon analogue of surface-enhanced Raman scattering (SERS), which has proven to be a powerful tool to study molecular structures and surface enhancements. However, few theoretical approaches to SEHRS exist and most neglect the atomistic descriptions of the metal surface and molecular resonance effects. In this work, we present two atomistic electrodynamics-quantum mechanical models to simulate SEHRS. The first is the discrete interaction model/quantum mechanical (DIM/QM) model, which combines an atomistic electrodynamics model of the nanoparticle with a time-dependent density functional theory description of the molecule. The second model is a dressed-tensors method that describes the molecule as a point-dipole and point-quadrupole object interacting with the enhanced local field and field-gradients (FG) from the nanoparticle. In both of these models, the resonance effects are treated efficiently by means of damped quadratic response theory. Using these methods, we simulate SEHRS spectra for benzene and pyridine. Our results show that the FG effects in SEHRS play an important role in determining both the surface selection rules and the enhancements. We find that FG effects are more important in SEHRS than in SERS. We also show that the spectral features of small molecules can be accurately described by accounting for the interactions between the molecule and the local field and FG of the nanoparticle. However, at short distances between the metal and molecule, we find significant differences in the SEHRS enhancements predicted using the DIM/QM and the dressed-tensors methods.

7.1 Introduction

Hyper-Raman scattering (HRS) is a nonlinear process in which the scattered photon is shifted relative to the second harmonic of the incident radiation ($\omega_s = 2\omega_L - \omega_k$, where ω_k is the vibrational frequency).^{14,19} Due to different selection rules, HRS can probe Raman inactive modes and excited states that are one-photon forbidden,^{18,137,348} and hence complements the information provided by Raman scattering. However, widespread use of this technique has been impeded by its extremely low cross sections, which are orders of magnitude smaller than its Raman counterparts.²⁶ To provide sufficient signal-to-noise for identifying molecular signatures, one routine strategy is to adsorb the target molecule on a metal nanoparticle surface.³⁴⁹ The enhanced HRS due to surface plasmons is termed surface-enhanced HRS (SEHRS).^{27,28,30,76,123,132,309}

SEHRS was first detected about 30 years ago^{27,28}, and since then a large number of experimental SEHRS studies have been reported highlighting its applications in bioscience,^{130,350} as well as the detection ability at the single molecule level.^{125,135} Furthermore, SEHRS can provide detailed information about two-photon properties, which is of relevance for understanding dye-molecules used in two-photon imaging techniques.^{137,138} SEHRS is an extremely sensitive probe of surface adsorbate structure due to a combination of large local field enhancements arising from surface plasmon excitations and potential large chemical enhancements.²⁸ The local field enhancements in SEHRS are expected to scale roughly as $|E(2\omega_s)|^2|E(\omega_L)|^4$.^{28,125,351} This is to be contrasted with the well established local field enhancements of $|E(\omega_s)|^2|E(\omega_L)|^2$ for surface-enhanced Raman scattering (SERS), where ω_L is the frequency of the incident light and ω_s the scattered frequency. Estimates for the enhancement in SEHRS have ranged from 10^{13} - 10^{20} .^{28,125} Early experiments on SEHRS have suggested that the chemical effects might be larger than that found in SERS.²⁸

Compared to the large amount of work focused on understanding and modeling SERS, only a handful of studies have been devoted to modeling SEHRS. A recent theoretical study has suggested larger chemical enhancement factors for SEHRS of 10^2 - 10^4 versus 10^1 - 10^2 for SERS.³¹² This was based on a simple two-states model that predicts that the SEHRS chemical enhancement scales as $(\omega_X/\omega_e)^6$, where ω_X is the HOMO-LUMO excitation energy of the free molecule and ω_e is the lowest charge-transfer (CT) excitation energy of the metal-molecule complex.³¹² Using the same two-states model, a scaling of $(\omega_X/\omega_e)^4$ was found for SERS.²⁸⁶ To understand the combined effect of the plasmon local field and the chemical effects, Mullin and co-worker³¹⁰ developed a hybrid model consisting of a time-dependent density functional theory (TDDFT) description of the molecule (and part of the metal) with a Mie theory description of the metal nanoparticle. Their work showed the need to include both the chemical and plasmonic near field effects to obtain simulated SEHRS spectra of pyridine that are in good agreement with experimental data. Electrodynamics simulations have been performed to understand structural optimization of the plasmonic nanostructures for SEHRS, including exploiting different selection rules to minimize the background second-harmonic generation signal from the nanostructure relative to the molecular signal.³⁵² The electrodynamic theory of SEHRS has also been extended beyond the dipole approximation to include dipole-quadrupole effect.³⁵³ However, so far the

methods developed have been restricted to continuum electrodynamics models for the metal nanoparticles and molecular response that is far from resonance.

In this work, we present two methods for simulating SEHRS that allow for resonance enhancements and an atomistic description of the metal nanoparticle. The first one is the discrete interaction model/quantum mechanical (DIM/QM) method.^{134,229,248,267,268,354,355} In the DIM/QM method, the nanoparticle is considered as a collection of interacting atoms, i.e., being represented atomistically, and thus the modeling of the influence of the local environment of a nanoparticle surface on the optical properties of a molecule is enabled. This model has previously been used to describe SERS,²⁷⁰ surface-enhanced Raman optical activity (SEROA),²⁴⁸ and plasmonic circular dichroism.³⁰⁷ Here this model is combined with a damped quadratic response formalism¹⁴⁰ that previously used for modeling resonance hyper-Raman effects.³⁵⁶ The second method is an extension of the dressed-tensors formalism^{248,269,270,351} to describe SEHRS. In the dressed-tensor method, the nanoparticle is treated using an atomistic electrodynamics model and the molecule is described as a point-dipole and point-quadrupole object that is interacting with the near-field and near-field-gradients (FG) arising from the nanoparticle. This method has previously been used to describe FG in SERS^{270,357} and SEROA.²⁴⁸

In the following, we will present the theory for both the DIM/QM and the dressed-tensors methods. Simulations of SEHRS of benzene using these two methods will be used to examine the role of the image field, the local field, and the FG. Distance effect of the SEHRS enhancement will be studied using pyridine as a probe molecule. Finally, we will discuss the importance of the FG effects in SEHRS.

7.2 Theory

7.2.1 The DIM/QM Method

In the DIM/QM method, one solves the time-dependent Kohn-Sham (TDKS) equations for a molecule placed near a metal nanoparticle. The effective TDKS equation for such a hybrid system can be written as^{134,229,267,268}

$$i \frac{\partial}{\partial t} \phi_i(\mathbf{r}, t) = h_{\text{KS}}[\rho(\mathbf{r}, t)] \phi_i(\mathbf{r}, t), \quad (7.1)$$

where $\rho(\mathbf{r}, t) = \sum_{i=1}^{\text{occ}} n_i |\phi_i(\mathbf{r}, t)|^2$ is the time-dependent density based on the occupation number n_i of the i th time-dependent orbital ϕ_i , and $h_{\text{KS}}[\rho(\mathbf{r}, t)]$ is referred to as the effective time-dependent Kohn-Sham operator,

$$h_{\text{KS}}[\rho(\mathbf{r}, t)] = -\frac{1}{2} \nabla^2 - \sum_I \frac{Z_I}{|\mathbf{r} - \mathbf{R}_I|} + \int \frac{\rho(\mathbf{r}, t)}{|\mathbf{r} - \mathbf{r}'|} d\mathbf{r}' + \frac{\delta E^{XC}}{\delta \rho(\mathbf{r}, t)} + \hat{V}^{\text{DIM}}(\mathbf{r}, t) + \hat{V}^{\text{pert}}(\mathbf{r}, t), \quad (7.2)$$

with the individual terms being the kinetic energy, the nuclear potential, the Coulomb potential, the exchange correlation (XC) potential, the embedding operator $\hat{V}^{\text{DIM}}(\mathbf{r}, t)$ that describes the molecule-metal interactions, and the external perturbation operator.

Considering the properties of interest are frequency-dependent, for convenience we will write all following equations in the frequency domain, where the subscripts α, β denote Cartesian coordinates, indices i, j denote QM electrons, m, n denote DIM atoms, I, J denote QM nuclei, and the Einstein summation convention is employed for Greek indices. The embedding and external operators are then given as^{134,229,267,268}

$$\hat{V}^{\text{DIM}}(\mathbf{r}, \omega) = \sum_j \hat{V}^{\text{pol}}(r_j, \omega) \quad (7.3)$$

and

$$\hat{V}^{\text{pert}}(\mathbf{r}, \omega) = \sum_j \hat{V}^{\text{ext}}(r_j, \omega) + \sum_j \hat{V}^{\text{loc}}(r_j, \omega), \quad (7.4)$$

respectively, in which the applied external potential $\hat{V}^{\text{ext}}(r_j, \omega)$ is routinely adopted for a regular isolated QM system while the polarization operator $\hat{V}^{\text{pol}}(r_j, \omega)$ and the local field operator $\hat{V}^{\text{loc}}(r_j, \omega)$ are uniquely included for the DIM/QM system. Both the polarization and local field operators can be further expressed in terms of the first-order real interaction tensors $T_{jm,\alpha}^{(1)}$, i.e.,^{134,229,267,268}

$$\hat{V}^{\text{pol}}(r_j, \omega) = \sum_m \mu_{m,\alpha}^{\text{ind}}(\omega) T_{jm,\alpha}^{(1)} \quad (7.5)$$

and

$$\hat{V}^{\text{loc}}(r_j, \omega) = \sum_m \mu_{m,\alpha}^{\text{ext}}(\omega) T_{jm,\alpha}^{(1)}, \quad (7.6)$$

where $T_{jm,\alpha}^{(1)}$ is damped at short distances to avoid over polarization. The $\mu_{m,\alpha}^{\text{ind}}(\omega)$ and $\mu_{m,\alpha}^{\text{ext}}(\omega)$ represent the frequency-dependent dipoles of the DIM subsystem as induced by the QM system and the external field, respectively, and it has been previously shown that they can be obtained by solving a set of linear equations.^{134,229,267,268}

We note in DIM/QM the density perturbation due to the $\hat{V}^{\text{pol}}(r_j, \omega)$ (hence $\hat{V}^{\text{DIM}}(r, \omega)$) operator is termed the image field, which provides a more realistic description of the molecule-nanoparticle interactions; whereas that due to the $\hat{V}^{\text{loc}}(r_j, \omega)$ operator is termed the local field, which accounts for the enhanced near field from the nanoparticle.

The frequency-dependent first hyperpolarizability β for the DIM/QM system can be expressed within a quadratic response formalism by utilizing the $2n + 1$ rule as³⁵⁴

$$\begin{aligned} \beta_{\alpha\beta\gamma}(-\omega_\sigma; \omega_1, \omega_2) = & \\ & \text{Tr}[n\{U^\alpha(-\omega_\sigma)G^\beta(\omega_1)U^\gamma(\omega_2) + U^\gamma(\omega_2)G^\beta(\omega_1)U^\alpha(-\omega_\sigma) \\ & + U^\beta(\omega_1)G^\gamma(\omega_2)U^\alpha(-\omega_\sigma) + U^\alpha(-\omega_\sigma)G^\gamma(\omega_2)U^\beta(\omega_1) \\ & + U^\gamma(\omega_2)G^\alpha(-\omega_\sigma)U^\beta(\omega_1) + U^\beta(\omega_1)G^\alpha(-\omega_\sigma)U^\gamma(\omega_2)\}] - \\ & \text{Tr}[n\{U^\alpha(-\omega_\sigma)U^\gamma(\omega_2)G^\beta(\omega_1) + U^\gamma(\omega_2)U^\alpha(-\omega_\sigma)G^\beta(\omega_1) \\ & + U^\beta(\omega_1)U^\alpha(-\omega_\sigma)G^\gamma(\omega_2) + U^\alpha(-\omega_\sigma)U^\beta(\omega_1)G^\gamma(\omega_2) \\ & + U^\gamma(\omega_2)U^\beta(\omega_1)G^\alpha(-\omega_\sigma) + U^\beta(\omega_1)U^\gamma(\omega_2)G^\alpha(-\omega_\sigma)\}] + \\ & \text{Tr}[g_{xc}(\mathbf{r}, \mathbf{r}', \mathbf{r}'', \omega_1, \omega_2)D^\alpha(-\omega_\sigma)D^\beta(\omega_1)D^\gamma(\omega_2)], \end{aligned} \quad (7.7)$$

where ω_1 and ω_2 denote the incident frequencies, ω_σ represents the sum of the incident frequencies, and “Tr” stands for the trace. Accounting for the zero diagonal block of the first-order transformation matrix U as previously discussed,²¹¹ this β expression shares the same form as what used for a regular isolated QM system.^{79,140} However, it is important to note that all matrices in it are now additionally contributed by both the local field operator and the DIM operator. For instance, the DIM/QM first-order KS matrix in the molecular orbital (MO) basis reads³⁵⁴

$$G_{ia}^\alpha(\omega) = \langle i | [\hat{V}_\alpha^{\text{ext}}(\mathbf{r}, \omega) + \hat{V}_\alpha^{\text{loc}}(\mathbf{r}, \omega) + \hat{V}^{\text{Coul}} + \hat{V}_{\text{xc}}(r) + \hat{V}_\alpha^{\text{DIM}}] | a \rangle, \quad (7.8)$$

where $\hat{V}_\alpha^{\text{loc}}(\mathbf{r}, \omega)$ and $\hat{V}_\alpha^{\text{DIM}}$ are the extra components. To be more precise, the local field operator is included in the dipole moment matrix H^α as³⁵⁴

$$H_{st}^\alpha = \langle \chi_s | \hat{\mu}_\alpha + \hat{V}_\alpha^{\text{loc}} | \chi_t \rangle. \quad (7.9)$$

The DIM/QM transformation matrix U is consequently dependent on both the local field and DIM operators as it can be related to the G matrix as^{140,211}

$$U_{ia}^\alpha(\pm\omega) = \frac{G_{ia}^\alpha(\pm\omega)}{\varepsilon_a^0 - \varepsilon_i^0 \mp (\omega + i\Gamma)}, \quad (7.10)$$

where only the elements from the occupied-virtual block of U are shown, Γ corresponds to a phenomenological energy broadening term for the excited state, and $\varepsilon_a^0, \varepsilon_i^0$ represent the KS one-electron energies of the virtual and occupied orbitals, respectively. Since the first-order density matrix D is given in terms of the U matrix as^{140,211}

$$D^\alpha(\pm\omega) = [C^0 U^\alpha(\pm\omega)] n C^{0\dagger} + C^0 n [C^0 U^\alpha(\mp\omega)]^\dagger, \quad (7.11)$$

where n is the occupation number matrix and C^0 is the unperturbed MO coefficients, both the local field operator and the DIM operator also have effects on it. All U , G and D matrices for the DIM/QM system can be obtained by solving the linear response equations as described previously,^{229,267,268} and the only term that requires additional calculation is the second-order xc kernel, $g_{xc}(\mathbf{r}, \mathbf{r}', \mathbf{r}'', \omega_1, \omega_2)$. By adopting the adiabatic local density approximation (ALDA)⁸¹, it can be calculated as^{79,140}

$$\begin{aligned} \text{Tr}[g_{xc}(\mathbf{r}, \mathbf{r}', \mathbf{r}'', \omega_1, \omega_2) D^\alpha(-\omega_\sigma) D^\beta(\omega_1) D^\gamma(\omega_2)] = \\ \int d^3\mathbf{r} g_{xc}^{\text{ALDA}}(\mathbf{r}, 0, 0) \rho^\alpha(\mathbf{r}, -\omega_\sigma) \rho^\beta(\mathbf{r}, \omega_1) \rho^\gamma(\mathbf{r}, \omega_2), \end{aligned} \quad (7.12)$$

where ρ^α, ρ^β , and ρ^γ are the perturbed densities that are also available from solving the linear response equations for the DIM/QM system.^{229,267,268}

7.2.2 The Dressed-Tensors Formalism

In the dressed-tensors formalism, the molecular response properties are evaluated in the presence of an inhomogeneous local field generated by a metal nanoparticle.^{269,270,351} The molecule is

described in terms of its dipolar and quadrupolar response properties and interacts with the metal nanoparticle through its near field E_{α}^{loc} and its near FG $E_{\alpha\beta}^{\text{loc}}$ arising from the plasmon excitation.^{270,351} The dressed first-hyperpolarizability β derivative with respect to normal mode Q_p can be written as

$$\begin{aligned}
\frac{\partial \beta_{\alpha\beta\gamma}^{\text{tot}}(-2\omega; \omega, \omega)}{\partial Q_p} = & \left[\delta_{\alpha\delta} + F_{\delta}^{\text{loc},\alpha}(2\omega) \right] \frac{\partial \beta_{\delta,\epsilon,\zeta}^{\mu\mu\mu}(-2\omega; \omega, \omega)}{\partial Q_p} \left[\delta_{\beta\epsilon} + F_{\epsilon}^{\text{loc},\beta}(\omega) \right] \left[\delta_{\gamma\zeta} + F_{\zeta}^{\text{loc},\gamma}(\omega) \right] \\
& + \frac{1}{3} \left[\delta_{\alpha\delta} + F_{\delta}^{\text{loc},\alpha}(2\omega) \right] \frac{\partial \beta_{\delta,\epsilon,\zeta\eta}^{\mu\mu\theta}(-2\omega; \omega, \omega)}{\partial Q_p} \left[\delta_{\beta\epsilon} + F_{\epsilon}^{\text{loc},\beta}(\omega) \right] F_{\zeta\eta}^{\text{loc},\gamma}(\omega) \\
& + \frac{1}{3} \left[\delta_{\alpha\delta} + F_{\delta}^{\text{loc},\alpha}(2\omega) \right] \frac{\partial \beta_{\delta,\epsilon\eta,\zeta}^{\mu\theta\mu}(-2\omega; \omega, \omega)}{\partial Q_p} F_{\epsilon\eta}^{\text{loc},\beta}(\omega) \left[\delta_{\gamma\zeta} + F_{\zeta}^{\text{loc},\gamma}(\omega) \right] \\
& + \frac{1}{3} F_{\delta\eta}^{\text{loc},\alpha}(2\omega) \frac{\partial \beta_{\delta\eta,\epsilon,\zeta}^{\theta\mu\mu}(-2\omega; \omega, \omega)}{\partial Q_p} \left[\delta_{\beta\epsilon} + F_{\epsilon}^{\text{loc},\beta}(\omega) \right] \left[\delta_{\gamma\zeta} + F_{\zeta}^{\text{loc},\gamma}(\omega) \right] \\
& + \frac{1}{9} \left[\delta_{\alpha\delta} + F_{\delta}^{\text{loc},\alpha}(2\omega) \right] \frac{\partial \beta_{\delta,\epsilon\eta,\zeta\kappa}^{\mu\theta\theta}(-2\omega; \omega, \omega)}{\partial Q_p} F_{\epsilon\eta}^{\text{loc},\beta}(\omega) F_{\zeta\kappa}^{\text{loc},\gamma}(\omega) \\
& + \frac{1}{9} F_{\delta\eta}^{\text{loc},\alpha}(2\omega) \frac{\partial \beta_{\delta\eta,\epsilon,\zeta\kappa}^{\theta\mu\theta}(-2\omega; \omega, \omega)}{\partial Q_p} \left[\delta_{\beta\epsilon} + F_{\epsilon}^{\text{loc},\beta}(\omega) \right] F_{\zeta\kappa}^{\text{loc},\gamma}(\omega) \\
& + \frac{1}{9} F_{\delta\eta}^{\text{loc},\alpha}(2\omega) \frac{\partial \beta_{\delta\eta,\epsilon\kappa,\zeta}^{\theta\theta\mu}(-2\omega; \omega, \omega)}{\partial Q_p} F_{\epsilon\kappa}^{\text{loc},\beta}(\omega) \left[\delta_{\gamma\zeta} + F_{\zeta}^{\text{loc},\gamma}(\omega) \right] \\
& + \frac{1}{27} F_{\delta\eta}^{\text{loc},\alpha}(2\omega) \frac{\partial \beta_{\delta\eta,\epsilon\kappa,\zeta\lambda}^{\theta\theta\theta}(-2\omega; \omega, \omega)}{\partial Q_p} F_{\epsilon\kappa}^{\text{loc},\beta}(\omega) F_{\zeta\lambda}^{\text{loc},\gamma}(\omega),
\end{aligned} \tag{7.13}$$

where $\delta_{\alpha\beta}$ is the Kronecker delta function, and $F_{\beta(\gamma)}^{\text{loc},\alpha}$ describes the local field (gradient) enhancement in the β (γ) direction resulting from polarization in the α direction. The molecular properties in terms of the second-order response properties are the dipole-dipole-dipole hyperpolarizability ($\beta^{\mu\mu\mu}$), the dipole-quadrupole-dipole hyperpolarizability ($\beta^{\mu\theta\mu}$), the quadrupole-dipole-dipole hyperpolarizability ($\beta^{\theta\mu\mu}$), the dipole-quadrupole-quadrupole hyperpolarizability ($\beta^{\mu\theta\theta}$), the quadrupole-dipole-quadrupole hyperpolarizability ($\beta^{\theta\mu\theta}$), the quadrupole-quadrupole-dipole hyperpolarizability ($\beta^{\theta\theta\mu}$), and the quadrupole-quadrupole-quadrupole hyperpolarizability ($\beta^{\theta\theta\theta}$), where the subscripts of them indicate the relevant Cartesian directions of the operators. These quadrupole-level hyperpolarizability tensors can all be obtained from the $2n + 1$ expression, and thus can be obtained by solving the linear response equations using the quadrupole operator in Eq. (7.9).

7.3 Computational Details

All calculations in this work were carried out using a locally modified version of the Amsterdam Density Functional (ADF) program package.^{63,64,141} Geometry optimization, as well as the vibrational frequencies and normal modes, was performed using the Becke-Perdew(BP86)^{87,88} XC potential with a triple- ζ polarized slater type (TZP) basis set from the ADF library. Unless otherwise stated, both dipole- and quadrupole-level response properties were calculated using the

statistical average of orbital model exchange-correlation potentials (SAOP)⁸⁹ with the TZP basis set. The SAOP potential was chosen since it has previously been shown to provide reasonably accurate hyperpolarizabilities for small molecules, see, e.g., Refs. 89, 90. The excited state lifetime is included phenomenologically using a damping parameter $\Gamma = 0.1$ eV, which was previously found to be acceptable.^{5,57}

Nanoparticles in this work were simulated using the discrete interaction model (DIM)^{265,266,358}, which treats the nanoparticle atomistically using classical electrodynamics. Silver (FCC) unit cells were used to build the icosahedral structures, and the frequency-dependent complex dielectric function of silver was obtained from Johnson and Christy.³⁵⁹ In the following we neglect quantum size effects that are important for nanoparticles with dimensions below 5 nm. These quantum size effects lead to a small blue shift of the plasmon excitation when the size decreases and a broadening of the peak. This effect could be included using coordination DIM,³⁵⁸ but it is not done in this work. Furthermore, retardation effects and solvent effects are not included in the simulations. For both the DIM/QM and the dressed-tensors approaches, the polarizability interaction model (PIM) was used, which describes the system as a collection of interacting polarizabilities.

The calculation of the differential cross sections for SEHRS adopts the same form as that used for HRS, which is given as¹⁹

$$\frac{d\sigma}{d\Omega} = \frac{16\pi^2 h^3 \alpha^3 \nu_s^4 P_i}{N c^2 e^6} \langle \beta'_{\alpha\beta\gamma} \rangle^2, \quad (7.14)$$

where α is the fine structure constant, ν_s is the frequency of the scattered radiation, P_i is the population of the initial vibrational state, N is the number of scatters per unit volume, h is Planck's constant, and c is the speed of light. The bracket indicates averaging over all orientations of the molecule with respect to the incident light, and the β -level expression for it can be found in Ref. 96. $\beta'_{\alpha\beta\gamma}$ is the transition DIM/QM (Dressed) hyperpolarizability, which is given as the partial derivative of the DIM/QM (Dressed) hyperpolarizability with respect to the normal mode Q_p ^{96,97}

$$\beta'_{\alpha\beta\gamma} = \sqrt{\frac{h}{8\pi^2 c \nu_p}} \frac{\partial \beta_{\alpha\beta\gamma}}{\partial Q_p}, \quad (7.15)$$

where ν_p is the vibrational frequency of the p th normal mode, and the derivatives were calculated by numerical three-point differentiation with respect to Cartesian displacements. All simulated spectra have been broadened by a Lorentzian with a full-width at half-maximum (fwhm) of 20 cm^{-1} .

7.4 Results and Discussion

7.4.1 SEHRS of Benzene

To test the implementations for both the DIM/QM and the dressed-tensors methods, we chose to study SEHRS of benzene on an Ag_{2057} icosahedral nanoparticle as a model system. This model system has previously been used to study the FG effects in the DIM/QM method for calculating SERS.²⁷⁰ The relative orientation for the two sub-systems is shown in Figure 7.1, where the

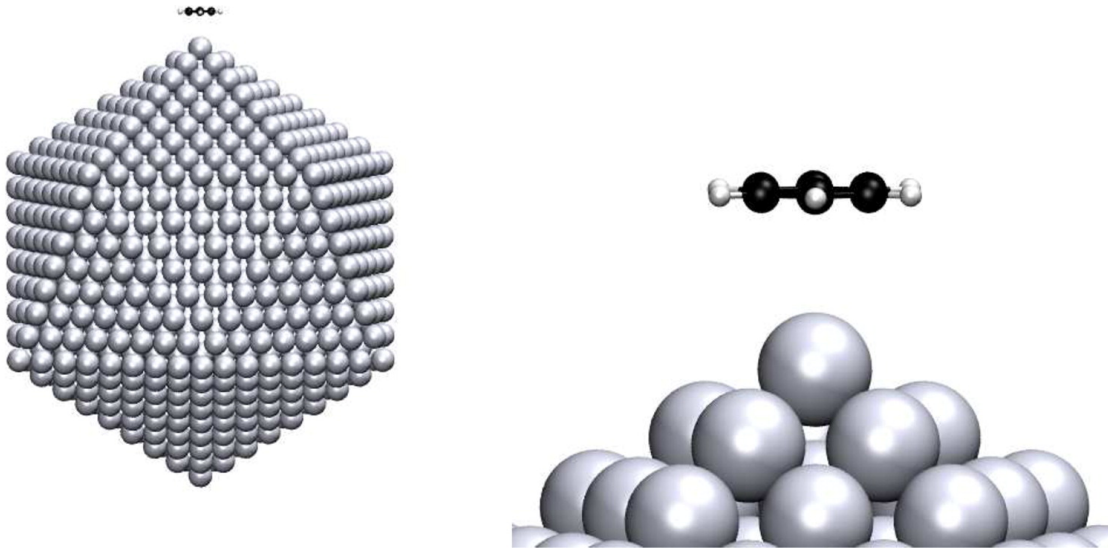


Figure 7.1. Orientation of benzene on an Ag_{2057} icosahedral nanoparticle. The distance between the center-of-mass of benzene and the nearest silver atom is 4.0 Å. The Ag_{2057} nanoparticle is 4.6 nm in diameter.

benzene molecule is placed flat on the metal nanoparticle with its center-of-mass (COM) set 4.0 Å away from the nearest silver atom.

In Figure 7.2(a) we plot the simulated normal HRS (NHRS) spectrum of benzene, which was obtained based on the static β tensors and assuming a laser frequency at 1064 nm for the cross section calculation. The SEHRS spectrum of benzene on the Ag_{2057} nanoparticle calculated using DIM/QM is shown in Figure 7.2(b) and the corresponding SEHRS spectrum calculated using the dressed-tensors method is shown in Figure 7.2(c). Both of the SEHRS spectra are calculated assuming an incident laser frequency of 343 nm, which corresponds to the plasmon excitation of the Ag_{2057} nanoparticle. The fields and FG needed in the dressed-tensors method have been calculated using the same nanoparticle adapted in the DIM/QM simulations, and thus enables a direct comparison between the two methods.

Comparing the SEHRS spectra with the NHRS spectrum, we see that they are very different. In comparison to the NHRS spectrum, we find all modes with the symmetry type a_{1g} (986 cm^{-1}), e_{1g} (837 cm^{-1}), or e_{2g} (604 , 1160 , and 1583 cm^{-1}) become observable in the SEHRS spectra, whereas the b_{1u} (1140 , and 1326 cm^{-1}) or b_{2u} (997 cm^{-1}) type modes are extremely weak. This can be related to the FG surface selection rules, which has been previously considered for SERS^{280,281} and will be discussed below. To aid the discussion, we also provide the graphic representations for some relevant normal modes in Figure 7.3. Among the SEHRS active modes, the “ring breathing” mode at 986 cm^{-1} exhibits the strongest signal, which is also found to be the most intense one for the experimental SERS spectrum of benzene.²⁸⁰ However, the ordering of mode relative intensities in SEHRS differs from that in SERS. More importantly, unlike the “ring breathing” mode that is strongly SERS- and SEHRS-active, we find the mode corresponding to the “C-C stretch” motion at 1326 cm^{-1} (b_{1u}) is strong in SERS but weak in SEHRS, in contrast,

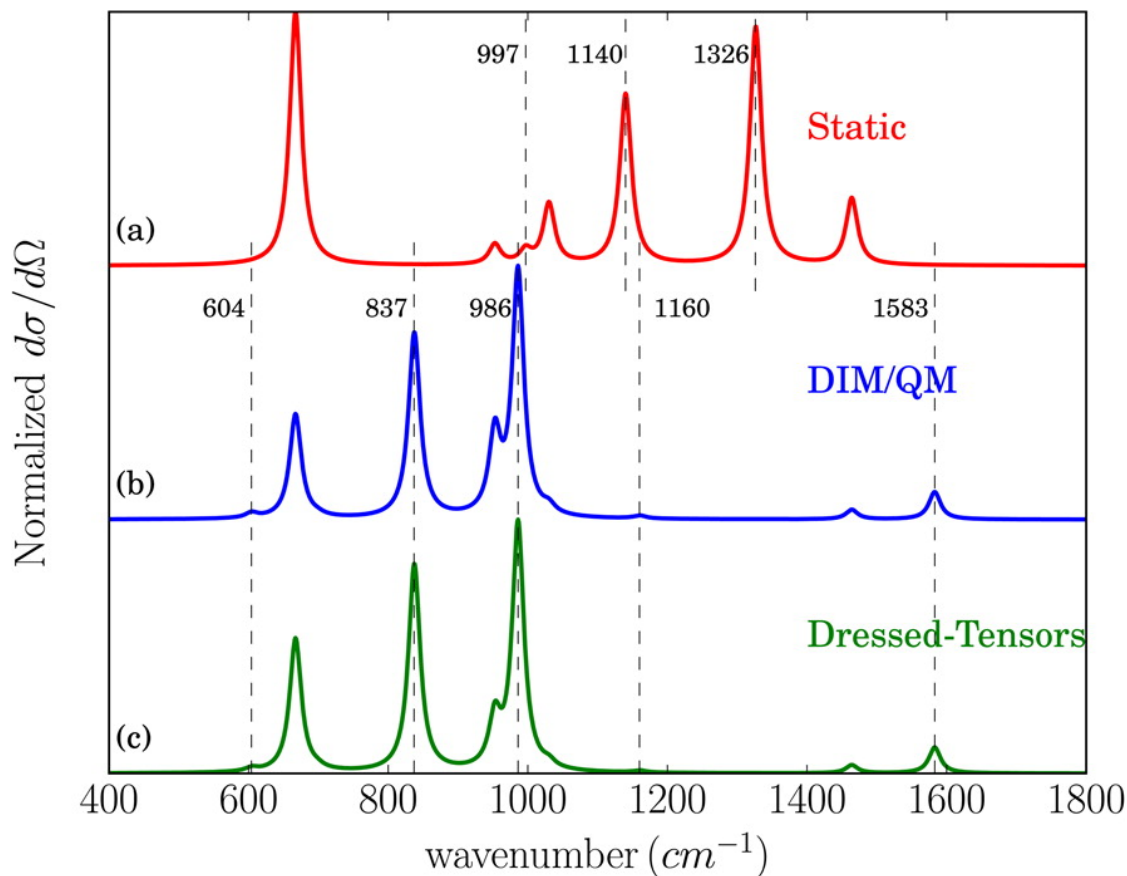


Figure 7.2. (a) Simulated normal HRS (NHRS) spectrum of an isolated benzene molecule. SEHRS spectra of benzene sitting flat on the vertex of an Ag_{2057} icosahedron simulated using (b) DIM/QM, and (c) the dressed-tensors method. An incident wavelength of 343 nm was used in the simulations. All spectra have been normalized with respect to their individual maximum cross section given in $\text{cm}^4 \cdot \text{s} \cdot \text{photon}^{-1} \cdot \text{sr}^{-1}$, i.e., Static: 2.4×10^{-65} ; DIM/QM: 560×10^{-60} ; Dressed-Tensors: 980×10^{-60} .

the degenerate mode that involves “ring torsion” at 953 cm^{-1} (e_{2u}) is SEHRS-active but weakly SERS-active.

The SEHRS spectra predicted using the dressed-tensors and the DIM/QM methods are nearly identical. Since the molecular geometry is identical, the only difference in these two models is how they describe the interactions with the plasmonic near field and the inclusion of the image field effects in DIM/QM. The good agreement on the strongly/weakly SEHRS-active modes shows that the interactions with the plasmonic near-field is described consistently in these two methods. However, as discussed previously,²⁴⁸ such good agreement between these two methods can only be expected for small molecules where the field-expansions used in the dressed-tensors method converge quickly. The absolute intensities predicted by the two methods are also very similar, although the dressed-tensors method predicts larger intensities.

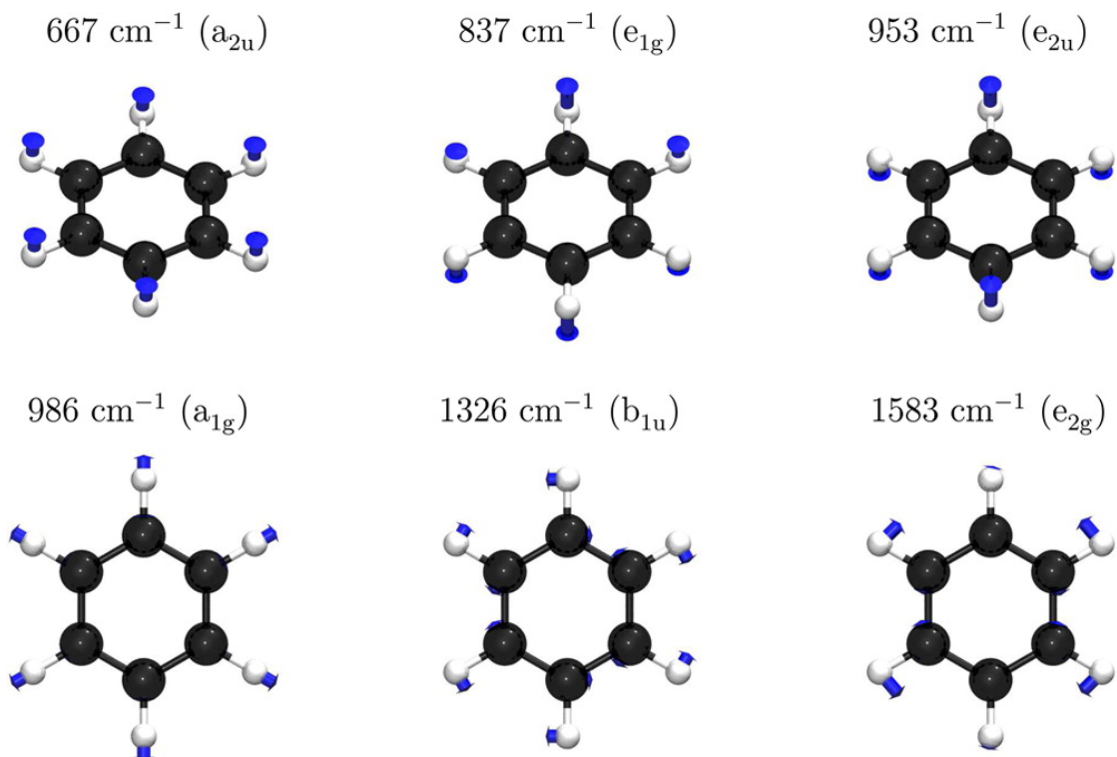


Figure 7.3. Specific normal modes of benzene.

7.4.2 Importance of Molecular Resonance, Image and Local Fields Effects

In the DIM/QM model, there are two distinct interactions between the molecule and the nanoparticle. The first is the image field, which accounts for the interactions between the charge distribution of the molecule and the nanoparticle in the absence of the external field perturbing the nanoparticle. The second is the local field, which arises from the excitations of the nanoparticle due to the external field. In addition to these, the HRS can also be enhanced by molecular resonance effects. In this section, we will consider the importance of each.

The plasmon resonance for the Ag_{2057} nanoparticle is found at 343 nm, which is close to being two-photon resonant (356 nm) with the degenerate ${}^1E_{1u}$ excited states of benzene at 178 nm. We note that this calculated excitation energy for benzene is in good agreement with the best theoretical estimate from high-level *ab initio* simulations reported by Silva-Junior *et al.*³⁶⁰ as well as the gas-phase experimental result.³⁶¹ Therefore, at this incident wavelength, the HRS of benzene is resonantly enhanced. This is illustrated in Figure 7.4(a), where we plot the resonance HRS (RHRS) of benzene at 343 nm. We see that the RHRS spectrum is dominated by the mode at 953 cm^{-1} (e_{2u}), which is only weakly present in the NHRS spectrum (Figure 7.2(a)). In Figure 7.4(b) we plot the SEHRS spectrum of benzene, where only the image field effects are included. We see that this spectrum is very similar to the RHRS spectrum as expected, since the image field effects only lead to a minor perturbation of the electronic structure of benzene. This small effect of the image field is consistent with the similar DIM/QM and dressed-tensors

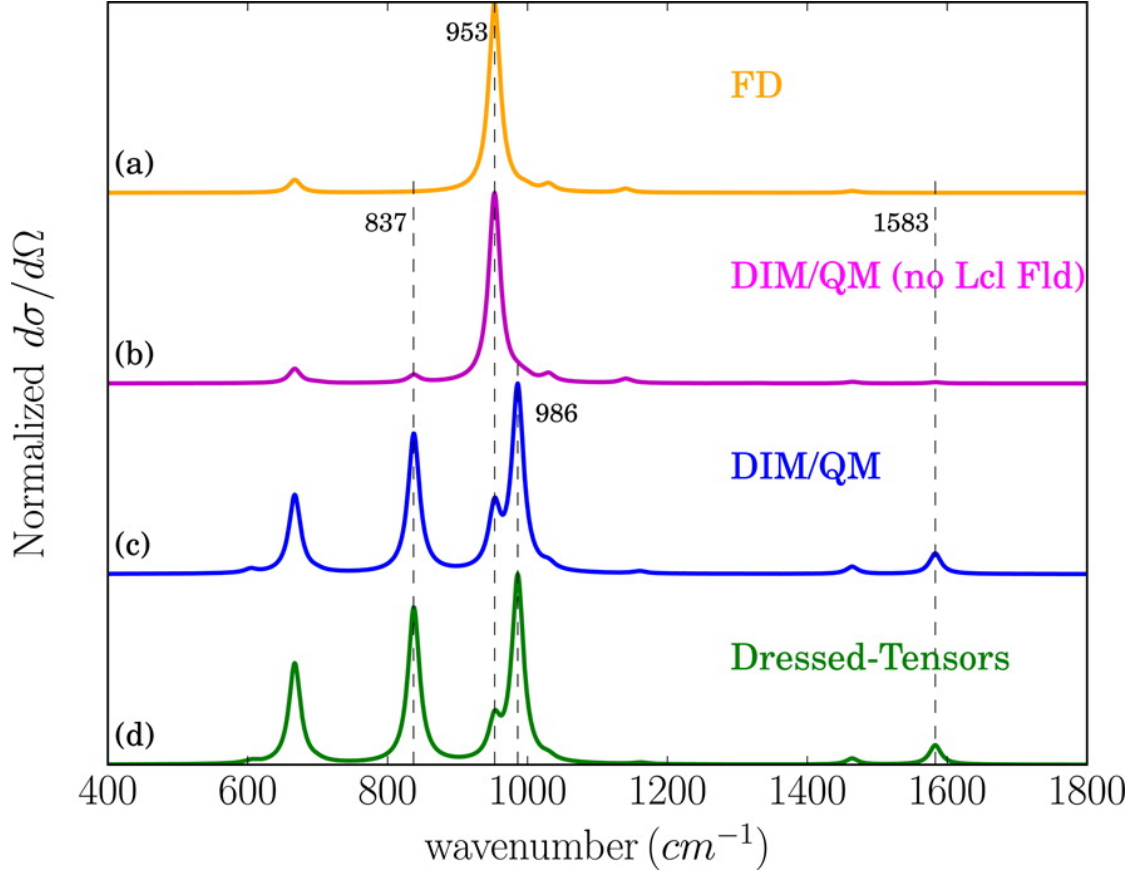


Figure 7.4. (a) Simulated RHRs spectrum of an isolated benzene molecule. SEHRS spectra of benzene sitting flat on the vertex of an Ag_{2057} icosahedron simulated using (b) DIM/QM without local fields, (c) DIM/QM with local fields, and (d) the dressed-tensors method with local fields. An incident wavelength of 343 nm was used in the simulations. All spectra have been normalized with respect to their individual maximum cross section given in $\text{cm}^4 \cdot \text{s} \cdot \text{photon}^{-1} \cdot \text{sr}^{-1}$, i.e., FD: 14.5×10^{-60} ; DIM/QM no local field: 13.7×10^{-60} ; DIM/QM: 560×10^{-60} ; Dressed-Tensors: 980×10^{-60} .

spectra shown in Figure 7.2. However, the image field does lead to a small symmetry breaking, which gives rise to weak modes at 837 (e_{1g}) and 1583 cm^{-1} (e_{2g}). When the local field effects are included in the DIM/QM SEHRS spectrum of benzene, we find that the modes at 667 (a_{2u}), 837 (e_{1g}), 986 (a_{1g}) cm^{-1} get preferentially enhanced; see Figure 7.4(c). These modes couple strongly to the plasmonic near fields, and become stronger than the mode that is strongly enhanced by molecular resonance at 953 cm^{-1} (e_{2u}).

The resonance enhancement of benzene is about 5 orders of magnitude for the mode at 953 cm^{-1} (e_{2u}). The DIM/QM spectrum calculated only including the image field effects give slightly smaller intensities than the RHRs spectrum. This is not very surprising since the image field itself does not lead to large local fields as the plasmon resonance is not excited by the external field, however, the cause of the intensity weakening in the SEHRS spectrum is not obvious. One possible explanation is that the molecule-metal interactions cause a slight shift of the excitation energy of benzene, which makes the two-photon resonance effect less pronounced at the given

incident frequency. The inclusion of the local field leads to a further 40-fold enhancement of RHRS spectrum. Thus, most of the enhancement arises from the resonant effect rather than the plasmon. This is because of the small size of the nanoparticle and the orientation of the benzene relative to the nanoparticle that does not facilitate a strong coupling with the plasmonic near-field. The calculated intensities using the dressed-tensors method are found to be about 1.5 times larger than those obtained using DIM/QM as shown in Figure 7.4(d). The larger intensities predicted by the dressed-tensors method are likely the results of less effective screening of the plasmonic near field as compared to DIM/QM. However, one cannot rule out the possibility that higher-order terms, such as octupoles in the expansion of the interactions between the molecule and the nanoparticle, could be non-negligible and lead to a reduction of the intensity.

7.4.3 The Field-Gradient Effects

An advantage of the dressed-tensors method is that the contribution from the plasmon near field and the FG can be easily separated and analyzed. This was previously done for SERS²⁷⁰ and here we will present a similar analysis for SEHRS. In Figure 7.5 we plot the total SEHRS spectrum of benzene and its decomposition into individual contributions. The contribution from the $|\beta^{\mu\mu\mu}|^2$ term that depends only on the local field is shown in Figure 7.5(a). Terms describing interactions with two local fields and one FG, i.e., $|\beta^{\mu\mu\theta}|^2 + |\beta^{\mu\theta\mu}|^2 + |\beta^{\theta\mu\mu}|^2$, are shown in Figure 7.5(b). Contributions arising from one local field and two FG interactions, $|\beta^{\mu\theta\theta}|^2 + |\beta^{\theta\mu\theta}|^2 + |\beta^{\theta\theta\mu}|^2$, with the nanoparticle are shown in Figure 7.5(c). Finally, the pure FG term, $|\beta^{\theta\theta\theta}|^2$, is shown in Figure 7.5(d).

As expected, when dressed with an homogeneous field only, modes that are already active in either the NHRS or the RHRS spectra, such as the ones at 667 (a_{2u}), 953 (e_{2u}), 1030 (e_{1u}), and 1464 (e_{1u}) cm^{-1} , are observed. The mode at 667 cm^{-1} (a_{2u}) is preferentially enhanced by the homogeneous field as this mode corresponds to motion that is parallel with the field; see Figure 7.3. For modes that have a symmetric out-of-plane motion, such as the one at 953 cm^{-1} shown in Figure 7.3, the homogeneous field also dominates the enhancement. On the other hand, the FG effects activate the NHRS-forbidden modes at 604 (e_{2g}), 837 (e_{1g}), 986 (a_{1g}), 1160 (e_{2g}) and 1583 (e_{2g}) cm^{-1} . These modes either possess an asymmetric out-of-plane motion or an in-plane motion, see depictions for three of them in Figure 7.3, and are enhanced by the couplings with both the local field and the FG through the $|\beta^{\mu\mu\theta}|^2 + |\beta^{\mu\theta\mu}|^2 + |\beta^{\theta\mu\mu}|^2$ terms. Contributions from $|\beta^{\mu\theta\theta}|^2 + |\beta^{\theta\mu\theta}|^2 + |\beta^{\theta\theta\mu}|^2$ terms enhance the mode at 667 cm^{-1} (a_{2u}) although to a smaller degree than enhancement from the homogeneous field. The pure FG term enhances the mode at 1583 cm^{-1} (e_{2g}) but this enhancement is rather small compared to the other terms. This indicates that the surface selection rules are dominated by the FG effects while most of the enhancement comes from the homogeneous field. Furthermore, it also illustrates that FG effects are essential to include in the dressed-tensors formalism in order to get good agreement with the DIM/QM method.

Another interesting feature of the FG effects is its ability to provide detailed information about the orientation of a molecule relative to the nanoparticle. Previously we showed²⁷⁰ that the experimental SERS spectrum of benzene could be successfully reproduced if a small tilt angle of 10° with respect to a spherical silver nanoparticle was assumed in the simulations. A nanoparticle

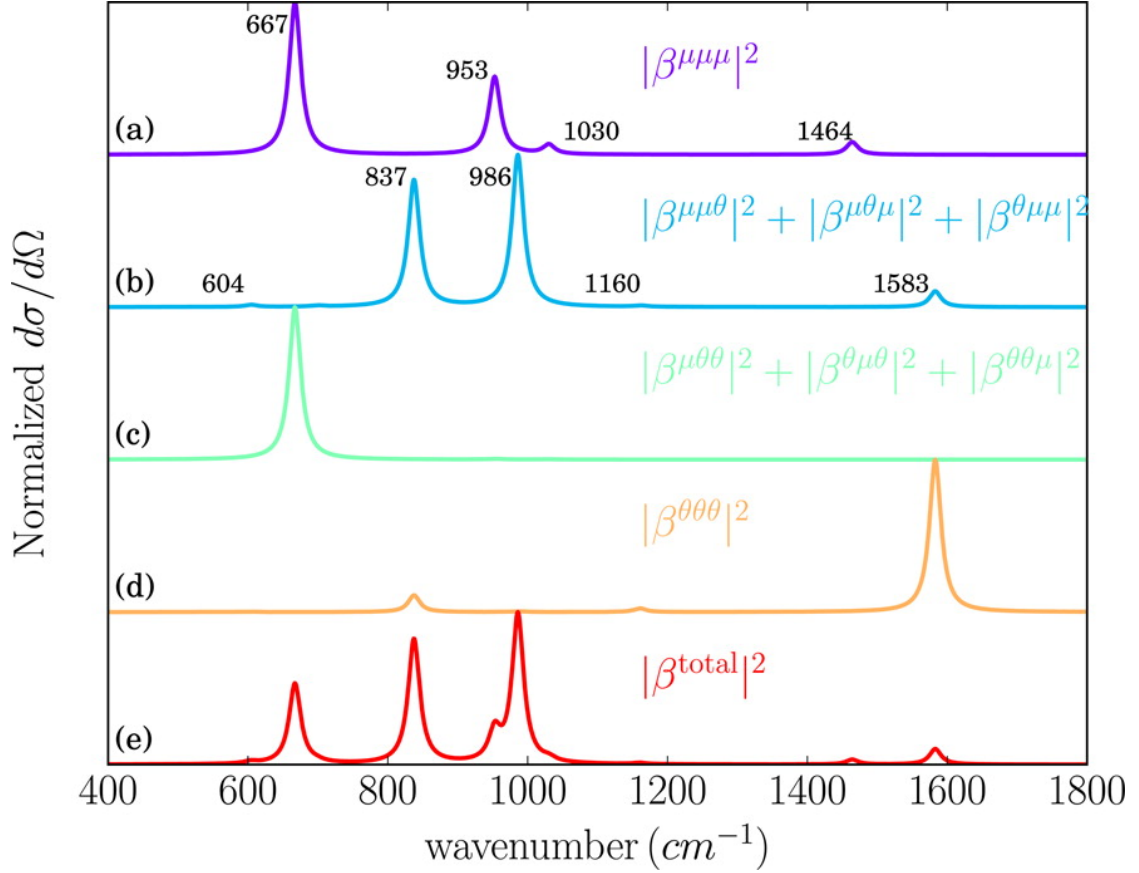


Figure 7.5. SEHRS spectrum of the benzene-silver model system simulated using the dressed-tensors method and its individual contributions. An incident wavelength of 343 nm was used in the simulations. All spectra have been normalized with respect to their individual maximum cross section given in $\text{cm}^4 \cdot \text{s} \cdot \text{photon}^{-1} \cdot \text{sr}^{-1}$, i.e., (a) 385×10^{-60} ; (b) 960×10^{-60} ; (c) 63×10^{-60} ; (d) 3.9×10^{-62} ; (e) 980×10^{-60} .

with a diameter of 20 bohr was used in the simulations to determine the ratio of FG to fields, where the diameter is a representation of the curvature of the local surface roughness responsible for these FG ratios and not the actual dimensions of the nanoparticles used in the experiments. Here we adopt the same model for the SEHRS simulations.

Since the experimental work is usually performed away from any molecular resonance, we chose to calculate the dipole- and quadrupole-level β tensors at the static limit. However, the local fields and FG are generated by a spherical silver nanoparticle with a plasmon resonance at 343 nm coinciding the wavelength of the incident light. In Figure 7.6(a) we plot the NHRS spectrum of benzene, and compare it with the dressed-tensor SEHRS spectra of benzene obtained without (Figure 7.6(b)) and with (Figure 7.6(c)) the FG contributions. In the absence of FG, we find that all NHRS active modes (667 (a_{2u}), 953 (e_{2u}), 997 (b_{2u}), 1030 (e_{1u}), 1140 (b_{1u}), 1326 (b_{1u}), and 1464 (e_{1u}) cm^{-1}) are enhanced, with the mode at 667 cm^{-1} experiencing the strongest enhancement. The FG effects enable the modes at 604 (e_{2g}), 837 (e_{1g}), 986 (a_{1g}), 1160 (e_{2g}) and 1583 (e_{2g}) cm^{-1} to be observed, and the spectrum looks very different from both the NHRS

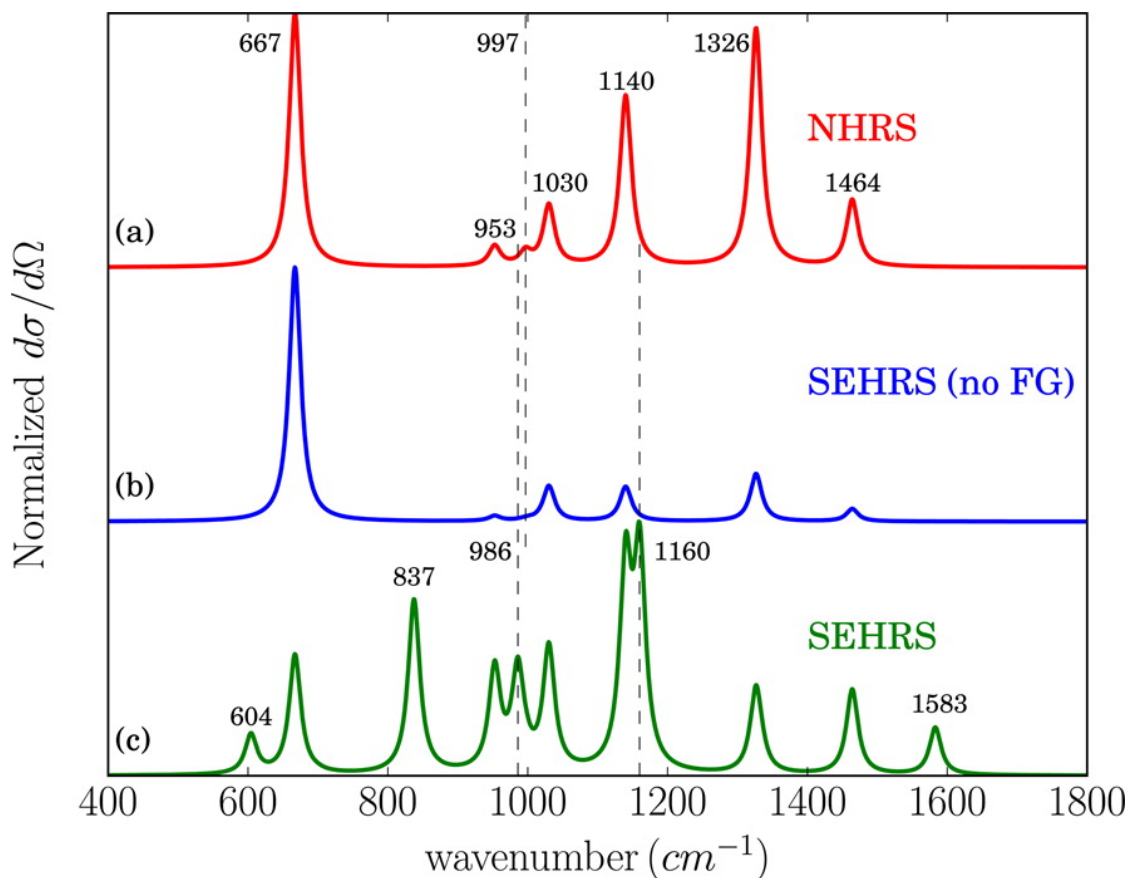


Figure 7.6. (a) Simulated NHRS spectrum of an isolated benzene molecule. SEHRS spectra of benzene titled at 10° with respect to the surface of a 20 bohr diameter silver sphere simulated using the dressed-tensors method (b) without, and (c) with the FG contributions. An incident wavelength of 343 nm was used in the simulations.

spectrum and the spectrum enhanced by an homogeneous field. Thus, these modes serve as direct indications of the importance of the FG effects in SEHRS for a given substrate. Due to the low NHRS cross section of benzene, few experimental data is available. An experimental SEHRS spectrum of benzene was reported by Li *et al.*³⁰⁹ using a nanoparticles-on-smooth-electrode substrate, which showed a strong band at 675 cm^{-1} in good agreement with the simulated SEHRS spectrum obtained without the FG effects shown in Figure 7.6(b). It is expected that the FG effects for this substrate would be small due to the smooth electrode surface. The SERS spectrum of pyridine from the same study, and under similar conditions, also did not show any FG enhanced modes.

7.4.4 SEHRS of Pyridine

In contrast to benzene, several experimental spectra are available for pyridine, making it a good benchmark system for theoretical simulations of SEHRS.^{310,312} Previous work has demonstrated that good agreement with experimental NHRS spectrum of pyridine can be achieved using a

large basis set. Therefore, we chose to adopt the ET-QZ3P-hypol basis set and a Ag_{10179} silver icosahedral nanoparticle with a diameter of 8.1 nm to simulate SEHRS of pyridine. Pyridine is chosen to bind to one of the vertices of the nanoparticle with a distance of 4.0 Å between the nitrogen atom and the nearest silver atom. The orientation of the pyridine molecule relative to the nanoparticle is shown in Figure 7.7. Two different sets of SEHRS simulations were done using both the DIM/QM and the dressed-tensors methods. In the first set of simulations, the frequency of the incident light was chosen to be on resonance with the plasmon excitation of the Ag_{10179} icosahedral nanoparticle at 343 nm. In the second set of simulations, the incident frequency was set equal to 686 nm, which corresponds to the scattered frequency being resonant with the plasmon excitation.

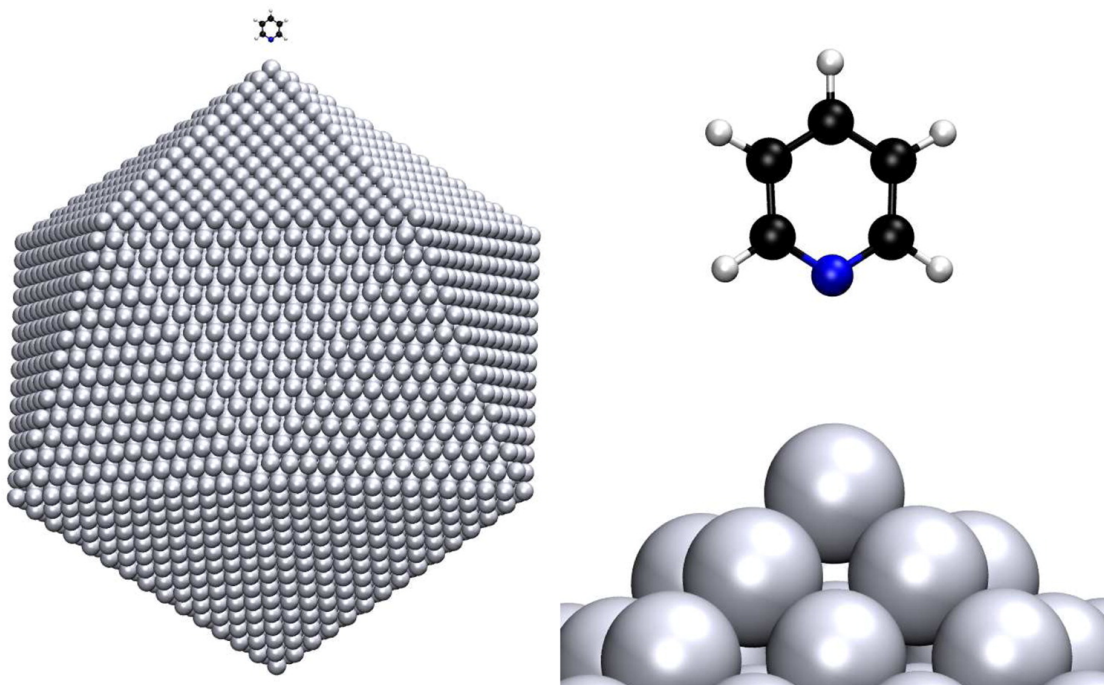


Figure 7.7. Orientation of pyridine on an Ag_{10179} icosahedral nanoparticle. The distance between the nitrogen atom in pyridine and the nearest silver atom is 4.0 Å. The Ag_{10179} nanoparticle is 8.1 nm in diameter.

In Figure 7.8 we plot the simulated SEHRS spectra obtained using the DIM/QM and the dressed-tensors methods at an incident frequency of 343 and 686 nm. For both frequencies, we find that the spectra obtained with the DIM/QM and the dressed-tensors methods are in good agreement. However, at 686 nm, the intensities obtained using the dressed-tensors method are about 5 times smaller than those obtained using DIM/QM. When the incident light is on resonance with the plasmon excitation, the two methods predict similar intensities. The intensities at 343 nm are about 6 orders of magnitude larger than those at 686 nm. One reason for this is a decrease in the field enhancement at 686 nm compared to at 343 nm, and this will be discussed in more detail below. More importantly is that, at 343 nm, the incident light is nearly two-photon resonant with three excited states of pyridine, which gives a large resonance enhancement of

around 10^6 . The excited states correspond to the 2^1B_2 state at 174 nm, the 3^1A_1 state at 171 nm, and the 3^1B_2 state at 169 nm. These calculated excitation energies for pyridine are in good agreement with the best theoretical estimates reported by Silva-Junior et al.³⁶⁰

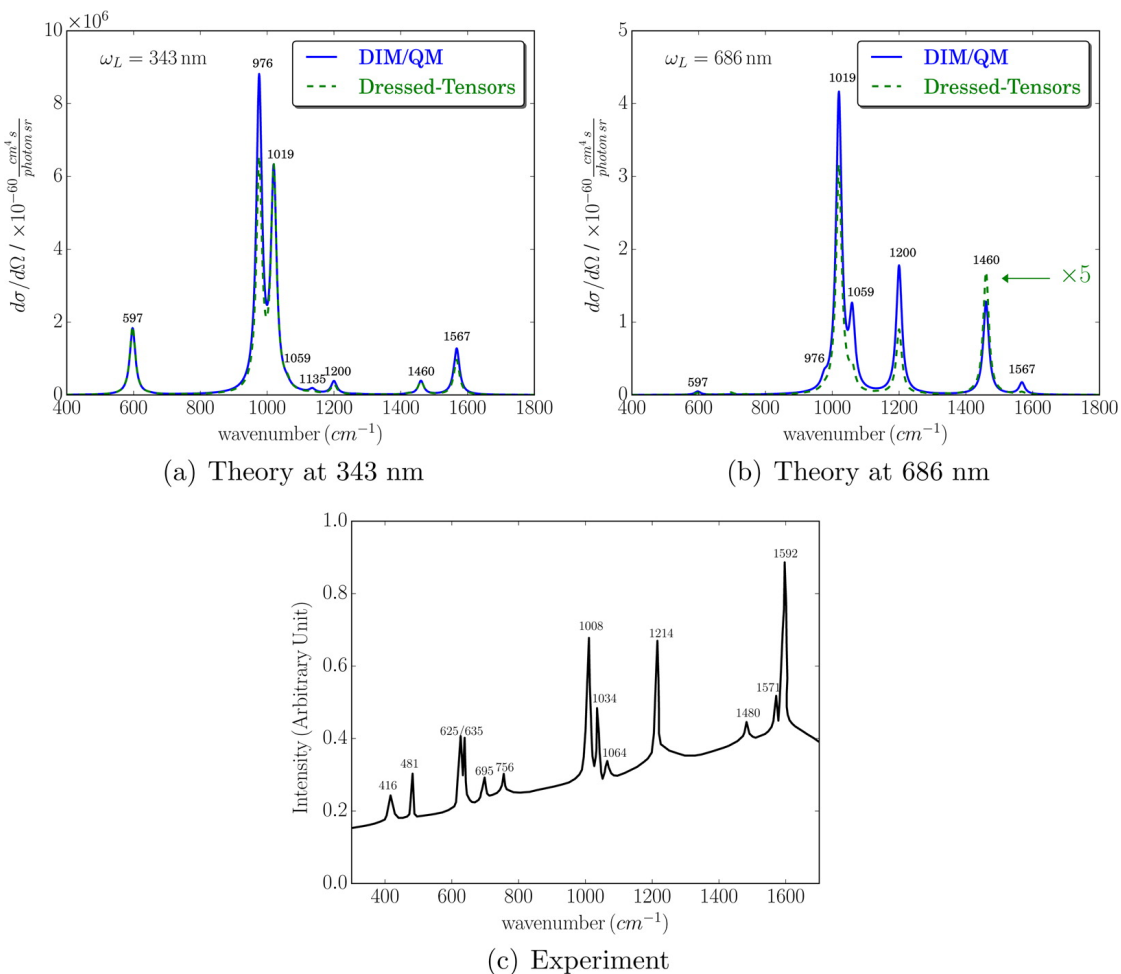


Figure 7.8. SEHRS spectra of pyridine sitting perpendicular to the vertex of an Ag_{10179} icosahedron simulated using the DIM/QM (blue solid curve) and the dressed-tensors (green dashed curve) methods. An incident wavelength of 343 (a) and 686 (b) nm were used in the simulations, respectively. Note that the intensities obtained by the dressed-tensor method at 686 nm is enlarged by 5 times. (c) The experimental SEHRS spectrum of pyridine on spinning Ag electrode taken from Ref. 28.

At 343 nm, the SEHRS spectrum is dominated by the two ring breathing modes at 976 and 1019 cm^{-1} , the ring deformation mode at 597 cm^{-1} and the symmetric ring stretch mode at 1567 cm^{-1} . Weaker bands are also seen at 1059, 1135, 1200, and 1460 cm^{-1} . Interestingly, at this wavelength, the simulated SEHRS spectrum looks similar to the experimental SERS spectrum.⁷⁹ This is likely a result of the two-photon resonance with S_1 of pyridine. The SEHRS spectrum at 686 nm shows similar modes but the relative intensities are drastically different. The ring breathing mode at 1019 cm^{-1} is now significantly more intense than the mode at 976 cm^{-1} . Also, the modes at 1059, 1200, and 1460 cm^{-1} are significantly enhanced compared to the spectrum at

343 nm. In comparison to the experimental work reported by Golab *et al.*²⁸, we find that the simulated spectra predict different relative intensities. In particular, the modes at 597 and 1567 cm^{-1} that correspond to the experimental modes at 625/635 and 1592 cm^{-1} are significantly underestimated; whereas for the mode at 1460 cm^{-1} that corresponds to the experimental mode at 1214 cm^{-1} , an overestimation is seen. Previous work has shown the importance of including the specific chemical interactions between pyridine and the nanoparticle in order to reproduce the experimental spectrum.^{310,312} Currently, such chemical effects are not included in the DIM/QM or the dressed-tensors methods but the results presented here show that SEHRS is very sensitive to the exact nature of the local field at the surface of the nanoparticle.

7.4.5 Enhancement Factors in SEHRS

The electromagnetic enhancement in SERS is given by $E_{\text{loc}}(\omega)$ as $|E_{\text{loc}}(\omega_L)|^2|E_{\text{loc}}(\omega_s)|^2$, where ω_L is the incident frequency and ω_s is the scattered frequency. Since the scattered photon in SERS has roughly the same energy as the incident one, the EF is often approximated as $|E_{\text{loc}}(\omega_L)|^4$. Similarly, the EF for SEHRS is given by $|E_{\text{loc}}(\omega_L)|^4|E_{\text{loc}}(\omega_s)|^2$.³⁶² In SEHRS, the scattered photon has roughly twice the energy of the incident generate photons and thus cannot be further simplified. However, these expressions for the EF in SERS and SEHRS assume that the local electric field is homogeneous over the dimensions of the molecule. If this is not the case, then the enhancement mechanism becomes significantly modified as previously discussed for SERS.^{270,351} This makes the electromagnetic enhancement mechanism for SEHRS more complex since one needs to consider enhancement at both the incident frequency (ω_L) and at the scattered frequency ($2\omega_L$).

To illustrate this, we choose to calculate the integrated EF for the pyridine spectra shown in Figure 7.8. The integrated EF is defined as

$$\text{EF}_{\text{int}} = \frac{I_{X-\text{Ag}}^{\text{tot}}}{I_X^{\text{tot}}} = \frac{\sum_k I_{X-\text{Ag}}^k}{\sum_j I_X^j}, \quad (7.16)$$

where $I_{X-\text{Ag}}^k$ is the intensity of the k^{th} normal mode of pyridine adsorbed to the silver nanoparticle and I_X^j is the intensity of the j^{th} normal mode for the free molecule. The intensity of the free molecule is calculated at the same frequency as used in the SEHRS calculations. For the SEHRS spectra at 343 nm, we find $\text{EF}_{\text{int}} = 2.9 \times 10^4$ using DIM/QM and $\text{EF}_{\text{int}} = 2.5 \times 10^4$ using the dressed-tensors method. At this wavelength, the incident light is on resonance with the plasmon excitation of the nanoparticle and we should expect the largest enhancement as $E_{\text{loc}}(\omega_L) > E_{\text{loc}}(\omega_s)$. Not surprisingly, the enhancement is much smaller at 686 nm, where we find $\text{EF}_{\text{int}} = 1724$ for DIM/QM and $\text{EF}_{\text{int}} = 251$ using the dressed-tensors method. In this case, the scattered light is on resonance with the plasmon and the enhancement is smaller as $E_{\text{loc}}(\omega_s) > E_{\text{loc}}(\omega_L)$.

These values are much smaller than the enhancements of 10^{11} estimated from experiments.^{28,29} However, it is difficult to directly compare the calculated EF with that measured experimentally. A better measure is to consider the ratio of SEHRS to SERS, and experimental estimates for this

range from 10^2 - 10^5 .^{28,143} Here we find the DIM/QM calculated ratios to be 49 and 40 at 343 and 686 nm, respectively, and the corresponding ones calculated using the dressed-tensors method are found as 33 and 8. All these values are much smaller than the experimental estimates. One reason for this is that a single nanoparticle is used in calculations, while for the experiments, the typically used nanoparticle aggregates or roughened silver electrode surfaces are often characterized by many different hotspots and thus active over a wider range of wavelengths. Furthermore, as mentioned previously, the chemical effects that are not included in this work could further increase the relative enhancement ratio and bring it closer to the experimental estimates.^{29,363}

We also investigate the distance effects on the SEHRS and SERS enhancements as shown in Figure 7.9, where the integrated EF for pyridine on the Ag_{10179} nanoparticle is plotted as a function of the distance from the surface. In the figure, we compare the results obtained using the DIM/QM and the dressed-tensors methods both with and without the FG effects. For both SERS and SEHRS, we find good agreement between the DIM/QM and the dressed-tensors methods once the distance is larger than 4 Å and the FG effects are included. For SERS, the FG effects only have a small effect on the integrated EF. Whereas for SEHRS, the integrated EF calculated without the FG effects are about a factor of 10 smaller even at 10 Å. We note that the FG effects are found to be important for distance up to around 50 Å, which is comparable to the diameter of the nanoparticle (80 Å). At distances shorter than 4 Å, we see significant difference between the integrated EF calculated using the DIM/QM and the dressed-tensors methods. For both SERS and SEHRS, we find that DIM/QM predicts much smaller enhancements due to the charge-distribution overlap between the molecule and the metal atoms. This effect is particularly strong for SEHRS and clearly demonstrates the importance of accounting for the FG effects and near-field screening when simulating the spectrum and the enhancements.

7.5 Conclusion

In conclusion, we have developed two methods to simulate SEHRS that enable an atomistic description of the metal nanoparticle and account for molecular resonance effects. The first model is the DIM/QM method, which combines an atomistic electrodynamics model for the nanoparticle with a TDDFT description of the molecule. In the second model, we treat the molecule as a point-dipole and point-quadrupole object interacting with the local electric field and FG generated by the metal nanoparticle. We have used both methods to simulate SEHRS of benzene and pyridine. The importance of the molecular resonances, image field, the local field, and the FG for determining the surface selection rules and enhancements in SEHRS have been analyzed. We have found that the FG effects in SEHRS play a significant role in determining the surface selection rules and enhancements. We also found that the FG effects are more important in SEHRS than in SERS. At short distances between the molecule and nanoparticle, we found significant differences between the enhancements predicted by the DIM/QM and the dressed-tensors methods. Discrepancies between our simulated spectra and that found experimentally point towards that the chemical effects need to be included in the simulations. The methods presented here should enable accurate simulations of SEHRS, especially for molecules on resonance where the spectral

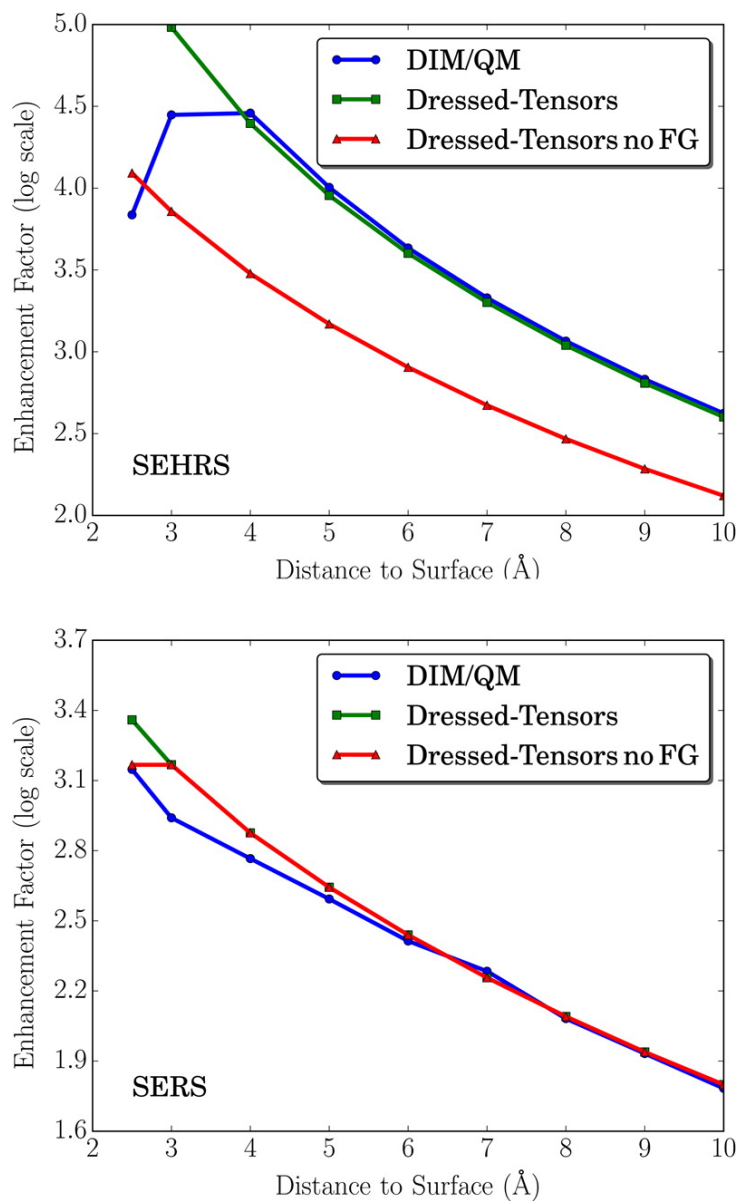


Figure 7.9. Simulated SEHRS (top) and SERS (bottom) EF_{int} (log scale) for pyridine sitting perpendicular to the vertex of an Ag_{10179} icosahedron using the DIM/QM (blue curve) and the dressed-tensors (green curve) methods, as well as the dressed-tensor method without the FG effects (red curve). The pyridine-silver model system was excited at 343 nm.

signatures are often dominated by the resonant effects.

Chapter 8 |

Surface-Enhanced Resonance Hyper-Raman Scattering Elucidates the Molecular Orientation of Rhodamine 6G on Silver Colloids

Hubert, T. K.*; Hu, Z.*; Jensen, L.; Camden, J. P. “*Surface-Enhanced Resonance Hyper-Raman Scattering Elucidates the Molecular Orientation of Rhodamine 6G on Silver Colloids*” *J. Phys. Chem. Lett.* **2017**, *8*, 1819. (*co-first authors)

Abstract

Herein, we utilize surface-enhanced hyper-Raman scattering (SEHRS) under resonance conditions to probe the adsorbate geometry of rhodamine 6G (R6G) on silver colloids. Our results show resonance SEHRS is highly sensitive to molecular orientation due to non-Condon effects, which do not appear in its linear counterpart surface-enhanced Raman scattering. Comparisons between simulated and measured SEHRS spectra reveal R6G adsorbs mostly perpendicular to the nanoparticle surface along the ethylamine groups with the xanthene ring oriented edgewise. Our results expand upon previous studies that rely on indirect, qualitative probes of R6G's orientation on plasmonic substrates. More importantly, this work represents the first determination of adsorbate geometry by SEHRS and opens up the possibility to study the orientation of single molecules in complex, plasmonic environments.

8.1 Introduction

The molecular orientation of surface adsorbates is of fundamental importance to many technologies utilizing plasmonic nanostructures. For example, the local geometry of the adsorbate is crucial to the design of next-generation functionalized nanostructures as geometry dictates the strength of the spectroscopic response,³⁶⁴ the ability to recognize analytes,³⁶⁵ and the way energy flows³⁶⁶ between the particle and the reporter molecule. Despite the importance of the problem, it is particularly challenging to probe molecular orientation on nanoparticle suspensions in aqueous solution. Traditional techniques such as sum-frequency generation vibrational spectroscopy (SFG-VS), high-resolution electron-energy loss spectroscopy (HREELS), and surface-infrared methods can provide insights into the orientation of molecules at the metal-air interface, but such methods are very difficult to realize in complex environments such as colloidal nanoparticle suspensions and particles imbedded in a matrix, e.g., serum or tissue.¹³⁰

As early as the 1980s, it was recognized that surface-enhanced Raman scattering (SERS) could be used to determine molecular orientation of surface adsorbates via surface-selection rules.^{367,368} These rules dictate that the SERS intensity for vibrational modes containing components of the bond polarizability tensor normal to the nanoparticle surface are preferentially enhanced as they align with the local electric field. Consequently, insights on adsorption geometries can be obtained by simply tracking the changes in relative intensity of the vibrational modes between SERS and normal Raman. In many cases, however, difficulties arise when extracting information on molecular orientation from these surface effects alone.³⁶⁹ For example, the most dramatic manifestations of the surface-selection rules occur when the molecule possesses vibrational modes and, hence, polarizability tensors with different symmetries. Unfortunately, the polarizability tensors have the same symmetry when on resonance with a single electronic transition, regardless of vibrational mode. Therefore, the use of surface-selection rules to determine geometry is greatly complicated when studying resonant molecules, which constitute some of the highest signal SERS probes. Overcoming these challenges could enable detection of the orientation of single molecules using surface-enhanced vibrational spectroscopies.

Many problems associated with bond symmetries can be avoided by measurement of higher-order terms. Field-gradient effects in SERS,²⁷⁷ for example, arise from a higher-order transition polarizability. As such, field-gradient effects enhance otherwise forbidden vibrational modes of different symmetry. These field gradient active modes can be used to determine the adsorbate geometry in SERS via the surface-selection rules;²⁷⁰ however, this approach is not expected to be generalizable as both a large molecular quadrupole transition polarizability and a strong field gradient are needed to produce a measurable effect.

Alternatively, the hyper-Raman effect provides access to additional vibrational modes without the need for a strong field gradient. In brief, vibrational hyper-Raman arises from the hyperpolarizability (β) and produces spontaneously scattered signal at frequencies shifted relative to the second harmonic of the excitation frequency, i.e., $2\omega_0 \pm \omega_\nu$ where ω_0 is the frequency of the driving field and ω_ν is the frequency of a molecular vibration. Despite evidence^{28,370-372} that surface-enhanced hyper-Raman scattering (SEHRS) offers heightened sensitivity to the analyte's

local environment and orientation compared to its linear counterpart, the surface-selection rules in SEHRS remain unexplored as a probe of adsorbate geometry.

In this Letter, we report the first use of SEHRS to determine the adsorbate orientation of rhodamine 6G (R6G) on silver colloids under resonance conditions with its lowest electronic state S_1 . Even though R6G is a common single-molecule SERS chromophore, the direct determination of its orientation on metal colloids has remained elusive due to the resonance enhancements. Interestingly, we find the orientation dependence of the SEHRS signal results from strong non-Condon effects in the hyper-Raman scattering, thereby, making SEHRS a much more sensitive probe of adsorbate geometry than SERS. Comparisons between theoretical calculations and experimentally measured SEHRS from aggregated silver colloids reveal R6G adsorbs mostly perpendicular to the nanoparticle. These results are consistent with the previous, qualitative orientation studies^{136,291} of R6G on silver substrates and represent the first demonstration of SEHRS to determine surface adsorption geometry.

8.2 Results and Discussion

Figure 8.1 displays the simulated SERS and SEHRS of R6G on resonance with S_1 at three extreme molecular orientations with respect to the nanoparticle surface. The response properties needed for the pure molecule were obtained using time-dependent wave packet formalism as previously described,^{97,137,138} in which both Franck-Condon (A-term) and non-Condon (B-term) effects are taken into account. The surface effects were included by adopting a recently developed dressed-tensors formalism,^{270,351,373} which describes the molecule as a point-dipole interacting with the enhanced local field from the nanoparticle. Details of the simulations are provided in the Supporting Information (SI). While the surface-selection rules in simulated SERS spectra (Figure 8.1A) lead to changes in overall intensity as a function of surface orientation, the intensity ratio between different modes remains nearly identical across all spectra. Thus, determining R6G's orientation by comparing this model with experimental SERS data requires knowing the absolute enhancement factor, which is challenging and an often imprecise measurement. Conversely, the surface-selection rules in simulated SEHRS spectra (Figure 8.1B) lead to marked changes between individual modes in addition to overall intensity changes as a function of orientation. Therefore, comparing these simulations with experimental SEHRS data offers a superior method for determining molecular orientation.

This orientation dependent behavior in the SEHRS simulations can be traced back to strong non-Condon effects (B_2 -term) that dominate the resonance hyper-Raman scattering (RHRS) of R6G at S_1 . As detailed in previous work,^{137,138} the first excited state of R6G is strongly one-photon allowed but only weakly two-photon allowed; therefore, the RHRS gains intensity through the vibrationally coupled two-photon transition moment (dS^{10}/dQ). This corresponds to intensity borrowing from the second excited state of R6G, S_2 , which is strongly two-photon allowed. For S_1 , the one-photon transition moment is dominated by contributions from a single state orientated along the xanthene ring for all vibrational modes, but the dominant contributions from dS^{10}/dQ differ in direction depending on the symmetry of the vibrational mode. Asymmetric

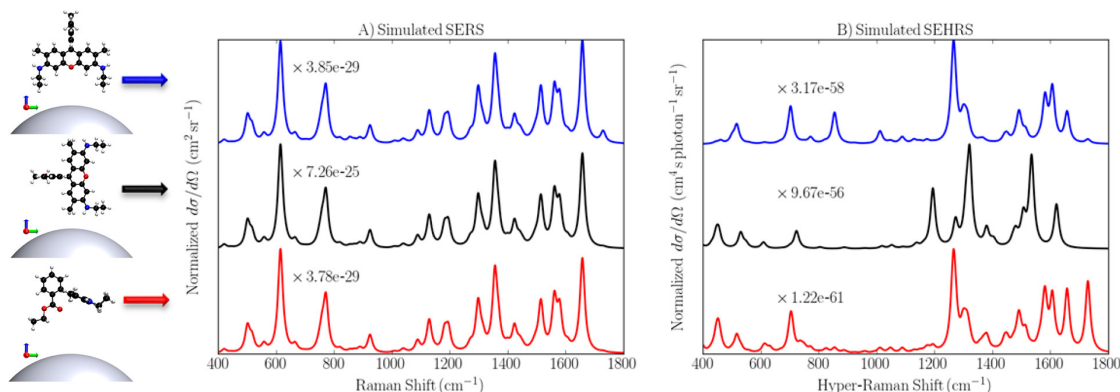


Figure 8.1. Effect of adsorbate geometry: (A) simulated SERS spectra of R6G on resonance with S_1 do not change as a function of adsorbate geometry (three limiting geometries given in inset); (B) simulated SEHRS spectra of R6G under identical conditions display significant changes in relative mode intensities.

modes, for example, lead to dS^{10}/dQ orientated along the direction as the one-photon transition moment, whereas symmetric modes lead to a different orientation. Thus, the β tensor points in different directions for vibrational modes of different symmetry, leading to orientation-dependent SEHRS. For illustration, unit sphere representations of the β tensor for the asymmetric mode at 1535.24 cm^{-1} and the symmetric mode at 1657.91 cm^{-1} are provided in Figure 8.2. In contrast to SEHRS, the SERS of R6G is dominated by Franck-Condon scattering (A-term) from one electronic state. The corresponding unit sphere representation illustrating nearly identical α tensor orientations for both asymmetric and symmetric modes as well as a detailed description of the non-Condon effects can be found in the SI.

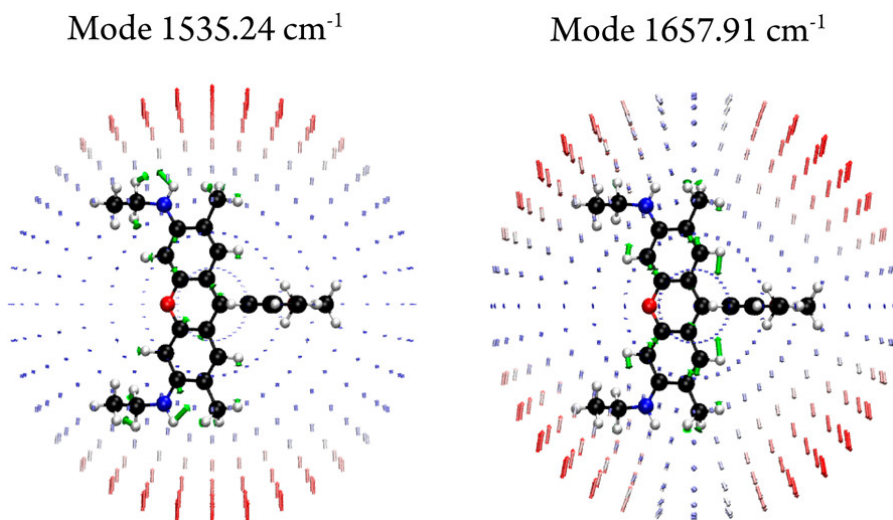


Figure 8.2. β unit sphere representations of R6G's modes at 1535.24 and 1657.91 cm^{-1} .

The inherent orientation dependence of the β tensor can be used to determine the absorption geometry of R6G by matching simulated and experimental SEHRS spectra. The SEHRS measurements were obtained from R6G (10^{-6} M) on aggregated silver colloids in water. This

concentration was expected to provide near monolayer coverage, so orientation estimates derived from these measurements likely reflect an average orientation. In brief, the orientation is determined by minimizing the spectral distance between the relative intensity of 7 important modes in the simulated and experimental spectra. Further information on experimental methods and a detailed description of the spectral matching procedure can be found in the SI. For reference, the initial orientation of R6G on the surface and the Euler angles used for rotation are depicted in Figure 8.3. This rotation scheme has been previously reported by Weiss *et al.*,³⁷⁴ where θ is the tilt angle between the z axis and the xy -plane, and ψ is the twist angle around the z axis.

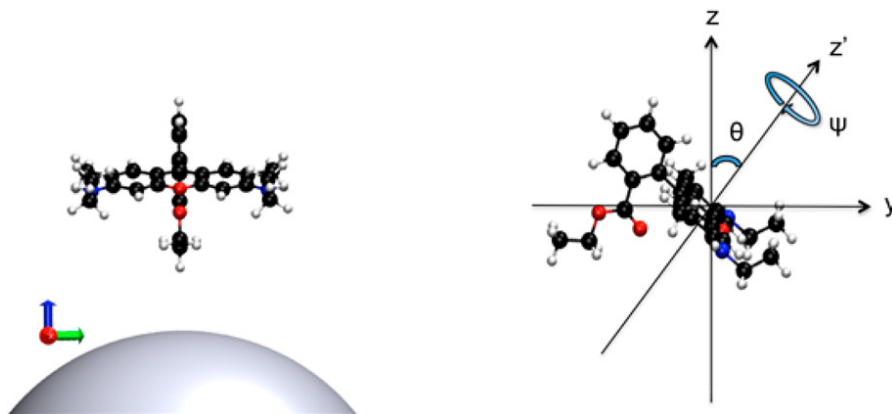


Figure 8.3. Left: Initial geometry of R6G on the surface. Right: Definition of the Euler angles used for rotation.

The orientation that best matches the experimental spectrum, displayed in Figure 8.4, corresponds to $\theta = 79^\circ$ and $\psi = 79^\circ$, in which R6G adsorbs edgewise on the xantheno ring along one of the ethylamine groups with a slight angle to the surface normal. Using the same predicted geometry, good agreement between theory and experiment is also found for the resonance SEHRS spectrum of R6G at S_2 (see SI). While $\theta = 79^\circ$ and $\psi = 79^\circ$ represent the best match at S_1 , it should be noted that there are multiple orientations that provide reasonable agreement between theory and experiment. Figure 8.5 illustrates this point with a contour map displaying the quality of the spectral match versus the two angles. The best spectral matches are found for two regions: $\theta = 50^\circ \rightarrow 90^\circ$, $\psi = 75^\circ \rightarrow 85^\circ$ and $\theta = 60^\circ \rightarrow 90^\circ$, $\psi = 90^\circ \rightarrow 100^\circ$. To provide a more comprehensive picture, we include the simulated SEHRS spectra of R6G as well as the corresponding orientations obtained at Euler angles residing near the boundaries of the two regions in the SI.

Similar to SERS, the surface-selection rules dictate that modes with a strong β_{zzz} component along the plasmonic near field direction will dominate the SEHRS spectrum. The appearance of both symmetric (e.g., 1657 cm^{-1}) and antisymmetric (e.g., 1535 cm^{-1}) modes in the experimental SEHRS spectrum can only arise for orientations with a slight tilt angle so as to provide large β_{zzz} components for all the observed modes. For further clarification, the orientation dependence of the β_{zzz} values for the two modes at 1535 and 1657 cm^{-1} is provided in the SI.

To the best of our knowledge, this represents the first direct determination of the adsorbate

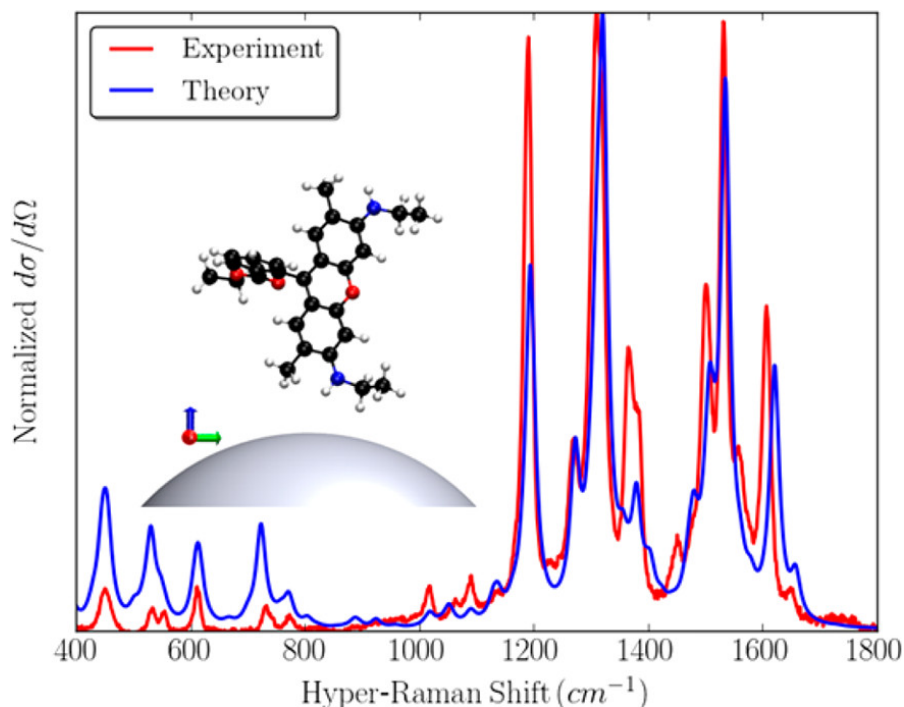


Figure 8.4. Comparison between experimental SEHRS (red trace) and theoretical calculations (blue trace) results in the predicted adsorbate geometry shown in the inset ($\theta = 79^\circ$, $\psi = 79^\circ$).

geometry of R6G on a silver colloid substrate to date. Our prediction is consistent with the orientation proposed by Klingsporn *et al.*²⁹¹ through a tip-enhanced Raman scattering study on an Ag (111) surface. More specifically, R6G is reported to sit perpendicular to the surface along its xanthene moiety by assuming the Raman frequency is mostly perturbed by the moieties near the surface. Darby *et al.*¹³⁶ also excludes the possibility that the electronic transition dipoles in R6G lie parallel to the surface of colloidal silver nanoparticles based on a thorough analysis of optical absorption enhancements. A nonparallel adsorptive geometry of R6G has been reported by Li *et al.*³⁷⁵ on silver colloids via the comparison between SERS intensity of R6G and its aminated derivative R-NH₂ as well as by Heinz *et al.*³⁷⁶ on a quartz substrate via a simple model designed for second harmonic generation. Both of these studies, however, predict R6G adsorbs along the front side of the xanthene ring similar to the geometry displayed in the top left inset in Figure 8.1. These predictions do not agree with those reported by Klingsporn *et al.*²⁹¹ and Darby *et al.*¹³⁶ and have been ruled out in our simulations as demonstrated in Figures 8.4 and 8.5. Furthermore, the edgewise adsorption orientation obtained herein is consistent with that determined for R6G on a quartz substrate in studies^{374,377,378} subsequent to the one reported by Heinz *et al.*³⁷⁶

8.3 Conclusion

This work has demonstrated that SEHRS is a more sensitive tool than SERS to probe the adsorbate geometry of R6G on silver colloids. By matching simulated and experimental SEHRS

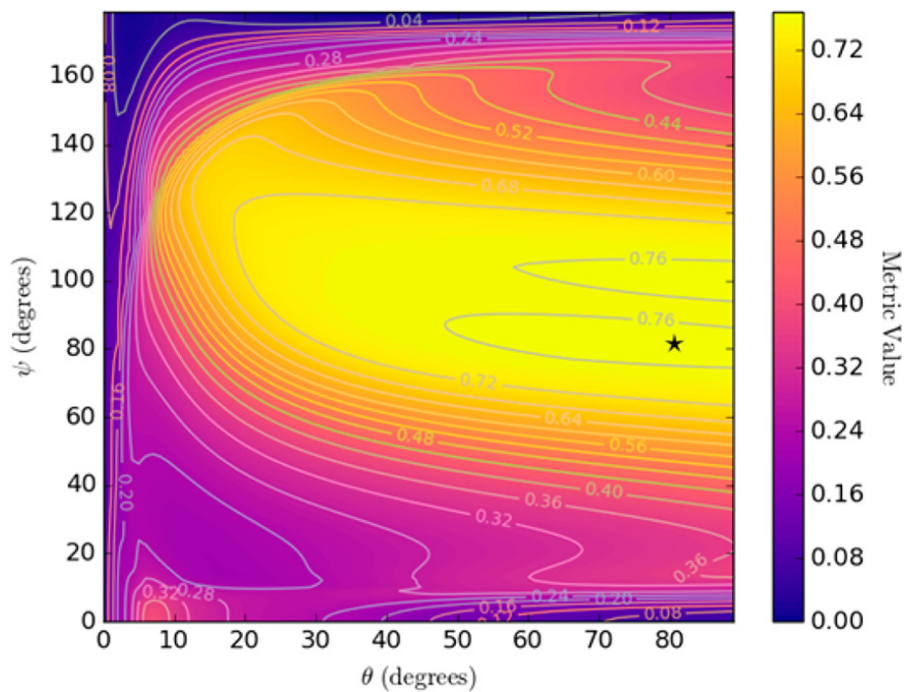


Figure 8.5. Orientation dependence of the agreement between theoretically calculated SEHRS spectra of R6G as a function of two Euler angles and the experimental data. The predicted orientation is marked with a “★”.

spectra for R6G, we find that R6G absorbs mostly perpendicular to the nanoparticle surface along the ethylamine groups, with the xanthene ring being placed edgewise. This work presents the first use of SEHRS to determine the absorption geometry of a molecule under resonance conditions and opens up the possibility to study the orientation of single molecules in complex plasmonic environments.

Part IV

Recent Research Progress

Chapter 9 | Application of Current Simulation Tools and Development of New Theoretical Methods

Abstract

In this chapter, a brief overview of recent research progress is provided. This contains two parts: application of current simulation tools and development of new theoretical methods. The first part includes some preliminary results for three projects: 1. A combined experimental and theoretical study on the surface-enhanced hyper-Raman scattering (SEHRS) of deuterated rhodamine 6G, in which the time-dependent wave packet formalism that allows for vibronic coupling simulations of hyper-Raman scattering is used; 2. A theoretical demonstration of the tip-enhanced hyper-Raman images at the single-molecule level, in which the discrete interaction model/quantum mechanical method (DIM/QM) that allows for SEHRS simulations is used; 3. A theoretical investigation on the third-harmonic generation of a Na_{20} dimer system, in which damped cubic response theory that allows for calculations of complex second hyperpolarizabilities is used. The second part includes a short version of the extended DIM/QM for simulating surface-enhanced two-photon absorption and surface-enhanced second hyper-Raman scattering.

9.1 Application of Current Simulation Tools

With the implementations of damped quadratic and cubic response theory,^{140,211} the extension of discrete interaction model/quantum mechanical method (DIM/QM) to the hyperpolarizability (β) level,³⁷³ and the previously developed vibronic coupling simulation package for nonlinear optical (NLO) processes,⁹⁷ many interesting NLO applications become possible. Here we briefly introduce three ongoing projects by showing their preliminary results found recently.

9.1.1 Surface-Enhanced Hyper-Raman Scattering of Deuterated Rhodamine 6G

Single-molecule (SM) surface-enhanced Raman scattering (SM-SERS), which makes SERS the only method that can simultaneously detect a single molecule and provide its chemical fingerprint, has become a well-established subfield of SERS in recent years.³² The initial approach to SM-SERS is intuitively straightforward, i.e., using low concentration.^{379,380} This idea originates from SM fluorescence, in which the dilution down to the picomolar range is typically needed. However, it remains challenging to directly apply this approach to SERS, mainly due to the non-uniformly distributed molecules adsorbed onto the metallic substrate.³² Moreover, SM-SERS often requires a “hot spot”, i.e., highly localized region that provides large electric field, to achieve detectable signals.³⁸¹ For the low-concentration approach, only a small portion of molecules are located at the “hot spots”, hence making the statistical analysis for the single-molecule proof less sound. The bi-analyte or isotopologue approach to SM-SERS, which uses two different SERS analytes at larger concentrations, improves the statistics, provides an appropriate platform to study “hot spots”, and has emerged as a rigorous procedure to prove single-molecule detection in SERS.^{225,226,382}

Recently, the surface-enhanced hyper-Raman scattering (SEHRS) from single molecules has been realized by means of the isotopologue approach.¹³⁵ In this study, Milojevich *et al.*¹³⁵ showed that for concentrations of less than three molecules per nanoparticle in experiment, the ensemble averaged SEHRS spectrum is dominantly characterized by single molecules. This experimental accomplishment truly inspires parallel theoretical studies, especially because the accurate electronic structure calculations are typically performed for single molecules. In collaboration with the Camden group, we have started to investigate the isotope effects on the SEHRS of rhodamine 6G (R6G) under (pre-)resonance conditions.

The left panel of Figure 9.1 displays the simulated two-photon absorption (TPA) spectra of both R6G (R6G-d0) and deuterated R6G (R6G-d4) with their structures shown in inset. The two nearly identical TPA spectra indicate that the isotopic editing does not perturb the molecular electronic structure, which is consistent with the previous finding based on their absorption spectra.²²⁶ The experimental SEHRS of R6G-d0 and R6G-d4 obtained at three different incident frequencies are shown in the right panel of Figure 9.1, in which 820 nm is the two-photon resonance energy with S_2 of R6G-d0(d4), 1064 nm is the two-photon resonance energy with S_1 of R6G-d0(d4), and 1266 nm is a two-photon pre-resonance energy with S_1 of R6G-d0(d4). Under (pre-)resonance conditions, we find SEHRS of R6G-d0 almost overlaps with that of R6G-d4. However, such

an overlapping becomes less pronounced in the lower frequency range as explicitly shown by Figure 9.2. Based on vibronic coupling simulations for hyper-Raman scattering (HRS) within a time-dependent wave packet formalism,⁹⁷ in Figure 9.2 we also show that this behavior can be accurately captured by theory.

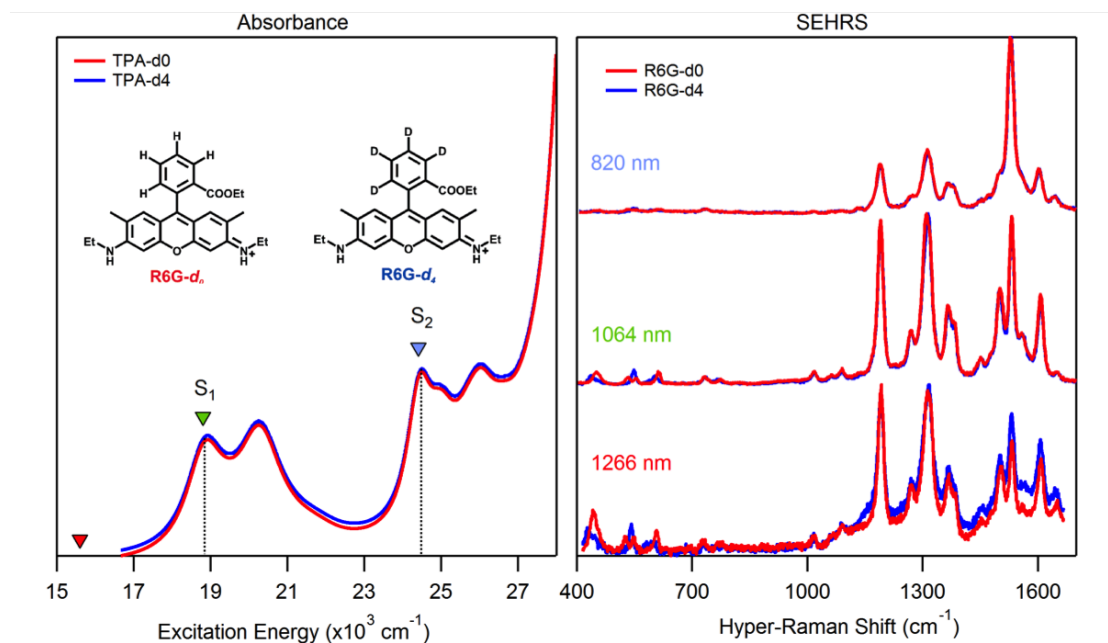


Figure 9.1. Left: Simulated TPA spectra of R6G-d0 and R6G-d4 (structures shown in inset). Right: Experimental SEHRS of R6G-d0 and R6G-d4 obtained at 820, 1064, and 1266 nm, respectively.

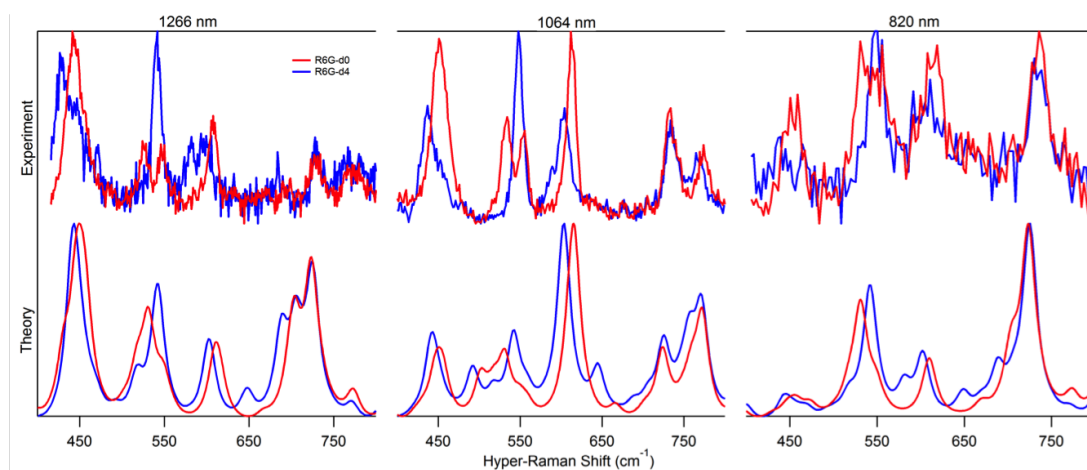


Figure 9.2. Experimental SEHRS and simulated HRS of R6G-d0 and R6G-d4 in the lower frequency range.

The next step for this project will be simulating SEHRS of R6G-d0 and R6G-d4 by means of a combined vibronic coupling and dressed-tensors approach,³⁸³ in which the orientation of R6G relative to the metal nanoparticles will be chosen according to the prediction reported in

Reference 383. This allows for the study on the interplay of the isotope effects and the surface selection rules, which may further motivate investigations on, e.g., the enhancement factor in SM-SEHRS, the chemical and electromagnetic contributions to SM-SEHRS, etc.

9.1.2 Tip-Enhanced Hyper-Raman Images at the Single-Molecule Level

Tip-enhanced Raman spectroscopy (TERS),^{384,385} which combines the high spatial resolution from scanning probe techniques and the rich chemical information provided by vibrational spectroscopy, has emerged as a promising approach to study both the structure and function of adsorbates on the nanometer length scale.²²³ In comparison to traditional techniques, TERS is unique in characterizing the heterogeneous distribution of adsorbates onto the nanoparticle via TER imaging, which can aid the identification of surface segregation and chemical contamination.²²³

The SMTER imaging was reported for the first time in ultrahigh vacuum (UHV) by Steidtner and Pettinger, where a lateral resolution of 15 nm was achieved.³⁸⁶ However, this level of resolution is not adequate to resolve a single molecule. Recently, Zhang *et al.*²²² improved the resolution down to less than 1 nm by tuning the plasmon resonance in line with the molecular vibronic transitions, which makes the inner structure and surface configuration of a single molecule visualized by TER images. An interesting phenomenon found in the same study²²² is the nonlinear dependence of the TERS response with respect to the incident laser power, which has been interpreted as related to the third-order nonlinear stimulated Raman scattering process. More recently, Duan *et al.*³⁸⁷ examined these nonlinear contributions by considering one stimulated Raman process and two hot luminescence processes, demonstrating that their main is to improve the resolution of the Raman image.

The nonlinearity of Raman scattering not only arises from the laser power as shown by Duan and co-worker³⁸⁷ but also the frequency of the laser. For example, the two-photon analogue of Raman scattering, i.e., hyper-Raman scattering, occurs for incident frequency to be half of its Raman counterpart.¹⁴ By adopting the tip-substrate model used for SMTER images,³⁸⁸ we simulate the single-molecule tip-enhanced hyper-Raman (SMTEHR) images by means of the discrete interaction model/quantum mechanical (DIM/QM) method at the β level.³⁷³

Figure 9.3 displays the vibrational motions for three normal modes of benzene, including both symmetrical and asymmetrical, as well as in- and out-of-plane features.

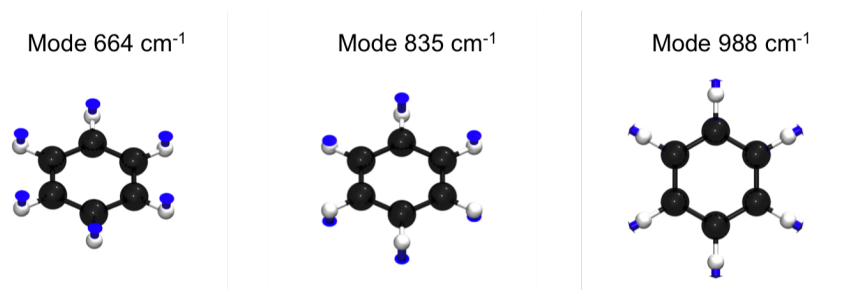


Figure 9.3. Vibrational motions for three modes of benzene.

The simulated TER and TEHR images for these three modes are shown in Figure 9.4, which

are obtained at $\omega = 400$ nm and $\omega = 800$ nm, respectively. We note that these TER images have been previously reported by Liu *et al.*,³⁸⁸ which clearly reflect the vibrational motions. For example, the out-of-plane C–H stretching at mode 664 cm^{-1} has been visualized as the elliptical regions near the hydrogen atoms, and the in-place “ring” breathing mode at 988 cm^{-1} exhibits a circular region around the molecule. In comparison to the three TER images, the corresponding TEHR ones are apparently not simply higher resolved but show quite different features, especially for modes with out-of-plane motions.

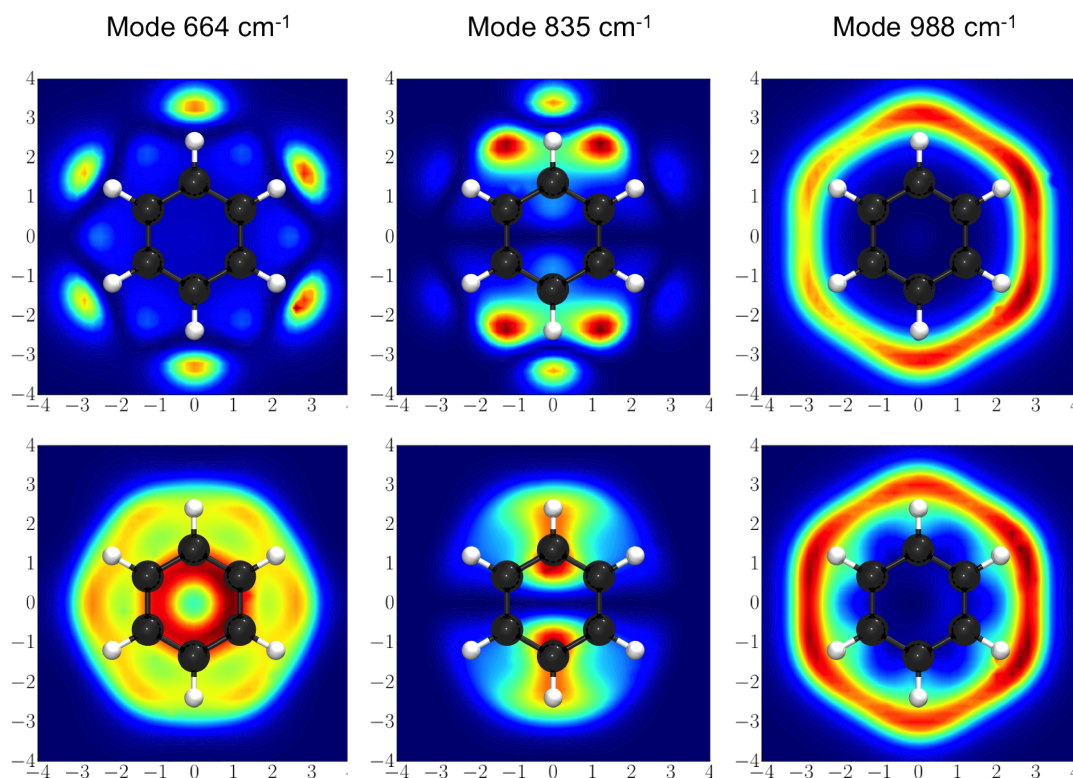


Figure 9.4. Top: Simulated TER images for three modes of benzene at $\omega = 400$ nm. Bottom: The corresponding TEHR image to each TER image above obtained at $\omega = 800$ nm.

The next step for this project will be simulating TER and TEHR images for the dimethyl-amino-nitrostilbene (DANS) molecule. DANS belongs to D- π -A push-pull family, and thus serves as an ideal candidate for the TER and TEHR imaging study on the charge-transfer characterizations. We think this study will be also helpful for interpreting the difference between the one- and two-photon Raman images shown above, yet, challenges may still remain.

9.1.3 Third-Harmonic Generation of a Na_{20} Dimer

Nonlinear plasmonics, a new research field that studies nonlinear optical properties (NLO) of plasmonic structures, has drawn significant attention in recent years.^{389,390} This becomes possible as the weak NLO processes can be strongly enhanced by the surface plasmons that are extremely

localized. Such a localization often persists down to the nanometer scale, and its ultimate limit is of fundamental interest due to its impact on plasmonic applications.³⁹¹ Recent experimental work demonstrated that the quantum tunneling limit of plasmonic enhancement can be probed by means of third harmonic generation (THG), indicated by a sharp reduction in the local field intensity.³⁹¹ This sudden drop has also been captured by a quantum corrected model (QCM)^{392,393} adapted in the same work.³⁹¹ However, the THG intensity there was obtained by integrating the cube of the local intensity rather than the cubic response tensor $\gamma(3\omega)$ that directly governs the THG process.

The QCM-based approach used in Reference 391 correctly predicts the trend of THG, especially at the onset of tunneling. However, it is over-simplified in such a way that the potential local field features that uniquely arise from $\gamma(3\omega)$ are completely missing. More importantly, this approach only focuses on the electric field intensity and thus could not provide information about the NLO tensors involved in THG. Herein, we utilize damped cubic response theory within a TDDFT framework²¹¹ to simulate THG with the $\gamma(3\omega)$ tensors, in which the needed localization scale is fulfilled by atomistic calculations.

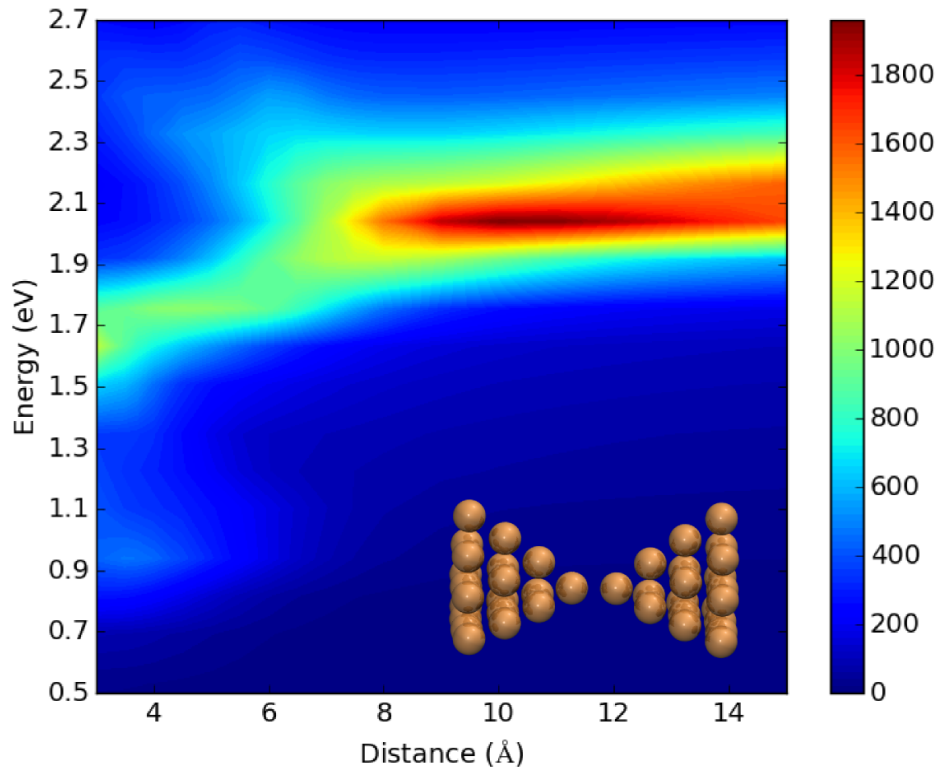


Figure 9.5. Simulated spectral evolution of the absorption cross-sections of a Na₂₀ dimer (inset) as a function of the distance between the vertex sodium atoms. Only the zz component of the $\alpha(\omega)$ is used for simulations.

Figure 9.5 displays the simulated spectral evolution of the absorption cross-sections of a sodium dimer model system as a function of the distance between the vertex sodium atoms, where only the component of the polarizability tensor $\alpha(\omega)$ that lies along the dimer axis, i.e., the zz direction, is used. The hybridized bonding dimer plasmon (BDP) is found for separation distance ranging from 7.5 to 15 Å, in which the redshift of BDP is clearly demonstrated as the distance decreases. For separation distance smaller than 7.5 Å, the BDP starts to be screened due to the tunneling current across the gap. On the other hand, the charge-transfer plasmon (CTP) starts to appear as the current between the gap increases, which is shown around 1.0 eV at a separation distance of 4 Å. All these behaviors are consistent with previous findings reported in Reference 394, indicating that the sodium dimer can serve as a reasonable model system for studying THG. Figure 9.6 displays the THG counterpart of Figure 9.5, where only the $zzzz$ -direction component is considered. The maximum THG intensity is found around 5 to 5.5 Å for all incident frequency energies, which indicates the tunneling limit to be 5 Å, falling within the upper boundary of CTP (4.0 Å) and the lower boundary of BDP (7.5 Å). This clearly demonstrates that our simulations can capture the sudden drop of THG found experimentally.

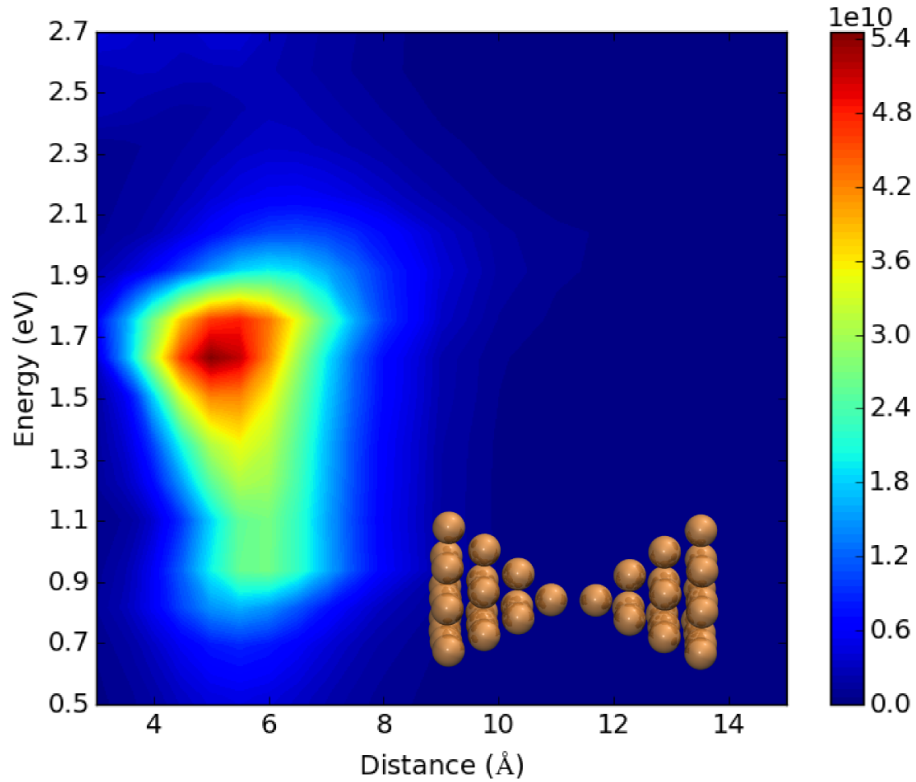


Figure 9.6. Simulated spectral evolution of the THG intensities of a Na_{20} dimer (inset) as a function of the distance between the vertex sodium atoms. Only the $zzzz$ component of the $\gamma(3\omega)$ is used for simulations.

The next step for this project will be simulating the local electric field induced by THG, and

comparing it with the cube of local field induced by α . By doing this, the unique effects on the local electric field obtained from the $\gamma(3\omega)$ tensor can be revealed. Besides this, we also plan to explore the difference between the resonant and nonresonant THG of this sodium dimer system. To our best knowledge, this will be the first simulations for the nonlinear versions of the plasmonic (resonant) and lightning rod (nonresonant) effects.

9.2 Development of New Theoretical Methods

The extension of DIM/QM to the β level has enabled the SEHRS simulations. However, in order to simulate even higher-order surface-enhanced nonlinear spectroscopies, such as surface-enhanced two-photon absorption (SETPA) and surface-enhanced second hyper-Raman scattering (SE2HRS), a further extension of DIM/QM to the γ level is needed. Here we report a short version of this implementation, provide the validation for it, and discuss its applications to SETPA and SE2HRS.

9.2.1 Surface-Enhanced Third-Order Nonlinear Optical Properties

Two-photon absorption (TPA), a nonlinear optical process that involves simultaneous absorption of two photons, has been of particular interest due to its applications in optical storage,¹¹ optical limiting,¹⁰ biological imaging,¹⁵⁵ and photodynamic therapy.³⁵ The nonlinearity of TPA provides deeper penetration into the sample while reducing the possible photodamage.^{395,396} However, the intrinsic low cross sections of TPA have posed a great challenge to its widespread use, especially in the biomedical area that generally requires greater penetration depth and spatial resolution.³⁹⁷ To overcome this limitation, two strategies have been routinely used to achieve stronger TPA. The first one focuses on the molecule itself, which exploits the structure-property relationship by “embedding” electron donor and acceptor groups into it;³⁹⁸ whereas the second one utilizes an external metal nanoparticle that supports surface localized plasmons.⁷⁶

Understanding the optical behavior of molecules near the vicinity of metal nanoparticles plays an important role in nanoscience. Through the well-established surface-enhanced Raman scattering (SERS)³⁹⁹, it has been previously demonstrated that the molecular linear response properties, i.e., polarizability α , can be strongly affected by the metal nanoparticles. Recent progress in surface-enhanced hyper-Raman scattering (SEHRS), the two photon analogue of SERS, has also contributed to the fundamental understanding of the plasmonic effects on the second-order NLO properties, i.e., hyperpolarizability β . However, much less is known about the third-order NLO properties, i.e., second hyperpolarizability γ .

Herein, we extend the discrete interaction model/quantum mechanical (DIM/QM) method²²⁹ to describe third-order NLO properties by accounting for the influence of surrounding nanoparticles. This allows for simulations of the surface-enhanced two-photon absorption (SETPA) and surface-enhanced second hyper-Raman scattering (SE2HRS) that are respectively governed by the intensity dependent refractive index (IDRI) $\gamma(-\omega; \omega, \omega, -\omega)$ and the third harmonic generation (THG) $\gamma(-3\omega; \omega, \omega, \omega)$ at the molecular level. In the following, we will report a short version of the DIM/QM γ implementation, show the validation of it by means of the finite field method, and discuss its application to SETPA and SE2HRS.

Similar as the α - and β -level DIM/QM implementations, we start by solving the effective time-dependent Kohn-Sham (TDKS) equation^{134,229,267,268}

$$i \frac{\partial}{\partial t} \phi_i(\mathbf{r}, t) = h_{\text{KS}}[\rho(\mathbf{r}, t)] \phi_i(\mathbf{r}, t), \quad (9.1)$$

with the effective KS operator being given as

$$h_{\text{KS}}[\rho(\mathbf{r}, t)] = -\frac{1}{2} \nabla^2 - \sum_I \frac{Z_I}{|\mathbf{r} - \mathbf{R}_I|} + \int \frac{\rho(\mathbf{r}, t)}{|\mathbf{r} - \mathbf{r}'|} d\mathbf{r}' + \frac{\delta E^{XC}}{\delta \rho(\mathbf{r}, t)} + \hat{V}^{\text{DIM}}(\mathbf{r}, t) + \hat{V}^{\text{pert}}(\mathbf{r}, t). \quad (9.2)$$

In the equation above, $\hat{V}^{\text{DIM}}(\mathbf{r}, \omega)$ is the embedding operator and $\hat{V}^{\text{pert}}(\mathbf{r}, \omega)$ is the external operator. These two operators can be further decomposed and written in terms of the polarization operator $\hat{V}^{\text{pol}}(r_j, \omega)$, the perturbation operator $\hat{V}^{\text{ext}}(r_j, \omega)$, and the local field operator $\hat{V}^{\text{loc}}(r_j, \omega)$, namely^{134,229,267,268}

$$\begin{aligned} \hat{V}^{\text{DIM}}(\mathbf{r}, \omega) &= \sum_j \hat{V}^{\text{pol}}(r_j, \omega) \\ &= \sum_j \sum_m \mu_{m,\alpha}^{\text{ind}}(\omega) T_{jm,\alpha}^{(1)} \end{aligned} \quad (9.3)$$

and

$$\begin{aligned} \hat{V}^{\text{pert}}(\mathbf{r}, \omega) &= \sum_j \hat{V}^{\text{ext}}(r_j, \omega) + \sum_j \hat{V}^{\text{loc}}(r_j, \omega) \\ &= \sum_j \hat{V}^{\text{ext}}(r_j, \omega) + \sum_j \sum_m \mu_{m,\alpha}^{\text{ext}}(\omega) T_{jm,\alpha}^{(1)}. \end{aligned} \quad (9.4)$$

$T_{jm,\alpha}^{(1)}$ here is the first-order real interaction tensor, and $\mu_{m,\alpha}^{\text{ind/ext}}(\omega)$ represents the frequency-dependent dipoles of the DIM subsystem as induced by the QM system/external field.^{134,229,267,268}

The frequency-dependent second hyperpolarizability γ for the DIM/QM system can be expressed within a cubic response formalism by utilizing the $2n + 1$ rule as²¹¹

$$\begin{aligned} &\gamma_{\alpha\beta\gamma\delta}(\mp\omega_\sigma; \pm\omega_1, \pm\omega_2, \pm\omega_3) = \\ &\text{Tr} \left[n \sum_P \left\{ U^\alpha(\mp\omega_\sigma) G^\beta(\pm\omega_1) U^{\gamma\delta}(\pm\omega_2, \pm\omega_3) + U^\beta(\pm\omega_1) G^\alpha(\mp\omega_\sigma) U^{\gamma\delta}(\pm\omega_2, \pm\omega_3) \right. \right. \\ &\quad - U^\alpha(\mp\omega_\sigma) U^\beta(\pm\omega_1) \varepsilon^{\gamma\delta}(\pm\omega_2, \pm\omega_3) - U^\beta(\pm\omega_1) U^\alpha(\mp\omega_\sigma) \varepsilon^{\gamma\delta\dagger}(\mp\omega_2, \mp\omega_3) \\ &\quad + U^\alpha(\mp\omega_\sigma) G^{\gamma\delta}(\pm\omega_2, \pm\omega_3) U^\beta(\pm\omega_1) + U^\beta(\pm\omega_1) G^{\gamma\delta}(\pm\omega_2, \pm\omega_3) U^\alpha(\mp\omega_\sigma) \\ &\quad - U^\alpha(\mp\omega_\sigma) U^{\gamma\delta}(\pm\omega_2, \pm\omega_3) \varepsilon^\beta(\pm\omega_1) - U^\beta(\pm\omega_1) U^{\gamma\delta}(\pm\omega_2, \pm\omega_3) \varepsilon^\alpha(\mp\omega_\sigma) \\ &\quad + U^{\gamma\delta\dagger}(\mp\omega_2, \mp\omega_3) U^\alpha(\mp\omega_\sigma) \varepsilon^\beta(\pm\omega_1) + U^{\gamma\delta\dagger}(\mp\omega_2, \mp\omega_3) U^\beta(\pm\omega_1) \varepsilon^\alpha(\mp\omega_\sigma) \\ &\quad \left. \left. - U^{\gamma\delta\dagger}(\mp\omega_2, \mp\omega_3) G^\alpha(\mp\omega_\sigma) U^\beta(\pm\omega_1) - U^{\gamma\delta\dagger}(\mp\omega_2, \mp\omega_3) G^\beta(\pm\omega_1) U^\alpha(\mp\omega_\sigma) \right\} \right] \\ &+ \text{Tr} \left[h_{xc}(\mathbf{r}, \mathbf{r}', \mathbf{r}'', \mathbf{r}''', \pm\omega_1, \pm\omega_2, \pm\omega_3) D^\alpha(\mp\omega_\sigma) D^\beta(+\omega_1) D^\gamma(\pm\omega_2) D^\delta(\pm\omega_3) \right. \\ &\quad \left. + \sum_P \left\{ g_{xc}(\mathbf{r}, \mathbf{r}', \mathbf{r}'', \pm\omega_2, \pm\omega_3) D^\alpha(\mp\omega_\sigma) D^\beta(\pm\omega_1) D^{\gamma\delta}(\pm\omega_2, \pm\omega_3) \right\} \right], \end{aligned} \quad (9.5)$$

where ω_1 , ω_2 , and ω_3 denote the three incident frequencies with ω_σ being the sum of them, “Tr” stands for the trace, and \sum_P represents a summation over corresponding terms obtained by

permuting $(\pm\omega_1, \beta)$ and $(\pm\omega_2, \pm\omega_3, \gamma\delta)$. Details about the permutation can be found in Reference 211.

We note that the γ expression above shares the same form as what used for a regular isolated QM system.²¹¹ However, it is important to note that all matrices in it account for the influence of the metal nanoparticle. This has been previously³⁷³ shown for all the first-order terms, i.e., U^α , G^α , ε^α and D^α matrices, and here we focus on the second-order terms such as the $U^{\beta\gamma}$, $G^{\beta\gamma}$, $\varepsilon^{\beta\gamma}$ and $D^{\beta\gamma}$ matrices. The second-order transformation matrix $U^{\beta\gamma}$ is given as

$$U_{ij}^{\beta\gamma}(\pm\omega_1, \pm\omega_2) = \begin{cases} \frac{1}{2} \left\{ U_{ij}^\beta(\pm\omega_1)U_{ij}^\gamma(\pm\omega_2) + U_{ij}^\gamma(\pm\omega_2)U_{ij}^\beta(\pm\omega_1) \right\} & \text{diagonal} \\ \frac{T_{ij}^{\beta\gamma}(\pm\omega_1, \pm\omega_2) + G_{ij}^{\beta\gamma}(\pm\omega_1, \pm\omega_2)}{\varepsilon_j^0 - \varepsilon_i^0 \mp (\omega_1 + \omega_2 + i\Gamma)} & \text{off-diagonal} \end{cases} \quad (9.6)$$

where

$$T_{ij}^{\beta\gamma}(\pm\omega_1, \pm\omega_2) = \sum_k^{all} \left[G_{ik}^\beta(\pm\omega_1)U_{kj}^\gamma(\pm\omega_2) + G_{ik}^\gamma(\pm\omega_2)U_{kj}^\beta(\pm\omega_1) - U_{ik}^\beta(\pm\omega_1)\varepsilon_{kj}^\gamma(\pm\omega_2) - U_{ik}^\gamma(\pm\omega_2)\varepsilon_{kj}^\beta(\pm\omega_1) \right]. \quad (9.7)$$

Since all the U^α , G^α , and ε^α matrices contain the DIM/QM components, the $U^{\beta\gamma}$ matrix is automatically DIM/QM characterized. Details about the inclusion of the $\hat{V}^{\text{DIM}}(\mathbf{r}, \omega)$ and $\hat{V}^{\text{loc}}(r_j, \omega)$ that are uniquely in DIM/QM can be found in Reference 373. Without loss of generality, the second-order perturbed density matrix $D^{\beta\gamma}$, the second-order molecular-orbital (MO) based KS matrix $G^{\beta\gamma}$, and the second-order Lagrangian multiplier matrix $\varepsilon^{\beta\gamma}$ also take the DIM/QM features into account. For example, $D^{\beta\gamma}$ is given as

$$D^{\beta\gamma}(\pm\omega_1, \pm\omega_2) = C^{\beta\gamma}(\pm\omega_1, \pm\omega_2)nC^{0\dagger} + C^0nC^{\beta\gamma\dagger}(\mp\omega_1, \mp\omega_2) + C^\beta(\pm\omega_1)nC^{\gamma\dagger}(\mp\omega_2) + C^\gamma(\pm\omega_2)nC^{\beta\dagger}(\mp\omega_1), \quad (9.8)$$

in which the second-order perturbed MO coefficients $C^{\beta\gamma}(\pm\omega_1, \pm\omega_2) = C^0U^{\beta\gamma}(\pm\omega_1, \pm\omega_2)$ depend on the $U^{\beta\gamma}$ matrix mentioned above. Then, $G^{\beta\gamma}$ and $\varepsilon^{\beta\gamma}$ matrices are subsequently DIM/QM dependent as they read

$$G^{\beta\gamma}(\pm\omega_1, \pm\omega_2) = C^{0\dagger} \left[D^{\beta\gamma}(\pm\omega_1, \pm\omega_2) \times (2J) + \nu_{xc}^{\beta\gamma}(\pm\omega_1, \pm\omega_2) \right] C^0 \quad (9.9)$$

and

$$\begin{aligned} \varepsilon^{\beta\gamma}(\pm\omega_1, \pm\omega_2) = & G^{\beta\gamma}(\pm\omega_1, \pm\omega_2) \\ & + G^\beta(\pm\omega_1)U^\gamma(\pm\omega_2) + G^\gamma(\pm\omega_2)U^\beta(\pm\omega_1) \\ & - U^\beta(\pm\omega_1)\varepsilon^\gamma(\pm\omega_2) - U^\gamma(\pm\omega_2)\varepsilon^\beta(\pm\omega_1) \\ & + \varepsilon^0U^{\beta\gamma}(\pm\omega_1, \pm\omega_2) - U^{\beta\gamma}(\pm\omega_1, \pm\omega_2)\varepsilon^0 \\ & \pm (\omega_1 + \omega_2 + i\Gamma)U^{\beta\gamma}(\pm\omega_1, \pm\omega_2), \end{aligned} \quad (9.10)$$

respectively. For details about the iteration process such as the self-consistent solutions to U^α and

$U^{\beta\gamma}$, as well as the adiabatic local density approximation to second- and third-order XC kernels (g_{xc} and h_{xc}), see Reference 211. It is also important to point out that, due to the inclusion of multiple incident frequencies and their different combinations at the second order, care must be taken when dealing the second-order couplings in the molecule-nanoparticle system and the frequency-dependent local field calculations from the nanoparticle.

To validate this implementation, we adopted the finite field (FF) method for comparison purpose. In the FF approach, γ can be obtained by differentiating lower order tensors that are perturbed by a small electric field. For example, the electric-field induced second harmonic generation (EFISHG) is given as

$$\gamma_{\alpha\beta\gamma\delta}(-2\omega; \omega, \omega, 0) = \lim_{E^d \rightarrow 0} \frac{\beta_{\alpha\beta\gamma}(-2\omega; \omega, \omega)|_{E=E^d}}{E^d}, \quad (9.11)$$

where $\beta_{\alpha\beta\gamma}(-2\omega; \omega, \omega)$ is the second harmonic generation (SHG). By choosing LiH as the test system, we compare the plasmon-assisted EFISHG obtained directly by the DIM/QM γ implementation with that based on the FF method. Note that the needed plasmon-assisted SHG for the later approach is obtained by the DIM/QM β implementation³⁷³ as previously described. In Table 9.1, we show the EFISHG results obtained at $\omega = 0.1$ a.u. for the dominant components, in which E^d is set to be 0.0001 a.u. for the FF method. Consider the intrinsic difference caused

Table 9.1. Simulated Plasmon-Assisted EFISHG for LiH

Property	DIM/QM γ		DIM/QM β with FF	
	Real	Imag	Real	Imag
$\gamma_{xxzz}(-2\omega; \omega, \omega, 0)$	3329737.36	5094650.79	3333656.58	5092361.42
$\gamma_{xzxx}(-2\omega; \omega, \omega, 0)$	-623053.14	-409824.95	-617999.42	-413940.75
$\gamma_{zzzz}(-2\omega; \omega, \omega, 0)$	-196349.99	-483044.99	-196316.00	-487285.83

by the numerical and analytical approaches and the sensitivity of the higher-order terms to the E^d , it is reasonable to conclude that the DIM/QM γ has been successfully implemented.

With the plasmon-assisted γ , one can simulate both SETPA and SE2HRS processes as their cross sections can be related to the $\gamma(-\omega; \omega, \omega, -\omega)$ and $\gamma(-3\omega; \omega, \omega, \omega)$ tensors, respectively. For SETPA, we will focus on elucidating how the molecular orientations and distances from the nanoparticles affect the TPA properties. This is motivated by the previous finding that the plasmon-enhanced linear absorption spectra are strongly dependent on these factors,²⁶⁷ and might further contribute to the understanding of how to control of the TPA enhancement. In addition to this, we are also interested in the magnitude of the enhancement for SETPA. With respect to the local field E , it is expected to scale as fourth power, i.e., $|E|^4$. Consider this scale is the same as that for SERS, an enhancement of at least 10^6 ought to be reached. For SE2HRS, we will focus on exploring its surface selection rules that are expected to more similar to the SERS than to SEHRS, as well as its enhancement that scales as $|E(3\omega)|^2|E(\omega)|^6$. In comparison to the enhancements of SERS ($|E(\omega)|^4$) and SEHRS ($|E(2\omega)|^2|E(\omega)|^4$), one should at least expect an $|E|^2$ larger enhancement for SE2HRS no matter if 3ω is also on resonance or not.

Part V

Summary and Outlook

Chapter 10 | Summary and Outlook

10.1 Dissertation Summary

This dissertation focused on developing new theoretical tools to calculate nonlinear optical (NLO) properties near the vicinity of metal nanoparticles and applying them to simulate surface-enhanced NLO spectroscopies, such as surface-enhanced hyper-Raman scattering (SEHRS), surface-enhanced two-photon absorption (SETPA), and surface-enhanced second hyper-Raman scattering (SE2HRS). The development of these new methods provided new insights into the plasmonic effects on the NLO properties, contributing to a comprehensive understanding of the area of surface-enhanced spectroscopies. As such, this dissertation was presented by four parts with the main ideas and theoretical background introduced in the first one, i.e., “Introductory Material”.

In the second part, “Describing Nonlinear Optical Properties with Damped Response Theory”, we presented the implementations of damped quadratic and cubic nonlinear response theory within a time-dependent density functional theory (TDDFT) for describing the NLO properties at the molecular level, i.e., the first hyperpolarizability (β) and the second hyperpolarizability (γ). We demonstrated that care must be taken when calculating higher-order response functions in the vicinity of one-photon poles due to the approximate kernels typically used in simulations. By utilizing the calculated β and γ tensors, we achieved the simulations of resonance hyper-Rayleigh scattering (HRayS), frequency-scanned hyper-Raman scattering (HRS), two-photon absorption (TPA), and third-harmonic generation (THG). We found that, on a per atom basis, the small silver clusters possess two-photon enhanced hyper-Rayleigh intensity comparable to that of larger nanoparticles. We showed that the hyper-Raman spectral features of crystal violet (CV) are dominated by strong A-term scattering across the range of its lowest two excitation energies. The TPA properties of thiolate-protected gold cluster $\text{Au}_{25}(\text{SR})_{18}^-$ were also reasonably obtained, which revealed that the one- and two-photon double resonance effect does not lead to significantly enhanced TPA cross sections.

In the third part, “Simulating Metal Surface Effects on Nonlinear Optical Properties”, we first presented a review of theoretical approaches for various linear and nonlinear surface-enhanced vibrational spectroscopies, and then focused on presenting two atomistic electrodynamics-quantum mechanical models for simulating SEHRS. The first one is the discrete interaction model/quantum mechanical (DIM/QM) model, which combines an atomistic electrodynamics model of the nanoparticle with a TDDFT description of the molecule. The second is a dressed-tensors

method that describes the molecule as a point-dipole and point-quadrupole object interacting with the enhanced local field and field-gradients (FG) from the nanoparticle. We found that FG effects in SEHRS were more important than its linear counterpart surface-enhanced Raman scattering (SERS), and mainly determined its surface selection rules and enhancements. We also demonstrated that SEHRS can be used as a spectroscopic tool to probe molecular adsorbate geometry on metal nanoparticles, and rhodamine 6G (R6G) was revealed to adsorb mostly perpendicular to the metal surface along the ethylamine groups with the xanthene ring oriented edgewise.

In the fourth part, “Recent Research Progress”, we presented a brief overview of recent research progress. This contains application of current simulation tools and development of new theoretical methods. For the application side, we are investigating the isotope effects on the SEHRS of R6G under (pre-)resonance conditions by means of a time-dependent wave packet formalism. Utilizing the DIM/QM method at the β level, we have recently achieved the tip-enhanced hyper-Raman images at the single-molecule level, and are currently further exploring this area. In addition to this, the THG of a Na_{20} dimer system is also under investigation with the help of damped cubic response theory, which is motivated to probe the ultimate limit of field localization for nonlinear plasmonics. For the method development side, we have successfully implemented the DIM/QM at the γ level, and are currently applying them to simulate SETPA and SE2HRS.

10.2 Future Directions for the Damped Nonlinear Response Theory

As developed in Part II of this dissertation, the damped quadratic and cubic response theory allows for a balanced description of all off-, near-, and on-resonance NLO properties for both molecules and metal clusters. This has enabled accurate and efficient simulations for many nonlinear optical processes, such as HRayS, HRS, TPA, and THG. However, all simulations are currently restricted to the gas phase and the limited XC functionals. Additionally, the adiabatically approximated exchange-correlation (XC) kernels used in nonlinear response theory have also been shown to cause spurious poles and overestimated TPA intensities.²¹¹

The solvent effects on the response properties, hence the related spectra, are normally shown as the position and magnitude of the spectral peaks. Such effects can be treated as perturbations of the molecular system, which are commonly described using continuum models^{400–402} or discrete interaction methods.^{403–406} To account for the solvent effects in damped nonlinear response theory, one can take advantage of the conductor-like screening Model (COSMO).^{407,408} Alternatively, the DIM/QM method introduced in Part III can not only deal with the influence of the nanoparticles but also the solvents on the molecule.

Conventional XC functionals fail to correctly describe the excitation energies that are charge-transfer characterized.⁴⁰⁹ This is often reflected as an underestimation of the excited states, and consequently causes redshift of the spectral peaks. To overcome this drawback, long-range corrected (LC)-functionals that separate the Coulomb operator into long- and short-range parts

have been introduced and shown great promise.^{410–412} Moore *et al.*²⁸⁵ recently demonstrated that the LC-functionals led to smaller but more reasonable SERS enhancement factors in comparison to traditional functionals. This is due to the correction to the energy difference between the highest occupied molecular orbital (HOMO) of the metal and the lowest unoccupied molecular orbital (LUMO) of the molecule. Therefore, to correctly predict the peak positions in molecular nonlinear spectra, as well as to better understand enhancement factor in SEHRS, it is necessary to make the LC-functionals available in the damped nonlinear response formalisms.

Adiabatically approximated XC kernels are typically employed in response theory for calculating optical properties within a TDDFT framework. However, we recently found that this approximation caused an overestimation of the TPA intensity due to the incorrect pole structures in nonlinear response theory.²¹¹ Parker and co-workers²¹⁹ recently demonstrated that these spurious pole effects were not only present in adiabatic TDDFT but also other approximate many-electron response functions. To solve this fundamental problem in nonlinear response theory within the TDDFT framework, one possible way is to develop frequency-dependent XC kernels so that the unexpected “spurious” poles can be cancelled out. The frequency-dependent second-order Bethe-Salpeter correlation kernel that recently introduced by Rebolini and Toulouse⁴¹³ might be one option. However, it remains unclear that to what extent this approach can alleviate the spurious pole effects.

10.3 Future Directions for the Nonlinear DIM/QM Method

As developed in Part III of this dissertation, the two atomistic electrodynamics-quantum mechanical models, i.e., DIM/QM method and dressed-tensors approach, allow for SEHRS simulations by also taking the molecular resonance effects into account. However, the QM part in each model adopts the damped quadratic response formalism. As a consequence, the nonlinear DIM/QM method is also suffering from the missing solvent effects, the limited XC functionals, and the spurious pole effects. In addition to this, although the polarization of the QM system, the molecular resonance effects, and the local field interactions can be well described by DIM/QM, other interactions such as dispersion and repulsion are missing or treated approximately using classical force fields.

These interactions are often categorized into the chemical effects in surface-enhanced spectroscopies, and in Chapter 7 we showed that they could likely contribute to a better agreement between the experimental and theoretical SEHRS of pyridine. In order to take them into account, the pyridine-Ag₂₀ model system has been previously proposed and shown great success.²⁸⁷ This mainly benefits from the plasmon-like absorption feature exhibited by the Ag₂₀ cluster, and also the affordable electronic structure calculations of the entire model system. However, the real plasmon excitations are missing due to the small size of Ag₂₀. As a consequence, failure has been shown to form a “hot spot” by using two Ag₂₀ clusters with a tip-to-tip configuration,²³³ further due to the non-plasmon-like dramatic decay of the local field (near-field) around the Ag₂₀ clusters. To account for the plasmon effects, Mullin *et al.*³¹⁰ proposed a hybrid model which embeds the Ag₂₀ model system into a more realistic spherical nanoparticle that described by Mie Theory.

However, this model does not include the molecular resonance effects, neglects atomistic features, and is restricted to certain morphologies of the nanoparticles. Therefore, to develop a robust model for simulating SEHRS, it is of great need to include the chemical effects in DIM/QM.

To achieve this, the initial step will be simply treating the molecule- Ag_{20} system as the QM part while keeping other features in DIM/QM the same. This requires appropriate XC functionals that can correctly describe the charge transfer process between the molecule and the Ag_{20} cluster. Additionally, the Ag_{20} cluster ought to be carefully placed near the molecule-DIM system to void the overlapping of the Ag atoms in the cluster and those in the DIM system. Next, similar as what was proposed by Mullin *et al.*,³¹⁰ the Ag_{20} cluster could also be embedded into the DIM-based nanoparticle. Consider the atomistic features of both the molecule and the nanoparticle, this requires a careful cut of the DIM system. However, such a sharp distortion of the nanoparticle might lead to less accurate DIM descriptions, which in general makes this approach difficult to realize. Alternatively, we can take advantage of the dressed-tensors approach. More specifically, the dipolar and quadrupolar β tensors calculated from the molecule- Ag_{20} system can be “dressed” using the local field and field-gradient from nanoparticles that are not distorted. This in principle should work but the double counting of the local field might be difficult to avoid. Finally, the frozen-density embedding (FDE) scheme⁴¹⁴ used for modeling solvent effects has drawn significant attention in recent years. With respect to the metal-nanoparticle system, it would ideally work in such a way to allow for full QM description of the molecule with a small portion of the metal atoms while providing much cheaper calculations for the rest metal atoms that are set to be “frozen”. This approach calculates the local field from the “frozen” and “unfrozen” parts separately, and thus technically evaluates the entire local field in the expected manner. However, the implementation of the FDE scheme into the DIM/QM framework is undoubtedly a great challenge.

Appendices

Appendix A

Supporting Information for: Simulating Third-order Nonlinear Optical Properties Using Damped Cubic Response Theory within Time-Dependent Density Functional Theory

A.1 Derivation of the Relationship Between $\varepsilon^{\alpha\beta\dagger}$ and $\varepsilon^{\alpha\beta}$

According to the damped second-order CPKS equation, the damped second-order Lagrangian multiplier matrices with arguments $(+\omega_1, +\omega_2)$ and $(-\omega_1, -\omega_2)$ are given as

$$\begin{aligned}
\varepsilon^{\alpha\beta}(+\omega_1, +\omega_2) &= G^{\alpha\beta}(+\omega_1, +\omega_2) \\
&\quad + G^\alpha(+\omega_1)U^\beta(+\omega_2) + G^\beta(+\omega_2)U^\alpha(+\omega_1) \\
&\quad - U^\alpha(+\omega_1)\varepsilon^\beta(+\omega_2) - U^\beta(+\omega_2)\varepsilon^\alpha(+\omega_1) \\
&\quad + \varepsilon^0 U^{\alpha\beta}(+\omega_1, +\omega_2) - U^{\alpha\beta}(+\omega_1, +\omega_2)\varepsilon^0 \\
&\quad + (\omega_1 + \omega_2 + i\Gamma)U^{\alpha\beta}(+\omega_1, +\omega_2)
\end{aligned} \tag{A.1}$$

and

$$\begin{aligned}
\varepsilon^{\alpha\beta}(-\omega_1, -\omega_2) &= G^{\alpha\beta}(-\omega_1, -\omega_2) \\
&\quad + G^\alpha(-\omega_1)U^\beta(-\omega_2) + G^\beta(-\omega_2)U^\alpha(-\omega_1) \\
&\quad - U^\alpha(-\omega_1)\varepsilon^\beta(-\omega_2) - U^\beta(-\omega_2)\varepsilon^\alpha(-\omega_1) \\
&\quad + \varepsilon^0 U^{\alpha\beta}(-\omega_1, -\omega_2) - U^{\alpha\beta}(-\omega_1, -\omega_2)\varepsilon^0 \\
&\quad - (\omega_1 + \omega_2 + i\Gamma)U^{\alpha\beta}(-\omega_1, -\omega_2)
\end{aligned} \tag{A.2}$$

respectively. Here we note that the expression for the negative argument has already transformed $+i\Gamma$ to $-i\Gamma$ by construction. Therefore, taking the adjoint of Eq. (A.2) leads to the following

equation that maintains the sign of $i\Gamma$

$$\begin{aligned}
\varepsilon^{\alpha\beta\dagger}(-\omega_1, -\omega_2) &= G^{\alpha\beta\dagger}(-\omega_1, -\omega_2) \\
&\quad + U^{\beta\dagger}(-\omega_2)G^{\alpha\dagger}(-\omega_1) + U^{\alpha\dagger}(-\omega_1)G^{\beta\dagger}(-\omega_2) \\
&\quad - \varepsilon^{\beta\dagger}(-\omega_2)U^{\alpha\dagger}(-\omega_1) - \varepsilon^{\alpha\dagger}(-\omega_1)U^{\beta\dagger}(-\omega_2) \\
&\quad + U^{\alpha\beta\dagger}(-\omega_1, -\omega_2)\varepsilon^{0\dagger} - \varepsilon^{0\dagger}U^{\alpha\beta\dagger}(-\omega_1, -\omega_2) \\
&\quad - (\omega_1 + \omega_2 + i\Gamma)U^{\alpha\beta\dagger}(-\omega_1, -\omega_2).
\end{aligned} \tag{A.3}$$

Using the facts $\varepsilon^{0\dagger} = \varepsilon^0$, $U^{a\dagger}(-\omega) = -U^a(+\omega)$, $G^{a\dagger}(-\omega) = G^a(+\omega)$, $\varepsilon^{a\dagger}(-\omega) = \varepsilon^a(+\omega)$ and $G^{ab\dagger}(-\omega_1, -\omega_2) = G^{ab}(+\omega_1, +\omega_2)$, and substituting the following equations

$$\begin{aligned}
\varepsilon^a(+\omega) &= G^a(+\omega) + \varepsilon^0 U^a(+\omega) - U^a(+\omega)\varepsilon^0 + (\omega + i\Gamma)U^a(+\omega) \\
G^a(+\omega) &= \varepsilon^a(+\omega) - \varepsilon^0 U^a(+\omega) + U^a(+\omega)\varepsilon^0 - (\omega + i\Gamma)U^a(+\omega)
\end{aligned} \tag{A.4}$$

into Eq. (A.3), one can obtain

$$\begin{aligned}
\varepsilon^{\alpha\beta\dagger}(-\omega_1, -\omega_2) &= G^{\alpha\beta}(+\omega_1, +\omega_2) \\
&\quad + G^\alpha(+\omega_1)U^\beta(+\omega_2) + G^\beta(+\omega_2)U^\alpha(+\omega_1) \\
&\quad - U^\alpha(+\omega_1)\varepsilon^\beta(+\omega_2) - U^\beta(+\omega_2)\varepsilon^\alpha(+\omega_1) \\
&\quad - \left[U^\alpha(+\omega_1)U^\beta(+\omega_2) + U^\beta(+\omega_2)U^\alpha(+\omega_1) \right] \varepsilon^0 \\
&\quad + \varepsilon^0 \left[U^\alpha(+\omega_1)U^\beta(+\omega_2) + U^\beta(+\omega_2)U^\alpha(+\omega_1) \right] \\
&\quad + (\omega_1 + \omega_2 + 2i\Gamma) \left[U^\alpha(+\omega_1)U^\beta(+\omega_2) + U^\beta(+\omega_2)U^\alpha(+\omega_1) \right] \\
&\quad + U^{\alpha\beta\dagger}(-\omega_1, -\omega_2)\varepsilon^0 - \varepsilon^0 U^{\alpha\beta\dagger}(-\omega_1, -\omega_2) \\
&\quad - (\omega_1 + \omega_2 + i\Gamma)U^{\alpha\beta\dagger}(-\omega_1, -\omega_2).
\end{aligned} \tag{A.5}$$

This can be rewritten using $W^{\alpha\beta}(+\omega_1, +\omega_2) = U^\alpha(+\omega_1)U^\beta(+\omega_2) + U^\beta(+\omega_2)U^\alpha(+\omega_1)$ as

$$\begin{aligned}
\varepsilon^{\alpha\beta\dagger}(-\omega_1, -\omega_2) &= G^{\alpha\beta}(+\omega_1, +\omega_2) \\
&\quad + G^\alpha(+\omega_1)U^\beta(+\omega_2) + G^\beta(+\omega_2)U^\alpha(+\omega_1) \\
&\quad - U^\alpha(+\omega_1)\varepsilon^\beta(+\omega_2) - U^\beta(+\omega_2)\varepsilon^\alpha(+\omega_1) \\
&\quad - W^{\alpha\beta}(+\omega_1, +\omega_2)\varepsilon^0 + \varepsilon^0 W^{\alpha\beta}(+\omega_1, +\omega_2) \\
&\quad + (\omega_1 + \omega_2 + 2i\Gamma)W^{\alpha\beta}(+\omega_1, +\omega_2) \\
&\quad + \left[W^{\alpha\beta}(+\omega_1, +\omega_2) - U^{\alpha\beta}(+\omega_1, +\omega_2) \right] \varepsilon^0 \\
&\quad - \varepsilon^0 \left[W^{\alpha\beta}(+\omega_1, +\omega_2) - U^{\alpha\beta}(+\omega_1, +\omega_2) \right] \\
&\quad - (\omega_1 + \omega_2 + i\Gamma) \left[W^{\alpha\beta}(+\omega_1, +\omega_2) - U^{\alpha\beta}(+\omega_1, +\omega_2) \right],
\end{aligned} \tag{A.6}$$

where the fact $U^{\alpha\beta\dagger}(-\omega_1, -\omega_2) = W^{\alpha\beta}(+\omega_1, +\omega_2) - U^{\alpha\beta}(+\omega_1, +\omega_2)$ is also adopted. Eq. (A.6) can be further simplified as

$$\begin{aligned}
\varepsilon^{\alpha\beta\dagger}(-\omega_1, -\omega_2) &= G^{\alpha\beta}(+\omega_1, +\omega_2) \\
&+ G^\alpha(+\omega_1)U^\beta(+\omega_2) + G^\beta(+\omega_2)U^\alpha(+\omega_1) \\
&- U^\alpha(+\omega_1)\varepsilon^b(+\omega_2) - U^\beta(+\omega_2)\varepsilon^\alpha(+\omega_1) \\
&+ \varepsilon^0 U^{\alpha\beta}(+\omega_1, +\omega_2) - U^{\alpha\beta}(+\omega_1, +\omega_2)\varepsilon^0 \\
&+ (\omega_1 + \omega_2 + i\Gamma)U^{\alpha\beta}(+\omega_1, +\omega_2) \\
&+ i\Gamma W^{\alpha\beta}(+\omega_1, +\omega_2),
\end{aligned} \tag{A.7}$$

which is equivalent to

$$\varepsilon^{\alpha\beta\dagger}(-\omega_1, -\omega_2) = \varepsilon^{\alpha\beta}(+\omega_1, +\omega_2) + i\Gamma W^{\alpha\beta}(+\omega_1, +\omega_2) \tag{A.8}$$

by substituting Eq. (A.1) into Eq. (A.7).

A.2 Derivation of the Reduced IDRI Second Hyperpolarizability

The full expression of IDRI can be obtained by substituting $\omega_1 = \omega$, $\omega_2 = \omega$, and $\omega_3 = -\omega$ into the general SOS equation for the second hyperpolarizability. To obtain the reduced form of it (γ^{TPA}) when ω is far from any one-photon resonances, we start by eliminating all pure one-photon terms in the full expression. This leads to a total of eight two-photon terms, where the dominant ones are given as

$$\begin{aligned} \frac{1}{\hbar^3} \sum_{m \neq 0} \sum_{n \neq 0} \sum_{p \neq 0} \left\{ \frac{\langle 0 | \mu^\alpha | m \rangle \langle m | \bar{\mu}^\delta | n \rangle \langle n | \bar{\mu}^\gamma | p \rangle \langle p | \mu^\beta | 0 \rangle}{(\omega_{m0} - \omega - i\Gamma)(\omega_{n0} - 2\omega - i\Gamma)(\omega_{p0} - \omega - i\Gamma)} \right. \\ + \frac{\langle 0 | \mu^\alpha | m \rangle \langle m | \bar{\mu}^\delta | n \rangle \langle n | \bar{\mu}^\beta | p \rangle \langle p | \mu^\gamma | 0 \rangle}{(\omega_{m0} - \omega - i\Gamma)(\omega_{n0} - 2\omega - i\Gamma)(\omega_{p0} - \omega - i\Gamma)} \\ + \frac{\langle 0 | \mu^\delta | m \rangle \langle m | \bar{\mu}^\alpha | n \rangle \langle n | \bar{\mu}^\gamma | p \rangle \langle p | \mu^\beta | 0 \rangle}{(\omega_{m0} - \omega + i\Gamma)(\omega_{n0} - 2\omega - i\Gamma)(\omega_{p0} - \omega - i\Gamma)} \\ \left. + \frac{\langle 0 | \mu^\delta | m \rangle \langle m | \bar{\mu}^\alpha | n \rangle \langle n | \bar{\mu}^\beta | p \rangle \langle p | \mu^\gamma | 0 \rangle}{(\omega_{m0} - \omega + i\Gamma)(\omega_{n0} - 2\omega - i\Gamma)(\omega_{p0} - \omega - i\Gamma)} \right\}, \end{aligned} \quad (\text{A.9})$$

equivalent to

$$\frac{1}{\hbar^3} \sum_n \left\{ \frac{S_{0n}^{\alpha\delta}(\omega + i\Gamma, \omega - i\Gamma) S_{0n}^{\beta\gamma}(\omega + i\Gamma, \omega + i\Gamma)}{\omega_{n0} - 2\omega - i\Gamma} \right\}. \quad (\text{A.10})$$

The expression above can be further rewritten as

$$\begin{aligned} \frac{1}{\hbar^3} \sum_n \left\{ \frac{S_{0n}^{\alpha\delta}(\omega - i\Gamma, \omega - i\Gamma) S_{0n}^{\beta\gamma}(\omega + i\Gamma, \omega + i\Gamma)}{\omega_{n0} - 2\omega - i\Gamma} \right. \\ \left. + \frac{\left[S_{0n}^{\alpha\delta}(\omega + i\Gamma, \omega - i\Gamma) - S_{0n}^{\alpha\delta}(\omega - i\Gamma, \omega - i\Gamma) \right] S_{0n}^{\beta\gamma}(\omega + i\Gamma, \omega + i\Gamma)}{\omega_{n0} - 2\omega - i\Gamma} \right\}, \end{aligned} \quad (\text{A.11})$$

where the first part corresponds to the reduced IDRI second hyperpolarizability (γ^{TPA}), and the second part that represents a two-photon interference term, equivalent to

$$\frac{1}{\hbar^3} \sum_n \left\{ \sum_m \left[\frac{\langle 0 | \mu^\alpha | m \rangle \langle m | \bar{\mu}^\delta | n \rangle}{\omega_{m0} - (\omega + i\Gamma)} - \frac{\langle 0 | \mu^\alpha | m \rangle \langle m | \bar{\mu}^\delta | n \rangle}{\omega_{m0} - (\omega - i\Gamma)} \right] \times \frac{S_{0n}^{\beta\gamma}(\omega + i\Gamma, \omega + i\Gamma)}{\omega_{n0} - 2\omega - i\Gamma} \right\}, \quad (\text{A.12})$$

was also eliminated as being found contributing insignificantly to the two-photon poles when ω is far from any one-photon resonances.

A.3 Comparison Between the SZ and STO-3G Basis Sets for the Response Properties of LiH at the TDDFT Level of Theory

In Table A.1, we represent the static α , β and γ values calculated at the TDDFT level of theory. All values in Table A.1 are given in a.u. and only non-duplicate ones are shown based on Kleinman symmetry. Note that all static values were obtained without the lifetime, i.e., $\Gamma = 0$ a.u..

Table A.1. Simulated static α , β and γ for LiH at the TDDFT level

Property	ADF Response	Dalton Response	Dalton SOS
	Real	Real	Real
$\alpha_{xx}(0; 0)$	20.59	20.76	20.76
$\alpha_{zz}(0; 0)$	8.21	8.70	8.70
$\beta_{zxx}(0; 0, 0)$	-344.18	-348.73	-353.87
$\beta_{zzz}(0; 0, 0)$	-344.20	-388.68	-359.93
$\gamma_{xxxx}(0; 0, 0, 0)$	-4411.62	-4342.09	-3817.62
$\gamma_{xxyy}(0; 0, 0, 0)$	-1470.54	-1448.30	-1272.54
$\gamma_{xxzz}(0; 0, 0, 0)$	9773.72	9949.16	10457.39
$\gamma_{zzzz}(0; 0, 0, 0)$	27999.94	32722.03	28675.12

Within the TDDFT framework, all the properties calculated using response theory through ADF are in good agreement with those calculated using both response theory and the SOS approach through Dalton. This is an indication that, though identical minimal basis sets are not available, adopting SZ basis set for ADF while STO-3G basis set for Dalton is a reasonable approach for comparison purpose. Despite the same basis set (STO-3G) is ensured, discrepancies between those Dalton response and Dalton SOS results can still be seen for NLO properties at the TDDFT level of theory.

A.4 Comparison Between Response Theory and the SOS Approach for the Response Properties of LiH at the FCI Level of Theory

In Table A.2, we represent the static α , β and γ values calculated at the FCI level of theory. Including the damping factor, in Table A.3 we also represent the resonant α and β values calculated at the FCI level of theory. All values in Tables A.2 and A.3 are given in a.u. and only non-duplicate ones are shown based on Kleinman symmetry. Note that all static values were obtained without the lifetime, i.e., $\Gamma = 0$ a.u., whereas the resonant α and β values were obtained using $\Gamma = 0.0034$ a.u. at frequency equal to 0.132 and 0.066 a.u., respectively. The resonant γ values are not provided here because the FCI response theory approach to damped γ is currently not available in Dalton.

Table A.2. Simulated static α , β and γ for LiH at the FCI level

Property	Dalton Response		Dalton SOS
	Real	Imag	Real
$\alpha_{xx}(0; 0)$	21.96		21.96
$\alpha_{zz}(0; 0)$	10.51		10.51
$\beta_{zxx}(0; 0, 0)$	-438.89		-438.89
$\beta_{zzz}(0; 0, 0)$	-589.49		-589.49
$\gamma_{xxxx}(0; 0, 0, 0)$	-348.62		-348.60
$\gamma_{xxyy}(0; 0, 0, 0)$	-116.21		-116.20
$\gamma_{xxzz}(0; 0, 0, 0)$	16746.73		16746.64
$\gamma_{zzzz}(0; 0, 0, 0)$	59615.29		59615.29

Table A.3. Simulated resonant α and β for LiH at the FCI level

Property	Dalton Response		Dalton SOS	
	Real	Imag	Real	Imag
$\alpha_{xx}(-\omega; \omega)$	44.37	2.36	44.37	2.36
$\alpha_{zz}(-\omega; \omega)$	43.13	150.45	43.13	150.45
$\beta_{xxz}(-2\omega; \omega, \omega)$	-1156.96	-96.93	-1156.99	-96.93
$\beta_{zxx}(-2\omega; \omega, \omega)$	-1549.46	-5406.59	-1549.51	-5406.58
$\beta_{zzz}(-2\omega; \omega, \omega)$	-3440.72	-15567.42	-3440.85	-15567.42

Within the FCI framework, all the properties calculated using response theory are nearly identical to those calculated using the SOS approach. This is expected for such an exact wavefunction method when the same basis (STO-3G) is ensured.

A.5 Comparison Between Response Theory and the SOS Approach for the NLO Processes of LiH at the TDDFT Level of Theory

EOPE:

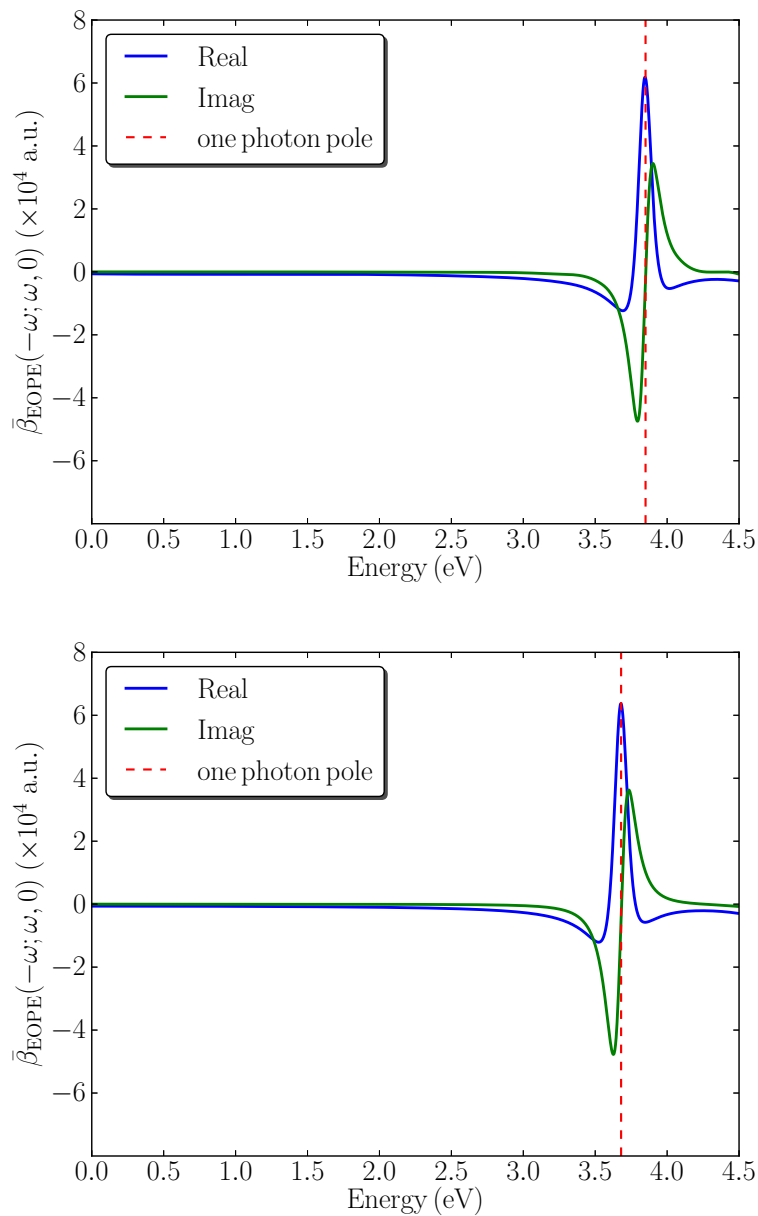


Figure A.1. Simulated EOPE spectra for LiH using (top) response theory and (bottom) the SOS approach at the TDDFT level of theory. The vertical “- -”line indicates the one photon resonance due to the excited state.

OR:

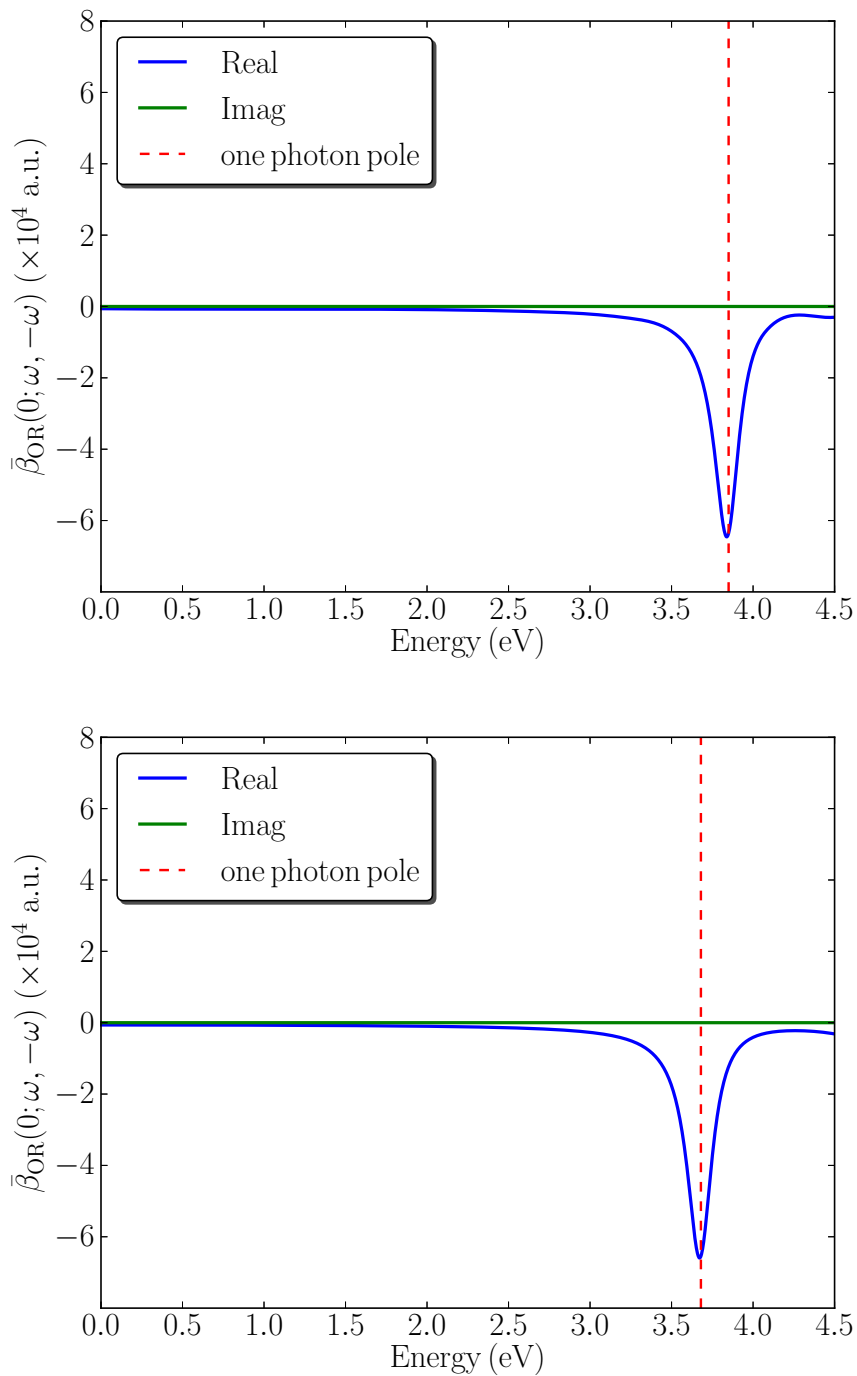


Figure A.2. Simulated OR spectra for LiH using (top) response theory and (bottom) the SOS approach at the TDDFT level of theory. The vertical “- -” line indicates the one photon resonance due to the excited state.

EFIOR:

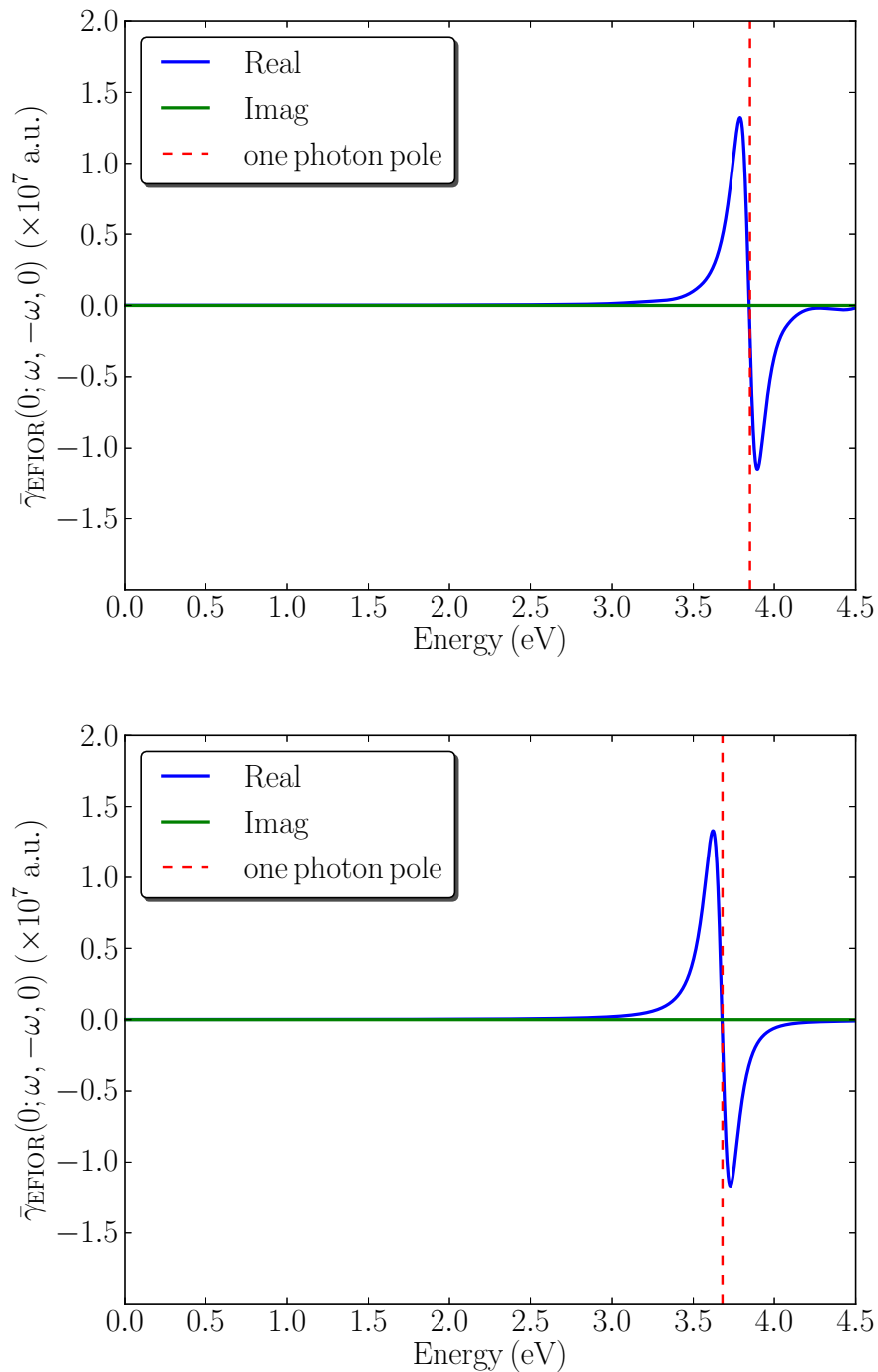


Figure A.3. Simulated EFIOR spectra for LiH using (top) response theory and (bottom) the SOS approach at the TDDFT level of theory. The vertical “- -” line indicates the one photon resonance due to the excited state.

EFISHG:

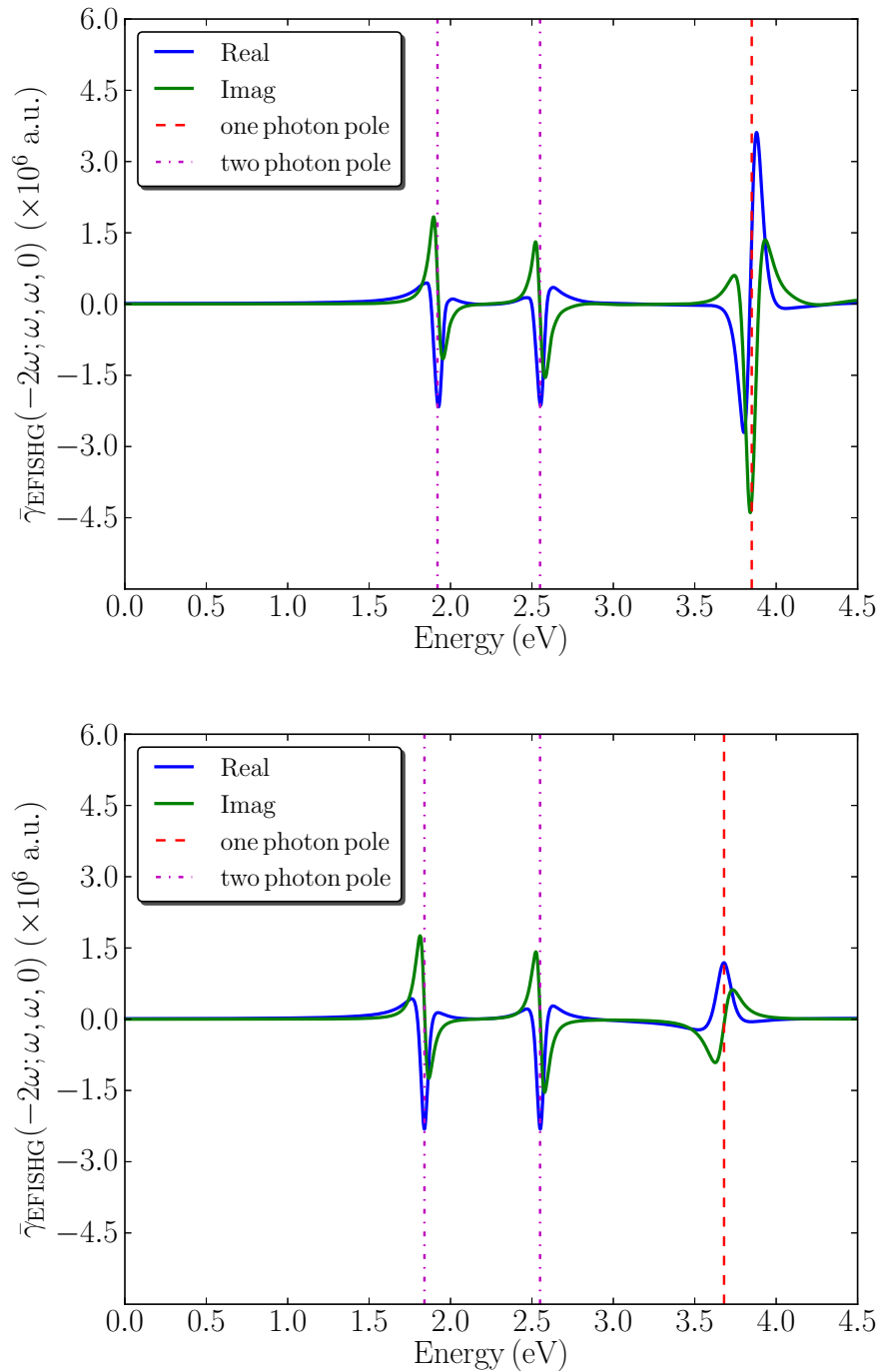


Figure A.4. Simulated EFISHG spectra for LiH using (top) response theory and (bottom) the SOS approach at the TDDFT level of theory. The vertical “- -” and “- .” lines indicate the one- and two-photon resonances due to the excited states, respectively.

THG:

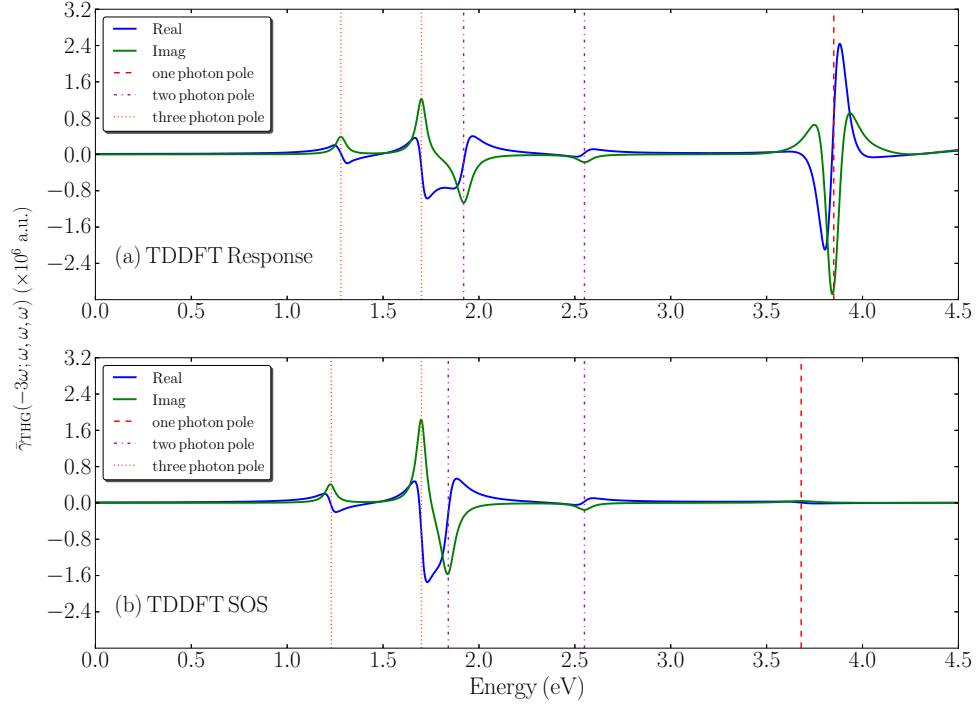


Figure A.5. Simulated THG spectra for LiH using (a) response theory and (b) the SOS approach at the TDDFT level of theory. The vertical “- -”, “- .”, and “. .” lines indicate the one-, two- and three-photon resonances due to the excited states, respectively.

For the pair of both β_{OR} and γ_{OKE} spectra, we note that the zero imaginary part is due to the orientational averaging rather than all zero tensor components. For the pair of γ_{THG} spectra, the magnitude and shape of the second three-photon poles, as well as the first two-photon poles, slightly differ from each other. This is because the band extrema distance (the one within 1.5 to 2.0 eV) in Figure A.5(b) is smaller than that in Figure A.5(a), which causes a more pronounced doubly resonant effect that contributed by the overlap between two- and three-photon resonances.

A.6 Derivation of the spectral representation for the first hyperpolarizability

We start with the first order transformation matrix (U) that can be obtained by solving the follow set of linear equations

$$\begin{pmatrix} U^\alpha(\omega) \\ U^{\alpha\dagger}(-\omega) \end{pmatrix} = - \left[\begin{pmatrix} A & B \\ B^* & A^* \end{pmatrix} - \omega \begin{pmatrix} -1 & 0 \\ 0 & 1 \end{pmatrix} \right]^{-1} \begin{pmatrix} V^\alpha \\ V^\alpha \end{pmatrix}, \quad (\text{A.13})$$

where V^α is the dipole matrix in the MO basis and the spectral representation of the response matrix reads

$$\begin{aligned} & \left[\begin{pmatrix} A & B \\ B^* & A^* \end{pmatrix} - \omega \begin{pmatrix} -1 & 0 \\ 0 & 1 \end{pmatrix} \right]^{-1} = \\ & \sum_n \frac{1}{\omega_n - \omega} \begin{pmatrix} X_n \\ Y_n \end{pmatrix} \begin{pmatrix} X_n \\ Y_n \end{pmatrix}^\dagger + \frac{1}{\omega_n + \omega} \begin{pmatrix} Y_n^* \\ X_n^* \end{pmatrix} \begin{pmatrix} Y_n^* \\ X_n^* \end{pmatrix}^\dagger. \end{aligned} \quad (\text{A.14})$$

Then, the elementary form of the transition dipole moment can be written as

$$\mu_{0n,ia}^\alpha = V_{ia}^\alpha (X_{n,ia} + Y_{n,ia}) \quad (\text{A.15})$$

and

$$\mu_{n0,ia}^\alpha = V_{ia}^\alpha (X_{n,ia}^* + Y_{n,ia}^*), \quad (\text{A.16})$$

where $i, j, \dots \in$ occupied (occ) orbitals, $a, b, \dots \in$ virtual (virt) orbitals, and the Cartesian component is represented as $\alpha, \beta, \gamma, \dots$ to avoid duplicate indices. This leads to the elementary form for the spectral representation of U as

$$U_{ia}^\alpha(+\omega) = \sum_n \frac{X_{n,ia} \mu_{n0,ia}^\alpha}{\omega_n - \omega} + \frac{Y_{n,ia}^* \mu_{0n,ia}^\alpha}{\omega_n + \omega} \quad (\text{A.17})$$

and

$$U_{ia}^{\alpha\dagger}(-\omega) = \sum_n \frac{Y_{n,ia} \mu_{n0,ia}^\alpha}{\omega_n - \omega} + \frac{X_{n,ia}^* \mu_{0n,ia}^\alpha}{\omega_n + \omega}. \quad (\text{A.18})$$

Recall that the trace (Tr) operation in the $2n + 1$ expression for β can be rewritten as the sums over both occ and all (occ + virt) orbitals,⁷⁸ i.e.,

$$\text{Tr}[nU^\alpha G^\beta U^\gamma] = n \sum_i^{\text{occ}} \sum_{kl}^{\text{all}} U_{ik}^\alpha G_{kl}^\beta U_{li}^\gamma \quad (\text{A.19})$$

and

$$\text{Tr}[nU^\alpha U^\gamma G^\beta] = n \sum_i^{\text{occ}} \sum_{kl}^{\text{all}} U_{ik}^\alpha U_{kl}^\gamma G_{li}^\beta. \quad (\text{A.20})$$

Notice that Ref. 78 uses $\text{Tr}[nU^\alpha U^\gamma \varepsilon^\beta]$ in Equation (A.20) but it is valid to replace ε with G here due to the zero diagonal block of U . Using the elementary form of U matrices and the first-order KS matrix

$$G_{ia}^\alpha(\pm\omega) = H_{ia}^\alpha + \sum_{j,b} K_{ia,jb}^{HXC} U_{jb}^\alpha(\pm\omega) + K_{ia,bj}^{HXC} U_{bj}^{\alpha*}(\mp\omega), \quad (\text{A.21})$$

Equations (A.19) and (A.20) can be rewritten as

$$\begin{aligned} n \sum_i^{\text{occ}} \sum_{kl}^{\text{all}} U_{ik}^\alpha(-\omega_\sigma) G_{kl}^\beta(+\omega_1) U_{li}^\gamma(+\omega_2) &= n \sum_i^{\text{occ}} \sum_{kl}^{\text{all}} \left\{ \right. \\ &\left[\sum_m \frac{X_{m,ik} \mu_{m0,ik}^\alpha}{\omega_m + \omega_\sigma} + \frac{Y_{m,ik}^* \mu_{0m,ik}^\alpha}{\omega_m - \omega_\sigma} \right] \left[H_{kl}^\beta + \sum_{j,b} K_{kl,jb}^{HXC} \left(\sum_n \frac{X_{n,jb} \mu_{n0,jb}^\beta}{\omega_n - \omega_1} + \frac{Y_{n,jb}^* \mu_{0n,jb}^\beta}{\omega_n + \omega_1} \right) + \right. \\ &\left. \sum_{j,b} K_{kl,bj}^{HXC} \left(\sum_n \frac{Y_{n,jb} \mu_{n0,jb}^\beta}{\omega_n - \omega_1} + \frac{X_{n,jb}^* \mu_{0n,jb}^\beta}{\omega_n + \omega_1} \right) \right] \left[\sum_p \frac{X_{p,li} \mu_{p0,li}^\gamma}{\omega_p - \omega_2} + \frac{Y_{p,li}^* \mu_{0p,li}^\gamma}{\omega_p + \omega_2} \right] \left. \right\} \end{aligned} \quad (\text{A.22})$$

and

$$\begin{aligned} n \sum_i^{\text{occ}} \sum_{kl}^{\text{all}} U_{ik}^\alpha(-\omega_\sigma) U_{kl}^\gamma(+\omega_1) G_{li}^\beta(+\omega_2) &= n \sum_i^{\text{occ}} \sum_{kl}^{\text{all}} \left\{ \right. \\ &\left[\sum_m \frac{X_{m,ik} \mu_{m0,ik}^\alpha}{\omega_m + \omega_\sigma} + \frac{Y_{m,ik}^* \mu_{0m,ik}^\alpha}{\omega_m - \omega_\sigma} \right] \left[\sum_p \frac{X_{p,kl} \mu_{p0,kl}^\gamma}{\omega_p - \omega_1} + \frac{Y_{p,kl}^* \mu_{0p,kl}^\gamma}{\omega_p + \omega_1} \right] \left[H_{li}^\beta + \sum_{j,b} K_{li,jb}^{HXC} \times \right. \\ &\left. \left(\sum_n \frac{X_{n,jb} \mu_{n0,jb}^\beta}{\omega_n - \omega_2} + \frac{Y_{n,jb}^* \mu_{0n,jb}^\beta}{\omega_n + \omega_2} \right) + \sum_{j,b} K_{li,bj}^{HXC} \left(\sum_n \frac{Y_{n,jb} \mu_{n0,jb}^\beta}{\omega_n - \omega_2} + \frac{X_{n,jb}^* \mu_{0n,jb}^\beta}{\omega_n + \omega_2} \right) \right] \left. \right\}, \end{aligned} \quad (\text{A.23})$$

respectively. We focus on the ALDA in response theory by extracting the terms containing the coupling matrix K^{HXC} from the $2n + 1$ expression of β , in which the one-photon dominant ones are found as

$$\begin{aligned} n \sum_p \sum_{ij}^{\text{occ}} \sum_b^{\text{virt}} \sum_{kl}^{\text{all}} \sum_{mnp \neq 0}^{\text{exc. no.}} &\left[\frac{Y_{m,ik}^* \mu_{0m,ik}^\alpha}{\omega_m - \omega_\sigma} \cdot K_{kl,jb}^{HXC} \cdot \frac{X_{n,jb} \mu_{n0,jb}^\beta}{\omega_n - \omega_1} \cdot \frac{X_{p,li} \mu_{p0,li}^\gamma}{\omega_p - \omega_2} \right. \\ &- \frac{Y_{m,ik}^* \mu_{0m,ik}^\alpha}{\omega_m - \omega_\sigma} \cdot \frac{X_{p,kl} \mu_{p0,kl}^\gamma}{\omega_p - \omega_1} \cdot K_{li,jb}^{HXC} \cdot \frac{X_{n,jb} \mu_{n0,jb}^\beta}{\omega_n - \omega_2} \\ &+ \frac{Y_{m,ik}^* \mu_{0m,ik}^\alpha}{\omega_m - \omega_\sigma} \cdot K_{kl,bj}^{HXC} \cdot \frac{Y_{n,jb} \mu_{n0,jb}^\beta}{\omega_n - \omega_1} \cdot \frac{X_{p,li} \mu_{p0,li}^\gamma}{\omega_p - \omega_2} \\ &\left. - \frac{Y_{m,ik}^* \mu_{0m,ik}^\alpha}{\omega_m - \omega_\sigma} \cdot \frac{X_{p,kl} \mu_{p0,kl}^\gamma}{\omega_p - \omega_1} \cdot K_{li,bj}^{HXC} \cdot \frac{Y_{n,jb} \mu_{n0,jb}^\beta}{\omega_n - \omega_2} \right], \end{aligned} \quad (\text{A.24})$$

For the expression above, X_n and Y_n are the spectral representation of the response vectors obtained from the linear response equations, and \sum_p represents a summation over corresponding terms obtained by permuting $(-2\omega, \alpha)$, $(+\omega, \beta)$, and $(+\omega, \gamma)$. If one considers the SHG case and

takes the finite lifetime of the excited state into account, Equation (A.24) becomes

$$\begin{aligned}
n \sum_p \sum_{ij}^{\text{occ virt}} \sum_b \sum_{kl}^{\text{all}} \sum_{mnp \neq 0}^{\text{exc. no.}} & \left[\frac{Y_{m,ik}^* \mu_{0m,ik}^\alpha \cdot K_{kl,jb}^{HXC} \cdot X_{n,jb} \mu_{n0,jb}^\beta \cdot X_{p,li} \mu_{p0,li}^\gamma}{(\omega_m - 2\omega - i\Gamma)(\omega_n - \omega - i\Gamma)(\omega_p - \omega - i\Gamma)} \right. \\
& - \frac{Y_{m,ik}^* \mu_{0m,ik}^\alpha \cdot X_{p,kl} \mu_{p0,kl}^\gamma \cdot K_{li,jb}^{HXC} \cdot X_{n,jb} \mu_{n0,jb}^\beta}{(\omega_m - 2\omega - i\Gamma)(\omega_p - \omega - i\Gamma)(\omega_n - \omega - i\Gamma)} \\
& + \frac{Y_{m,ik}^* \mu_{0m,ik}^\alpha \cdot K_{kl,bj}^{HXC} \cdot Y_{n,jb} \mu_{n0,jb}^\beta \cdot X_{p,li} \mu_{p0,li}^\gamma}{(\omega_m - 2\omega - i\Gamma)(\omega_n - \omega - i\Gamma)(\omega_p - \omega - i\Gamma)} \\
& \left. - \frac{Y_{m,ik}^* \mu_{0m,ik}^\alpha \cdot X_{p,kl} \mu_{p0,kl}^\gamma \cdot K_{li,bj}^{HXC} \cdot Y_{n,jb} \mu_{n0,jb}^\beta}{(\omega_m - 2\omega - i\Gamma)(\omega_p - \omega - i\Gamma)(\omega_n - \omega - i\Gamma)} \right]. \tag{A.25}
\end{aligned}$$

Notice that, in addition to the part $\sum_p U^\alpha(-\omega_\sigma)[G^\beta(+\omega_1), U^\gamma(+\omega_2)]$ being addressed above, the $2n + 1$ expression of β has another part that contains the second-order xc kernel, i.e.,

$$\text{Tr}[g_{xc}^{\text{ALDA}} D^\alpha(-\omega_\sigma) D^\beta(+\omega_1) D^\gamma(+\omega_2)]. \tag{A.26}$$

This term is also adiabatically approximated and potentially has a significant contribution to β in the vicinity of one-photon poles. However, as shown in Figure A.6, we find it barely affects the shape or intensity of the one-photon structure in the SHG spectrum, and thus was not included within the derivation above.

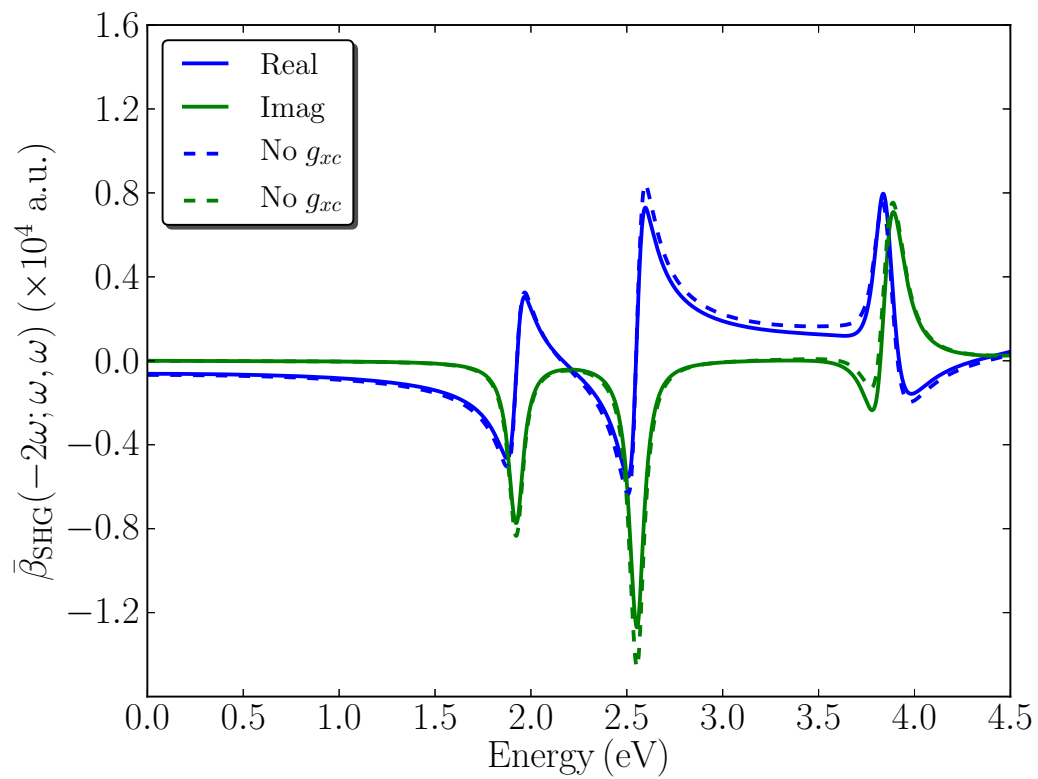


Figure A.6. Simulated SHG spectrum for LiH using response theory at the TDDFT level of theory. The dashed lines indicate the real and imaginary SHG values that were calculated by setting Equation (A.26) equal to zero, respectively

Appendix B

Supporting Information for: Importance of Double-Resonance Effects in Two-Photon Absorption Properties of $\text{Au}_{25}(\text{SR})_{18}^-$

B.1 TPA Cross Sections on a per Gold Atom Basis as a Function of the Cluster Size

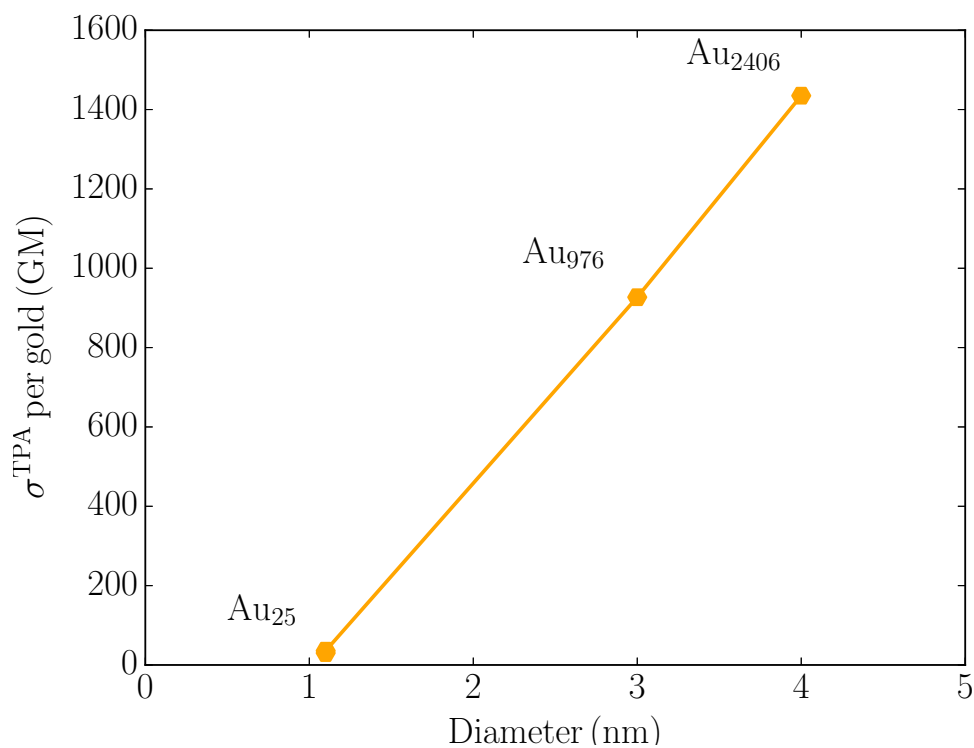


Figure B.1. TPA cross section on a per atom basis for three different gold species. The values for the $\text{Au}_{25}(\text{SH})_{18}^-$ cluster is based on simulations while those for the Au_{976} and the Au_{2406} nanoparticles were obtained using the experimental data from Ref. 2.

Appendix C

Supporting Information for: Surface-Enhanced Resonance Hyper-Raman Scattering Elucidates the Molecular Orientation of Rhodamine 6G on Silver Colloids

C.1 Experimental Methods

Silver colloids were prepared using a modified Lee and Meisel method¹³⁹ that relies on citrate reduction in ultra-pure water. Aliquots of the silver colloid solution were incubated with rhodamine 6G (R6G, Sigma) for 1 hr and then aggregated with 1M NaBr (Alfa Aesar). The same R6G sample (10^{-6} M) was used for all surface-enhanced hyper-Raman scattering (SEHRS) spectra.

A 532 nm pumped optical parametric oscillator (APE, PicoEmerald, ~ 6 ps, 80 MHz) provided fundamental wavelengths at 1064 nm and 820 nm for SEHRS measurements on resonance with S_1 and S_2 , respectively. SEHRS spectra were recorded with laser power/exposure times of 2 mW/30 s for S_1 and 2 mW/2 min for S_2 . The scattered signal was collected in the backscattering geometry on an inverted Nikon microscope (Nikon, Ti-U) with a $20\times$ objective (Nikon, NA=0.5, air), coupled into a dispersive imaging spectrometer (PI Acton Research, $f=0.3$ m, 1200g/mm grating), and detected by a liquid-nitrogen cooled, back-illuminated, Deep Depletion eXcelon CCD (PIXIS, Spec-10, Princeton Instruments). The spectra were background subtracted using a peak-fitting routine in Igor software (Wavemetrics) that assumed Lorentzian peak shape and a cubic baseline.

C.2 Theoretical Methods

Geometry optimization and normal mode calculations were carried out using NWChem at the B3LYP/6-311G* level of theory,⁴¹⁵ where all vibrational frequencies were scaled by a factor of 0.98. These calculations provide detailed information about molecular vibrations and infrared (IR) band intensities, which further aid the mapping of modes between experiment and theory. The components needed for calculating the transition polarizability (α') and hyperpolarizability (β') tensors, i.e., dimensionless displacements (Δ), transition dipole moment derivatives ($d\mu/dQ$), and two-photon transition moment derivatives (dS/dQ), were extracted from the response properties

obtained by Dalton 2.0 at the B3LYP/6-311G* level of theory,⁴¹⁶ where the three-point numerical differentiation is applied. To facilitate comparison with experiment, solvent shifts (0.20 to 0.56 eV) have also been applied to each excitation. The simulation procedure has been previously described in detail;⁹⁷ here, we present a brief version of it by introducing both the Frank-Condon (A-term) and non-Condon (Herzberg-Teller, i.e., B-term) terms involved in the transition response property calculations. After this, we demonstrate the inclusion of surface effects, i.e., the bridge between resonance Raman scattering/resonance hyper-Raman scattering (RRS/RHRS) and their surface-enhanced counterparts, using a dressed-tensors formalism, followed by the differential cross section calculations.

C.2.1 Transition Response Properties for Molecules

In the vibronic coupling model,⁹⁷ the transition polarizability can be written as $\alpha' = A + B$. With respect to the k th excited state, the A- and B-terms are given as

$$A = \sum_k (\mu^{0k})^{\text{eq}} (\mu^{k0})^{\text{eq}} L_a [E^{k0}, \Delta_\nu^{k0}, \omega_\nu, \omega_E, g_k(t)], \quad (\text{C.1})$$

and

$$B = \sum_k \sum_a \left\{ (\mu^{0k})^{\text{eq}} \frac{\partial \mu^{k0}}{\partial Q_a} M_a [E^{k0}, \Delta_\nu^{k0}, \omega_\nu, \omega_E, g_k(t)] + \frac{\partial \mu^{0k}}{\partial Q_a} (\mu^{k0})^{\text{eq}} N_b [E^{k0}, \Delta_\nu^{k0}, \omega_\nu, \omega_E, g_k(t)] \right\}, \quad (\text{C.2})$$

where $(\mu^{0k})^{\text{eq}}$ represents the transition dipole moment evaluated at ground-state equilibrium geometry, $\partial \mu^{0k} / \partial Q_a$ refers to the transition dipole moment derivative with respect to the normal mode. The E^{k0} , Δ_ν^{k0} , ω_ν , ω_E , and $g_k(t)$ stand for the electronic excitation energy, the vibronic coupling constant for the normal mode with frequency ω_ν , the vibrational frequency, the incident frequency, and the broadening function for the k th excited state, respectively. Finally, the L , M_a , and N_b are the line shape functions.

Similarly, the transition hyperpolarizability (β') can also be written in terms of the A- and B-terms. However, due to the additional two-photon transition dipole moment (S^{k0}) involved for β' , the B-term is further divided into the B₁- and B₂-terms, making $\beta' = A + B_1 + B_2$. With respect to the k th excited state, one can also write the A-, B₁-, and B₂-terms here in a similar form as the α' case above, i.e.,

$$A = \sum_k (\mu^{0k})^{\text{eq}} (S^{k0})^{\text{eq}} L [E^{k0}, \Delta_\nu^{k0}, \omega_\nu, \omega_E, g_k(t)], \quad (\text{C.3})$$

$$B_1 = \sum_k \frac{\partial \mu^{0k}}{\partial Q_a} (S^{k0})^{\text{eq}} M_a [E^{k0}, \Delta_\nu^{k0}, \omega_\nu, \omega_E, g_k(t)], \quad (\text{C.4})$$

and

$$B_2 = \sum_k (\mu^{0k})^{\text{eq}} \frac{\partial S^{k0}}{\partial Q_a} N_b [E^{k0}, \Delta_\nu^{k0}, \omega_\nu, \omega_E, g_k(t)], \quad (\text{C.5})$$

where the closure over the intermediate vibrational states has been employed for simplification.

C.2.2 Surface Effects on Transition Response Properties

By combining a dressed-tensors formalism for surface-enhanced Raman scattering (SERS)²⁷⁰ with the time-dependent wave packet formalism⁹⁷ used in this work, the surface effects on the vibronic theory-based α' has been previously achieved.⁴¹⁷ Here, we further extend it to describe the surface effects on the vibronic theory-based β' by adopting a recently developed dressed-tensors formalism for SEHRS.³⁷³ For simplification and efficiency, all surface effects are included by describing the molecule as a point-dipole interacting with the enhanced local field from a spherical nanoparticle (dipolar model). The “dressed” or surface-enhanced α' , i.e., α'^{tot} , can be written as^{270,351,417}

$$\begin{aligned}\alpha'_{\alpha\beta}{}^{\text{tot}} &= [\delta_{\alpha\gamma} + F_{\gamma}^{\text{loc},\alpha}(\omega_S)] \alpha'_{\gamma\delta}(-\omega_S; \omega_L) [\delta_{\beta\delta} + F_{\delta}^{\text{loc},\beta}(\omega_L)] \\ &= [\delta_{\alpha\gamma} + F_{\gamma}^{\text{loc},\alpha}(\omega)] \alpha'_{\gamma\delta}(-\omega; \omega) [\delta_{\beta\delta} + F_{\delta}^{\text{loc},\beta}(\omega)],\end{aligned}\quad (\text{C.6})$$

where $\delta_{\alpha\beta}$ is the Kronecker delta function and $F_{\beta}^{\text{loc},\alpha}$ describes the local field enhancement in the β Cartesian direction resulting from polarization in the α direction. Note that the Einstein summation convention is employed for Greek indices, and the Raman shifted frequency (ω_S) is also assumed to be identical to the incident laser frequency (ω_L), i.e., ω here. The local field from the model nanoparticle is given as²⁷⁰

$$F_{\beta}^{\alpha}(\omega; \mathbf{R}) = \left(\frac{3R_{\beta}R_{\gamma}}{|\mathbf{R}|^5} - \frac{\delta_{\beta\gamma}}{|\mathbf{R}|^3} \right) \alpha_{\gamma\alpha}^S(\omega), \quad (\text{C.7})$$

where \mathbf{R} describes the vector separation between the molecule and dipolar sphere. $\alpha^S(\omega)$ is an isotropic and frequency-dependent polarizability with respect to some coordinate system Q_S , which is given in terms of the sphere radius a and material’s complex and frequency-dependent dielectric constant $\varepsilon(\omega)$ as²⁷⁰

$$\alpha^S(\omega) = a^3 \frac{\varepsilon(\omega) - 1}{\varepsilon(\omega) + 2}. \quad (\text{C.8})$$

Similarly, assuming the hyper-Raman shifted frequency (ω'_S) is the same as twice of the incident frequency (ω_L), the “dressed” or surface-enhanced β' , i.e., β'^{tot} , can be written as^{351,373}

$$\begin{aligned}\beta'_{\alpha\beta\gamma}{}^{\text{tot}} &= [\delta_{\alpha\delta} + F_{\delta}^{\text{loc},\alpha}(\omega'_S)] \beta'_{\delta\epsilon\zeta}(-\omega_S; \omega_L, \omega_L) [\delta_{\beta\epsilon} + F_{\epsilon}^{\text{loc},\beta}(\omega_L)] [\delta_{\gamma\zeta} + F_{\zeta}^{\text{loc},\gamma}(\omega_L)] \\ &= [\delta_{\alpha\delta} + F_{\delta}^{\text{loc},\alpha}(2\omega)] \beta'_{\delta\epsilon\zeta}(-2\omega; \omega, \omega) [\delta_{\beta\epsilon} + F_{\epsilon}^{\text{loc},\beta}(\omega)] [\delta_{\gamma\zeta} + F_{\zeta}^{\text{loc},\gamma}(\omega)].\end{aligned}\quad (\text{C.9})$$

All local fields here can be obtained in the same manner as the SERS case²⁷⁰ because one only needs the nanoparticle radius, the dielectric constant, and the separation vector between the molecule and the nanoparticle. However, it is worth pointing out, unlike the SERS case that only requires the calculation of the local field once, two separate local field calculations are needed for SEHRS due to the noticeable difference between the incident (ω) and scattered (2ω) frequencies.

Although SERS simulations with both local field and field-gradient (FG) effects can provide

orientation information for benzene and pyridine,²⁷⁰ we found for R6G only very small contributions from FG likely due to the dominant A-term scattering in RRS at S_1 . In contrast, SEHRS with local field alone gives orientation information for R6G, attributed to its nonlinearity that yields the dominant B₂-term scattering in RHRS at S_1 . See Section C.3 below for a detailed discussion of the A- and B-term scattering in RRS and RHRS. In the simulations we used a spherical nanoparticle with a diameter of about 100 nm. Note that the diameter only represents the strong local field along the surface normal and not the actual dimensions of the nanoparticles used in the experiments.

C.2.3 Differential Cross Section Calculations

We calculate the differential cross sections for SERS and SEHRS by adopting the same forms previously used for RRS and RHRS, respectively, where a perpendicular measurement of the scattered light is assumed with respect to the incident radiation, and the orientation averaging is performed to take various molecular orientations into account.⁹⁷ For SERS, it is given as

$$\frac{d\sigma}{d\Omega} = \frac{\pi^2}{\epsilon_0^2} \sum_I N_{pI} (\omega - \omega_{p0})^4 \left(\frac{45\alpha_{pI}^2 + 7\gamma_{pI}^2}{45} \right), \quad (\text{C.10})$$

where N_{pI} accounts for the Boltzmann population of mode Q_p (only the lowest vibrational state is often assumed significantly populated), and α_{pI} and γ_{pI} represent the isotropic and anisotropic average of the polarizability, respectively. See Reference 97 for the detailed expressions for N_{pI} , α_{pI} , and γ_{pI} .

The SEHRS differential cross section is given as⁹⁷

$$\frac{d\sigma}{d\Omega} = \frac{16\pi^2 h^3 \alpha^3 (2\omega - \omega_{p0})}{c^2 e^6} \sum_I N_{pI} \sum_{\alpha\beta} \langle (\beta_{\alpha\beta}^{pI}(\omega, Q_p))^2 \rangle, \quad (\text{C.11})$$

where α is a fine structure constant, and the hyper-Raman intensity activity coefficient, $\sum_{\alpha\beta} \langle (\beta_{\alpha\beta}^{pI}(\omega, Q_p))^2 \rangle$, can be further divided into two parts as

$$\sum_{\alpha\beta} \langle (\beta_{\alpha\beta}^{pI}(\omega, Q_p))^2 \rangle = \langle (\beta_{\alpha\alpha}^{pI})^2 \rangle + \langle (\beta_{\alpha\beta}^{pI})^2 \rangle. \quad (\text{C.12})$$

The detailed expressions for $\langle (\beta_{\alpha\alpha}^{pI})^2 \rangle$ and $\langle (\beta_{\alpha\beta}^{pI})^2 \rangle$ can also be found in Reference 97.

C.3 A- and B-Terms in RRS and RHRS of R6G at S_1

RRS of R6G at S_1 is dominated by the A-term scattering due to the large transition dipole moment (μ). For this type of scattering, the key feature of α' is governed by the product of two μ 's, i.e., $\mu^{0k} * \mu^{k0}$, as shown in Eq. C.1. At S_1 , μ mainly lies along the y direction (along the xanthene ring here). Therefore, α'_{yy} is the dominant component in α' for all modes as $\mu_y^{0k} * \mu_y^{k0}$ gives the maximum product. As an illustration, in Figure C.1 we plot the α unit sphere representations of

R6G's modes at 1535.24 and 1657.81 cm^{-1} , where nearly identical features are shown, regardless of the symmetrical or asymmetrical motion of the mode. This clearly differs their β counterparts shown in the Chapter 8.

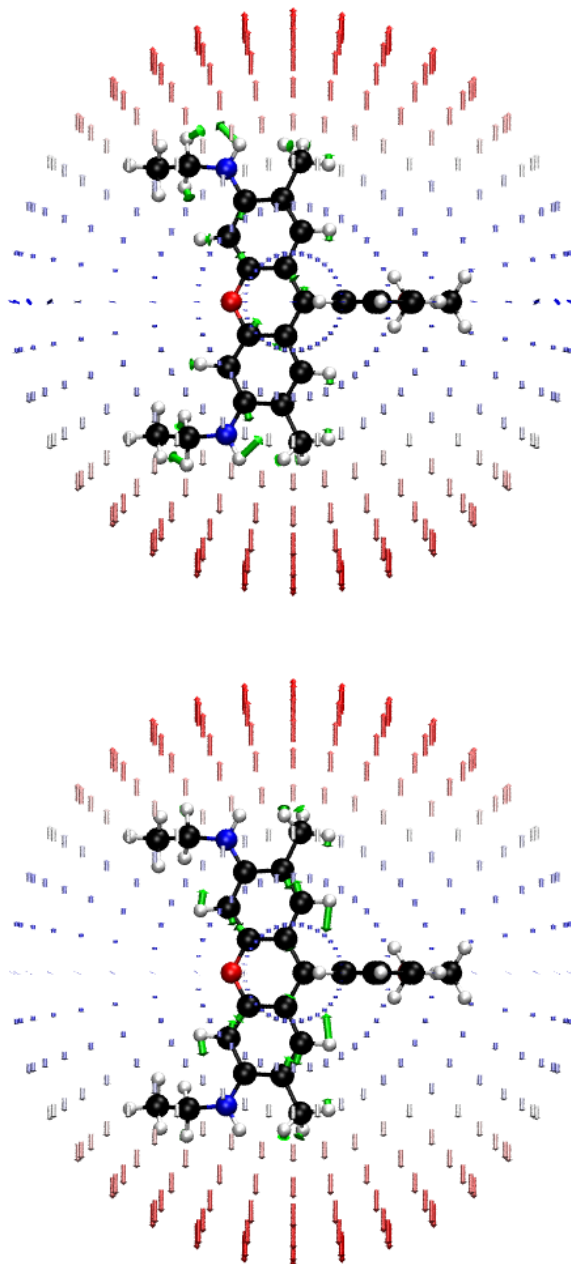


Figure C.1. α unit sphere representations for R6G's modes at (top) 1535.24 and (bottom) 1657.91 cm^{-1} .

RHRS of R6G at S_1 is dominated by the B_2 -term scattering because S_1 is strongly one-photon-allowed but weakly two-photon allowed.¹³⁸ For this type of scattering, the key feature of β' is

governed by the product of μ and the two-photon transition dipole moment derivative (dS/dQ), i.e., $\mu^{0k} * \frac{dS^{k0}}{dQ}$, as shown in Eq. C.5. Although μ mainly lies along the y direction (μ_y^{0k}) as mentioned above, the $\frac{dS^{k0}}{dQ}$ term is given in 6 directions ($xx, yy, zz, xy(yx), xz(zx), yz(zy)$) and differs for all modes. For example, $\frac{dS_{yy}^{k0}}{dQ}$ gives the largest value for the mode at 1535.24 cm^{-1} ; whereas for the mode at 1657.91 cm^{-1} , we find the dominant component is $\frac{dS_{xy}^{k0}}{dQ}$. This kind of behavior can be related to the symmetrical or asymmetrical motions of the modes. Also see Section C.6 for the orientation dependence of the two modes' β_{zzz} components when the surface effects are included. Because of this unique feature at the RHRS level, we can extract orientation information from SEHRS of R6G at S_1 .

C.4 Spectral Matching of the Experimental SEHRS of R6G

We match the simulated and experimental SEHRS spectra of R6G at both S_1 and S_2 simultaneously by comparing the normalized intensities of seven modes between experiment and theory, where the agreement is quantified using a ‘‘spectral distance’’ metric (vide infra). The comparison is made at each pair of θ (ranges from 0° to 180° at a step size of 1°) and ψ (ranges from 0° to 360° at a step size of 1°). The mode mapping (Table C.1) between experiment and theory is based on the assignments reported by Watanabe *et al.*,⁴¹⁸ as well as our own calculated molecular vibrations and IR intensities.

Table C.1. Modes Chosen for Comparison

Nth Mode	Experiment (S_1/S_2) cm^{-1}	Theory cm^{-1}
1st	611.7/618.8	609.67
2nd	1191.0/1189.8	1194.51
3rd	1310.6/1312.6	1321.48
4th	1500.8/1503.3	1507.17
5th	1531.6/1528.1	1535.25
6th	1607.0/1601.9	1621.34
7th	1649.0/1645.9	1657.91

We note that the seven modes chosen here include one with symmetric motion and six with asymmetric motions, where the former one provides the orientation sensitivity while the latter ones ensure the main spectral shapes to be correctly captured. The ‘‘spectral distance’’ metric is calculated at each pair of θ and ψ angles by first normalizing both the experimental and theoretical SEHRS intensities individually, which is given as

$$d = \sqrt{\sum_{i=1}^7 (\text{Exp}_{i\text{th mode}}^{\text{Intensity}} - \text{Theo}_{i\text{th mode}}^{\text{Intensity}})^2}. \quad (\text{C.13})$$

Because of the simultaneous comparisons for data at both S_1 and S_2 , we will always obtain two metric values at each orientation. Therefore, we further take the average of the individual ‘‘distance’’ metric values for both S_1 and S_2 . The heat map shown in Figure 8.5 was generated by

plotting $(1 - d_{\text{norm}})$, where d_{norm} is the normalized distance metric.

C.5 Simulated SEHRS Spectra at Optimal Geometry and Boundary Regions

In this section, we plot the simulated SEHRS spectrum of R6G at S_2 for orienting it to the optimal geometry, i.e., $\theta = 79^\circ$ and $\psi = 79^\circ$. We also plot the simulated SEHRS spectra of R6G at both S_1 and S_2 for four orientations of R6G, i.e., $\theta = 50^\circ$ and $\psi = 75^\circ$, $\theta = 60^\circ$ and $\psi = 90^\circ$, $\theta = 85^\circ$ and $\psi = 90^\circ$, and $\theta = 90^\circ$ and $\psi = 100^\circ$. These four pairs of θ and ψ angles serve as the boundary geometries according to the heat map shown in Figure 8.5. Here, we show that, in comparison to the simulated SEHRS spectrum obtained using the optimal geometry, i.e., $\theta = 79^\circ$ and $\psi = 79^\circ$, none of these four orientations provide simulated SEHRS spectra in better agreement with the experiment.

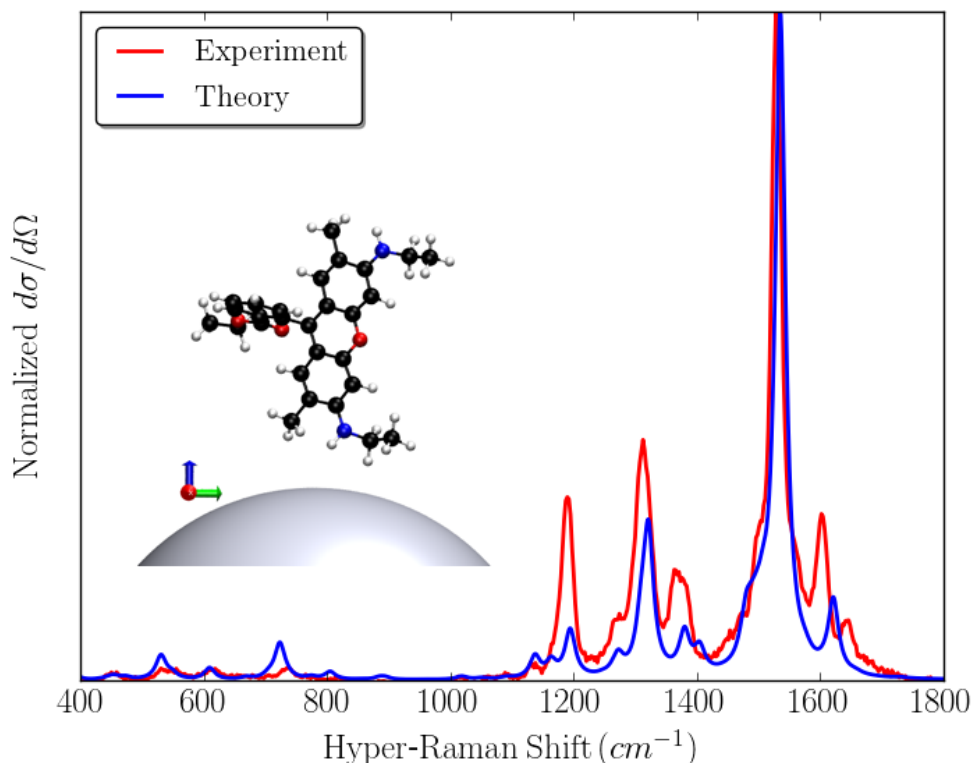


Figure C.2. Comparison between S_2 -experiment (red trace) and S_2 -theory (blue trace) results in the predicted adsorbate geometry shown in the inset $\theta = 79^\circ$ and $\psi = 79^\circ$.

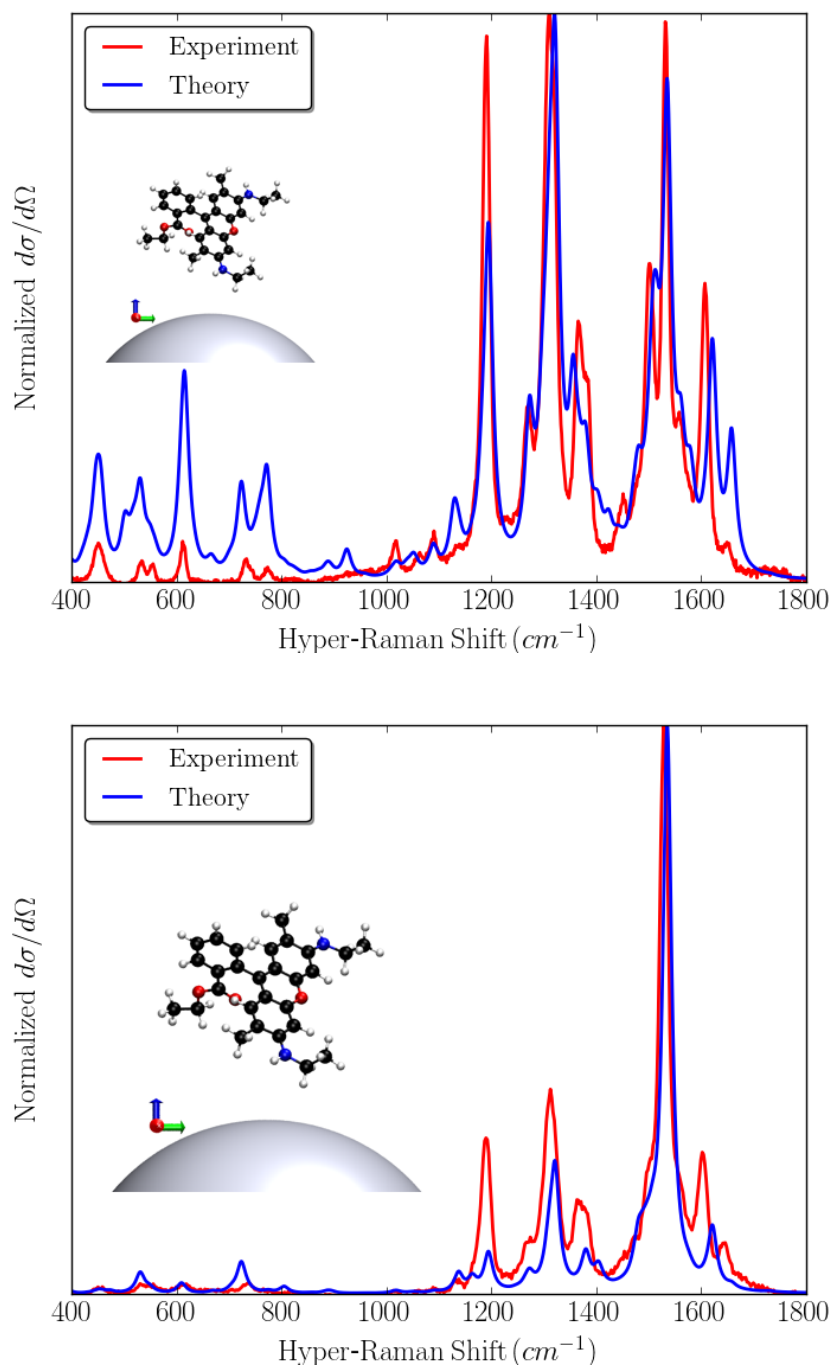


Figure C.3. Comparison between (top) S₁-experiment (red trace) and S₁-theory (blue trace), and (bottom) S₂-experiment (red trace) and S₂-theory (blue trace), results for the adsorbate geometry with $\theta = 50^\circ$ and $\psi = 75^\circ$

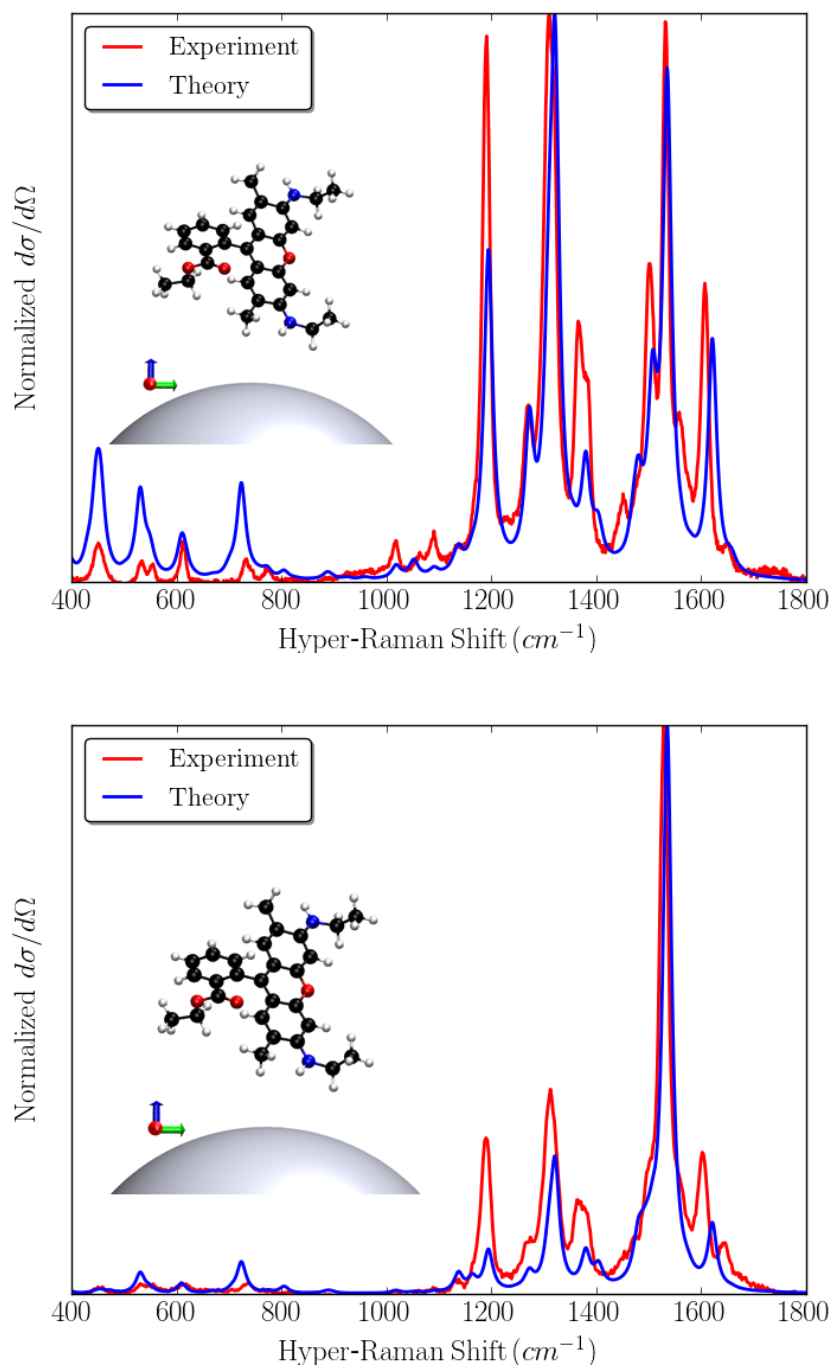


Figure C.4. Comparison between (top) S_1 -experiment (red trace) and S_1 -theory (blue trace), and (bottom) S_2 -experiment (red trace) and S_2 -theory (blue trace), results for the adsorbate geometry with $\theta = 60^\circ$ and $\psi = 90^\circ$

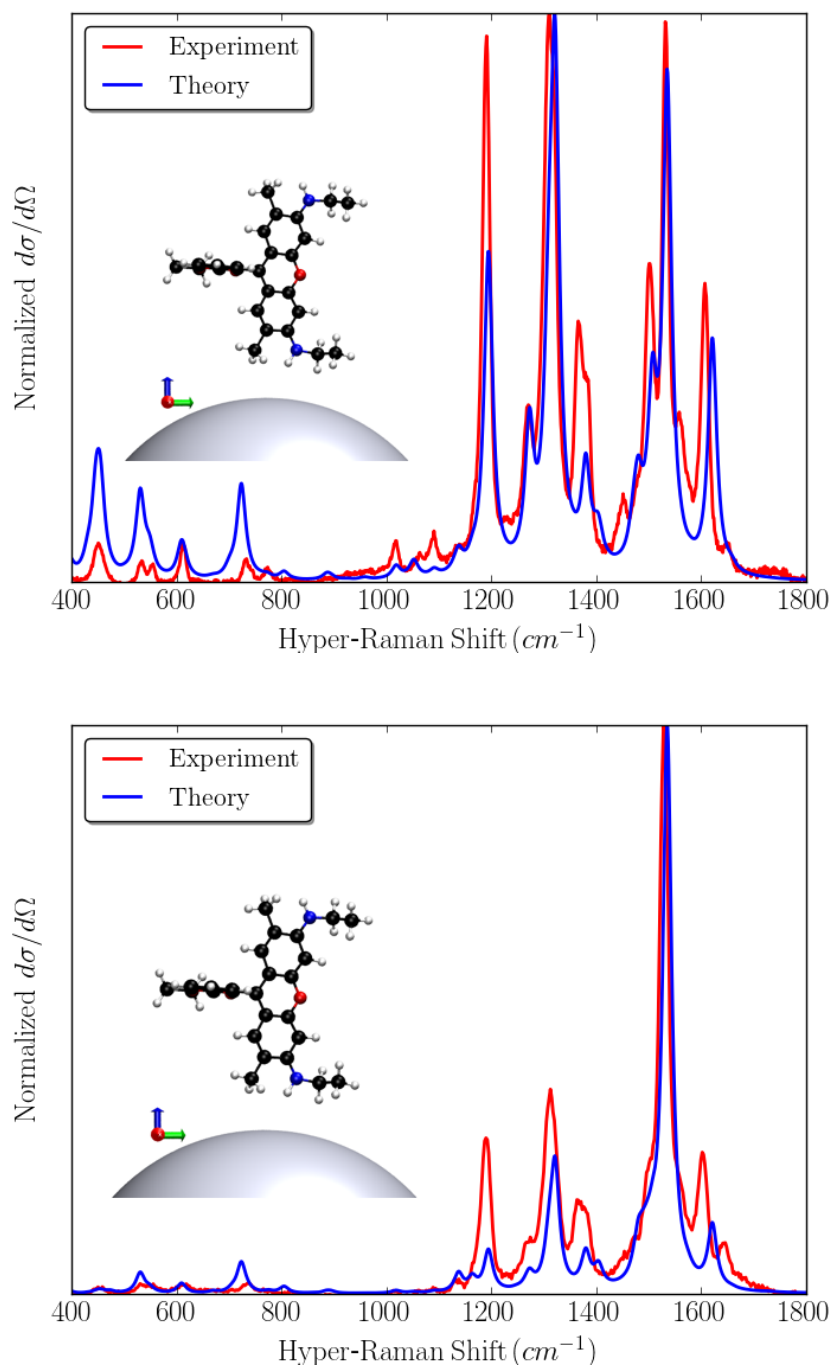


Figure C.5. Comparison between (top) S_1 -experiment (red trace) and S_1 -theory (blue trace), and (bottom) S_2 -experiment (red trace) and S_2 -theory (blue trace), results for the adsorbate geometry with $\psi = 90^\circ$, $\theta = 85^\circ$

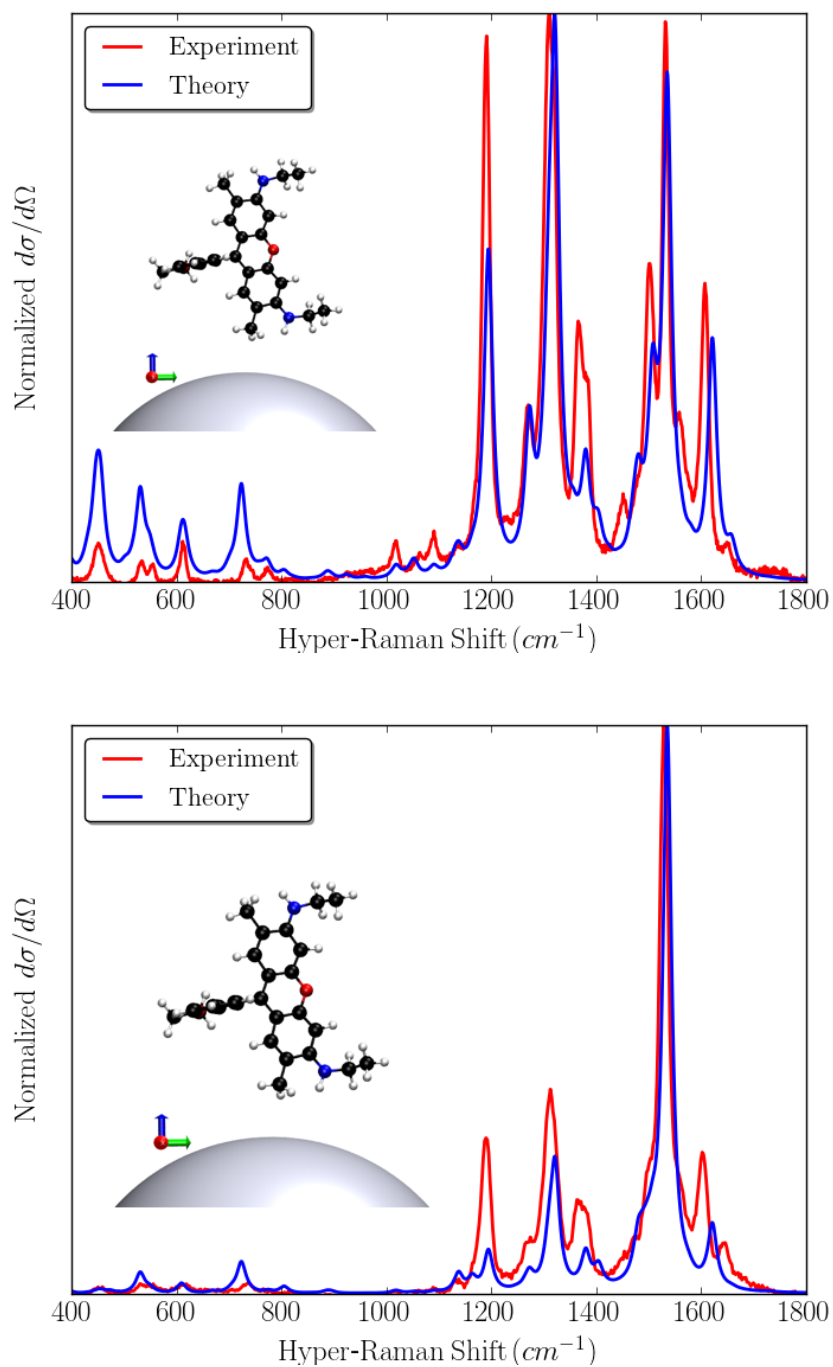


Figure C.6. Comparison between (top) S_1 -experiment (red trace) and S_1 -theory (blue trace), and (bottom) S_2 -experiment (red trace) and S_2 -theory (blue trace), results for the adsorbate geometry with $\theta = 90^\circ$ and $\psi = 100^\circ$

C.6 Orientation Dependence of the β_{zzz} Values

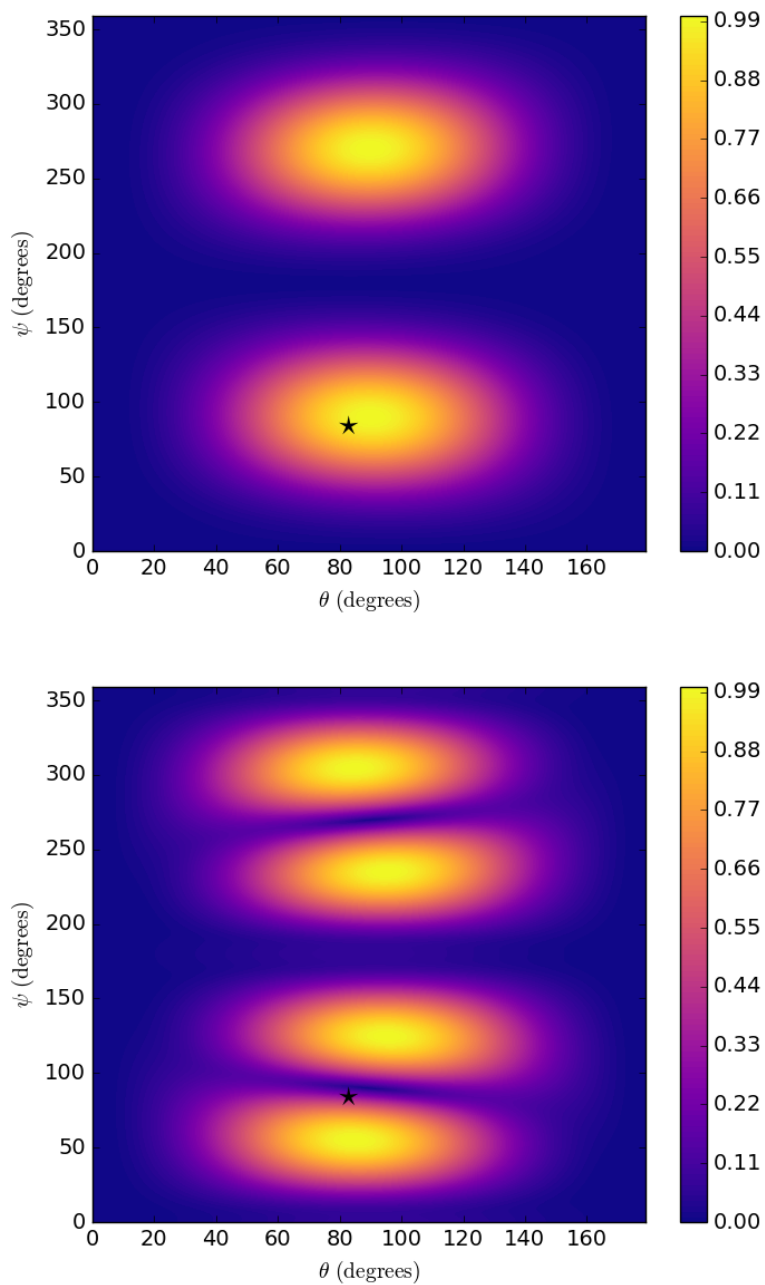


Figure C.7. The β_{zzz} values of (top) mode 1535.24 cm^{-1} and (bottom) mode 1657.91 cm^{-1} depicted as a function of the θ and ψ angles.

Bibliography

- [1] Kanis, D. R.; Ratner, M. A.; Marks, T. J. *Chem. Rev.* **1994**, *94*, 195.
- [2] Ramakrishna, G.; Varnavskit, O.; Kim, J.; Lee, D.; Goodson, T. *J. Am. Chem. Soc.* **2008**, *130*, 5032.
- [3] Kristensen, K.; Kauczor, J.; Kjærgaard, T.; Jørgensen, P. *J. Chem. Phys.* **2009**, *131*, 044112.
- [4] Norman, P.; Bishop, D. M.; Jensen, H. J. A.; Oddershede, J. *J. Chem. Phys.* **2001**, *115*, 10323–10334.
- [5] Jensen, L.; Autschbach, J.; Schatz, G. C. *J. Chem. Phys.* **2005**, *122*, 224115.
- [6] Norman, P.; Bishop, D. M.; Jensen, H. J. A.; Oddershede, J. *J. Chem. Phys.* **2005**, *123*, 194103.
- [7] Clays, K.; Persoons, A. *Phys. Rev. Lett.* **1991**, *66*, 2980–2983.
- [8] Clays, K.; Persoons, A. *Rev. Sci. Instrum.* **1992**, *63*, 3285–3289.
- [9] Clays, K.; Hendrickx, E.; Triest, M.; Verbiest, T.; Persoons, A.; Dehu, C.; Bredas, J. L. *Science* **1993**, *262*, 1419–1422.
- [10] Tutt, L. W.; Kost, A. *Nature* **1992**, *356*, 225–226.
- [11] Parthenopoulos, D. A.; Rentzepis, P. M. *Science* **1989**, *245*, 843–845.
- [12] Hales, J. M.; Matichak, J.; Barlow, S.; Ohira, S.; Yesudas, K.; Brédas, J.-L.; Perry, J. W.; Marder, S. R. *Science* **2010**, *327*, 1485–1488.
- [13] Fuentes-Hernandez, C.; Ramos-Ortiz, G.; Tseng, S.-Y.; Gaj, M. P.; Kippelen, B. *J. Mater. Chem.* **2009**, *19*, 7394–7401.
- [14] Myers Kelley, A. *Ann. Rev. Phys. Chem.* **2010**, *61*, 41–61.
- [15] Long, D. A. *The Raman Effect: A Unified Treatment of the Theory of Raman Scattering by Molecules*; John Wiley & Sons, Ltd.: West Sussex, England, 2002; pp 85–152, 221–270.
- [16] Leng, W.; Myers Kelley, A. *J. Phys. Chem. A* **2008**, *112*, 5925.
- [17] Drobizhev, M.; Karotki, A.; Kruk, M.; Rebane, A. *Chem. Phys. Lett.* **2002**, *355*, 175–182.
- [18] Milojevich, C. B.; Silverstein, D. W.; Jensen, L.; Camden, J. P. *ChemPhysChem* **2011**, *12*, 101–103.
- [19] Ziegler, L. D. *J. Raman Spectrosc.* **1990**, *21*, 769.
- [20] Shimada, R.; Kano, H.; o Hamaguchi, H. *J. Chem. Phys.* **2008**, *129*, 024505.

- [21] Fleischmann, M.; Hendra, P.; McQuillan, A. *Chem. Phys. Lett.* **1974**, *26*, 163 – 166.
- [22] Jeanmaire, D. L.; Van Duyne, R. P. *J. Electroanal. Chem.* **1977**, *84*, 1–20.
- [23] Albrecht, M. G.; Creighton, J. A. *J. Am. Chem. Soc.* **1977**, *99*, 5215–5217.
- [24] Moskovits, M. *Rev. Mod. Phys.* **1985**, *57*, 783–826.
- [25] Sharma, B.; Frontiera, R. R.; Henry, A.-I.; Ringe, E.; Van Duyne, R. P. *Mater. Today* **2012**, *15*, 16–25.
- [26] Jensen, L.; Aikens, C. M.; Schatz, G. C. *Chem. Soc. Rev.* **2008**, *37*, 1061–1073.
- [27] Murphy, D. V.; Raben, K. U. V.; Chang, R. K.; Dorain, P. B. *Chem. Phys. Lett.* **1982**, *85*, 43.
- [28] Golab, J. T.; Sprague, J. R.; Carron, K. T.; Schatz, G. C.; Van Duyne, R. P. *J. Chem. Phys.* **1988**, *88*, 7942–7951.
- [29] Yang, W.-H.; Schatz, G. C. *J. Chem. Phys.* **1992**, *97*, 3831.
- [30] Yang, W.-H.; Hulteen, J.; Schatz, G. C.; Van Duyne, R. P. *J. Chem. Phys.* **1996**, *104*, 4313.
- [31] Lombardi, J. R.; Birke, R. L. *J. Chem. Phys.* **2012**, *136*, 144704.
- [32] Le Ru, E. C.; Etchegoin, P. G. *Ann. Rev. Phys. Chem.* **2012**, *63*, 65–87.
- [33] Hosoi, H.; Yamaguchi, S.; Mizuno, H.; Miyawaki, A.; Tahara, T. *J. Phys. Chem. B* **2008**, *112*, 2761.
- [34] Drobizhev, M.; Tillo, S.; Makarov, N. S.; Hughes, T. E.; Rebane, A. *J. Phys. Chem. B* **2009**, *113*, 855.
- [35] Kim, S.; Ohulchanskyy, T. Y.; Pudavar, H. E.; Pandey, R. K.; Prasad, P. N. *J. Am. Chem. Soc.* **2007**, *129*, 2669–2675.
- [36] Achelle, S.; Couleaud, P.; Baldeck, P.; Teulade-Fichou, M.-P.; Maillard, P. *Eur. J. Org. Chem.* **2011**, *2011*, 1271–1279.
- [37] De Boni, L.; Correa, D. S.; Silva, D. L.; Goncalves, P. J.; Zilio, S. C.; Parra, G. G.; Borissevitch, I. E.; Canuto, S.; Mendonca, C. R. *J. Chem. Phys.* **2011**, *134*, 014509.
- [38] Heesink, G. J. T.; Ruiter, A. G. T.; van Hulst, N. F.; Bölger, B. *Phys. Rev. Lett.* **1993**, *71*, 999–1002.
- [39] Flipse, M. C.; de Jonge, R.; Woudenberg, R. H.; Marsman, A. W.; van Walree, C. A.; Jenneskens, L. W. *Chem. Phys. Lett.* **1995**, *245*, 297 – 303.
- [40] Noordman, O.; van Hulst, N. *Chem. Phys. Lett.* **1996**, *253*, 145 – 150.
- [41] Kaatz, P.; Shelton, D. P. *J. Chem. Phys.* **1996**, *105*, 3918.
- [42] Kaatz, P.; Donley, E. A.; Shelton, D. P. *J. Chem. Phys.* **1998**, *108*, 849–856.
- [43] Olbrechts, G.; Strobbe, R.; Clays, K.; Persoons, A. *Rev. Sci. Instrum.* **1998**, *69*, 2233–2241.
- [44] Hendrickx, E.; Clays, K.; Persoons, A. *Acc. Chem. Res.* **1998**, *31*, 675–683.
- [45] Kuzyk, M. G. *Phys. Rev. Lett.* **2000**, *85*, 1218–1221.

- [46] Kuzyk, M. G. *J. Sel. Top. Quant. Electron.* **2001**, *7*, 774–780.
- [47] Tripathy, K.; Moreno, J. P.; Kuzyk, M. G.; Coe, B. J.; Clays, K.; Kelley, A. M. *J. Chem. Phys.* **2004**, *121*, 7932–7945.
- [48] Johnson, R. C.; Li, J.; Hupp, J. T.; Schatz, G. C. *Chem. Phys. Lett.* **2002**, *356*, 534 – 540.
- [49] Hao, E. C.; Schatz, G. C.; Johnson, R. C.; Hupp, J. T. *J. Chem. Phys.* **2002**, *117*, 5963–5966.
- [50] Nappa, J.; Russier-Antoine, I.; Benichou, E.; Jonin, C.; Brevet, P. F. *J. Chem. Phys.* **2006**, *125*, 184712.
- [51] Russier-Antoine, I.; Benichou, E.; Bachelier, G.; Jonin, C.; Brevet, P. F. *J. Phys. Chem. C* **2007**, *111*, 9044–9048.
- [52] Runge, E.; Gross, E. K. U. *Phys. Rev. Lett.* **1984**, *52*, 997–1000.
- [53] Gross, E. K. U.; Kohn, W. *Adv. Quantum Chem.* **1990**, *21*, 255–291.
- [54] Van Leeuwen, R. *Int. J. Mod. Phys. B* **2001**, *15*, 1969–2023.
- [55] Casida, M. E. In *Recent Advances in Density-Functional Methods*; Chong, D. P., Ed.; World Scientific: Singapore, 1995.
- [56] Casida, M. E. In *Recent Developments and Applications of Modern Density Functional Theory*; Seminario, J. M., Ed.; Elsevier: Amsterdam, 1996.
- [57] Jensen, L.; Zhao, L. L.; Autschbach, J.; Schatz, G. C. *J. Chem. Phys.* **2005**, *123*, 174110.
- [58] Autschbach, J.; Jensen, L.; Schatz, G. C.; Tse, Y. C. E.; Krykunov, M. *J. Phys. Chem. A* **2006**, *110*, 2461–2473.
- [59] Jiemchooraj, A.; Norman, P.; Sernelius, B. E. *J. Chem. Phys.* **2005**, *123*, 124312.
- [60] Ekström, U.; Norman, P.; Carravetta, V.; Ågren, H. *Phys. Rev. Lett.* **2006**, *97*, 143001.
- [61] Norman, P. *AIP Conf. Proc.* **2007**, *963*, 176.
- [62] Milne, B. F.; Norman, P.; Nogueira, F.; Cardoso, C. *Phys. Chem. Chem. Phys.* **2013**, *15*, 14814–14822.
- [63] te Velde, G.; Bickelhaupt, F. M.; Baerends, E. J.; Fonseca Guerra, C.; van Gisbergen, S. J. A.; Snijders, J. G.; Ziegler, T. *J. Comput. Chem.* **2001**, *22*, 931–967.
- [64] Fonseca Guerra, C.; Snijders, J. G.; te Velde, G.; Baerends, E. J. *Theor. Chem. Acc.* **1998**, *99*, 391–403.
- [65] Baerends, E. et al. Amsterdam Density Functional. 2013; <http://www.scm.com>.
- [66] Mikkelsen, K. V.; Luo, Y.; Ågren, H.; Jørgensen, P. *J. Chem. Phys.* **1994**, *100*, 8240–8250.
- [67] Norman, P.; Luo, Y.; Jonsson, D.; Ågren, H.; Sylvester-Hvid, K. O.; Mikkelsen, K. V. *J. Chem. Phys.* **1997**, *107*, 9063–9066.
- [68] Bartkowiak, W.; Zalesny, R.; Niewodniczański, W.; Leszczynski, J. *J. Phys. Chem. A* **2001**, *105*, 10702–10710.
- [69] Jensen, L.; van Duijnen, P. T. *J. Chem. Phys.* **2005**, *123*, 074307.
- [70] Hammond, J. R.; Kowalski, K. *J. Chem. Phys.* **2009**, *130*, 194108.

- [71] Stählerin, M.; Burland, D.; Rice, J. *Chem. Phys. Lett.* **1992**, *191*, 245 – 250.
- [72] Huyskens, F. L.; Huyskens, P. L.; Persoons, A. P. *J. Chem. Phys.* **1998**, *108*, 8161–8171.
- [73] Chui, T. W.; Wong, K. Y. *J. Chem. Phys.* **1998**, *109*, 1391–1396.
- [74] Revillod, G.; Russier-Antoine, I.; Benichou, E.; Jonin, C.; Brevet, P.-F. *J. Phys. Chem. B* **2005**, *109*, 5383–5387.
- [75] Campo, J.; Painelli, A.; Terenziani, F.; Van Regemorter, T.; Beljonne, D.; Goovaerts, E.; Wenseleers, W. *J. Am. Chem. Soc.* **2010**, *132*, 16467–16478.
- [76] Morton, S. M.; Silverstein, D. W.; Jensen, L. *Chem. Rev.* **2011**, *111*, 3962–3994.
- [77] Boyd, R. W. *Nonlinear Optics*; Academic Press: San Diego, CA, 1992.
- [78] Karna, S. P.; Dupuis, M. *J. Comput. Chem.* **1991**, *12*, 487–504.
- [79] van Gisbergen, S. J. A.; Snijders, J. G.; Baerends, E. J. *J. Chem. Phys.* **1998**, *109*, 10644–10656, journal article.
- [80] Krykunov, M.; Autschbach, J. *J. Chem. Phys.* **2005**, *123*, 114103.
- [81] Banerjee, A.; Harbola, M. *Eur. Phys. J. D* **1999**, *5*, 201–206.
- [82] Ye, A.; Autschbach, J. *J. Chem. Phys.* **2006**, *125*, 234101.
- [83] Ángyán, J. G. *J. Math. Chem.* **2009**, *46*, 1–14.
- [84] Rice, J. E.; Amos, R. D.; Colwell, S. M.; Handy, N. C.; Sanz, J. *J. Chem. Phys.* **1990**, *93*, 8828–8839.
- [85] Colwell, S. M.; Murray, C. W.; Handy, N. C.; Amos, R. D. *Chem. Phys. Lett.* **1993**, *210*, 261 – 268.
- [86] Lee, A. M.; Colwell, S. M. *J. Chem. Phys.* **1994**, *101*, 9704–9709.
- [87] Becke, A. D. *Phys. Rev. A* **1988**, *38*, 3098–3100.
- [88] Perdew, J. P. *Phys. Rev. B* **1986**, *33*, 8822–8824.
- [89] Schipper, P. R. T.; Gritsenko, O. V.; van Gisbergen, S. J. A.; Baerends, E. J. *J. Chem. Phys.* **2000**, *112*, 1344–1352.
- [90] Jensen, L.; van Duijnen, P. T.; Snijders, J. G. *J. Chem. Phys.* **2003**, *119*, 12998–13006.
- [91] Sun, H.; Autschbach, J. *ChemPhysChem* **2013**, *14*, 2450–2461.
- [92] van Lenthe, E.; Baerends, E. J.; Snijders, J. G. *J. Chem. Phys.* **1993**, *99*, 4597–4610.
- [93] van Lenthe, E.; Baerends, E. J.; Snijders, J. G. *J. Chem. Phys.* **1994**, *101*, 9783–9792.
- [94] Willetts, A.; Rice, J. E.; Burland, D. M.; Shelton, D. P. *J. Chem. Phys.* **1992**, *97*, 7590–7599.
- [95] Bishop, D. M. *Adv. Quantum Chem.* **1994**, *25*, 1.
- [96] Quinet, O.; Champagne, B.; van Gisbergen, S. J. A. *Int. J. Quantum Chem.* **2005**, *106*, 599.
- [97] Silverstein, D. W.; Jensen, L. *J. Chem. Phys.* **2012**, *136*, 064111.

- [98] Olsen, J.; Jørgensen, P. *J. Chem. Phys.* **1985**, *82*, 3235–3264.
- [99] Kristensen, K.; Kauczor, J.; Thorvaldsen, A. J.; Jørgensen, P.; Kjærgaard, T.; Rizzo, A. *J. Chem. Phys.* **2011**, *134*, 214104.
- [100] Prasad, P. N.; Williams, D. J. *Introduction to nonlinear optical effects in molecules and polymers*; Wiley: New York, 1991.
- [101] Sałek, P.; Helgaker, T.; Vahtras, O.; Ågren, H.; Jonsson, D.; Gauss, J. *Mol. Phys.* **2005**, *103*, 439–450.
- [102] Kosenkov, D.; Slipchenko, L. V. *J. Phys. Chem. A* **2011**, *115*, 392–401.
- [103] Autschbach, J.; Srebro, M. *Acc. Chem. Res.* **2014**, *47*, 2592–2602.
- [104] Audebert, P.; Kamada, K.; Matsunaga, K.; Ohta, K. *Chem. Phys. Lett.* **2003**, *367*, 62–71.
- [105] Myers Kelley, A.; Shoute, L. C. T.; Blanchard-Desce, M.; Bartholomew, G. P.; Bazan, G. C. *Mol. Phys.* **2006**, *104*, 1239–1247.
- [106] Loison, C.; Antoine, R.; Broyer, M.; Dugourd, P.; Guthmuller, J.; Simon, D. *Chem. Eur. J.* **2008**, *14*, 7351–7357.
- [107] Castet, F.; Bogdan, E.; Plaquet, A.; Ducasse, L.; Champagne, B.; Rodriguez, V. *J. Chem. Phys.* **2012**, *136*, 024506.
- [108] Félix, C.; Sieber, C.; Harbich, W.; Buttet, J.; Rabin, I.; Schulze, W.; Ertl, G. *Chem. Phys. Lett.* **1999**, *313*, 105.
- [109] Fedrigo, S.; Harbich, W.; Buttet, J. *Phys. Rev. B* **1993**, *47*, 10706–10715.
- [110] He, G. S.; Tan, L.-S.; Zheng, Q.; Prasad, P. N. *Chem. Rev.* **2008**, *108*, 1245–1330, PMID: 18361528.
- [111] Zipfel, W. R.; Williams, R. M.; Webb, W. W. *Nat. Biotechnol.* **2003**, *21*, 1369–1377.
- [112] Castet, F.; Rodriguez, V.; Pozzo, J.-L.; Ducasse, L.; Plaquet, A.; Champagne, B. *Acc. Chem. Res.* **2013**, *46*, 2656–2665, PMID: 23865890.
- [113] Boyd, R. W. *Nonlinear Optics, 3rd ed.*; Academic Press: Burlington, MA, 2008.
- [114] Roke, S.; Gonella, G. *Ann. Rev. Phys. Chem.* **2012**, *63*, 353–378, PMID: 22263911.
- [115] Zyss, J.; Ledoux, I. *Chem. Rev.* **1994**, *94*, 77–105.
- [116] Le Floch, V.; Brasselet, S.; Zyss, J.; Cho, B. R.; Lee, S. H.; Jeon, S.-J.; Cho, M.; Min, K. S.; Suh, M. P. *Adv. Mater.* **2005**, *17*, 196–200.
- [117] Duxbury, D. F. *Chem. Rev.* **1993**, *93*, 381–433.
- [118] Angeloni, L.; Smulevich, G.; Marzocchi, M. P. *J. Raman Spectrosc.* **1979**, *8*, 305–310.
- [119] Baranov, A. V.; Bobovich, Y. S.; Petrov, V. K. *Zh. Eksp. Theo. Fiz.* **1985**, *88*, 753.
- [120] Lipscomb, L. A.; Nie, S.; Feng, S.; Yu, N.-T. *Chem. Phys. Lett.* **1990**, *170*, 457 – 461.
- [121] Persaud, I.; Grossman, W. E. L. *J. Raman Spectrosc.* **1993**, *24*, 107–112.
- [122] Zyss, J.; Van, T. C.; Dhenaut, C.; Ledoux, I. *Chem. Phys.* **1993**, *177*, 281 – 296.

- [123] Kneipp, K.; Kneipp, H.; Seifert, F. *Chem. Phys. Lett.* **1995**, *233*, 519.
- [124] Schneider, S.; Brehm, G.; Freunschdt, P. *Phys. Status Solidi B* **1995**, *189*, 37–42.
- [125] Kneipp, K.; Kneipp, H.; Itzkan, I.; Dasari, R. R.; Feld, M. S. *Chem. Phys.* **1999**, *247*, 155–162.
- [126] Li, W.-H.; Li, X.-Y.; Yu, N.-T. *Chem. Phys. Lett.* **1999**, *312*, 28.
- [127] Beljonne, D.; Wenseleers, W.; Zojer, E.; Shuai, Z.; Vogel, H.; Pond, S.; Perry, J.; Marder, S.; Brédas, J.-L. *Adv. Funct. Mater.* **2002**, *12*, 631–641.
- [128] Rao, Y.; Guo, X.-m.; Tao, Y.-S.; Wang, H.-f. *J. Phys. Chem. A* **2004**, *108*, 7977–7982.
- [129] Kneipp, H.; Kneipp, K. *J. Raman Spectrosc.* **2005**, *36*, 551.
- [130] Kneipp, J.; Kneipp, H.; Kneipp, K. *Proc. Natl. Acad. Sci. USA* **2006**, *103*, 17149.
- [131] Leng, W.; Yasseri, A. A.; Sharma, S.; Li, Z.; Woo, H. Y.; Vak, D.; Bazan, G. C.; Myers Kelley, A. *Anal. Chem.* **2006**, *78*, 6279.
- [132] Leng, W.; Myers Kelley, A. *J. Am. Chem. Soc.* **2006**, *128*, 3492–3493.
- [133] Ikeda, K.; Takase, M.; Sawai, Y.; Nabika, H.; Murakoshi, K.; Uosaki, K. *J. Chem. Phys.* **2007**, *127*, 111103.
- [134] Morton, S. M.; Jensen, L. *J. Chem. Phys.* **2010**, *133*, 074103.
- [135] Milojevic, C. B.; Mandrell, B. K.; Turley, H. K.; Iberi, V.; Best, M. D.; Camden, J. P. *J. Phys. Chem. Lett.* **2013**, *4*, 3420–3423.
- [136] Darby, B. L.; Auguié, B.; Meyer, M.; Pantoja, A. E.; Le Ru, E. C. *Nat. Photonics* **2016**, *10*, 40–45.
- [137] Milojevic, C. B.; Silverstein, D. W.; Jensen, L.; Camden, J. P. *J. Am. Chem. Soc.* **2011**, *133*, 14590.
- [138] Milojevic, C. B.; Silverstein, D. W.; Jensen, L.; Camden, J. P. *J. Phys. Chem. C* **2013**, *117*, 3046–3054.
- [139] Lee, P. C.; Meisel, D. *J. Phys. Chem.* **1982**, *86*, 3391–3395.
- [140] Hu, Z.; Autschbach, J.; Jensen, L. *J. Chem. Phys.* **2014**, *141*, 124305.
- [141] Baerends, E. et al. Amsterdam Density Functional. 2014.
- [142] Chung, Y. C.; Ziegler, L. D. *J. Chem. Phys.* **1988**, *88*, 7287.
- [143] Simmons, P. D.; Turley, H. K.; Silverstein, D. W.; Jensen, L.; Camden, J. P. *J. Phys. Chem. Lett.* **2015**, *6*, 5067–5071.
- [144] Ehrlich, J. E.; Wu, X. L.; Lee, I.-Y. S.; Hu, Z.-Y.; Röckel, H.; Marder, S. R.; Perry, J. W. *Opt. Lett.* **1997**, *22*, 1843–1845.
- [145] W. Spangler, C. *J. Mater. Chem.* **1999**, *9*, 2013–2020.
- [146] Neto, N. M. B.; Oliveira, S. L.; Misoguti, L.; Mendonca, C. R.; Goncalves, P. J.; Borissevitch, I. E.; Dinelli, L. R.; Romualdo, L. L.; Batista, A. A.; Zilio, S. C. *J. Appl. Phys.* **2006**, *99*, 123103.

- [147] Hales, J. M.; Cozzuol, M.; Screen, T. E. O.; Anderson, H. L.; Perry, J. W. *Opt. Express* **2009**, *17*, 18478–18488.
- [148] Strickler, J. H.; Webb, W. W. *Opt. Lett.* **1991**, *16*, 1780–1782.
- [149] Shen, Y.; Swiatkiewicz, J.; Jakubczyk, D.; Xu, F.; Prasad, P. N.; Vaia, R. A.; Reinhardt, B. A. *Appl. Opt.* **2001**, *40*, 938–940.
- [150] Corredor, C. C.; Huang, Z.-L.; Belfield, K. D.; Morales, A. R.; Bondar, M. V. *Chem. Mater.* **2007**, *19*, 5165–5173.
- [151] Dvornikov, A. S.; Walker, E. P.; Rentzepis, P. M. *J. Phys. Chem. A* **2009**, *113*, 13633–13644.
- [152] Köhler, R. H.; Cao, J.; Zipfel, W. R.; Webb, W. W.; Hanson, M. R. *Science* **1997**, *276*, 2039–2042.
- [153] Miller, M. J.; Wei, S. H.; Parker, I.; Cahalan, M. D. *Science* **2002**, *296*, 1869–1873.
- [154] Zipfel, W. R.; Williams, R. M.; Christie, R.; Nikitin, A. Y.; Hyman, B. T.; Webb, W. W. *Proc. Natl. Acad. Sci. USA* **2003**, *100*, 7075–7080.
- [155] Clark, T. B.; Orr, M. E.; Flynn, D. C.; Goodson, T. *J. Phys. Chem. C* **2011**, *115*, 7331–7338.
- [156] Mizrahi, V.; Saifi, M. A.; Andrejco, M. J.; DeLong, K. W.; Stegeman, G. I. *Opt. Lett.* **1989**, *14*, 1140–1142.
- [157] Nanda, K. D.; Krylov, A. I. *J. Chem. Phys.* **2015**, *142*, 064118.
- [158] Helgaker, T.; Coriani, S.; Jørgensen, P.; Kristensen, K.; Olsen, J.; Ruud, K. *Chem. Rev.* **2012**, *112*, 543–631.
- [159] Macak, P.; Luo, Y.; Ågren, H. *Chem. Phys. Lett.* **2000**, *330*, 447.
- [160] Kamarchik, E.; Krylov, A. I. *J. Phys. Chem. Lett.* **2011**, *2*, 488–492.
- [161] Silverstein, D. W.; Jensen, L. *J. Chem. Phys.* **2012**, *136*, 064110.
- [162] Bishop, D. M.; Kirtman, B.; Kurtz, H. A.; Rice, J. E. *J. Chem. Phys.* **1993**, *98*, 8024–8030.
- [163] Bishop, D. M.; Pipin, J.; Kirtman, B. *J. Chem. Phys.* **1995**, *102*, 6778–6786.
- [164] Ingamells, V. E.; Papadopoulos, M. G.; Raptis, S. G. *Chem. Phys. Lett.* **1999**, *307*, 484–492.
- [165] Torruellas, W. E.; Zaroni, R.; Stegeman, G. I.; Möhlmann, G. R.; Erdhuisen, E. W. P.; Horsthuis, W. H. G. *J. Chem. Phys.* **1991**, *94*, 6851–6856.
- [166] Beljonne, D.; Brédas, J. L.; Cha, M.; Torruellas, W. E.; Stegeman, G. I.; Hofstraat, J. W.; Horsthuis, W. H. G.; Möhlmann, G. R. *J. Chem. Phys.* **1995**, *103*, 7834–7843.
- [167] Antonov, L.; Kamada, K.; Ohta, K.; Kamounah, F. S. *Phys. Chem. Chem. Phys.* **2003**, *5*, 1193–1197.
- [168] Day, P. N.; Nguyen, K. A.; Pachter, R. *J. Phys. Chem. B* **2005**, *109*, 1803–1814.
- [169] Day, P. N.; Nguyen, K. A.; Pachter, R. *J. Chem. Phys.* **2006**, *125*, 094103.
- [170] Autschbach, J. *ChemPhysChem* **2011**, *12*, 3224–3235.
- [171] Jansik, B.; Salek, P.; Jonsson, D.; Vahtras, O.; Ågren, H. *J. Chem. Phys.* **2005**, *122*, 054107.

- [172] Orr, B.; Ward, J. *Mol. Phys.* **1971**, *20*, 513–526.
- [173] Pérez-Moreno, J.; Kuzyk, M. G. *J. Chem. Phys.* **2005**, *123*, 194101.
- [174] Pérez-Moreno, J.; Clays, K.; Kuzyk, M. G. *J. Chem. Phys.* **2008**, *128*, 084109.
- [175] McClain, W. M. *J. Chem. Phys.* **1971**, *55*, 2789.
- [176] Beerepoot, M. T. P.; Friese, D. H.; List, N. H.; Kongsted, J.; Ruud, K. *Phys. Chem. Chem. Phys.* **2015**, *17*, 19306–19314.
- [177] Göppert-Mayer, M. *Ann. Phys.* **1931**, *401*, 273.
- [178] "DALTON, a molecular electronic structure program, Release Dalton2011 (2011), see <http://daltonprogram.org/>".
- [179] Shelton, D. P.; Rice, J. E. *Chem. Rev.* **1994**, *94*, 3–29.
- [180] Bishop, D. M. *Rev. Mod. Phys.* **1990**, *62*, 343–374.
- [181] Hättig, C.; Christiansen, O.; Jørgensen, P. *Chem. Phys. Lett.* **1998**, *282*, 139–146.
- [182] Dalgaard, E. *Phys. Rev. A* **1982**, *26*, 42–52.
- [183] Li, Z.; Suo, B.; Liu, W. *J. Chem. Phys.* **2014**, *141*, 244105.
- [184] Ou, Q.; Bellchambers, G. D.; Furche, F.; Subotnik, J. E. *J. Chem. Phys.* **2015**, *142*, 064114.
- [185] Subotnik, J. E.; Alguire, E. C.; Ou, Q.; Landry, B. R.; Fatehi, S. *Acc. Chem. Res.* **2015**, *48*, 1340–1350.
- [186] Eriksen, J. J.; Sauer, S. P.; Mikkelsen, K. V.; Christiansen, O.; Jensen, H. J. A.; Kongsted, J. *Mol. Phys.* **2013**, *111*, 1235–1248.
- [187] Daniel, M.-C.; Astruc, D. *Chem. Rev.* **2004**, *104*, 293.
- [188] Hakkinen, H. *Chem. Soc. Rev.* **2008**, *37*, 1847–1859.
- [189] Jin, R. *Nanoscale* **2010**, *2*, 343.
- [190] Dreaden, E. C.; Alkilany, A. M.; Huang, X.; Murphy, C. J.; El-Sayed, M. A. *Chem. Soc. Rev.* **2012**, *41*, 2740–2779.
- [191] Fernando, A.; Weerawardene, K. L. D. M.; Karimova, N. V.; Aikens, C. M. *Chem. Rev.* **2015**, *115*, 6112–6216, PMID: 25898274.
- [192] Jin, R.; Zeng, C.; Zhou, M.; Chen, Y. *Chem. Rev.* **2016**, *116*, 10346–10413, PMID: 27585252.
- [193] Qian, H.; Zhu, Y.; Jin, R. *Proc. Natl. Acad. Sci. USA* **2012**, *109*, 696–700.
- [194] Malola, S.; Lehtovaara, L.; Enkovaara, J.; Häkkinen, H. *ACS Nano* **2013**, *7*, 10263–10270.
- [195] Jadzinsky, P. D.; Calero, G.; Ackerson, C. J.; Bushnell, D. A.; Kornberg, R. D. *Science* **2007**, *318*, 430–433.
- [196] Heaven, M. W.; Dass, A.; White, P. S.; Holt, K. M.; Murray, R. W. *J. Am. Chem. Soc.* **2008**, *130*, 3754.
- [197] Akola, J.; Walter, M.; Whetten, R. L.; Häkkinen, H.; Grönbeck, H. *J. Am. Chem. Soc.* **2008**, *130*, 3756.

- [198] Zhu, M.; Aikens, C. M.; Hollander, F. J.; Schatz, G. C.; Jin, R. *J. Am. Chem. Soc.* **2008**, *130*, 5883.
- [199] Walter, M.; Akola, J.; Lopez-Acevedo, O.; Jadzinsky, P. D.; Calero, G.; Ackerson, C. J.; Whetten, R. L.; Grönbeck, H.; Häkkinen, H. *Proc. Natl. Acad. Sci. USA* **2008**, *105*, 9157.
- [200] Aikens, C. M. *J. Phys. Chem. C* **2008**, *112*, 19797.
- [201] Aikens, C. M. *J. Phys. Chem. A* **2009**, *113*, 10811.
- [202] Yau, S. H.; Varnavski, O.; Theodore Goodson, I. *Acc. Chem. Res.* **2013**, *46*, 1506–1516, PMID: 23651457.
- [203] Philip, R.; Chantharasupawong, P.; Qian, H.; Jin, R.; Thomas, J. *Nano Lett.* **2012**, *12*, 4661–4667, PMID: 22845756.
- [204] Russier-Antoine, I.; Bertorelle, F.; Vojkovic, M.; Rayane, D.; Salmon, E.; Jonin, C.; Dugourd, P.; Antoine, R.; Brevet, P.-F. *nanoscale* **2014**, *6*, 13572–13578.
- [205] Knoppe, S.; Vanbel, M.; van Cleuvenbergen, S.; Vanpraet, L.; Bürgi, T.; Verbiest, T. *J. Phys. Chem. C* **2015**, *119*, 6221–6226.
- [206] Olesiak-Banska, J.; Waszkielewicz, M.; Matczyszyn, K.; Samoc, M. *RSC Adv.* **2016**, *6*, 98748–98752.
- [207] Knoppe, S.; Häkkinen, H.; Verbiest, T. *J. Phys. Chem. C* **2015**, *119*, 27676–27682.
- [208] Van Steerteghem, N.; Van Cleuvenbergen, S.; Deckers, S.; Kumara, C.; Dass, A.; Hakkinen, H.; Clays, K.; Verbiest, T.; Knoppe, S. *Nanoscale* **2016**, *8*, 12123–12127.
- [209] Day, P. N.; Nguyen, K. A.; Pachter, R. *J. Chem. Theor. Comput.* **2010**, *6*, 2809.
- [210] Qian, H.; Xiao, Y.; Liu, Z. *Nature Comm.* **2016**, *7*, 13153.
- [211] Hu, Z.; Autschbach, J.; Jensen, L. *J. Chem. Theor. Comput.* **2016**, *12*, 1294–1304, PMID: 26841327.
- [212] Ensley, T. R.; Hu, H.; Reichert, M.; Ferdinandus, M. R.; Peceli, D.; Hales, J. M.; Perry, J. W.; Li, Z.; Jang, S.-H.; Jen, A. K.-Y.; Marder, S. R.; Hagan, D. J.; Stryland, E. W. V. *J. Opt. Soc. Am. B* **2016**, *33*, 780–796.
- [213] Aikens, C. M. *J. Phys. Chem. Lett.* **2011**, *2*, 99–104, PMID: 26295527.
- [214] Devadas, M. S.; Bairu, S.; Qian, H.; Sinn, E.; Jin, R.; Ramakrishna, G. *J. Phys. Chem. Lett.* **2011**, *2*, 2752–2758.
- [215] Zhang, H.-F.; Stender, M.; Zhang, R.; Wang, C.; Li, J.; Wang, L.-S. *J. Phys. Chem. B* **2004**, *108*, 12259–12263.
- [216] Terenziani, F.; Katan, C.; Badaeva, E.; Tretiak, S.; Blanchard-Desce, M. *Adv. Mater.* **2008**, *20*, 4641–4678.
- [217] Day, P. N.; Pachter, R.; Nguyen, K. A.; Bigioni, T. P. *J. Phys. Chem. A* **2016**, *120*, 507–518, PMID: 26730764.
- [218] Sanader, Z.; Krstic, M.; Russier-Antoine, I.; Bertorelle, F.; Dugourd, P.; Brevet, P.-F.; Antoine, R.; Bonacic-Koutecky, V. *Phys. Chem. Chem. Phys.* **2016**, *18*, 12404–12408.

- [219] Parker, S. M.; Roy, S.; Furche, F. *J. Chem. Phys.* **2016**, *145*, 134105.
- [220] Vigil, S. R.; Kuzyk, M. G. *J. Opt. Soc. Am. B* **2001**, *18*, 679–691.
- [221] Willets, K. A.; Van Duyne, R. P. *Ann. Rev. Phys. Chem.* **2007**, *58*, 267–297.
- [222] Zhang, R.; Zhang, Y.; Dong, Z. C.; Jiang, S.; Zhang, C.; Chen, L. G.; Zhang, L.; Liao, Y.; Aizpurua, J.; Luo, Y.; Yang, J. L.; Hou, J. G. *Nature* **2013**, *498*, 82–86.
- [223] Sonntag, M. D.; Pozzi, E. A.; Jiang, N.; Hersam, M. C.; Duyne, R. P. V. *J. Phys. Chem. Lett.* **2014**, *5*, 3125–3130, PMID: 26276323.
- [224] Keller, E. L.; Brandt, N. C.; Cassabaum, A. A.; Frontiera, R. R. *Analyst* **2015**, *140*, 4922–4931.
- [225] Le Ru, E. C.; Meyer, M.; Etchegoin, P. G. *J. Phys. Chem. B* **2006**, *110*, 1944–1948.
- [226] Dieringer, J. A.; Lettan, R. B.; Scheidt, K. A.; Van Duyne, R. P. *J. Am. Chem. Soc.* **2007**, *129*, 16249–16256.
- [227] Sonntag, M. D.; Klingsporn, J. M.; Garibay, L. K.; Roberts, J. M.; Dieringer, J. A.; Seideman, T.; Scheidt, K. A.; Jensen, L.; Schatz, G. C.; Van Duyne, R. P. *J. Phys. Chem. C* **2012**, *116*, 478–483.
- [228] Zhang, Y.; Zhen, Y.-R.; Neumann, O.; Day, J. K.; Nordlander, P.; Halas, N. J. *Nature Comm.* **2014**, *5*, 4424.
- [229] Payton, J. L.; Morton, S. M.; Moore, J. E.; Jensen, L. *Acc. Chem. Res.* **2014**, *47*, 88–99.
- [230] Osawa, M.; Matsuda, N.; Yoshii, K.; Uchida, I. *J. Phys. Chem.* **1994**, *98*, 12702–12707.
- [231] Wu, D.-Y.; Liu, X.-M.; Huang, Y.-F.; Ren, B.; Xu, X.; Tian, Z.-Q. *J. Phys. Chem. C* **2009**, *113*, 18212–18222.
- [232] Huang, Y.-F.; Zhu, H.-P.; Liu, G.-K.; Wu, D.-Y.; Ren, B.; Tian, Z.-Q. *J. Am. Chem. Soc.* **2010**, *132*, 9244–9246.
- [233] Zhao, L. L.; Jensen, L.; Schatz, G. C. *Nano Lett.* **2006**, *6*, 1229–1234.
- [234] Jensen, L.; Zhao, L. L.; Schatz, G. C. *J. Phys. Chem. C* **2007**, *111*, 4756–4764.
- [235] King, F. W.; Duyne, R. P. V.; Schatz, G. C. *J. Chem. Phys.* **1978**, *69*, 4472–4481.
- [236] Moskovits, M. *J. Chem. Phys.* **1978**, *69*, 4159–4161.
- [237] Moskovits, M. *Solid State Commun.* **1979**, *32*, 59–62.
- [238] Kerker, M.; Wang, D.-S.; Chew, H. *Appl. Opt.* **1980**, *19*, 4159–4174.
- [239] Gersten, J. I. *J. Chem. Phys.* **1980**, *72*, 5779–5780.
- [240] Gersten, J. I. *J. Chem. Phys.* **1980**, *72*, 5780–5781.
- [241] Gersten, J.; Nitzan, A. *J. Chem. Phys.* **1980**, *73*, 3023–3037.
- [242] Metiu, H.; Das, P. *Ann. Rev. Phys. Chem.* **1984**, *35*, 507–536.
- [243] Moskovits, M. *J. Raman Spectrosc.* **2005**, *36*, 485–496.

- [244] Le Ru, E. C.; Etchegoin, P. G. *Principles of Surface-Enhanced Raman Spectroscopy*; Elsevier, 2009.
- [245] Silberstein, L. *Philos. Mag.* **1917**, *33*, 521–533.
- [246] Jensen, L.; Astrand, P.; Osted, A.; Kongsted, J.; Mikkelsen, K. *J. Chem. Phys.* **2002**, *116*, 4001–4010.
- [247] Sonntag, M. D.; Chulhai, D.; Seideman, T.; Jensen, L.; Van Duyne, R. P. *J. Am. Chem. Soc.* **2013**, *135*, 17187–17192.
- [248] Chulhai, D. V.; Jensen, L. *J. Phys. Chem. A* **2014**, *118*, 9069–9079.
- [249] Efrima, S.; Metiu, H. *J. Chem. Phys.* **1979**, *70*, 1602–1613.
- [250] Efrima, S.; Metiu, H. *J. Chem. Phys.* **1979**, *70*, 1939–1947.
- [251] Efrima, S.; Metiu, H. *J. Chem. Phys.* **1979**, *70*, 2297–2309.
- [252] Litz, J. P.; Brewster, R. P.; Lee, A. B.; Masiello, D. J. *J. Phys. Chem. C* **2013**, *117*, 12249–12257.
- [253] Masiello, D. J. *Int. J. Quantum Chem.* **2014**, *114*, 1413–1420.
- [254] Corni, S.; Tomasi, J. *J. Chem. Phys.* **2001**, *114*, 3739–3751.
- [255] Corni, S.; Tomasi, J. *J. Chem. Phys.* **2002**, *117*, 7266–7278.
- [256] Corni, S.; Tomasi, J. *J. Chem. Phys.* **2002**, *116*, 1156–1164.
- [257] Jørgensen, S.; Ratner, M. A.; Mikkelsen, K. V. *J. Chem. Phys.* **2001**, *115*, 3792–3803.
- [258] Neuhauser, D.; Lopata, K. *J. Chem. Phys.* **2007**, *127*, 154715.
- [259] Lopata, K.; Neuhauser, D. *J. Chem. Phys.* **2009**, *130*, 104707.
- [260] Arcisauskaitė, V.; Kongsted, J.; Hansen, T.; Mikkelsen, K. V. *Chem. Phys. Lett.* **2009**, *470*, 285–288.
- [261] Masiello, D. J.; Schatz, G. C. *Phys. Rev. A* **2008**, *78*, 042505.
- [262] Masiello, D. J.; Schatz, G. C. *J. Chem. Phys.* **2010**, *132*, 064102.
- [263] Chen, H.; McMahon, J. M.; Ratner, M. A.; Schatz, G. C. *J. Phys. Chem. C* **2010**, *114*, 14384–14392.
- [264] Watson, M. A.; Rappoport, D.; Lee, E. M. Y.; Olivares-Amaya, R.; Aspuru-Guzik, A. *J. Chem. Phys.* **2012**, *136*, 024101–14.
- [265] Jensen, L. L.; Jensen, L. *J. Phys. Chem. C* **2008**, *112*, 15697–15703.
- [266] Jensen, L. L.; Jensen, L. *J. Phys. Chem. C* **2009**, *113*, 15182–15190.
- [267] Morton, S. M.; Jensen, L. *J. Chem. Phys.* **2011**, *135*, 134103.
- [268] Payton, J. L.; Morton, S. M.; Moore, J. E.; Jensen, L. *J. Chem. Phys.* **2012**, *136*, 214103.
- [269] Janesko, B. G.; Scuseria, G. E. *J. Chem. Phys.* **2006**, *125*, 124704.
- [270] Chulhai, D. V.; Jensen, L. *J. Phys. Chem. C* **2013**, *117*, 19622–19631.

- [271] Barron, L. D. In *Molecular Light Scattering and Optical Activity*, 2nd ed.; Barron, L. D., Ed.; Cambridge University Press, 2004.
- [272] Yang, W.-H.; Schatz, G. C.; Duyne, R. P. V. *J. Chem. Phys.* **1995**, *103*, 869–875.
- [273] Jensen, L.; Åstrand, P.-O.; Mikkelsen, K. V. *Int. J. Quantum Chem.* **2001**, *84*, 513–522.
- [274] Ayars, E. J.; Hallen, H. D.; Jahncke, C. L. *Phys. Rev. Lett.* **2000**, *85*, 4180–4183.
- [275] Hallen, H. D.; Jahncke, C. L. *J. Raman Spectrosc.* **2003**, *34*, 655–662.
- [276] Banik, M.; El-Khoury, P. Z.; Nag, A.; Rodriguez-Perez, A.; Guarrotttxena, N.; Bazan, G. C.; Apkarian, V. A. *ACS Nano* **2012**, *6*, 10343–10354.
- [277] Aikens, C. M.; Madison, L. R.; Schatz, G. C. *Nat. Photonics* **2013**, *7*, 508–510.
- [278] Takase, M.; Ajiki, H.; Mizumoto, Y.; Komeda, K.; Nara, M.; Nabika, H.; Yasuda, S.; Ishihara, H.; Murakoshi, K. *Nat. Photonics* **2013**, *7*, 550–554.
- [279] Feibelman, P. J. *Phys. Rev. B* **1975**, *12*, 1319–1336.
- [280] Moskovits, M.; DiLella, D. P.; Maynard, K. J. *Langmuir* **1988**, *4*, 67–76.
- [281] Sass, J. K.; Neff, H.; Moskovits, M.; Holloway, S. *J. Phys. Chem.* **1981**, *85*, 621–623.
- [282] Moskovits, M.; DiLella, D. P. *J. Chem. Phys.* **1980**, *73*, 6068–6075.
- [283] Wolkow, R. A.; Moskovits, M. *J. Chem. Phys.* **1986**, *84*, 5196–5199.
- [284] Polubotko, A. *Phys. Lett. A* **1990**, *146*, 81–84.
- [285] Moore, J. E.; Morton, S. M.; Jensen, L. *J. Phys. Chem. Lett.* **2012**, *3*, 2470–2475.
- [286] Morton, S. M.; Jensen, L. *J. Am. Chem. Soc.* **2009**, *131*, 4090–4098.
- [287] Zhao, L.; Jensen, L.; Schatz, G. C. *J. Am. Chem. Soc.* **2006**, *128*, 2911–2919.
- [288] Zhao, X.; Liu, S.; Li, Y.; Chen, M. *Spectrochim. Acta A* **2010**, *75*, 794–798.
- [289] Champion, A.; Kambhampati, P. *Chem. Soc. Rev.* **1998**, *27*, 241–250.
- [290] Albrecht, A. C. *J. Chem. Phys.* **1961**, *34*, 1476–1484.
- [291] Klingsporn, J. M.; Jiang, N.; Pozzi, E. A.; Sonntag, M. D.; Chulhai, D.; Seideman, T.; Jensen, L.; Hersam, M. C.; Duyne, R. P. V. *J. Am. Chem. Soc.* **2014**, *136*, 3881–3887.
- [292] Lombardi, J. R.; Birke, R. L. *J. Phys. Chem. C* **2008**, *112*, 5605–5617.
- [293] Kim, K.; Kim, K. L.; Lee, H. B.; Shin, K. S. *J. Phys. Chem. C* **2012**, *116*, 11635–11642.
- [294] Valley, N.; Greeneltch, N.; Van Duyne, R. P.; Schatz, G. C. *J. Phys. Chem. Lett.* **2013**, *4*, 2599–2604.
- [295] Zayak, A. T.; Hu, Y. S.; Choo, H.; Bokor, J.; Cabrini, S.; Schuck, P. J.; Neaton, J. B. *Phys. Rev. Lett.* **2011**, *106*, 083003.
- [296] Barron, L. D.; Buckingham, A. D. *Chem. Phys. Lett.* **2010**, *492*, 199–213.
- [297] Efrima, S. *Chem. Phys. Lett.* **1983**, *102*, 79–82.
- [298] Efrima, S. *J. Chem. Phys.* **1985**, *83*, 1356–1362.

- [299] Hecht, L.; Barron, L. D. *Chem. Phys. Lett.* **1994**, *225*, 519–524.
- [300] Hecht, L.; Barron, L. *J. Mol. Struct.: THEOCHEM* **1995**, *348*, 217–220, Molecular Spectroscopy and Molecular Structure 1994.
- [301] Janesko, B. G.; Scuseria, G. E. *J. Phys. Chem. C* **2009**, *113*, 9445–9449.
- [302] Bouř, P. *J. Chem. Phys.* **2007**, *126*, 136101.
- [303] Novák, V.; Šebestík, J.; Bouř, P. *J. Chem. Theor. Comput.* **2012**, *8*, 1714–1720.
- [304] Acevedo, R.; Lombardini, R.; Halas, N. J.; Johnson, B. R. *J. Phys. Chem. A* **2009**, *113*, 13173–13183.
- [305] Lombardini, R.; Acevedo, R.; Halas, N. J.; Johnson, B. R. *J. Phys. Chem. C* **2010**, *114*, 7390–7400.
- [306] Abdali, S.; Blanch, E. W. *Chem. Soc. Rev.* **2008**, *37*, 980–992.
- [307] Chulhai, D. V.; Jensen, L. *J. Phys. Chem. A* **2015**, *119*, 5218–5223.
- [308] Jensen, L. *J. Phys. Chem. A* **2009**, *113*, 4437–4444.
- [309] Li, X.-Y.; Huang, Q.-J.; Petrov, V. I.; Xie, Y.-T.; Luo, Q.; Yu, X.; Yan, Y.-J. *J. Raman Spectrosc.* **2005**, *36*, 555.
- [310] Mullin, J.; Valley, N.; Blaber, M. G.; Schatz, G. C. *J. Phys. Chem. A* **2012**, *116*, 9574–9581.
- [311] Kneipp, K.; Kneipp, H.; Kneipp, J. In *Plasmonics: Theory and Applications*; Shahbazyan, T. V., Stockman, M. I., Eds.; Challenges and Advances in Computational Chemistry and Physics; Springer Netherlands, 2013; Vol. 15; pp 103–124.
- [312] Valley, N.; Jensen, L.; Autschbach, J.; Schatz, G. C. *J. Chem. Phys.* **2010**, *133*, 054103.
- [313] Shoute, L. C. T.; Bartholomew, G. P.; Bazan, G. C.; Myers Kelley, A. *J. Chem. Phys.* **2005**, *122*, 184508.
- [314] Shoute, L. C. T.; Blanchard-Desce, M.; Myers Kelley, A. *J. Phys. Chem. A* **2005**, *109*, 10503–10511.
- [315] Silverstein, D. W.; Milojevich, C. B.; Camden, J. P.; Jensen, L. *J. Phys. Chem. C* **2013**, *117*, 20855–20866.
- [316] Eisenthal, K. B. *Chem. Rev.* **1996**, *96*, 1343–1360.
- [317] Liu, D.; Ma, G.; Levering, L. M.; Allen, H. C. *J. Phys. Chem. B* **2004**, *108*, 2252–2260.
- [318] Du, Q.; Superfine, R.; Freysz, E.; Shen, Y. R. *Phys. Rev. Lett.* **1993**, *70*, 2313–2316.
- [319] Hu, D.; Yang, Z.; Chou, K. C. *J. Phys. Chem. C* **2013**, *117*, 15698–15703.
- [320] Miyamae, T.; Ito, E.; Noguchi, Y.; Ishii, H. *J. Phys. Chem. C* **2011**, *115*, 9551–9560.
- [321] Miyamae, T.; Takada, N.; Tsutsui, T. *Appl. Phys. Lett.* **2012**, *101*, 073304.
- [322] Yamaguchi, S.; Tahara, T. *J. Phys. Chem. C* **2015**, *119*, 14815–14828.
- [323] Chen, Z.; Shen, Y. R.; Somorjai, G. A. *Ann. Rev. Phys. Chem.* **2002**, *53*, 437–465.
- [324] Shen, Y. R.; Ostroverkhov, V. *Chem. Rev.* **2006**, *106*, 1140–1154.

- [325] Ye, S.; Luo, Y. *Sci. China Chem.* **2014**, *57*, 1646–1661.
- [326] Ishiyama, T.; Imamura, T.; Morita, A. *Chem. Rev.* **2014**, *114*, 8447–8470.
- [327] Alieva, E.; Kuzik, L.; Yakovlev, V. *Chem. Phys. Lett.* **1998**, *292*, 542–546.
- [328] Alieva, E.; Petrov, Y.; Yakovlev, V.; Eliel, E.; van der Ham, E.; Vreken, Q.; van der Meer, A.; Sychugov, V. *JETP Lett.* **1997**, *66*, 609–613.
- [329] Baldelli, S.; Eppler, A. S.; Anderson, E.; Shen, Y.-R.; Somorjai, G. A. *J. Chem. Phys.* **2000**, *113*, 5432–5438.
- [330] Zhang, D.; Dougal, S. M.; Yeganeh, M. S. *Langmuir* **2000**, *16*, 4528–4532.
- [331] Humbert, C.; Busson, B.; Abid, J.-P.; Six, C.; Girault, H.; Tadjeddine, A. *Electrochim. Acta* **2005**, *50*, 3101–3110.
- [332] Pluchery, O.; Humbert, C.; Valamanesh, M.; Lacaze, E.; Busson, B. *Phys. Chem. Chem. Phys.* **2009**, *11*, 7729–7737.
- [333] Lis, D.; Caudano, Y.; Henry, M.; Demoustier-Champagne, S.; Ferain, E.; Cecchet, F. *Adv. Opt. Mater.* **2013**, *1*, 244–255.
- [334] Liu, W. T.; Shen, Y. R. *Proc. Natl. Acad. Sci. USA* **2014**, *111*, 1293–1297.
- [335] Yeh, Y. L.; Lei, J.; Chen, S. Y.; Chang, A. H. H.; Lin, C. K.; He, R. X.; Lin, S. H. *Sci. China Chem.* **2015**, DOI: 10.1002/jccs.201500044.
- [336] Lotem, H.; Lynch, R. T.; Bloembergen, N. *Phys. Rev. A* **1976**, *14*, 1748–1755.
- [337] Cheng, J.-X.; Xie, X. S. *J. Phys. Chem. B* **2003**, *108*, 827–840.
- [338] Thorvaldsen, A. J.; Ferrighi, L.; Ruud, K.; Agren, H.; Coriani, S.; Jorgensen, P. *Phys. Chem. Chem. Phys.* **2009**, *11*, 2293–2304.
- [339] Liang, E.; Weippert, A.; Funk, J.-M.; Materny, A.; Kiefer, W. *Chem. Phys. Lett.* **1994**, *227*, 115–120.
- [340] Baltog, I.; Baibarac, M.; Lefrant, S. *Phys. Rev. B* **2005**, *72*, 245402.
- [341] Addison, C. J.; Konorov, S. O.; Brolo, A. G.; Blades, M. W.; Turner, R. F. *J. Phys. Chem. C* **2009**, *113*, 3586–3592.
- [342] Ichimura, T.; Hayazawa, N.; Hashimoto, M.; Inouye, Y.; Kawata, S. *J. Raman Spectrosc.* **2003**, *34*, 651–654.
- [343] Steuwe, C.; Kaminski, C. F.; Baumberg, J. J.; Mahajan, S. *Nano Lett.* **2011**, *11*, 5339–5343.
- [344] Yampolsky, S.; Fishman, D. A.; Dey, S.; Hulkko, E.; Banik, M.; Potma, E. O.; Apkarian, V. A. *Nat. Photonics* **2014**, *8*, 650–656.
- [345] Chew, H.; Wang, D. S.; Kerker, M. *J. Opt. Soc. Am. B* **1984**, *1*, 56–66.
- [346] Hua, X.; Voronine, D. V.; Ballmann, C. W.; Sinyukov, A. M.; Sokolov, A. V.; Scully, M. O. *Phys. Rev. A* **2014**, *89*, 043841.
- [347] Parkhill, J. A.; Rappoport, D.; Aspuru-Guzik, A. *J. Phys. Chem. Lett.* **2011**, *2*, 1849–1854.
- [348] Schmid, W.; Schrötter, H. *Chem. Phys. Lett.* **1977**, *45*, 502.

- [349] Gruenke, N. L.; Cardinal, M. F.; McAnally, M. O.; Frontiera, R. R.; Schatz, G. C.; Van Duyne, R. P. *Chem. Soc. Rev.* **2016**, *45*, 2263–2290.
- [350] Turley, H. K.; Camden, J. P. *Chem. Commun.* **2014**, *50*, 1472–1474.
- [351] Chulhai, D. V.; Hu, Z.; Moore, J. E.; Chen, X.; Jensen, L. *Ann. Rev. Phys. Chem.* **2016**, *67*, 541–564.
- [352] Butet, J.; Martin, O. J. F. *J. Phys. Chem. C* **2015**, *119*, 15547–15556.
- [353] Polubotko, A. M.; Smirnov, V. P. *J. Raman Spectrosc.* **2012**, *43*, 380–388.
- [354] Rinaldi, J. M.; Morton, S. M.; Jensen, L. *Mol. Phys.* **2013**, *111*, 1322–1331.
- [355] Moore, J. E.; Jensen, L. *J. Phys. Chem. C* **2016**, *120*, 5659–5666.
- [356] Turley, H. K.; Hu, Z.; Silverstein, D. W.; Cooper, D. A.; Jensen, L.; Camden, J. P. *J. Phys. Chem. C* **2016**, *120*, 20936–20942.
- [357] Chulhai, D. V.; Chen, X.; Jensen, L. *J. Phys. Chem. C* **2016**, *120*, 20833–20842.
- [358] Chen, X.; Moore, J.; Zekarias, M.; Jensen, L. *Nature Comm.* **2015**, *6*, 8921.
- [359] Johnson, P. B.; Christy, R. W. *Phys. Rev. B* **1972**, *6*, 4370–4379.
- [360] Silva-Junior, M. R.; Schreiber, M.; Sauer, S. P. A.; Thiel, W. *J. Chem. Phys.* **2008**, *129*, 104103.
- [361] Bolovinos, A.; Philis, J.; Pantos, E.; Tsekeris, P.; Andritsopoulos, G. *J. Chem. Phys.* **1981**, *75*, 4343–4349.
- [362] Camden, J. P.; Dieringer, J. A.; Zhao, J.; Van Duyne, R. P. *Acc. Chem. Res.* **2008**, *41*, 1653–1661.
- [363] Zeman, E. J.; Schatz, G. C. *J. Phys. Chem.* **1987**, *91*, 634–643.
- [364] Kearns, H.; Sengupta, S.; Sasselli, I. R.; Bromley III, L.; Faulds, K.; Tuttle, T.; Bedics, M. A.; Detty, M. R.; Velarde, L.; Graham, D.; Smith, W. E. *Chem. Sci.* **2016**, *7*, 5160–5170.
- [365] Petrovykh, D. Y.; Pérez-Dieste, V.; Opdahl, A.; Kimura-Suda, H.; Sullivan, J. M.; Tarlov, M. J.; Himpel, F. J.; Whitman, L. J. *J. Am. Chem. Soc.* **2006**, *128*, 2–3, PMID: 16390092.
- [366] Bhowmick, S.; Saini, S.; Shenoy, V. B.; Bagchi, B. *J. Chem. Phys.* **2006**, *125*, 181102.
- [367] Creighton, J. *Surf. Sci.* **1983**, *124*, 209 – 219.
- [368] Moskovits, M.; Suh, J. S. *J. Phys. Chem.* **1984**, *88*, 5526–5530.
- [369] Le Ru, E. C.; Meyer, S. A.; Artur, C.; Etchegoin, P. G.; Grand, J.; Lang, P.; Maurel, F. *Chem. Commun.* **2011**, *47*, 3903–3905.
- [370] Yu, N.-T.; Nie, S.; Lipscomb, L. A. *J. Raman Spectrosc.* **2005**, *21*, 797.
- [371] Hulteen, J. C.; Young, M. A.; Van Duyne, R. P. *Langmuir* **2006**, *22*, 10354.
- [372] Gohlke, M.; Heiner, Z.; Kneipp, J. *Phys. Chem. Chem. Phys.* **2015**, *17*, 26093–26100.
- [373] Hu, Z.; Chulhai, D. V.; Jensen, L. *J. Chem. Theor. Comput.* **2016**, *12*, 5968–5978.

- [374] Weiss, P. A.; Silverstein, D. W.; Jensen, L. *J. Phys. Chem. Lett.* **2014**, *5*, 329–335.
- [375] Li, P.; Zhou, X.; Liu, H.; Yang, L.; Liu, J. *J. Raman Spectrosc.* **2013**, *44*, 999–1003.
- [376] Heinz, T. F.; Chen, C. K.; Ricard, D.; Shen, Y. R. *Phys. Rev. Lett.* **1982**, *48*, 478–481.
- [377] Hill, W.; Werner, L.; Marlow, F. *Ber. Bunsen. Phys. Chem.* **1991**, *95*, 1453–1458.
- [378] Kikteva, T.; Star, D.; Zhao, Z.; Baisley, T. L.; Leach, G. W. *J. Phys. Chem. B* **1999**, *103*, 1124–1133.
- [379] Nie, S. M.; Emory, S. R. *Science* **1997**, *275*, 1102–1106.
- [380] Kneipp, K.; Wang, Y.; Kneipp, H.; Perelman, L. T.; Itzkan, I.; Dasari, R. R.; Feld, M. S. *Phys. Rev. Lett.* **1997**, *78*, 1667–1670.
- [381] Le Ru, E. C.; Etchegoin, P. G.; Meyer, M. *J. Chem. Phys.* **2006**, *125*, 204701.
- [382] Etchegoin, P. G.; Meyer, M.; Blackie, E.; Le Ru, E. C. *Anal. Chem.* **2007**, *79*, 8411–8415.
- [383] Turley, H. K.; Hu, Z.; Jensen, L.; Camden, J. P. *J. Phys. Chem. Lett.* **2017**, *8*, 1819–1823, PMID: 28383922.
- [384] Anderson, M. S. *Appl. Phys. Lett.* **2000**, *76*, 3130–3132.
- [385] Stöckle, R. M.; Suh, Y. D.; Deckert, V.; Zenobi, R. *Chem. Phys. Lett.* **2000**, *318*, 131–136.
- [386] Steidtner, J.; Pettinger, B. *Phys. Rev. Lett.* **2008**, *100*, 236101.
- [387] Duan, S.; Tian, G.; Ji, Y.; Shao, J.; Dong, Z.; Luo, Y. *J. Am. Chem. Soc.* **2015**, *137*, 9515–9518.
- [388] Liu, P.; Chulhai, D. V.; Jensen, L. *ACS Nano* **2017**, *11*, 5094–5102, PMID: 28463555.
- [389] Kauranen, M.; Zayats, A. V. *Nat. Photonics* **2012**, *6*, 737–748.
- [390] Butet, J.; Brevet, P.-F.; Martin, O. J. F. *ACS Nano* **2015**, *9*, 10545–10562, PMID: 26474346.
- [391] Hajjisaalem, G.; Nezami, M. S.; Gordon, R. *Nano Lett.* **2014**, *14*, 6651–6654.
- [392] Savage, K. J.; Hawkeye, M. M.; Esteban, R.; Borisov, A. G.; Aizpurua, J.; Baumberg, J. J. *Nature* **2012**, *491*, 574–577.
- [393] Esteban, R.; Borisov, A. G.; Nordlander, P.; Aizpurua, J. *Nature Comm.* **2012**, *3*, 825.
- [394] Barbry, M.; Koval, P.; Marchesin, F.; Esteban, R.; Borisov, A. G.; Aizpurua, J.; Sánchez-Portal, D. *Nano Lett.* **2015**, *15*, 3410–3419.
- [395] Denk, W.; Strickler, J. H.; Webb, W. W. *Science* **1990**, *248*, 73–76.
- [396] So, P. T. C.; Dong, C. Y.; Masters, B. R.; Berland, K. M. *Annu. Rev. Biomed. Eng.* **2000**, *2*, 399–429.
- [397] Cohanoschi, I.; Hernández, F. E. *J. Phys. Chem. B* **2005**, *109*, 14506–14512, PMID: 16852828.
- [398] Albota, M. et al. *Science* **1998**, *281*, 1653.
- [399] Schatz, G. C.; Van Duyne, R. P. In *Handbook of Vibrational Spectroscopy*; Chalmers, J. M., Griffiths, P. R., Eds.; John Wiley and Sons, Ltd: New York, 2002; Vol. 1; pp 759–774.

- [400] Tomasi, J.; Persico, M. *Chem. Rev.* **1994**, *94*, 2027–2094.
- [401] Tomasi, J.; Mennucci, B.; Cammi, R. *Chem. Rev.* **2005**, *105*, 2999–3094.
- [402] Cossi, M.; Rega, N.; Scalmani, G.; Barone, V. *J. Comput. Chem.* **2003**, *24*, 669–681.
- [403] Warshel, A.; Levitt, M. *J. Mol. Biol.* **1976**, *103*, 227–249.
- [404] Bash, P. A.; Field, M. J.; Karplus, M. *J. Am. Chem. Soc.* **1987**, *109*, 8092–8094.
- [405] Jacob, C. R.; Neugebauer, J.; Jensen, L.; Visscher, L. *Phys. Chem. Chem. Phys.* **2006**, *8*, 2349–2359.
- [406] Car, R.; Parrinello, M. *Phys. Rev. Lett.* **1985**, *55*, 2471–2474.
- [407] Klamt, A.; Schuurmann, G. *J. Chem. Soc., Perkin Trans. 2* **1993**, 799–805.
- [408] Pye, C. C.; Ziegler, T. *Theor. Chim. Acta* **1999**, *101*, 396–408.
- [409] Dreuw, A.; Head-Gordon, M. *J. Am. Chem. Soc.* **2003**, *126*, 4007–4016.
- [410] Iikura, H.; Tsuneda, T.; Yanai, T.; Hirao, K. *J. Chem. Phys.* **2001**, *115*, 3540–3544.
- [411] Vydrov, O. A.; Scuseria, G. E. *J. Chem. Phys.* **2006**, *125*, 234109.
- [412] Yanai, T.; Tew, D. P.; Handy, N. C. *Chem. Phys. Lett.* **2004**, *393*, 51–57.
- [413] Rebolini, E.; Toulouse, J. *J. Chem. Phys.* **2016**, *144*, 094107.
- [414] Neugebauer, J.; Louwarse, M. J.; Baerends, E. J.; Wesolowski, T. A. *J. Chem. Phys.* **2005**, *122*, 094115.
- [415] Bylaska, E. J. et al. NWChem, A Computational Chemistry Package for Parallel Computers, Version 5.1. Pacific Northwest National Laboratory: Richland, Washington 99352-0999, USA, 2007; A modified version.
- [416] DALTON, a molecular electronic structure program, release 2.0. 2005; see <http://www.kjemi.uio.no/software/dalton/dalton.html>.
- [417] Chiang, N.; Jiang, N.; Chulhai, D. V.; Pozzi, E. A.; Hersam, M. C.; Jensen, L.; Seideman, T.; Van Duyne, R. P. *Nano Lett.* **2015**, *15*, 4114–4120.
- [418] Watanabe, H.; Hayazawa, N.; Inouye, Y.; Kawata, S. *J. Phys. Chem. B* **2005**, *109*, 5012–5020, PMID: 16863161.

Vita

Zhongwei Hu

Education

- 2012 to 2017 Ph.D., Chemistry
The Pennsylvania State University
University Park, PA
- 2008 to 2012 B.S., Mathematics; Minor, Chemistry
Juniata College
Huntingdon, PA

Awards and Honors

- 2015/2016 Chemistry Travel Award
2015 Donald and Barbara Weyenberg Graduate Fellowship
2012 Incoming Class New Graduate Student Fellowship
2012 The Alice G. Blaisdell Prizes in Mathematics
2012 The Dr. Andrew B. and Maria F. Brumbaugh Science Prize
2012 The Mathematical Contest in Modeling Honorable Mention
2011/2012 Hypercube Scholar Award
2009 Samuel J. Steinberger, Jr. Memorial Award

Publications

- Z. Hu** and L. Jensen; "Importance of Double-Resonance Effects in Two-Photon Absorption Properties of $\text{Au}_{25}(\text{SR})_{18}^-$ " *Chem. Sci.* **2017**, *8*, 4595.
- H. K. Turley,* **Z. Hu.**,* L. Jensen and J. P. Camden; "Surface-Enhanced Resonance Hyper-Raman Scattering Elucidates Molecular Orientation of Rhodamine 6G on Silver Colloids" *J. Phys. Chem. Lett.* **2017**, *8*, 1819.
- Z. Hu**, D. V. Chulhai and L. Jensen; "Simulating Surface-Enhanced Hyper-Raman Scattering Using Atomistic Electrostatics-Quantum Mechanical Methods" *J. Chem. Theory Comput.* **2016**, *12*, 5968.
- H. K. Turley, **Z. Hu.**, D. W. Silverstein, D. A. Cooper, L. Jensen and J. P. Camden; "Probing Two-Photon Molecular Properties with Hyper-Raman Scattering: A Combined Experimental and Theoretical Study of Crystal Violet" *J. Phys. Chem. C* **2016**, *120*, 20936
- D. V. Chulhai, **Z. Hu**, J. E. Moore, X. Chen and L. Jensen; "Theory of Linear and Nonlinear Surface-Enhanced Vibrational Spectroscopy" *Annu. Rev. Phys. Chem.* **2016**, *67*, 541–564.
- Z. Hu.**, J. Autschbach, and L. Jensen; "Simulating Third-Order Nonlinear Optical Properties Using Damped Cubic Response Theory within Time-Dependent Density Functional Theory" *J. Chem. Theory Comput.* **2016**, *12* 1294.
- Z. Hu.**, J. Autschbach, and L. Jensen; "Simulation of Resonance Hyper-Rayleigh Scattering of Molecules and Metal Clusters Using a Time-Dependent Density Functional Theory Approach" *J. Chem. Phys.* **2014**, *141*2 124305.